Ab initio description of second-harmonic generation from crystal surfaces

Nicolas Tancogne-Dejean

Thèse présentée pour obtenir le grade de

Docteur de l'École polytechnique

Spécialité : Physique

par

Nicolas TANCOGNE-DEJEAN

Ab initio description of second-harmonic generation from crystal surfaces

Thèse soutenue publiquement le 21 septembre 2015 devant le jury composé de :

Prof.	Stefano OSSICINI	Rapporteur
Dr.	Christophe DELERUE	Rapporteur
Prof.	Benoît BOULANGER	Examinateur
Dr.	Phuong Mai DINH	Examinateur
Prof.	Luca PERFETTI	Examinateur
Dr.	Christian BROUDER	Examinateur
Dr.	Valérie VÉNIARD	Directrice de thèse

We can only see a short distance ahead, but we can see plenty there that needs to be done.
Alan Turing

Contents

Preface iii

Abbreviations and notations vii

I Background 1

1 Introduction 3
- 1.1 Historical background . . . 3
- 1.2 Second-harmonic generation . . . 4
- 1.3 Microscopic-macroscopic connection . . . 7
- 1.4 Longitudinal-transverse and optical limit . . . 11
- 1.5 Present work . . . 16

2 Second-harmonic generation in reflection 19
- 2.1 Second-order polarization induced by incident light . . . 21
- 2.2 Harmonic field inside the material . . . 22
- 2.3 Reflected harmonic light from a surface . . . 24
- 2.4 Bulk contribution . . . 26

3 (Time-Dependent) Density-Functional Theory in a nutshell 29
- 3.1 Time-dependent perturbation theory . . . 29
- 3.2 Density-Functional Theory (DFT) . . . 32
- 3.3 Time-Dependent Density-Functional Theory (TDDFT) . . . 36
- 3.4 Perturbation theory and TDDFT . . . 38
- 3.5 TDDFT in practice . . . 42

4 Silicon and its (001) surface 47
- 4.1 Silicon . . . 47
- 4.2 The role of silicon surfaces in novel applications . . . 48
- 4.3 The (001) surface of silicon . . . 49
- 4.4 Geometries and reconstructions . . . 50

II Microscopic theory of second-harmonic generation from crystal surfaces **55**

5 Microscopic theory of surface second-harmonic generation **57**

5.1 Extracting the surface second-harmonic generation spectra 58

5.2 Discussions 69

6 Effects of nonlocal operators on surface second-harmonic generation **79**

6.1 Nonlocal operators and perturbation theory 80

6.2 Numerical results 86

III Local-field effects in surface optical properties **91**

7 *Ab initio* macroscopic linear and second-order optical properties of crystal surfaces: From the slab to the single surface **93**

7.1 Macroscopic dielectric tensor of crystal surfaces 94

7.2 Optical limit for the surface macroscopic dielectric function 96

7.3 Calculation of $\epsilon_M^{S,LL}$ in TDDFT 98

7.4 Macroscopic second-order tensor of crystal surfaces 99

7.5 Properties of the surface macroscopic quantities 106

8 Local-field effects for linear optical properties of thin-films and surfaces **109**

8.1 Local-field effects and super-cells 110

8.2 Mixed-space approach 113

8.3 Selected-G approach 116

8.4 Discussion 121

IV Application to Silicon Surfaces **127**

9 Local-field effects on second-harmonic generation from surfaces **129**

9.1 Local-Field Effects on the clean Si(001) SHG spectra 130

9.2 Hydrogenated surfaces and local-field effects 132

9.3 Comparison with experimental results 134

10 Excitonic effects on second-harmonic generation from silicon surfaces **141**

10.1 The α-kernel as a post-processing 142

10.2 Excitonic effects on the surface second-harmonic generation 147

Concluding remarks **151**

V Appendices **153**

A Fourier transforms **155**

B Maxwell's equations **159**

C Second-harmonic reflection coefficients for some symmetries **163**

D Matrix elements of $\mathcal{V}$ in a plane-waves basis **167**

E Divergence-free expression of $\chi^S_{\rho\rho\rho}$ **169**

F Macroscopic surface response functions **175**

G Analytical expression of $\tilde{v}_{\mathbf{G_1},\mathbf{G_2}}(\mathbf{q})$ **177**

H Mixed-space equations for SHG **179**

I Optical properties of single surfaces **181**

List of publications **186**

List of codes **188**

Bibliography **191**

Preface

> The field of nonlinear spectroscopy has matured rapidly but still has much potential for further exploration and exploitation. The applications in chemistry, biology, medicine, materials technology, and especially in the field of communications and information processing are numerous. Alfred Nobel would have enjoyed this interaction of physics and technology.
>
> Nicolaas Bloembergen, Nobel Lecture, 1981

Only one year after the invention of the laser in 1960, researchers showed that laser light could be converted from one color to another. Using a red ruby laser light and a quartz crystal, Frankel and coworkers have demonstrated the possibility to create an ultraviolet radiation from red light. This was the first demonstration of a nonlinear optical phenomenon.
More than 50 years after the first experimental observation of second-harmonic generation, the theoretical description of second-harmonic generation is still under debate, whereas it is well understood from an experimental point of view. This is the gap that this thesis aims to fill.
More precisely, the goal of this work is to improve the theoretical description and understanding of the generation of second-harmonic from the surfaces of crystalline semiconductors.
When applying an external electric field to a dielectric material, electric dipoles are created at a microscopic level. These dipoles are responsible for the apparition, inside the material, of an induced field. The fluctuations of the electric field at a microscopic level, the density fluctuations or any kind of microscopic inhomogeneities must be taken into account when describing the optical properties of a system. These effects are often referred as "local-field effects".
These local-field effects have been widely studied in the past and in particular their effects on the optical properties of bulk materials are now well established. In the case of surfaces, the theoretical description and the numerical simulations are more intricate than for bulk materials. The abrupt change in the electronic density leads to a huge variation of the electric field at the interface with vacuum. As a result, strong effects of the local-field are expected, in particular in the direction perpendicular to the plane of the surface.
The goal of this thesis is to quantify how important these effects are for the linear and second-order optical properties of surfaces.
This thesis is organised in four parts. The Part I focuses on the theoretical background, necessary to understand the development reported in this thesis.
Part II presents the first theoretical results of this thesis, improving the microscopic description of second-harmonic generation at crystal surfaces. A macroscopic theory of second-harmonic genera-

tion from crystal surfaces is developed in Part III, in order to account for local-field effects.
The last part of this thesis, Part IV, is dedicated to the application of the theory developed to silicon surfaces. The numerical simulations have been focused on the Si(001) surface, and the macroscopic formalism developed during this thesis has been applied to three surface reconstructions, namely the clean Si(001)2×1, the monohydride Si(001)2×1:H and the dihydride Si(001)1×1:2H surfaces. Comparison with available experimental results is also reported.

Abbreviations

AFM	Atomic Force Microscope
BZ	Brillouin zone
BSE	Bethe-Salpeter equation
(TD)DFT	(Time-Dependent) Density-Functional Theory
EFISH	Electric Field Induced Second-Harmonic
HEG	Homogeneous Electron Gas
HK	Hohenberg-Kohn
IPA	Independent-Particle Approximation
KS	Kohn-Sham
LDA	Local-Density Approximation
LF	Local-fields
LRC	Long-Range Contribution
RA	Reflectance Anisotropy
RPA	Random Phase Approximation
SHG	Second-Harmonic Generation
TD	Time Dependent
XC	Exchange-Correlation

Notations

General

$\mathbf{r}$	A point in 3-D space, (x, y, z)
t	An instant in time
ω	A frequency (time Fourier transform)
$\mathbf{k}$	A vector in reciprocal space
$\mathbf{q}$	A vector inside the first Brillouin zone
$\mathbf{G}$	A reciprocal lattice vector, also referred as $\mathbf{G}$-vector
$f[n]$	A *functional* f of the function n

(TD)-DFT and response functions

E_{tot}	Ground-state total energy
$n_0(\mathbf{r})$	Ground-state electronic density
$n(\mathbf{r}, t)$	TD electronic density
$\mathbf{j}(\mathbf{r}, t)$	TD electronic current
Ψ	Interacting many-body wave-function
ϕ_i	Single-particle or Kohn-Sham wave-function
$\chi_0^{(1)}$, $\chi_{\rho\rho}^{(0)}$	Independent-particle density-density response function
$\chi^{(1)}$, $\chi_{\rho\rho}^{(1)}$	Fully interacting density-density response function
$\chi_0^{(2)}$, $\chi_{\rho\rho\rho}^{(0)}$	Independent-particle density-density-density response function
$\chi^{(2)}$, $\chi_{\rho\rho\rho}^{(2)}$	Fully interacting density-density-density response function

Varia

η	Positive infinitesimal
c	Speed of light in the vacuum
ϵ_0	Vacuum permittivity
$\overleftrightarrow{\mathbb{1}}$	Unit dyadic

If not stated differently, atomic units are used throughout this thesis.

Part I

Background

1. Introduction

The aim of this chapter is twofold. In a first part, I present the nonlinear optics and in particular second-harmonic generation. Some examples of the applications of second-harmonic generation are presented, showing how important this phenomenon is for many fields of physics, biology, etc.
The second part of this chapter is dedicated to the connection between the microscopic and the macroscopic description of the light-matter interaction. In particular, I will present how we can define the measurable macroscopic quantities and how we can link them to the microscopic quantities describing the system. Also, I will show that within the long-wavelength approximation, the calculation of optical properties can be restricted to the calculation of the longitudinal response to a longitudinal perturbation.

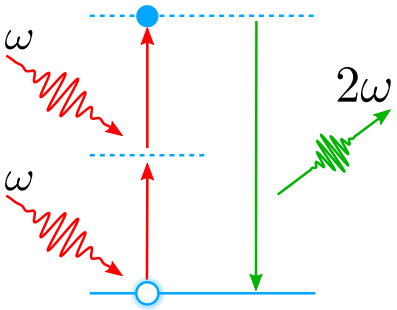

Fig. 1.1: Sketch of the second-harmonic generation process

1.1 Historical background

The first nonlinear optical process which has been observed experimentally is the Kerr effect, named after John Kerr who discovered it in 1877 [1]. This Kerr effect corresponds to a change in the refractive index of a material, proportionally to the square of the applied electric field. Later, it has been discovered in 1893 by Friedrich Carl Alwin Pockels that a birefringence can also be induced proportionally to the electric field. This effect is nowadays known as the Pockels effect or the linear electro-optic effect; by opposition to the Kerr effect which is sometimes referred as the quadratic electro-optic effect. But this is only in 1961, with the discovery of Second-Harmonic Generation (SHG) by Peter Franken and its colleagues [2], that the field of nonlinear optics really starts to exist. Using a quartz crystal, they managed to double the frequency of the red light of a ruby laser, halving its wavelength from 694.2 nm to an ultraviolet wavelength of 347.1 nm. The discovery of second-harmonic generation is important for two reasons. First, an ordinary light is non-coherent, so a laser was required for generating harmonics. This explains the gap in time between the discovery of Kerr and Pockels effects and the one of the second-harmonic generation. Second, it was the first nonlinear phenomenon where a coherent output was obtained from a coherent input.
From the discovery of SHG, the field of nonlinear optics grew quickly. In 1962, Bass *et al.* discovered the optical rectification, where a quasi-static polarization is induced by an electric field [3]. In 1967, New *et al.* observed in gases for the first time the third-harmonic generation [4]. The same year, Lee

et al. discovered that applying a dc-electric field to a nonlinear medium was changing the intensity of the second-harmonic generation [5], a process which is now referred as the Electric Field Induced Second-Harmonic Generation (EFISH). Numerous other nonlinear optical effects have also been discovered since 1961 and the discovery of the second-harmonic generation; and nowadays nonlinear optics is used in many fields of the physics, biology or chemistry but also in neurosciences, in surgery, in data transmission and more recently for producing x-ray laser radiations.

1.2 Second-harmonic generation

In the case of a weak excitation, of frequency ω, the electric polarization $\mathbf{P}$ is related to the electric field $\mathbf{E}$ by the relation

$$P_i(\omega) = \sum_j \chi_{ij}^{(1)}(\omega) E_j(\omega), \tag{1.1}$$

where P_i and E_j are Cartesian components of $\mathbf{P}$ and $\mathbf{E}$ with $i, j \in \{x, y, z\}$.
This relation defines the linear dielectric susceptibility $\chi^{(1)}$. This regime corresponds to the linear optics, where the response is proportional to the perturbing electric field. The tensor $\chi^{(1)}$ describes the absorption of light, the reflection at surfaces as well as the loss functions.
When the perturbing electric field is more intense, nonlinear effects are no more negligible and we must account for them.
It is possible to generalize the expression Eq. (1.1) (where we have omitted position and frequency arguments for sake of simplicity)

$$P_i = \sum_j \chi_{ij}^{(1)} E_j + \sum_{jk} \chi_{ijk}^{(2)} E_j E_k + \sum_{jkl} \chi_{ijkl}^{(3)} E_j E_k E_l + \dots \tag{1.2}$$

where $\chi_{ijk}^{(2)}$ is a third rank tensor (meaning a 3 indices tensor and so 27 components), which characterizes the second-order nonlinear susceptibility. Due to the symmetric role of the electric fields, this tensor follows the permutation rule $\chi_{ijk}^{(2)} = \chi_{ikj}^{(2)}$.
If we consider the incident fields as being the superposition of two fields oscillating respectively at frequencies ω_1 and ω_2, it is possible to obtain many phenomena, summarized in Tab. 1.1.
The $\chi_{ijkl}^{(3)}$ tensor describes new phenomena such as the four-waves mixing or the Kerr effect. If the

Second-order process	Definition
Frequency doubling	$\chi^{(2)}(-2\omega_1, \omega_1, \omega_1)$
Optical rectification	$2\chi^{(2)}(0, \omega_1, -\omega_1)$
Sum frequency	$2\chi^{(2)}(-\omega_1 - \omega_2, \omega_1, \omega_2)$
Frequency difference	$2\chi^{(2)}(-\omega_1 + \omega_2, \omega_1, \omega_2)$

Tab. 1.1: List of different effects that can occur when two beams oscillating respectively at frequencies ω_1 and ω_2 propagate in a medium which exhibits a non-zero second-order nonlinear susceptibility. In this table, we use the convention where the emitted signal is denoted with a minus sign. Nevertheless this convention is not used in this thesis.

perturbation is not so intense, we can expect the expansion in power of the electric field Eq. (1.2) to

converge, and thus to have $|\chi^{(2)}_{ijk}| \gg |\chi^{(3)}_{ijkl}|$. This is not the case for strong laser-fields, *e.g.*, the High-Harmonic Generation (HHG), where a lot of harmonics are obtained with a similar intensity [6]. In this thesis, the perturbing laser-field is considered to be weak enough that the expansion Eq. (1.2) converges.

As suggested by the title of this thesis, among all possible nonlinear phenomena, only the second-order nonlinear process where $\omega_1 = \omega_2 = \omega$, and known as the second-harmonic generation, will be considered. The second-harmonic generation process can be explained in a very simple version by the sketch presented in Fig. 1.1. In this picture, two virtual states are involved, *i.e.*, they do not correspond to the energy levels of the system. The sketch in Fig. 1.1 describes the absorption of two photon at the frequency ω and the relaxation to the ground-state by the emission of a photon, whose frequency is 2ω; due to the conservation of energy.

Obviously, this simple view could not be used to describe real crystals, which are many-body systems; with more levels involved, and where electrons are interacting with the other electrons and with the holes. How these many-body effects affect the second-harmonic generation from surfaces is the primary question that this thesis aims to address.

1.2.1 Applications of second-harmonic generation

Here I give some applications of second-harmonic generation. The goal is not to give an exhaustive list of all possible applications but to show how important this phenomenon is for many domains of science, including physics, chemistry or biology.

Frequency conversion

The major application of second-harmonic generation is the frequency conversion. SHG is thus able to extend the available coherent light sources to shorter wavelengths. Nowadays it is almost impossible to imagine an experimental optical set-up including lasers without a nonlinear crystal. The number of available laser frequencies being limited, second-harmonic generation is an easy and powerful way for generating new laser frequencies.

As a consequence, the search of new nonlinear crystals with a high SHG efficiency is still an intensive area of research, as shown by the literature published on this subject recently [7–11]. But more recently, a new area of research has emerged, focusing on new ways for obtaining second-harmonic generation; for novel applications. Among these new applications, we find for instance the on-chip integrated components with enhanced second-harmonic generation, as nanowires [12, 13]; or new materials such as layered Transition-Metal Dichalcogenide (TMDs) [14–16].

Second-harmonic microscopy, biological tissues and neurones imaging

One of the most interesting properties of SHG is its sensitivity to the symmetries of the system and in particular to the inversion symmetry. Along the years, numerous applications have emerged, where second-harmonic generation plays the key role. Among them, we find the second-harmonic microscopy, where one uses centro-symmetric substrates in order to image non-centrosymmetric particles or molecules, see Fig. 1.2(a-b). By shining the substrate with a laser and collecting only the

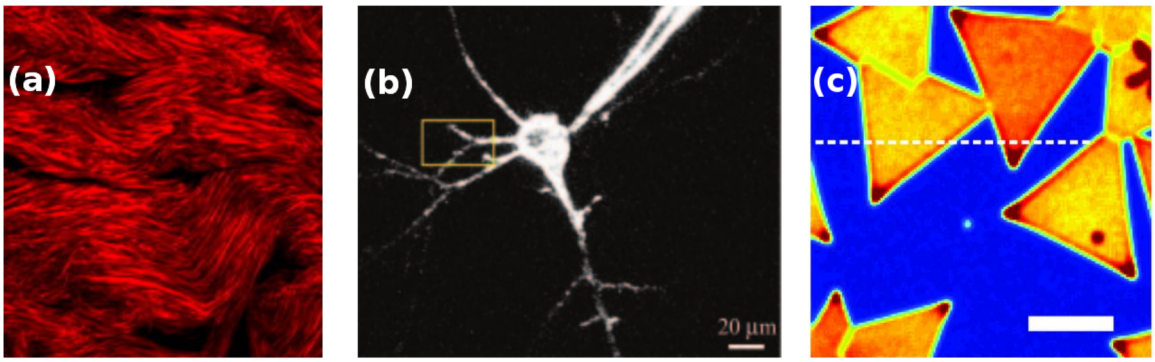

Fig. 1.2: (a) SHG imaging of collagen in 20 μm rat-foot flexor tendon cryosections. From Ref. [17]. (b) SHG measurements of membrane potential in pyramidal neurons from hippocampal cultures and neocortical brain slices. From Ref. [18]. (c) SHG image of discrete triangular islands of MoS_2 crystals. From Ref. [19].

second-harmonic signal, one obtains a high-sensitivity microscope, detecting single nanoparticles, *e.g.* Refs. [20, 21].
This sensitivity is also used for imaging biological tissues and in particular, for the collagen fibres; which are made of two distinct types of collagen, one being centro-symmetric, the other one not. This is a major advantage for the second-harmonic generation over the linear optical techniques which are unable to provide us with a contrast between the different kinds of collagen [17, 22].
The same idea is used in neuroscience to study neurones, with a high resolution SHG imaging [18].

Characterization of thin films, interfaces and surfaces

The use of the sensitivity to symmetries of SHG is not only restricted to biology and neurosciences. Surface science makes also an extensive use of SHG for the characterization of thin films [23–25], interfaces [26–29], surfaces [30–34], and more recently monolayer materials as TMDs [15, 19], see Fig. 1.2(c). In these cases, the second-harmonic generation is used as an *in situ*, non-invasive and non-destructive probe. Various techniques have been developed, allowing real-time monitoring of semiconductors growth, surface reconstruction determination, *etc*.
The experimental set-up is sketched in Fig. 1.3. A great force of SHG is that in experiments, one can vary the incoming polarization, choose the angle of incidence, select the out-going polarization or rotate the sample. This gives access to a lot of information and, going further, it is possible to identify specific fingerprints of some structures, see, for instance for surfaces, Ref. [35]. In SHG surface applications, the main condition is that the bulk material used is centro-symmetric. As a consequence, the second-harmonic signal originates only from the symmetry-breaking regions as defects, interfaces and, more importantly, surfaces.

1.2.2 Second-harmonic generation related phenomena

Some phenomena are related to the second-harmonic generation and in particular to the propagation of the pump and harmonic waves inside the medium.

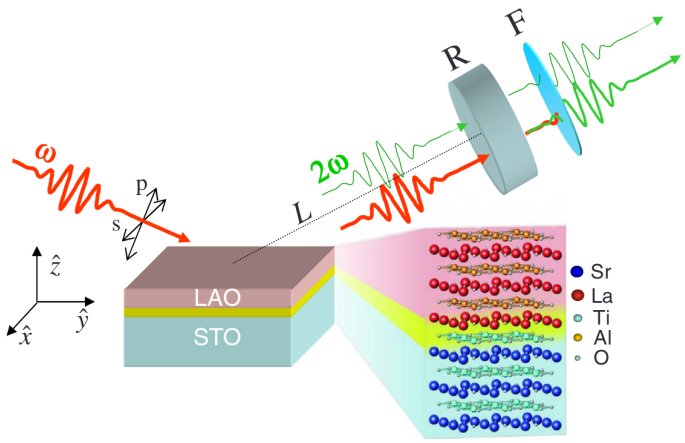

Fig. 1.3: An SHG experiment for probing the structural properties of an interface. Taken from Ref. [36]

Pump depletion

The pump depletion is a phenomenon that occurs when the conversion to second-harmonic inside the nonlinear medium becomes important, with respect of the linear absorption of light. When this is the case, the intensity of the pump decreases quickly inside the medium. As a consequence, the observed second-harmonic signal intensity is lower than expected, because only a small region of the material contributes to the SHG signal. However, this thesis focuses on the calculation of the second-order nonlinear susceptibility $\chi^{(2)}$ and not on the propagation of the pump or the harmonic light inside the medium. As the pump depletion does not affect the second-order susceptibility, this phenomena is not discussed in this thesis.

Finite linewidth effects

The laser sources have always a finite line-width. In particular, the line-width of the pumping laser, have a influence on the emitted second-harmonic signal. The effects of the finite line-width of a laser source can always be obtained by considering a superposition of monochromatic waves. Therefore, only strictly monochromatic waves are considered in this thesis and no effect of the finite line-width of the interacting waves is discussed in this thesis.

1.3 Microscopic-macroscopic connection

Throughout this thesis, I will extensively discuss about microscopic and macroscopic quantities. The microscopic quantities to which I refer are quantities that fluctuate in space at the scale of the microscopic world. The fluctuations of the charges and of the electromagnetic field are of the order of 0.1 nm or less. This number is small in comparison to the associated numbers for the optical probes used in experiments; *e.g.*, the infra-red wavelength of a Ti:sapphire laser being 780 nm.
Thus in experiments, all microscopic quantities are averaged by measurement devices in space and all the fluctuations vanish. Therefore, the physical or measurable quantities are macroscopic quantities which are smooth and slowly varying in space. Some examples of these quantities are the

transmission/reflection coefficients, the absorption spectra or the loss functions. In the case of the generation of second-harmonic by reflection of light on a surface, the measurable quantities are the reflection coefficients, as explained more in details in Chap. 2.
The measurable quantities, or macroscopic quantities, are entirely determined by the microscopic quantities. The procedure which links the microscopic quantities (described by microscopic Maxwell equations, see Eqs. B.1) to the macroscopic quantities (macroscopic Maxwell equations, Eqs. B.9) is called the macroscopic averaging.
The question of the definition of this averaging procedure is not simple and requires some care. Different definitions can be found in the literature, *e.g.*, Refs. [37–40]. As pointed out in Ref. [39], this procedure depends on the nature of the system. In this thesis we adopt the approach of R. Del Sole and E. Fiorino [38] for dealing with periodic systems.

1.3.1 Local-fields

When applying an external electric field $\mathbf{E}^{\text{ext}}$ to a dielectric material, electric dipoles are created at a microscopic level. These dipoles are responsible for the apparition, inside the material, of an induced field $\mathbf{E}^{\text{ind}}$. The total electric field felt by electrons is microscopic and is thus given by these two contributions; $\mathbf{E} = \mathbf{E}^{\text{ext}} + \mathbf{E}^{\text{ind}}$. Taking into account the effects due to the presence of the induced field, but also due to the density fluctuations or any kind of microscopic inhomogeneities, is a challenging task. These effects are often referred as the *local-field effects*.
In the case of bulk materials, the local-field effects have been widely studied and in particular their effects on the optical properties are now well established. Their effects on optical properties of surfaces is still an open question, mainly because the theoretical description and the numerical simulations in the case of surfaces are more intricate than for bulk materials. The abrupt change in the electronic density at the interface with vacuum leads to a huge variation of the electric field. As a result, strong effects of the local field are expected, in particular in the direction perpendicular to the plane of the surface. This thesis aims to quantify how important these effects are for the linear and the second-order optical properties of surfaces.

1.3.2 Macroscopic quantities

From a theoretical point of view, the inclusion of the local-field effects is closely related to the macroscopic averaging mentioned previously. In this thesis, the inclusion of the local-field effects follows the formalism of Ref. [38], which has been extended to the second-order by Luppi *et al.* in Ref. [41] and Huebener *et al.* in Ref. [42,43]. The first step in this approach is to define a perturbing field, such as

$$\mathbf{E}^{P} = \mathbf{E}^{\text{ext}} + \mathbf{E}^{\text{ind},T} = \mathbf{E} - \mathbf{E}^{\text{ind},L}, \tag{1.3}$$

where $\mathbf{E}$ is the total microscopic field, $\mathbf{E}^{\text{ext}}$ is the external field and $\mathbf{E}^{\text{ind},T}$ and $\mathbf{E}^{\text{ind},L}$ are respectively the transverse and the longitudinal components of the field induced by the external perturbation.
In this thesis, I will focus on two macroscopic quantities, the macroscopic dielectric tensor and second-order susceptibility tensor. The macroscopic dielectric tensor is defined as the link between the macroscopic first-order electric displacement and the macroscopic total electric field. In frequency

space reciprocal space, this relation reads as

$$\mathbf{D}_M^{(1)}(\mathbf{q};\omega) = \overset{\leftrightarrow}{\epsilon}_M(\mathbf{q};\omega)\mathbf{E}_M(\mathbf{q};\omega). \tag{1.4}$$

The macroscopic second-order susceptibility is defined as the link between three measurable quantities, the macroscopic second-order polarization $\mathbf{P}_M^{(2)}$ and the two macroscopic incoming total electric fields $\mathbf{E}_M$,

$$\mathbf{P}_M^{(2)}(\mathbf{q};\omega) = \sum_{\mathbf{q_1},\mathbf{q_2}} \int d\omega_1 d\omega_2 \overset{\leftrightarrow}{\chi}_M^{(2)}(\mathbf{q},\mathbf{q_1},\mathbf{q_2};\omega_1,\omega_2)\mathbf{E}_M(\mathbf{q_1};\omega_1)\mathbf{E}_M(\mathbf{q_2};\omega_2)\delta_{\mathbf{q},\mathbf{q_1}+\mathbf{q_2}}\delta(\omega-\omega_1-\omega_2). \tag{1.5}$$

Note that the delta functions ensure the conservation of the energy and the conservation of the momentum.

The first-order polarization is related to the perturbing electric field via the quasi-polarisability tensor, denoted $\overset{\leftrightarrow}{\tilde{\alpha}}^{(1)}$. The time Fourier transform of this definition reads as [38]

$$\mathbf{P}^{(1)}(\mathbf{r};\omega) = \int d^3\mathbf{r_1}\, \overset{\leftrightarrow}{\tilde{\alpha}}^{(1)}(\mathbf{r},\mathbf{r_1};\omega)\mathbf{E}^P(\mathbf{r_1};\omega). \tag{1.6}$$

Similarly, the second-order polarization is given by

$$\mathbf{P}^{(2)}(\mathbf{r};\omega) = \int d^3\mathbf{r_1}d^3\mathbf{r_2} \int d\omega_1 d\omega_2 \delta(\omega-\omega_1-\omega_2)\, \overset{\leftrightarrow}{\tilde{\alpha}}^{(2)}(\mathbf{r},\mathbf{r_1},\mathbf{r_2};\omega_1,\omega_2)\mathbf{E}^P(\mathbf{r_1};\omega_1)\mathbf{E}^P(\mathbf{r_2};\omega_2), \tag{1.7}$$

where $\overset{\leftrightarrow}{\tilde{\alpha}}^{(2)}$ is the second-order quasi-polarisability [41]. Assuming a periodic crystal, it is possible to perform the space Fourier transform of Eq. (1.6) and Eq. (1.7)

$$\mathbf{P}_{\mathbf{G}}^{(1)}(\mathbf{q};\omega) = \sum_{\mathbf{G_1}} \left[\, \overset{\leftrightarrow}{\tilde{\alpha}}^{(1)}(\mathbf{q};\omega)\right]_{\mathbf{G}\mathbf{G_1}} \mathbf{E}_{\mathbf{G_1}}^P(\mathbf{q};\omega), \tag{1.8a}$$

$$\begin{aligned}\mathbf{P}_{\mathbf{G}}^{(2)}(\mathbf{q};\omega) = &\sum_{\mathbf{q_1}\mathbf{q_2}}^{BZ} \sum_{\mathbf{G_1}\mathbf{G_2}} \int d\omega_1 d\omega_2 \delta_{\mathbf{q},\mathbf{q_1}+\mathbf{q_2}}\delta(\omega-\omega_1-\omega_2) \\ &\times \left[\, \overset{\leftrightarrow}{\tilde{\alpha}}^{(2)}(\mathbf{q},\mathbf{q_1},\mathbf{q_2};\omega_1,\omega_2)\right]_{\mathbf{G}\mathbf{G_1}\mathbf{G_2}} \mathbf{E}_{\mathbf{G_1}}^P(\mathbf{q_1};\omega_1)\mathbf{E}_{\mathbf{G_2}}^P(\mathbf{q_2};\omega_2).\end{aligned} \tag{1.8b}$$

where $\mathbf{q}$, $\mathbf{q_1}$ and $\mathbf{q_2}$ are vectors in the first Brillouin zone (BZ), $\mathbf{G}$, $\mathbf{G_1}$, and $\mathbf{G_2}$ are reciprocal lattice vectors, and the notations $\mathbf{P}_{\mathbf{G}}(\mathbf{q};\omega)$ and $\left[\, \overset{\leftrightarrow}{\tilde{\alpha}}^{(1)}(\mathbf{q};\omega)\right]_{\mathbf{G}\mathbf{G_1}}$ stand respectively for $\mathbf{P}(\mathbf{q}+\mathbf{G};\omega)$ and $\overset{\leftrightarrow}{\tilde{\alpha}}^{(1)}(\mathbf{q}+\mathbf{G},\mathbf{q}+\mathbf{G_1};\omega)$.

In reciprocal space, the macroscopic averaging procedure consists in keeping only the $\mathbf{G}=\mathbf{0}$ component [44], or, following the idea of Refs. [39, 40], this procedure is defined by a *projector* on the averaged part, denoted P_a, whose expression in reciprocal space is $P_a = \delta_{\mathbf{G}0}$.
In Eqs. (1.8), the first- and second-order microscopic polarizations are explicit functions of the perturbing field, whereas the macroscopic ones depend upon the macroscopic total electric field. To

express the microscopic polarizations in terms of the total electric field, we use the relation between the perturbing field and the total electric field obtained from Maxwell equations [41], which reads as

$$\mathbf{E}^P_{\mathbf{G}}(\mathbf{q};\omega) = \mathbf{E}_{\mathbf{G}}(\mathbf{q};\omega) + 4\pi \frac{\mathbf{q}+\mathbf{G}}{|\mathbf{q}+\mathbf{G}|} P^L_{\mathbf{G}}(\mathbf{q};\omega), \tag{1.9}$$

where P^L is the longitudinal part of the polarization (see App. B.3 for the definition of the longitudinal and transverse parts). After some algebra that the interested reader can find detailed in Ref. [41, 45], we obtain the expression of the macroscopic dielectric tensor

$$\overset{\leftrightarrow}{\epsilon}_M(\mathbf{q};\omega) = \overset{\leftrightarrow}{\mathbb{1}} + 4\pi \big[\overset{\leftrightarrow}{\tilde{\alpha}}^{(1)}(\mathbf{q};\omega)\big]_{\mathbf{00}} \left[\frac{\overset{\leftrightarrow}{\mathbb{1}} + 4\pi \frac{\mathbf{q}}{q}\frac{\mathbf{q}}{q} \frac{\big[\overset{\leftrightarrow}{\tilde{\alpha}}^{(1)}(\mathbf{q};\omega)\big]_{\mathbf{00}}}{1 - 4\pi\big[\tilde{\alpha}^{(1),LL}(\mathbf{q};\omega)\big]_{\mathbf{00}}}}{}\right], \tag{1.10}$$

with $\tilde{\alpha}^{(1),LL}$ the longitudinal-longitudinal part of $\overset{\leftrightarrow}{\tilde{\alpha}}^{(1)}$ and of the expression of the macroscopic second-order susceptibility

$$\begin{aligned}\overset{\leftrightarrow}{\chi}^{(2)}_M(\mathbf{q},\mathbf{q_1},\mathbf{q_2};\omega_1,\omega_2) = &\left[\overset{\leftrightarrow}{\mathbb{1}} + 4\pi \frac{\big[\overset{\leftrightarrow}{\tilde{\alpha}}^{(1)}(\mathbf{q};\omega)\big]_{\mathbf{00}}}{1 - 4\pi\big[\tilde{\alpha}^{(1),LL}(\mathbf{q};\omega)\big]_{\mathbf{00}}} \frac{\mathbf{q}}{q}\frac{\mathbf{q}}{q}\right] . \big[\overset{\leftrightarrow}{\tilde{\alpha}}^{(2)}(\mathbf{q},\mathbf{q_1},\mathbf{q_2};\omega_1,\omega_2)\big]_{\mathbf{000}} : \\ &\times \left[\overset{\leftrightarrow}{\mathbb{1}} + 4\pi \frac{\mathbf{q_1}}{q_1}\frac{\mathbf{q_1}}{q_1} \frac{\big[\overset{\leftrightarrow}{\tilde{\alpha}}^{(1)}(\mathbf{q_1};\omega_1)\big]_{\mathbf{00}}}{1 - 4\pi\big[\tilde{\alpha}^{(1),LL}(\mathbf{q_1};\omega_1)\big]_{\mathbf{00}}}\right] \left[\overset{\leftrightarrow}{\mathbb{1}} + 4\pi \frac{\mathbf{q_2}}{q_2}\frac{\mathbf{q_2}}{q_2} \frac{\big[\overset{\leftrightarrow}{\tilde{\alpha}}^{(1)}(\mathbf{q_2};\omega_2)\big]_{\mathbf{00}}}{1 - 4\pi\big[\tilde{\alpha}^{(1),LL}(\mathbf{q_2};\omega_2)\big]_{\mathbf{00}}}\right].\end{aligned} \tag{1.11}$$

1.3.3 Comparison with the Lorentz model

A well-known model for the local-field correction is the Lorentz model, which has been intensively discussed in the literature, see Refs. [46–48] and references therein. Therefore it is interesting to compare the results obtained with this model to the exact results obtained above.
In the Lorentz model of the local field, the local field at any point of a crystal is given by the sum of the applied external field and an induced field created by neighbouring dipoles

$$\mathbf{E}^{\text{loc}}(\omega) = \mathbf{E}^{\text{ext}}(\omega) + \mathbf{E}^{\text{dip}}(\omega),$$

with $\mathbf{E}^{\text{dip}}(\omega) = \frac{4\pi}{3}\mathbf{P}(\omega)$ for a cubic media [46].
In that case, the polarization, up to the second-order, is given by [49]

$$\mathbf{P}(\omega) = \Big[1 - \frac{4\pi}{3}\alpha^{(1)}(\omega)\Big]^{-1}\Big(\alpha^{(1)}(\omega)\mathbf{E}^{\text{ext}}(\omega) + \overset{\leftrightarrow}{\alpha}^{(2)}(\omega,\omega_1,\omega_2)\mathbf{E}^{\text{loc}}(\omega_1)\mathbf{E}^{\text{loc}}(\omega_2)\Big), \tag{1.12}$$

where $\alpha^{(1)}$ and $\overset{\leftrightarrow}{\alpha}^{(2)}$ are first- and second-order polarisabilities. When neglecting the contribution of $\mathbf{P}^{(2)}$ to $\mathbf{E}^{\text{loc}}$, we obtain the expression of the macroscopic dielectric function and second-order susceptibility in the Lorentz model [49]

$$\epsilon_{\text{Lorentz}}(\omega) = 1 + 4\pi\alpha^{(1)}(\omega)\Big[\frac{1}{1 - \frac{4\pi}{3}\alpha^{(1)}(\omega)}\Big], \tag{1.13a}$$

$$\overset{\leftrightarrow}{\chi}{}^{(2)}_{\text{Lorentz}}(\omega,\omega_1,\omega_2) = \Big[\frac{1}{1-\frac{4\pi}{3}\alpha^{(1)}(\omega)}\Big]\overset{\leftrightarrow}{\alpha}{}^{(2)}(\omega,\omega_1,\omega_2)\Big[\frac{1}{1-\frac{4\pi}{3}\alpha^{(1)}(\omega_1)}\Big]\Big[\frac{1}{1-\frac{4\pi}{3}\alpha^{(1)}(\omega_2)}\Big]. \quad (1.13b)$$

These expressions are very similar to the exact expressions Eq. (1.10) and Eq. (1.11), and in particular, the terms in the brackets account equally for the local-field effects in both cases. Moreover, if we assume the cubic symmetry, the dielectric tensor reduces to its longitudinal-longitudinal-longitudinal part [41].

$$\overset{\leftrightarrow}{\chi}{}^{(2)}_{M}(\mathbf{q},\mathbf{q_1},\mathbf{q_2};\omega_1,\omega_2) = \epsilon^{LL}_{M}(\omega)\,\overset{\leftrightarrow}{\tilde{\alpha}}{}^{(2),LLL}(\mathbf{q},\mathbf{q_1},\mathbf{q_2};\omega_1,\omega_2)\epsilon^{LL}_{M}(\omega_1)\epsilon^{LL}_{M}(\omega_2), \quad (1.14)$$

whereas the Lorentz model gives [50,51]

$$\overset{\leftrightarrow}{\chi}{}^{(2)}_{\text{Lorentz}}(\omega,\omega_1,\omega_2) = \left[\frac{\epsilon_{\text{Lorentz}}(\omega)+2}{3}\right]\overset{\leftrightarrow}{\alpha}{}^{(2)}(\omega,\omega_1,\omega_2)\left[\frac{\epsilon_{\text{Lorentz}}(\omega_1)+2}{3}\right]\left[\frac{\epsilon_{\text{Lorentz}}(\omega_2)+2}{3}\right] \quad (1.15)$$

Interestingly, the Lorentz model is found to give very similar analytical expression of the local-field correction, compared to the exact expressions obtained from the macroscopic-microscopic connection. Nevertheless, in the latter, no approximation has been introduced, in particular concerning the symmetry of the system, whereas the Lorentz model is restricted to a cubic symmetry. Moreover, the Lorentz model contains the polarisabilities (*i.e.*, responses to the applied external field) whereas the the macroscopic-microscopic connection yield formulae containing the quasi-polarisabilities (*i.e.*, responses to the perturbing field). Note that the Lorentz model for the local field can be improved by replacing the Lorentz factor $\frac{\epsilon+2}{3}$ by a more realistic expression, see for instance, Ref. [52].
Even if the Lorentz model has been used to investigate experimentally the local-field effects, *e.g.*, in a dense atomic vapor [53], it is numerically valid only in the low-energy region, far from resonances and is not really used in practice.

1.4 Longitudinal-transverse and optical limit

The optical limit and the dipole approximation play an important role in the *ab initio* description of optical properties. Here I report some important results, for the linear and nonlinear second-order optical properties, related to the optical limit, also called long-wavelength approximation.

1.4.1 Dielectric tensor

Let us consider a periodic, non-magnetic ($\mathbf{H} = \mathbf{B}$) crystal, without external charges.
In the longitudinal-transverse basis (see App. B.3 for the definition of longitudinal and transverse fields), the dielectric tensor reads as[1]

$$\overset{\leftrightarrow}{\epsilon}{}_{M}(\mathbf{q};\omega) = \begin{pmatrix} \epsilon^{LL}_{M}(\mathbf{q};\omega) & \epsilon^{LT}_{M}(\mathbf{q};\omega) \\ \epsilon^{TL}_{M}(\mathbf{q};\omega) & \epsilon^{TT}_{M}(\mathbf{q};\omega) \end{pmatrix}. \quad (1.16)$$

[1]Here ϵ^{LL}_M is a scalar, ϵ^{LT}_M and ϵ^{TL}_M are vectors and ϵ^{TT}_M is a 2×2 matrix.

Inserting the definition of the macroscopic dielectric function into Maxwell equations (see Eqs B.19) yields the equation of propagation for the macroscopic electric field

$$|\mathbf{q}|^2 \mathbf{E}^T(\mathbf{q};\omega) = \frac{\omega^2}{c^2} \overleftrightarrow{\epsilon}_M(\mathbf{q};\omega)\mathbf{E}(\mathbf{q};\omega), \tag{1.17}$$

where $\mathbf{q}$ is the momentum of the photon.

This equation gives directly the familiar normal modes [38, 39, 54]. If the electric field is purely longitudinal ($\mathbf{E} = \mathbf{E}^L$), we obtain the condition of propagation of the plasmon, $\epsilon_M^{TL}(\mathbf{q};\omega) = 0$. In the case of a purely transverse electric field, we obtain the dispersion relation of the photon, $|\omega^2 \overleftrightarrow{\epsilon}_M^{TT}(\mathbf{q};\omega) - c^2 q^2 \overleftrightarrow{\mathbb{1}}| = 0$.

It is worthwhile to notice that the dispersion relation of the photon involves only transverse components of $\overleftrightarrow{\epsilon}_M$. This is in contrast with the Time-Dependent Density-Functional Theory (presented later in Chap. 3), which gives access to the longitudinal-longitudinal (LL) part of the dielectric tensor only. Nevertheless, we can show that the LL part of the dielectric tensor is sufficient for accessing every interesting quantity, within the long-wavelength approximation.

Let us consider the long-wavelength limit.[2] This approximation corresponds to a vanishing momentum, $\mathbf{q} \to 0$. Any quantity can therefore be expanded in terms of power of $\mathbf{q}$. The dipole approximation corresponds to the truncation of this expansion at the lowest-order in $\mathbf{q}$.

The tensors $\overleftrightarrow{\epsilon}_M(\mathbf{q};\omega)$ and $\overleftrightarrow{\tilde{\alpha}}^{(1)}(\mathbf{q},\mathbf{q};\omega)$ are analytic; their limit for $\mathbf{q} \to 0$ does not depend on the direction of $\mathbf{q}$. Let us denote these limits $\overleftrightarrow{\epsilon}_M(\omega)$ and $\overleftrightarrow{\tilde{\alpha}}^{(1)}(\omega)$.[3]

Let us now assume that the tensor $\overleftrightarrow{\tilde{\alpha}}^{(1)}(\omega)$ is diagonalisable, meaning that the crystal exhibits three principal axis $\mathbf{n_i}$. This is the case for all the crystal classes but monoclinic and triclinic crystals [55]. In the case of monoclinic and triclinic crystals, the tensor can still be diagonal, but this is not true in general.

In the basis of the principal axis, and within the long-wavelength limit, the dielectric tensor is found to be diagonal, from Eq. (1.10) and using the relation $\mathbf{n_i}.\overleftrightarrow{\tilde{\alpha}}^{(1)} = \tilde{\alpha}_{ii}^{(1)}\mathbf{n_i}$; with the i-th component of the dielectric tensor ϵ_M^{ii}, given by

$$\epsilon_M^{ii}(\omega) = \mathbf{n_i}.\overleftrightarrow{\epsilon}_M(\omega).\mathbf{n_i} = \frac{1}{1 - 4\pi\tilde{\alpha}^{LL}(\mathbf{n_i};\omega)}, \tag{1.18}$$

whereas $\epsilon_M^{ij}(\omega) = 0$ for $i \neq j$.

Thereby, the dielectric tensor and the quasi-polarisability are diagonal in the same basis, and the components are given by

$$\epsilon_M^{ii}(\omega) = \epsilon_M^{LL}(\mathbf{q} \to 0;\omega), \qquad \frac{\mathbf{q}}{|\mathbf{q}|} = \mathbf{n_i}. \tag{1.19}$$

[2] The range of validity of this approximation can be easily estimated. Assuming the lattice parameter of silicon ($a_0 \sim 5.4$Å) as the characteristic length of the system, the long-wavelength limit corresponds to $\lambda \gg a_0$. If we choose the energy of the photon to be smaller than $22.5eV$, the wavelength is already such that $\lambda > 10a_0$. This approximation is perfectly suitable for the low-energy region of the optical spectra.

[3] Proving the analyticity of the dielectric tensor is far from been simple or obvious, see Ref. [38].

Let us consider now that the tensor $\overset{\leftrightarrow}{\tilde{\alpha}}^{(1)}(\omega)$ is not diagonalisable, as it is the case for monoclinic and triclinic symmetries. For these crystals, the components of the dielectric tensor can still be computed from the LL part of the dielectric tensor. To illustrate that, I take the example of a monoclinic crystal whose basal plane is perpendicular to the z-axis. In this special case, the dielectric tensor reads as

$$\overset{\leftrightarrow}{\epsilon}_M(\omega) = \begin{pmatrix} \epsilon_M^{xx}(\omega) & \epsilon_M^{xy}(\omega) & 0 \\ \epsilon_M^{xy}(\omega) & \epsilon_M^{yy}(\omega) & 0 \\ 0 & 0 & \epsilon_M^{zz}(\omega) \end{pmatrix}. \tag{1.20}$$

Computing the LL part of $\overset{\leftrightarrow}{\epsilon}_M(\omega)$ for $\mathbf{q} = \frac{\mathbf{n_x} \pm \mathbf{n_y}}{\sqrt{2}}$ gives

$$\mathbf{q}.\overset{\leftrightarrow}{\epsilon}_M(\omega).\mathbf{q} = \frac{\epsilon_M^{xx}(\omega) + \epsilon_M^{yy}(\omega)}{2} \pm \epsilon_M^{xy}(\omega). \tag{1.21}$$

We obtain easily that

$$\epsilon_M^{xy}(\omega) = \frac{1}{2}\Big(\epsilon_M^{LL}(q\frac{\mathbf{n_x} + \mathbf{n_y}}{\sqrt{2}};\omega) - \epsilon_M^{LL}(q\frac{\mathbf{n_x} - \mathbf{n_y}}{\sqrt{2}};\omega)\Big), \qquad q \to 0, \tag{1.22}$$

whereas the $\epsilon_M^{ii}(\omega)$ elements are obtained using Eq. (1.19).
Therefore, in the dipole approximation, within the long-wavelength limit, the dielectric tensor can be entirely computed from LL calculations. It is worthwhile to notice that this result is true for any symmetry class and valid independently of the level of approximation used for computing the dielectric tensor.
From the knowledge of the entire dielectric tensor in one basis, the dielectric tensor can be computed in any basis. Obviously, this result is no more valid out of the dipole approximation.

Longitudinal-transverse coupling

In the basis of the principal axis (if the dielectric tensor is diagonalisable), and within the long-wavelength limit, there is no longitudinal-transverse coupling ($\epsilon_M^{TL}(\mathbf{q} \to 0;\omega) = 0$) and no transverse-longitudinal coupling ($\epsilon_M^{LT}(\mathbf{q} \to 0;\omega) = 0$). Indeed, if the macroscopic electric field is longitudinal (transverse), and propagates along (perpendicular to) a principal axis, the macroscopic electric displacement $\mathbf{D}_M$ obtained is along (perpendicular to) the same principal axis, and is also longitudinal (transverse).
Nevertheless, a longitudinal-transverse coupling is non-vanishing in other basis than the principal axis basis, even if the dielectric tensor is diagonalisable;[4] except for the cubic symmetry, for which the dielectric tensor is diagonal in any basis.

Cubic crystals

The distinction between the transverse and the longitudinal parts of the dielectric tensor in the long-wavelength limit, *i.e.*, for a vanishing momentum, is meaningless. This can be illustrated easily with

[4] Also, if $\mathbf{q} \neq 0$, the principal axis depend on $\mathbf{q}$ and are not aligned *a priori* with $\mathbf{q}$. Therefore it is no more possible to calculate the entire dielectric tensor from longitudinal calculations if $\mathbf{q} \neq 0$.

the example of cubic crystals. Indeed, in any basis, as the longitudinal-transverse couplings vanish, we have the two equations

$$\begin{aligned} \mathbf{D}_M(\mathbf{q}\to 0;\omega) &= \overset{\leftrightarrow}{\epsilon}_M(\omega)\mathbf{E}_M(\mathbf{q}\to 0;\omega), \\ \mathbf{D}^T_M(\mathbf{q}\to 0;\omega) &= \overset{\leftrightarrow}{\epsilon}^{TT}_M(\mathbf{q}\to 0;\omega)\mathbf{E}^T_M(\mathbf{q}\to 0;\omega), \end{aligned} \qquad \frac{\mathbf{q}}{|\mathbf{q}|} = \mathbf{n_j} \tag{1.23}$$

that can be projected on the principal axis $\mathbf{n_i}$, with $i \neq j$, yielding

$$\begin{aligned} D^{T,i}_M(\mathbf{q}\to 0;\omega) &= \epsilon^{ii}_M(\omega)E^{T,i}_M(\mathbf{q}\to 0;\omega), \\ D^{T,i}_M(\mathbf{q}\to 0;\omega) &= \epsilon^{TT,ii}_M(\mathbf{q}\to 0;\omega)E^{T,i}_M(\mathbf{q}\to 0;\omega). \end{aligned} \qquad \frac{\mathbf{q}}{|\mathbf{q}|} = \mathbf{n_j} \tag{1.24}$$

Using Eq. (1.18), we obtain that

$$\epsilon^{TT,ii}_M(q\mathbf{n_j};\omega) = \epsilon^{LL}_M(q\mathbf{n_i};\omega), \qquad q\to 0 \quad \text{and} \quad i\neq j. \tag{1.25}$$

This result is valid as soon as the dielectric tensor is diagonalisable, but for cubic crystals, this relation becomes $\overset{\leftrightarrow}{\epsilon}^{TT}_M(\mathbf{q}\to 0;\omega) = \epsilon^{LL}_M(\mathbf{q}\to 0;\omega)\overset{\leftrightarrow}{\mathbb{1}}$, for any $\mathbf{q}$, because all the directions are equivalent. This shows that the denomination longitudinal or transverse loses its meaning in the long-wavelength limit. This result has been discussed by P. Noziéres and D. Pines in Ref. [56], in the special context of the random-phase approximation. Nevertheless, as pointed out in Ref. [57], this result is general and is not restricted to some specific approximations on the calculation of the dielectric tensor.

1.4.2 Second-order susceptibility

Similar considerations for the second-order susceptibility are beyond the scope of this thesis. Already, the link between the components of $\chi^{(2)}_M$ and its longitudinal-longitudinal-longitudinal (LLL) part is non-trivial. In this section, I show how it is possible to obtain the components of the second-order susceptibility from its LLL part only, that we can compute from Time-Dependent Density Functional Theory (see Chap. 3).

Let us assume the analyticity of the second-order susceptibility $\chi^{(2)}_M(\mathbf{q},\mathbf{q_1},\mathbf{q_2};\omega,\omega_1,\omega_2)$ and the second-order quasi-polarisability $\tilde{\alpha}^{(2)}(\mathbf{q},\mathbf{q_1},\mathbf{q_2};\omega,\omega_1,\omega_2)$[5]. It is thus possible to define $\chi^{(2)}_M(\omega,\omega_1,\omega_2)$ and $\tilde{\alpha}^{(2)}(\omega,\omega_1,\omega_2)$ as their respective limits for $\mathbf{q_1}\to 0$ and $\mathbf{q_2}\to 0$.

The different components of $\overset{\leftrightarrow}{\chi}^{(2)}_M$ can be obtained from Eq. (1.11). There is in total four groups of components for $\chi^{(2)}_M$, organised by group of indices. Their calculation from the longitudinal-longitudinal-longitudinal (LLL) part of the dielectric tensor only is not obvious, and depends on the symmetries of the crystal. We omit here the frequency dependence in second-order tensor for conciseness.

Components: $\chi^{(2)}_{M,iii}$

The diagonal elements of the susceptibility tensor are given by

$$\chi^{(2)}_{M,iii} = \mathbf{n_i}.\,\chi^{(2)}_M : \mathbf{n_i}.\,\mathbf{n_i} = \epsilon^{ii}_M(2\omega)\alpha^{(2)}_{iii}\epsilon^{ii}_M(\omega)\epsilon^{ii}_M(\omega),$$

[5]The analyticity of the $\chi^{(2)}_M$ tensor will be proven in Chap. 7.

which are obviously related to the LLL part of susceptibility

$$\chi^{(2)}_{M,iii} = \chi^{(2)LLL}_{M}(2\mathbf{q},\mathbf{q},\mathbf{q}), \qquad \mathbf{q}\to 0, \quad \frac{\mathbf{q}}{|\mathbf{q}|} = \mathbf{n_i}.$$

These diagonal components can always be computed from the LLL part of the tensor, regardless of the symmetries of the system.

Components: $\chi^{(2)}_{M,iij} = \chi^{(2)}_{M,iji}$

Using the relations

$$(\mathbf{n_i}+\mathbf{n_j}).\chi^{(2)}_{M} : \mathbf{n_i}.\mathbf{n_j} = \chi^{(2)}_{M,iij} + \chi^{(2)}_{M,jij},$$
$$(\mathbf{n_i}-\mathbf{n_j}).\chi^{(2)}_{M} : \mathbf{n_i}.\mathbf{n_j} = \chi^{(2)}_{M,iij} - \chi^{(2)}_{M,jij},$$

we can obtain

$$2\chi^{(2)}_{M,iij} = \chi^{(2)LLL}_{M}(\mathbf{n_i}+\mathbf{n_j},\mathbf{n_i},\mathbf{n_j}) + \chi^{(2)LLL}_{M}(-\mathbf{n_i}+\mathbf{n_j},-\mathbf{n_i},\mathbf{n_j}) \tag{1.27}$$

Therefore, the components of $\chi^{(2)}_{M,iij} = \chi^{(2)}_{M,iji}$ can always be computed from the LLL part of the tensor, regardless the symmetries of the crystal; at the cost of computing two longitudinal responses.

Components: $\chi^{(2)}_{M,ijj}$

Using $\frac{\mathbf{q_1}}{|\mathbf{q_1}|} = \mathbf{n_i}$ and $\frac{\mathbf{q_2}}{|\mathbf{q_2}|} = \frac{\mathbf{n_i}+\mathbf{n_j}}{\sqrt{2}}$, we obtain that

$$\frac{1}{2}\left(\chi^{(2)}_{M,iij} + \chi^{(2)}_{M,ijj} + (1+\sqrt{2})(\chi^{(2)}_{M,jji} + \chi^{(2)}_{M,jjj})\right) = \chi^{(2),LLL}_{M}(\mathbf{q_1}+\mathbf{q_2},\mathbf{q_1},\mathbf{q_2},2\omega,\omega;\omega) \tag{1.28}$$

By combining this expression with the two previous results, it is possible to calculate the components ijj of the second-order susceptibility tensor. Note that in general, the terms on the left-hand side are not all non-zero for the same symmetry and therefore, this equation get simpler for many of the symmetries.

Components: $\chi^{(2)}_{M,ijk} = \chi^{(2)}_{M,ikj}$**,** $i\neq j\neq k$

There is no simple general expression for obtaining these components from the longitudinal part of the second-order susceptibility tensor. However, for some symmetry classes, these components can be easily obtained, *e.g.*, cubic crystals. In that case, the only non-zero components are the $\chi^{(2)}_{M,ijk}$. By choosing $\frac{\mathbf{q_1}}{|\mathbf{q_1}|} = \frac{\mathbf{q_2}}{|\mathbf{q_2}|} = \frac{\mathbf{q}}{|\mathbf{q}|} = \frac{\mathbf{n_i}+\mathbf{n_j}+\mathbf{n_k}}{\sqrt{3}}$, we obtain that

$$\chi^{(2)}_{M,ijk}(2\omega,\omega,\omega) = \frac{1}{6}\chi^{(2)LLL}_{M}(2\mathbf{q},\mathbf{q},\mathbf{q};2\omega,\omega,\omega).$$

Obviously, the choices presented here are not unique are clever choices can be found, based on the specific symmetries of the crystal considered.

1.5 Present work

The study of optical properties of surfaces is driven by one main motivation: understanding how the presence of the surface modifies the bulk optical properties and related spectroscopic techniques. This fundamental question has many practical implications: optical spectroscopies are now used routinely, *e.g.*, for monitoring and controlling of the surface growth in real time [58]; moreover, it is now well established that physical properties of nano-scaled systems are strongly influenced by their surface behavior [59].

Over the last years, experimental and theoretical approaches have considerably advanced, deepening our understanding of the processes occurring at the surface of materials. However, these optical properties result of an intricate interplay of numerous effects and achieving a correct theoretical description of surfaces is far from being simple. First of all, the atomic relaxation at the interface with vacuum is responsible for a change in the electronic properties of the material, creating for instance surface states that can be located in the gap of the material [60]. The local-field and other effects related to many-particle physics, such as electron-hole interactions, occurring in all spectroscopic measurements must be properly included. Their precise description for surfaces is nevertheless quite involved [61].

In this thesis, the optical properties of surfaces are computed using the common approach which relies on the super-cell technique and the slab geometry. Unfortunately, the definition of a *surface* dielectric tensor (or second-order susceptibility) is still unclear, and the difference between the optical response of a thin film (made of two surfaces) and the optical response of a semi-infinite system, with a single surface, has not really being investigated so far, in particular when local-field effects are included.

The aim of this thesis is to clarify the definition of the *surface* optical properties and to give the theoretical background needed for computing linear and second-order optical properties of a single surface, from calculations performed in slab geometry. The Chap. 5 and Chap. 6 are dedicated to the theory behind the calculation of the surface second-harmonic spectra in super-cell geometry, at a microscopic level.

A macroscopic formalism, allowing us to obtain the first and second-order optical properties of surfaces is then developed in Chap. 7, allowing us to include the local-field effects. Chap.8 presents how we can treat a truly isolated slab, from a periodic super-cell approach.
I present in Chap 9, for the first time, *ab initio* calculations of the local-field effects on surface second-harmonic generation spectra. Also, an insight of the excitonic effects on the surface second-harmonic spectra is presented in Chap. 10.

Summary

As a summary, I have presented in this chapter the phenomenon of second-harmonic generation, several of its applications and some related phenomena. Then I have presented how the macroscopic quantities, directly related to quantities measured in experiments depend on the microscopic quantities, fluctuating on the nanoscale. I have also discussed about the longitudinal and transverse parts of

the optical responses, showing in particular that within the long-wavelength limit, the longitudinal response to longitudinal perturbations is sufficient for describing the first- and second-order optical properties of any crystals. Finally, the scope and the organisation of the thesis have been presented.

2. Second-harmonic generation in reflection

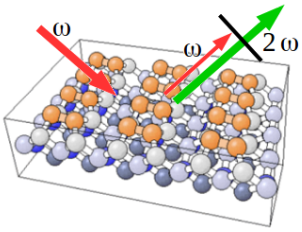

The properties of the nonlinear media, *i.e.*, the intensity and polarization dependence of SHG, are often measured in reflection for bulk materials [62, 63], interfaces [64–69], and layered materials [70, 71]. In such a set-up, a monochromatic laser, oscillating at the frequency ω, reflects on the surface of a material, yielding two waves. One is a fraction of the fundamental light, reflected following the Fresnel laws. The other one is the second-harmonic emitted by the nonlinear medium and oscillating at the frequency 2ω. A filter is used to discard between the reflected fundamental light and the second-harmonic signal, which contains the information concerning the material investigated. Thus, by controlling the polarizations or the angle of incidence, one can easily probe the nonlinear or symmetry properties of a wide class of materials.

The first theoretical description of second-harmonic generation from surfaces is due to Bloembergen and Pershan [72], followed by papers from Tom *et al.* [64], and Mizhahi and Sipe [73]. Along the years, the generation of second-harmonic from surfaces has been widely studied, resulting in a theoretical description, which is a generalization of Fresnel reflection coefficients for the case of the SHG. The second-harmonic reflection coefficients or generalized reflection coefficients, denoted R, are defined as the ratio of the reflected second-harmonic intensity to the square of the fundamental intensity

$$R(\omega) = \frac{I_{\text{out}}(2\omega)}{I_{\text{in}}(\omega)^2}, \tag{2.1}$$

where the intensity $I(\omega)$ is related to the electric field by the relation $I(\omega) = \frac{c}{2\pi}|E(\omega)|^2$.

In the most general case, these reflection coefficients depend upon the input polarization, the measured polarization, the incidence angle and the azimuthal angle in the plane of the surface.

In experiments, the fundamental and reflected waves are often p-polarized or s-polarized. In that case and in order to distinguish between the four different possible combinations of polarizations, R is annotated with two letters (s or p), the first one standing for the polarization of the fundamental wave and the second one for the reflected wave.[1]

For instance, R_{sp} denotes the second-harmonic reflection coefficient obtained for a s-polarized incident wave and p-polarized reflected wave.[2]

[1] Any other possible polarization will be labelled by α, as explained in Fig. 2.1(a).

[2] Sometimes, one can also find in the literature a q-polarized light, corresponding to the polarization at 45° between s and p. Also, the reader must be careful when comparing with the literature because some authors use the opposite convention.

Despite the growing interest in SHG, the literature remains unclear concerning the derivation of the reflection coefficients, ant it is not always easy to understand what is the phenomenological treatment in the derivation of that coefficients, an exception been Ref. [73].
The aim of this chapter is to present a comprehensive derivation of the expressions of the different reflection coefficients, for both surface and bulk contributions, based on the work of Ref. [73].

Modelling the experiment

The experiment is modelled by a semi-infinite medium as represented in Fig. 2.1. The z-axis is chosen to be perpendicular to the surface plane. The upper half-space ($z > 0$) corresponds to the vacuum region whereas the lower half-space is filled with the probed medium. The angle between the incident beam and the normal to the surface (z-axis) is denoted θ_i (see Fig. 2.1(a)). In the surface plane ($x - y$ plane), the azimuthal angle, *i.e.*, the angle between the projection of the incident beam and the x-axis, is called ϕ. The formalism presented here is a *macroscopic* formalism, therefore the medium is considered to be homogeneous and isotropic for the linear properties, implying that only one refracted ray is propagating. The dielectric tensor $\overleftrightarrow{\epsilon}_M(\mathbf{r}, \mathbf{r}'; \omega)$ is thus replaced by a macroscopic dielectric function, denoted $\epsilon(\omega)$. [3]
As shown by Bloembergen and Pershan in Ref. [72], the harmonic waves reflected and transmitted at the boundary of a nonlinear medium follow a generalized Fresnel law. In the case of SHG, this leads to a reflected wave propagating along a direction that exhibits the same angle to the normal, denoted θ_r, than the fundamental light. Therefore, we only keep $\theta = \theta_i = \theta_r$ in our notations. Following Ref. [73], we express any electric field $\mathbf{E}(\mathbf{r})$ for $z \neq 0$, as the sum of two waves, an upward-

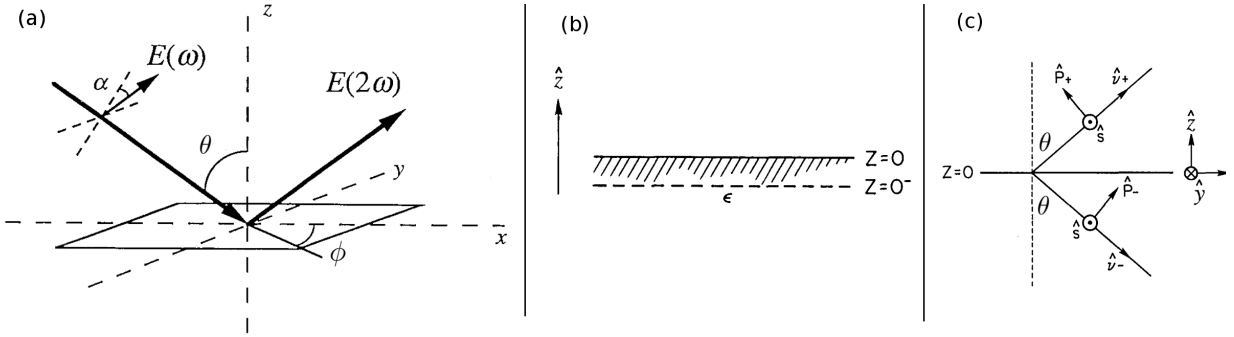

Fig. 2.1: (a) SHG geometry in reflection from a surface. θ is the incidence angle and ϕ is the azimuthal angle. α is the polarization angle in the plane of incidence: the p-polarization corresponds to $\alpha = 0°$ and the s-polarization corresponds to $\alpha = 90°$. Adapted from Ref. [74]. (b) A sheet of nonlinear polarization is considered at $z = 0^-$, surrounded by an isotropic and homogeneous linear medium, characterised by a macroscopic dielectric function $\epsilon(\omega)$. (c) Representation of the $\hat{\mathbf{s}}$, $\hat{\mathbf{p}}$ and $\hat{\mathbf{q}}$ vectors, as explained in the text.

propagating wave and a downward-propagating wave, denoted respectively $\mathbf{E}_+(\mathbf{r})$ and $\mathbf{E}_-(\mathbf{r})$.
The electric field reads as

$$\mathbf{E}(\mathbf{r}) = \mathbf{E}_+(\mathbf{r})\Theta(z) + \mathbf{E}_-(\mathbf{r})\Theta(-z), \qquad z \neq 0, \tag{2.2}$$

[3] Taking into account the anisotropy of the dielectric tensor is simple but makes the notations heavier.

where $\Theta(z)$ is the Heaviside function, $\Theta(z) = 1$ as $z > 0$ and 0 elsewhere.
The wave-vectors for upward/downward propagating waves are written as

$$\begin{aligned}\mathbf{q}^i_+(\omega) &= q_{||}(\omega)\hat{\boldsymbol{\kappa}} + q^i_\perp(\omega)\hat{\mathbf{z}},\\ \mathbf{q}^i_-(\omega) &= q_{||}(\omega)\hat{\boldsymbol{\kappa}} - q^i_\perp(\omega)\hat{\mathbf{z}},\end{aligned} \tag{2.3}$$

where $\hat{\boldsymbol{\kappa}}$ is the in-plane unit vector defined by $\hat{\boldsymbol{\kappa}} = \cos(\phi)\hat{\mathbf{x}} + \sin(\phi)\hat{\mathbf{y}}$ and i can be the medium (m) or the vacuum (v). We define $q_{||}$ to be the in-plane component of the wave-vector and $q_\perp$ the out-of-plane component of the wave-vector. Here $q^i(\omega)^2 = \epsilon_i(\omega)\left(\frac{\omega}{c}\right)^2$and $q^i_\perp(\omega) = \left(\epsilon_i(\omega)\frac{\omega^2}{c^2} - q^2_{||}(\omega)\right)^{1/2} = \frac{\omega}{c}\left(\epsilon_i(\omega) - \sin^2(\theta)\right)^{1/2}$, $q^i_\perp$ being chosen to have $\mathrm{Im}[q^i_\perp] \geq 0$ and $\mathrm{Re}[q^i_\perp] \geq 0$ if $\mathrm{Im}[q^i_\perp] = 0$. This convention allows us to be sure that the wave associated with $\mathbf{q}^i_+$ is upward propagating and that the one associated with $\mathbf{q}^i_-$ is downward-propagating.
The s and p polarizations are defined by the following unit vectors

$$\begin{aligned}\hat{\mathbf{s}} &= \hat{\boldsymbol{\kappa}} \times \hat{\mathbf{z}},\\ \hat{\mathbf{p}}^i_\pm &= \frac{(q_{||}\hat{\mathbf{z}} \mp q^i_\perp \hat{\boldsymbol{\kappa}})}{q^i}.\end{aligned}$$

This is illustrated in Fig. 2.1(c). For conciseness, we omit the frequency dependence here.
One can easily check that we have the following relations

$$\begin{aligned}\hat{\mathbf{s}} \times \hat{\mathbf{q}}^i_\pm &= \hat{\mathbf{p}}^i_\pm,\\ \hat{\mathbf{q}}^i_\pm \times \hat{\mathbf{p}}^i_\pm &= \hat{\mathbf{s}},\\ \hat{\mathbf{p}}^i_\pm \times \hat{\mathbf{s}} &= \hat{\mathbf{q}}^i_\pm,\end{aligned} \tag{2.4}$$

where $\hat{\mathbf{q}}^i_\pm = \mathbf{q}^i_\pm/q^i$. Thus $(\hat{\mathbf{s}}; \hat{\mathbf{q}}^i_+; \hat{\mathbf{p}}^i_+)$ and $(\hat{\mathbf{s}}; \hat{\mathbf{q}}^i_-; \hat{\mathbf{p}}^i_-)$ are direct basis.
Therefore, the wave associated with $\hat{\mathbf{q}}^i_+$ (respectively $\hat{\mathbf{q}}^i_-$) only propagates along $\hat{\mathbf{s}}$ and $\hat{\mathbf{p}}^i_+$ (respectively $\hat{\mathbf{p}}^i_-$).
From Maxwell equations, the upward and the downward propagating waves read as

$$\begin{aligned}\mathbf{E}^i_+(\mathbf{r};\omega) &= (E^i_{s+}(\omega)\hat{\mathbf{s}} + E^i_{p+}(\omega)\hat{\mathbf{p}}^i_+(\omega))e^{i\mathbf{q}^i_+(\omega)\mathbf{r}},\\ \mathbf{B}^i_+(\mathbf{r};\omega) &= \sqrt{\epsilon_i(\omega)}(E^i_{p+}(\omega)\hat{\mathbf{s}} - E^i_{s+}(\omega)\hat{\mathbf{p}}^i_+(\omega))e^{i\mathbf{q}^i_+(\omega)\mathbf{r}},\\ \mathbf{E}^i_-(\mathbf{r};\omega) &= (E^i_{s-}(\omega)\hat{\mathbf{s}} + E^i_{p-}(\omega)\hat{\mathbf{p}}^i_-(\omega))e^{i\mathbf{q}^i_-(\omega)\mathbf{r}},\\ \mathbf{B}^i_-(\mathbf{r};\omega) &= \sqrt{\epsilon_i(\omega)}(E^i_{p-}(\omega)\hat{\mathbf{s}} - E^i_{s-}(\omega)\hat{\mathbf{p}}^i_-(\omega))e^{i\mathbf{q}^i_-(\omega)\mathbf{r}}.\end{aligned} \qquad z \neq 0 \tag{2.5}$$

2.1 Second-order polarization induced by incident light

In this section, we will give the expression of the second-order polarization induced by the incident field. Let us denote the incident field in the vacuum $\mathbf{E}_{\text{in}}(\omega)$. The polarization of that field is denoted $\hat{\mathbf{e}}^{\mathbf{in}}(\omega)$ which can be $\hat{\mathbf{s}}$ or $\hat{\mathbf{p}}_-(\omega)$; depending if the field is s- or p-polarised. This incident field reads as

$$\mathbf{E}_{\text{in}}(\mathbf{r};\omega) = \left(E^s_{\text{in}}(\omega)\hat{\mathbf{s}} + E^p_{\text{in}}(\omega)\hat{\mathbf{p}}^v_-(\omega)\right)e^{i(\mathbf{q}_{||}(\omega)\mathbf{r}_{||} - q^v_\perp(\omega)z)} = \hat{\mathbf{e}}^{\mathbf{in}}(\omega)|E_{\text{in}}(\omega)|e^{i(\mathbf{q}_{||}(\omega)\mathbf{r}_{||} - q^v_\perp(\omega)z)}. \tag{2.6}$$

Polarisation	Reflection	Transmission
s	$r^s_{ij}(\omega) = \frac{q^i_\perp(\omega) - q^j_\perp(\omega)}{q^i_\perp(\omega) + q^j_\perp(\omega)}$	$t^s_{ij}(\omega) = \frac{2q^i_\perp(\omega)}{q^i_\perp(\omega) + q^j_\perp(\omega)}$
p	$r^p_{ij}(\omega) = \frac{q^i_\perp(\omega)\epsilon_j(\omega) - q^j_\perp(\omega)\epsilon_i(\omega)}{q^i_|(\omega)\epsilon_j(\omega) + q^j_|(\omega)\epsilon_i(\omega)}$	$t^p_{ij}(\omega) = \frac{2q^i_\perp(\omega)\sqrt{\epsilon_j(\omega)\epsilon_i(\omega)}}{q^i_|(\omega)\epsilon_j(\omega) + q^j_|(\omega)\epsilon_i(\omega)}$

Tab. 2.1: Fresnel coefficients in reflection and in transmission for s- and p-polarized lights.

At the interface with the medium, this field is transmitted. The change in phase and amplitude of the wave at the boundary is described by the Fresnel transmission coefficients (see Tab. 2.1). t^{pol}_{ij} denotes the transmission coefficient where pol is the polarization and can be s or p, and i and j can be the medium (m) or the vacuum (v). The field inside the medium, denoted $\mathbf{E}^\omega(\mathbf{r})$, is given by

$$\mathbf{E}^\omega(\mathbf{r}) = \left(E^s_{\text{in}}(\omega)t^s_{vm}(\omega)\hat{\mathbf{s}} + E^p_{\text{in}}(\omega)t^p_{vm}(\omega)\hat{\mathbf{p}}^m_-(\omega)\right)e^{i(\mathbf{q}_{||}(\omega)\mathbf{r}_{||} - q^m_\perp(\omega)z)} = \hat{\mathbf{e}}^\omega |E_{\text{in}}(\omega)| e^{i(\mathbf{q}_{||}(\omega)\mathbf{r}_{||} - q^m_\perp(\omega)z)}, \tag{2.7}$$

where the change in direction of the field has been taken into account by replacing $q^v_\perp(\omega)$ by $q^m_\perp(\omega)$, $\hat{\mathbf{p}}^v_-(\omega)$ by $\hat{\mathbf{p}}^m_-(\omega)$ and $\hat{\mathbf{e}}^{\mathbf{in}}(\omega)$ by $\hat{\mathbf{e}}^\omega$. Here $\hat{\mathbf{e}}^\omega = \left[\hat{\mathbf{s}}t^s_{vm}(\omega)\hat{\mathbf{s}} + \hat{\mathbf{p}}^m_-(\omega)t^p_{vm}(\omega)\hat{\mathbf{p}}^v_-(\omega)\right]\hat{\mathbf{e}}^{\mathbf{in}}(\omega)$.
This incident field in the medium, $\mathbf{E}^\omega$, leads to the apparition of a second-order polarization in the medium, denoted $\mathbf{P}^{(2)}$, which is given by

$$\mathbf{P}^{(2)}(\mathbf{r}; 2\omega) = \int_{-\infty}^{0} d^3\mathbf{r}' \int_{-\infty}^{0} d^3\mathbf{r}'' \overleftrightarrow{\chi}^{(2)}(\mathbf{r}, \mathbf{r}', \mathbf{r}''; \omega, \omega) : \mathbf{E}^\omega(\mathbf{r}')\mathbf{E}^\omega(\mathbf{r}''), \tag{2.8}$$

where $\overleftrightarrow{\chi}^{(2)}$ is the macroscopic second-order susceptibility of the medium.
Introducing the expression of the field inside the medium, $\mathbf{E}^\omega$, in Eq. (2.8) gives directly

$$\mathbf{P}^{(2)}(\mathbf{r}; 2\omega) = \int_{-\infty}^{0} d^3\mathbf{r}' \int_{-\infty}^{0} d^3\mathbf{r}'' \overleftrightarrow{\chi}^{(2)}(\mathbf{r}, \mathbf{r}', \mathbf{r}''; \omega, \omega) : \hat{\mathbf{e}}^\omega\hat{\mathbf{e}}^\omega |E_{\text{in}}|^2 e^{i(\mathbf{q}_{||}(\omega)(\mathbf{r}'_{||} + \mathbf{r}''_{||}) - q^m_\perp(\omega)(z' + z''))}. \tag{2.9}$$

2.2 Harmonic field inside the material

In this section, we consider the non-linearity to originate only from the surface region. The bulk contribution to the generation of second-harmonic is treated later in Sec. 2.4. The expression of the polarization Eq. (2.9) is general and no approximation has been introduced at that stage. Following Ref. [73], instead of using Eq. (2.9), we consider a second-order polarization having the following form

$$\mathbf{P}^{(2)}(\mathbf{r}; 2\omega) = \overleftrightarrow{\chi}^{(2)S}(\omega, \omega) : \hat{\mathbf{e}}^\omega\hat{\mathbf{e}}^\omega |E_{\text{in}}|^2 e^{2i(\mathbf{q}_{||}(\omega)\mathbf{r}_{||} - q^m_\perp(\omega)z)}\delta(z - z_0), \tag{2.10}$$

where the second-order susceptibility is replaced by a second-order surface susceptibility $\overleftrightarrow{\chi}^{(2)S}$, assumed to be local and homogeneous in the plane of the surface. Moreover, the surface polarization is assumed to be a polarization sheet located at $z = z_0$. This is where the phenomenological treatment

stems. In order to ease notations, we define the quantity $\boldsymbol{\mathcal{P}}(2\omega)$ as

$$\mathbf{P}^{(2)}(\mathbf{r};2\omega) = \boldsymbol{\mathcal{P}}(2\omega)e^{2i(\mathbf{q}_{||}(\omega)\mathbf{r}_{||}-q_{\perp}^{m}(\omega)z)}\delta(z-z_0), \tag{2.11}$$

where $\boldsymbol{\mathcal{P}}(2\omega) = \overset{\leftrightarrow}{\chi}^{(2)S}(\omega,\omega) : \hat{\mathbf{e}}^{\omega}\hat{\mathbf{e}}^{\omega}|E_{\text{in}}(\omega)|^2$.
This second-order polarization becomes a source term in Maxwell equations that leads to the second-harmonic field created at the surface of the medium. The reflected harmonic light will thus be given by the solution of the upward-propagating second-harmonic wave in presence of the second-order polarization as a source term.
As pointed out by Mizrahi *et al.* [73], the position of the polarization sheet ($z_0 = 0^-$ or $z_0 = 0^+$) only results in a change of the normalisation factor in front of the expression of the reflection coefficients, and does not modify the weight of the different components of the $\overset{\leftrightarrow}{\chi}^{(2)S}$ tensor in the expression of the reflection coefficients. Throughout this thesis, I use formulae derived for a second-order polarization sheet located at $z_0 = 0^-$.
From the macroscopic Maxwell equations (B.9), without magnetisation and in presence of a polarization of the form Eq. (2.11), we get the following set of equations

$$\begin{aligned}\boldsymbol{\nabla}\times\mathbf{B}(\mathbf{r};2\omega) - i\tilde{\Omega}\epsilon(2\omega)\mathbf{E}(\mathbf{r};2\omega) &= 4\pi i\tilde{\Omega}\mathbf{P}^{(2)}(\mathbf{r};2\omega),\\ \boldsymbol{\nabla}\times\mathbf{E}(\mathbf{r};2\omega) - i\tilde{\Omega}\mathbf{B}(\mathbf{r};2\omega) &= 0,\end{aligned} \tag{2.12}$$

where $\tilde{\Omega} = \frac{2\omega}{c}$.
The physical solution of the Maxwell equations inside the medium (which excludes exponentially diverging waves) has the following form

$$\mathbf{E}^{2\omega}(\mathbf{r}) = \left[\mathbf{E}_{+}^{m}(2\omega)\Theta(z-z_0)e^{-iq_{\perp}^{m}(2\omega)z_0} + \mathbf{E}_{-}^{m}(2\omega)\Theta(z_0-z)e^{iq_{\perp}^{m}(2\omega)z_0} + \mathcal{E}(2\omega)\delta(z-z_0)\right]e^{i\mathbf{q}_{||}(2\omega)\mathbf{r}_{||}}, \tag{2.13a}$$

$$\mathbf{B}^{2\omega}(\mathbf{r}) = \left[\mathbf{B}_{+}^{m}(2\omega)\Theta(z-z_0)e^{-iq_{\perp}^{m}(2\omega)z_0} + \mathbf{B}_{-}^{m}(2\omega)\Theta(z_0-z)e^{iq_{\perp}^{m}(2\omega)z_0} + \mathcal{B}(2\omega)\delta(z-z_0)\right]e^{i\mathbf{q}_{||}(2\omega)\mathbf{r}_{||}}. \tag{2.13b}$$

We now search for the coefficients $E_{s\pm}^{m}(2\omega)$ and $E_{p\pm}^{m}(2\omega)$ of Eq. (2.5), considering the following relations

$$\begin{aligned}\mathcal{E} &= \mathcal{E}_s\hat{\mathbf{s}} + \mathcal{E}_\kappa\hat{\boldsymbol{\kappa}} + \mathcal{E}_\perp\hat{\mathbf{z}},\\ \boldsymbol{\nabla}\Theta(z-z_0) &= \hat{\mathbf{z}}\delta(z-z_0),\\ \boldsymbol{\nabla}\delta(z-z_0) &= \hat{\mathbf{z}}\delta'(z-z_0),\end{aligned} \tag{2.14}$$

with δ' being the derivative of the Dirac δ distribution. Considering that different orders of singularities (δ and δ') must cancel separately, we obtain from the equation $\boldsymbol{\nabla}\times\mathbf{E}(\mathbf{r};2\omega) - i\tilde{\Omega}\mathbf{B}(\mathbf{r};2\omega) = 0$,

$$\begin{aligned}&E_{p+}^{m} + E_{p-}^{m} + i\frac{q_{||}q^{m}}{q_{\perp}^{m}}\mathcal{E}_z - i\frac{\tilde{\Omega}q^{m}}{q_{\perp}^{m}}\mathcal{B}_s = 0,\\ &E_{s+}^{m} - E_{s-}^{m} - i\tilde{\Omega}\mathcal{B}_\kappa = 0,\\ &\mathcal{E}_\kappa = \mathcal{E}_s = \mathcal{B}_\perp = 0.\end{aligned} \tag{2.15}$$

Doing the same for the equation $\boldsymbol{\nabla}\times\mathbf{B}(\mathbf{r};2\omega)-i\tilde{\Omega}\epsilon(2\omega)\mathbf{E}(\mathbf{r};2\omega)=4\pi i\tilde{\Omega}\mathbf{P}(\mathbf{r};2\omega)$ leads to the relations

$$\begin{aligned}
E^m_{p+}-E^m_{p-}&=-4\pi i\frac{\tilde{\Omega}}{\epsilon^{1/2}}\mathcal{P}_\kappa,\\
E^m_{s+}+E^m_{s-}&=4\pi i\frac{\tilde{\Omega}q^m}{\epsilon^{1/2}q^m_\perp}\mathcal{P}_s,\\
\mathcal{E}_\perp&=-\frac{1}{\epsilon}\mathcal{P}_\perp,\\
\mathcal{B}_s&=\mathcal{B}_\kappa=0.
\end{aligned}\tag{2.16}$$

Putting everything together leads to the expression of the wanted coefficients

$$\begin{aligned}
E^m_{s\pm}(2\omega)&=E^m_s(2\omega)=\frac{2\pi i\tilde{\Omega}^2}{q^m_\perp(2\omega)}\hat{\mathbf{s}}.\boldsymbol{\mathcal{P}}(2\omega),\\
E^m_{p\pm}(2\omega)&=\frac{2\pi i\tilde{\Omega}^2}{q^m_\perp(2\omega)}\hat{\mathbf{p}}_\pm(2\omega).\boldsymbol{\mathcal{P}}(2\omega).
\end{aligned}\tag{2.17}$$

2.3 Reflected harmonic light from a surface

Knowing the expression of the upward-propagating second-harmonic field, we can now look at the expression of the reflected harmonic light in the vacuum. Assuming the expression Eq. (2.17) for the coefficients of the second-harmonic field, the electric field oscillating at the frequency 2ω and induced in the medium, denoted $\mathbf{E}^{2\omega}(\mathbf{r})$, reads as

$$\mathbf{E}^{2\omega}(\mathbf{r})=\frac{2\pi i\tilde{\Omega}^2}{q^m_\perp(2\omega)}\boldsymbol{\mathcal{P}}(2\omega)e^{i(\mathbf{q}_{||}(2\omega)\mathbf{r}_{||}-q^m_\perp(2\omega)z)}.\tag{2.18}$$

At the interface with the vacuum, this upward-propagating field is transmitted into the vacuum, yielding the field $\mathbf{E}_{\text{out}}(\mathbf{r};2\omega)$; which is the second-harmonic field measured during the experiment. We obtain that

$$\mathbf{E}_{\text{out}}(\mathbf{r};2\omega)=\frac{2\pi i\tilde{\Omega}^2}{q^m_\perp(2\omega)}\hat{\mathbf{e}}^{\mathbf{2\omega}}\boldsymbol{\mathcal{P}}(2\omega)e^{i(\mathbf{q}_{||}(\mathbf{2\omega})\mathbf{r}_{||}-q^m_\perp(2\omega)z)},\tag{2.19}$$

with $\hat{\mathbf{e}}^{2\omega}=\hat{\mathbf{e}}^{\mathbf{out}}(2\omega)\left[\hat{\mathbf{s}}t^s_{mv}(2\omega)\hat{\mathbf{s}}+\hat{\mathbf{p}}^v_+(2\omega)t^p_{mv}(2\omega)\hat{\mathbf{p}}^m_+(2\omega)\right]$, $\hat{\mathbf{e}}^{\mathbf{out}}(2\omega)$ being the measured polarization. The intensity of the second-harmonic field in the vacuum is finally given by

$$I_{\text{out}}(2\omega)\;=\;\frac{c}{2\pi}|\mathbf{E}_{\text{out}}(2\omega)|^2=\frac{8\pi^3}{c}\left|\frac{\tilde{\Omega}^2}{q^v_\perp(2\omega)}\right|^2\left|\frac{q^v_\perp(2\omega)}{q^m_\perp(2\omega)}\right|^2\left|\hat{\mathbf{e}}^{2\omega}.\overset{\leftrightarrow}{\chi}^{(2)S}(\omega,\omega):\hat{\mathbf{e}}^{\omega}\hat{\mathbf{e}}^{\omega}\right|^2 I^2_{\text{in}}(\omega).\tag{2.20}$$

Inserting the definition of the $\tilde{\Omega}$ and $q^v_\perp(2\omega)$, the general form of the reflection coefficients is found to be

$$R(\theta,\phi,\omega)=\frac{32\pi^3\omega^2}{c^3}\frac{1}{\cos^2(\theta)}\left|\frac{q^v_\perp(2\omega)}{q^m_\perp(2\omega)}\right|^2\left|\hat{\mathbf{e}}^{2\omega}.\overset{\leftrightarrow}{\chi}^{(2)S}(\omega,\omega):\hat{\mathbf{e}}^{\omega}\hat{\mathbf{e}}^{\omega}\right|^2.\tag{2.21}$$

We obtain in the S.I. unit system gives

$$R(\theta,\phi,\omega) = \frac{\omega^2}{2c^3\epsilon_0}\frac{1}{\cos^2(\theta)}\left|\frac{q_\perp^v(2\omega)}{q_\perp^m(2\omega)}\right|^2\left|\hat{\mathbf{e}}^{2\omega}.\overset{\leftrightarrow}{\chi}^{(2)S}(\omega,\omega):\hat{\mathbf{e}}^{\omega}\hat{\mathbf{e}}^{\omega}\right|^2. \tag{2.22}$$

This reflection coefficient has a unit in the S.I. system of cm^2/W. One has to be careful here that the second-order susceptibility is label with the S superscript because it is a *surface* second-order susceptibility, expressed in the S.I. unit system in pm^2/V, whereas the second-order susceptibility is expressed in pm/V in the S.I unit system.
In order to obtain the expression of the different reflection coefficients used in the literature, we have to replace $\hat{\mathbf{e}}^{\mathbf{in}}(\omega)$ and $\hat{\mathbf{e}}^{\mathbf{out}}(2\omega)$ by the wanted polarizations; *e.g.*, the R_{ps} coefficient (sometimes referred in the literature as p-in s-out), is obtained by choosing $\hat{\mathbf{e}}^{\mathbf{in}}(\omega) = \hat{\mathbf{p}}_-^v(\omega)$ and $\hat{\mathbf{e}}^{\mathbf{out}}(2\omega) = \hat{\mathbf{s}}$.
In that case, Eq. (2.22) becomes

$$R_{ps}(\theta,\phi,\omega) = \frac{32\pi^3\omega^2}{c^3}\frac{1}{\cos^2(\theta)}\left|t_{mv}^s(2\omega)t_{vm}^p(\omega)^2\right|^2\left|\frac{q_\perp^v(2\omega)}{q_\perp^m(2\omega)}\right|^2\left|\hat{\mathbf{s}}.\overset{\leftrightarrow}{\chi}^{(2)S}(\omega,\omega):\hat{\mathbf{p}}_-^m(\omega)\hat{\mathbf{p}}_-^m(\omega)\right|^2. \tag{2.23}$$

Then, from Eq.(2.4), and using the definition of $\hat{\boldsymbol{\kappa}}$, we obtain that

$$\begin{aligned}\hat{\mathbf{s}} &= \sin(\phi)\hat{\mathbf{x}} - \cos(\phi)\hat{\mathbf{y}},\\ \hat{\mathbf{p}}_\pm^m(\omega) &= \frac{c}{\sqrt{\epsilon(\omega)}\omega}\left[\mp q_\perp^m(\omega)\cos(\phi)\hat{\mathbf{x}} \mp q_\perp^m(\omega)\sin(\phi)\hat{\mathbf{y}} + q_{||}(\omega)\hat{\mathbf{z}}\right].\end{aligned} \tag{2.24}$$

Notice that in the case of an arbitrary input polarization with an angle α, see Fig. 2.1(a), we have $\hat{\mathbf{e}}^{\mathbf{in}}(\omega) = \cos\alpha\hat{\mathbf{p}}_-^v(\omega) + \sin\alpha\hat{\mathbf{s}}$.
I consider now the special case of a $4mm$ or higher symmetry surface, where the only non-zero components of the $\chi^{(2)S}$ tensor are $\chi_{|||\perp}^{(2)S} = \chi_{xxz}^{(2)S} = \chi_{yyz}^{(2)S}$, $\chi_{\perp|||}^{(2)S} = \chi_{zxx}^{(2)S} = \chi_{zyy}^{(2)S}$ and $\chi_{\perp\perp\perp}^{(2)S} = \chi_{zzz}^{(2)S}$.
This symmetry corresponds, for instance, to the case of the Si(001)1x1:2H (dihydride) silicon surface. The same components also appear in the expressions of the reflection coefficients for the clean Si(001)2×1 and the Si(001)2×1:H surfaces (see Chapter. 4 for more details concerning these surfaces), even if they have less symmetries than the dihydride surface. [4]
From the previous equations, we obtain the expressions for the four reflection coefficients

$$\begin{aligned}R_{pp}(\theta,\omega) = {}& \frac{32\pi^3\omega^2}{c^3}\tan^2\theta\left|\frac{t_{mv}^p(2\omega)t_{vm}^p(\omega)^2}{\sqrt{\epsilon(2\omega)}\epsilon(\omega)}\right|^2\left|\frac{q_\perp^v(2\omega)}{q_\perp^m(2\omega)}\right|^2\\ &\times\left|\sin^2\theta\chi_{\perp\perp\perp}^{(2)S}(\omega) + \frac{c^2}{\omega^2}q_\perp^m(\omega)^2\chi_{\perp|||}^{(2)S}(\omega) - \frac{c^2}{\omega^2}q_\perp^m(2\omega)q_\perp^m(\omega)\chi_{|||\perp}^{(2)S}(\omega)\right|^2,\end{aligned} \tag{2.25a}$$

[4] As explained by Sipe *et al.* in Ref. [75], these two surfaces exhibit a macroscopic averaged symmetry, which is different from the single domain symmetry. For instance, the Si(001)2×1 surface has an equal population (1×2) and (2×1) domains with a m-symmetry. It results in an averaged $p2mm$ symmetry for this surface, due to the size of the laser spot, compared to the small size of a single domain. Even if one was able to produce large enough domain, bigger than the laser spot size, this does not correspond to industrial Si surfaces, which are of major interest. This averaged symmetry is confirmed by experimental measurements performed by Rotational Anisotropy SHG (RASHG), where one can analyse the symmetries of a surface.

$$R_{sp}(\theta,\omega) = \frac{32\pi^3\omega^2}{c^3}\tan^2\theta\left|\frac{t^p_{mv}(2\omega)t^s_{vm}(\omega)^2}{\sqrt{\epsilon(2\omega)}}\right|^2\left|\frac{q^v_\perp(2\omega)}{q^m_\perp(2\omega)}\right|^2\left|\chi^{(2)S}_{\perp\parallel\parallel}(\omega)\right|^2, \tag{2.25b}$$

$$R_{ps}(\omega) = R_{ss}(\omega) = 0. \tag{2.25c}$$

Due to the symmetries, the two coefficients associated with a measured s-polarization are zero. Moreover, R_{pp} and R_{sp} do not depend on the azimuthal angle ϕ, due to the in-plane isotropy of the surface ($4mm$ symmetry class). This last point has been used in Ref. [76,77] to separate the contributions to the signal from the surface and from the bulk part of the material, for the dihydride surface. The careful reader will also note that the R_{pp} coefficient contains contributions from all the non-zero components. The expressions of these coefficients, obtained without assuming any symmetry, and in the case of other symmetries are given in App. C.

2.4 Bulk contribution

So far, I do not have discussed the contribution coming from the bulk part of the material to the reflected signal. There are three different cases in which the bulk can contribute to the reflected harmonic waves: i) The case of the non-centrosymmetric bulk. In that case, the signal is dominated by the bulk dipolar contribution. ii) The case of centrosymmetric material, where the dipolar contribution vanishes, but not the quadrupolar contribution. The quadrupolar contribution has been found non-negligible in some cases; compared to the surface signal [78–80]. iii) A material, having or not the inversion symmetry, under an electric field, and therefore producing an Electric Field Induced Second-Harmonic (EFISH) contribution. This last point will not be discuss here but is discussed extensively in Ref. [81]. All these cases can be treated using the same approach than presented in the previous sections of this chapter. Following Ref. [73], I first consider a general expression for the nonlinear polarization in the medium, given by

$$\mathbf{P}^{(2)}(\mathbf{r};2\omega) = \overset{\leftrightarrow}{\chi}^{(2)}(\omega,\omega) : \mathbf{E}^\omega(\mathbf{r})\mathbf{E}^\omega(\mathbf{r}) + \gamma_B(\omega)\boldsymbol{\nabla}[\mathbf{E}^\omega(\mathbf{r}).\mathbf{E}^\omega(\mathbf{r})], \tag{2.26}$$

where $\mathbf{E}^\omega(\mathbf{r})$ is the fundamental electric field inside the material, $\overset{\leftrightarrow}{\chi}^{(2)}$ is the bulk second-order susceptibility tensor and γ_B serves for describing the quadrupolar response of the bulk part of the material. Here I have chosen a simple expression for the quadrupolar contribution, where only the isotropic part has been considered. More precise expressions for the quadrupolar part can be obtained by adding extra terms, as done in Ref. [64] for instance.
Introducing the expression of $\mathbf{E}^\omega(\mathbf{r})$ in the expression of the polarization gives

$$\mathbf{P}^{(2)}(\mathbf{r};2\omega) = \left(\overset{\leftrightarrow}{\chi}^{(2)}(\omega,\omega) + \gamma_B(\omega)\left[2iq_\parallel(\omega)\hat{\kappa} - 2iq^m_\perp(\omega)\hat{\mathbf{z}}\right]\right) : \hat{\mathbf{e}}^\omega\hat{\mathbf{e}}^\omega|E_{\text{in}}|^2 e^{2i(\mathbf{q}_{||}(\omega)\mathbf{r}_{||} - q^m_\perp(\omega)z)}. \tag{2.27}$$

As explained in Ref. [73], this polarization can be seen as the sum of individual sheets of polarization, as introduced previously, located at a distance z from the surface. This allows us to use the same formalism as introduced previously for describing the harmonic field generated inside the medium. At the interface with the vacuum, the field is modified according to the Fresnel coefficients. The electric

field that reaches the detector is thus $\mathbf{E}_{\text{out}}(z;2\omega) = \mathbf{E}_{\text{out}}(z=0^+;2\omega)e^{iq_\perp^v(2\omega)z} = \mathbf{E}_{\text{out}}(2\omega)e^{iq_\perp^v(2\omega)z}$, with

$$\begin{aligned}\mathbf{E}_{\text{out}}(2\omega) &= \frac{2\pi i\tilde{\Omega}^2}{q_\perp^m(2\omega)}\hat{\mathbf{e}}^{\mathbf{2}\omega}\int_{-\infty}^{0} dz' e^{-iq_\perp^m(2\omega)z'}\mathbf{P}^{(2)}(z';2\omega) \\ &= \frac{2\pi i\tilde{\Omega}^2}{q_\perp^m(2\omega)}\hat{\mathbf{e}}^{\mathbf{2}\omega}\left(\frac{i\overset{\leftrightarrow}{\chi}^{(2)}(\omega,\omega) - 2\gamma_B(\omega)\left[q_\parallel(\omega)\hat{\kappa} - q_\perp^m(\omega)\hat{\mathbf{z}}\right]}{q_\perp^v(2\omega)+2q_\perp^v(\omega)}\right) : \hat{\mathbf{e}}^\omega\hat{\mathbf{e}}^\omega|E_{\text{in}}|^2 e^{2i\mathbf{q}_{||}(\omega)\mathbf{r}_{||}}\end{aligned}$$

where $e^{-iq_\perp^m(2\omega)z'}$ describes the propagation in the medium from the polarization sheet located at $-z'$ to the interface at 0^-. The second line comes from the fact that we consider an absorbing medium (see Ref. [73]). The coefficients are identical to the one defined in the case of a surface polarization. In the following, I focus on the example of a cubic symmetry for a medium that lack inversion symmetry. This is for instance the case of GaAs and the expression presented bellow has been used in Ref. [63] for extracting the xyz component from its experimental reflection spectrum. The contribution of the quadrupolar term in a centro-symmetric material can be obtained similarly.
In the case of a cubic material, the second-order susceptibility has only one non-zero component, $\chi^{(2)}_{xyz}$. The reflection coefficients in that case have the general form

$$R(\theta,\phi,\omega) = \frac{32\pi^3\omega^2}{c^3}\frac{1}{\cos^2\theta}\left|\frac{q_\perp^v(2\omega)}{q_\perp^m(2\omega)[q_\perp^m(2\omega)+2q_\perp^m(\omega)]}\right|^2\left|\hat{\mathbf{e}}^{\mathbf{2}\omega}\overset{\leftrightarrow}{\chi}^{(2)}(\omega,\omega) : \hat{\mathbf{e}}^\omega\hat{\mathbf{e}}^\omega\right|^2, \tag{2.28}$$

or in the S.I. unit sytem[5],

$$R(\theta,\phi,\omega) = \frac{\omega^2}{2c^3\epsilon_0}\frac{1}{\cos^2\theta}\left|\frac{q_\perp^v(2\omega)}{q_\perp^m(2\omega)[q_\perp^m(2\omega)+2q_\perp^m(\omega)]}\right|^2\left|\hat{\mathbf{e}}^{\mathbf{2}\omega}\overset{\leftrightarrow}{\chi}^{(2)}(\omega,\omega) : \hat{\mathbf{e}}^\omega\hat{\mathbf{e}}^\omega\right|^2. \tag{2.29}$$

The expressions of the four usual reflection coefficients are given in App. C.

Conclusion

In this chapter, I have reported the derivation of the expressions of the generalized reflection coefficients. They describe how the second-harmonic light is generated by reflection of a fundamental light on a surface. We have seen that a second-order polarization is induced by the incident light and how that polarization, acting as a source term for the Maxwell equations, yields a second-harmonic field, reflected from the surface. This formalism allows us to treat both bulk and surface dipolar contributions and also the other bulk contributions such as the bulk quadrupolar and the EFISH; for any combination of input and output polarizations of the light. Moreover, if we want to obtain the contributions coming from the bulk medium and its surface at the same time, the reflection coefficients can be obtained by the mean of Eq. 2.19, using an effective polarization given by

$$\boldsymbol{\mathcal{P}}_{\text{eff}}(2\omega) = \left(\overset{\leftrightarrow}{\chi}^{(2)S}(\omega,\omega) + \frac{i\overset{\leftrightarrow}{\chi}^{(2)}(\omega,\omega) - 2\gamma_B(\omega)\left[q_\parallel(\omega)\hat{\boldsymbol{\kappa}} - q_\perp^m(\omega)\hat{\mathbf{z}}\right]}{[q_\perp^m(2\omega)+2q_\perp^m(\omega)]}\right) : \hat{\mathbf{e}}^\omega\hat{\mathbf{e}}^\omega|E_{\text{in}}|^2. \tag{2.30}$$

[5]Notice that in this expression, $\overset{\leftrightarrow}{\chi}^{(2)}$ is a bulk second-order susceptibility, expressed in pm/V in the S.I. unit system.

To conclude, we have presented here a simple model for the generation of second-harmonic in reflection from surfaces. Some features are missing and can be added to account, for instance, for multiple reflections from a cover oxide layer [82], the anisotropy of the linear medium or corrections to the Fresnel reflection coefficients due to the presence of the surface [83].
Nevertheless, the difficulty here is not contained in such possible improvements of the description of the reflection of light but in a quantitative *ab initio* description of the macroscopic second-order response function of the surface part of the material. In the next chapter, I briefly present the (time-dependent) density-functional theory and how this framework allows us to compute the second-order susceptibility tensor $\overleftrightarrow{\chi}^{(2)}$ from the perturbation theory.

3. (Time-Dependent) Density-Functional Theory in a nutshell

> Sometimes one can improve the theories in the sense of discovering a quicker, more efficient way of doing a given calculation.
>
> Sir John Anthony Pople, Nobel prize co-winner for the DFT

This chapter aims to review the fundamental background of the Density-Functional Theory (DFT) and Time-Dependent Density-Functional theory (TDDFT). This exact theories give respectively access to the ground-state and excited states of the many-body systems. The ground-state gives access to numerous properties of the system such as the total energy, the electron density or the correlation functions.
The optical properties, as many other properties, are not properties of the ground-state and require the knowledge of the excited states. For obtaining the excited states, one can use the Time-Dependent Density-Functional Theory (TDDFT), which has been proven to give reliable results for the calculation of linear and nonlinear optical properties of bulk materials [84] and interfaces [29].
If the interaction that drives the system out of its ground-state is small, the time-dependent perturbation theory can simplify the task associated to calculation of optical properties.
This chapter is organised as follows. As excitations in the frame of this thesis are restricted to small perturbations of the entire system, I first discuss how within the framework of time-dependent perturbation theory, one can obtain the linear and the second-order response functions, describing the linear and nonlinear optical properties. Then I briefly review the static and time-dependent Density-Functional Theory, as well as some common approximations. Finally, some numerical details related to the calculation performed during this thesis are presented.

3.1 Time-dependent perturbation theory

In perturbation theory, the interaction between light and electrons is treated as a *perturbation*. This perturbation induces a *response* inside the system. More precisely it induces a current and a density, respectively denoted $\mathbf{j}_{\text{ind}}$ and n_{ind}.

3.1.1 Induced current and induced density

As it is customary for a perturbative approach, the two induced quantities are expended in power of the perturbation. The first-order terms describe the linear response of the system and are denoted respectively $\mathbf{j}^{(1)}_{\text{ind}}$ and $n^{(1)}_{\text{ind}}$. Similarly, the second-order induced current and density, denoted $\mathbf{j}^{(2)}_{\text{ind}}$ and $n^{(2)}_{\text{ind}}$, describe the nonlinear second-order phenomena, such as second-harmonic generation.
We start by considering the total single-electron Hamiltonian $H(t)$ that reads as

$$H(t) = H_0 + H_I(t),$$

where H_0 is the unperturbed time-independent Hamiltonian and $H_I(t)$ is the time-dependent interaction Hamiltonian due to the interaction of the electrons with the electromagnetic field. We switch on the perturbation adiabatically at $t_0 = -\infty$. The interaction Hamiltonian is made of a first-order contribution plus a second-order contribution, such as $H_I(t) = H_I^{(1)}(t) + H_I^{(2)}(t)$, with [44]

$$H_I^{(1)}(t) = \int d^3\mathbf{r}\hat{n}(\mathbf{r})\phi^P(\mathbf{r},t) - \frac{1}{c}\int d^3\mathbf{r}\hat{\mathbf{j}}(\mathbf{r})\mathbf{A}^P(\mathbf{r},t), \tag{3.1a}$$

$$H_I^{(2)}(t) = \frac{1}{2c^2}\int d^3\mathbf{r}\hat{n}(\mathbf{r})\mathrm{A}^P(\mathbf{r},t)^2, \tag{3.1b}$$

where ϕ^P is the scalar potential, $\mathbf{A}^P$ the vector potential, and $\hat{n}$ and $\hat{\mathbf{j}}$ are respectively the density and the current operators, defined by

$$\hat{n}(\mathbf{r}) = \sum_i \delta(\mathbf{r} - \mathbf{r_i}), \tag{3.2a}$$

$$\hat{\mathbf{j}}(\mathbf{r}) = \frac{1}{2}\sum_i \left[\mathbf{p}_i\delta(\mathbf{r} - \mathbf{r_i}) + \delta(\mathbf{r} - \mathbf{r_i})\mathbf{p}_i\right]. \tag{3.2b}$$

To obtain the induced current and the induced density, it is necessary to evaluate the expectation values of these operators with respect to the Schrödinger many-body wave-functions $\Psi(t)$. For deriving these expressions, it is common in perturbation theory to use the interaction representation, where the wave-functions $\Psi_I(t)$ are given by

$$\Psi_I(t) = e^{iH_0(t-t_0)}\Psi(t_0), \qquad i\frac{\partial}{\partial t}\Psi_I(t) = e^{iH_0(t-t_0)}H_I e^{-iH_0(t-t_0)}\Psi_I(t) = H_{I,I}\Psi_I(t), \tag{3.3}$$

where $H_{I,I}$ describes the interaction in interaction representation.
From perturbation theory, up to second-order, using the Baker-Hausdorff theorem [85], we obtain that

$$\begin{aligned}\mathbf{j}_{\text{ind}}(\mathbf{r},t) &= \langle\Psi_I(t)|\hat{\mathbf{j}}_{\text{ind}}(\mathbf{r},t)|\Psi_I(t)\rangle \\ &= \langle\hat{\mathbf{j}}_{\text{ind}}(\mathbf{r},t)\rangle - i\int_{t_0}^{t} dt'\langle\left[\hat{\mathbf{j}}_{\text{ind}}(\mathbf{r},t), H_{I,I}(t')\right]\rangle - \int_{t_0}^{t}dt'\int_{t_0}^{t'}dt''\langle\left[\left[\hat{\mathbf{j}}_{\text{ind}}(\mathbf{r},t), H_{I,I}(t')\right], H_{I,I}(t'')\right]\rangle,\end{aligned} \tag{3.4}$$

where we use the notation $\langle\hat{O}\rangle = \langle\Psi_0(t_0)|\hat{O}|\Psi_0(t_0)\rangle$, Ψ_0 being the ground-state many-body wave-function. A similar formula holds for the induced density. From the general expression of the in-

duced current, it is easy to obtain the expression of, says, the first-order induced current [44]

$$\mathbf{j}^{(1)}_{\text{ind}}(\mathbf{r},t) = -\frac{1}{c}\langle\hat{n}(\mathbf{r})\rangle\mathbf{A}^P(\mathbf{r},t) + \frac{i}{c}\int d^3\mathbf{r}'\int dt'\theta(t-t')\langle\Big[\hat{\mathbf{j}}_I(\mathbf{r},t),\hat{\mathbf{j}}_I(\mathbf{r}',t')\Big]\rangle\mathbf{A}^P(\mathbf{r}',t') - i\int d^3\mathbf{r}'\int dt'\theta(t-t')\langle\Big[\hat{\mathbf{j}}_I(\mathbf{r},t),\hat{n}_I(\mathbf{r}',t')\Big]\rangle\phi^P(\mathbf{r}',t').$$

The expressions of the second-order induced current or first- and second-order induced density are not shown for conciseness, but can be obtained in a similar way.
It is interesting to define response functions [44], which link the perturbation to the response and contains all the physics that we want to describe. At the first- and the second-order, the response functions have the general form [41, 44]

$$\chi_{AB}(\mathbf{r},t,\mathbf{r}',t') = i\theta(t-t')\langle\Big[\hat{\mathbf{A}}_I(\mathbf{r},t),\hat{\mathbf{B}}_I(\mathbf{r}',t')\Big]\rangle, \tag{3.6a}$$

$$\chi_{ABC}(\mathbf{r},t,\mathbf{r_1},t_1,\mathbf{r_2},t_2) = \theta(t-t_1)\theta(t-t_2)T\langle\Big[\Big[\hat{\mathbf{A}}_I(\mathbf{r},t),\hat{\mathbf{B}}_I(\mathbf{r_1},t_1)\Big],\hat{\mathbf{C}}_I(\mathbf{r_2},t_2)\Big]\rangle, \tag{3.6b}$$

where A, B and C can be $\mathbf{j}$ or n, and T is the time-ordering operator. For instance, if we choose $A = B = C = \mathbf{j}$, we get at first-order the so-called *current-current* response function $\chi_{\mathbf{jj}}$ and at second-order the *current-current-current* response function $\chi_{\mathbf{jjj}}$. From Eqs. (3.6), it is obvious that the response functions are causal and that

$$\chi_{AB}(\mathbf{r},t,\mathbf{r}',t') = 0 \quad \text{for} \quad t' > t,$$
$$\chi_{ABC}(\mathbf{r},t,\mathbf{r_1},t_1,\mathbf{r_2},t_2) = 0 \quad \text{for} \quad t_1 > t \quad \text{or} \quad t_2 > t.$$

Also, if we replace the operators in Eqs. (3.6), by their Schrödinger representation, we obtain that the response functions are invariant by translation in time

$$\chi_{AB}(\mathbf{r},t,\mathbf{r}',t') = \chi_{AB}(\mathbf{r},\mathbf{r}',t-t') \quad \text{for} \quad t' > t,$$
$$\chi_{ABC}(\mathbf{r},t,\mathbf{r_1},t_1,\mathbf{r_2},t_2) = \chi_{ABC}(\mathbf{r},\mathbf{r_1},\mathbf{r_2},t-t_1,t-t_2) \quad \text{for} \quad t_1 > t \quad \text{or} \quad t_2 > t.$$

In total there are 4 response functions at the first-order and 8 at the second-order, leading to relatively complex expressions for the induced quantities. However it is possible to rearrange all the terms, using *gauge-invariance* [44, 45], and by introducing the expression of the perturbing electric field $\mathbf{E}^P$.[1] After some algebra that the interested reader can find in Ref. [45], the induced current and the induced density are given in frequency space by [2]

$$\mathbf{j}^{(1)}_{\text{ind}}(\mathbf{r};\omega) = \frac{i}{\omega}\langle\hat{n}(\mathbf{r})\rangle\mathbf{E}^P(\mathbf{r};\omega) - \frac{i}{\omega}\int d^3\mathbf{r}'\chi_{\mathbf{jj}}(\mathbf{r},\mathbf{r}';\omega)\mathbf{E}^P(\mathbf{r}';\omega), \tag{3.9a}$$

[1] The perturbing field is given by

$$\mathbf{E}^P(\mathbf{r};\omega) = \frac{i\omega}{c}\mathbf{A}^P(\mathbf{r};\omega) - \frac{\partial}{\partial\mathbf{r}}\phi^P(\mathbf{r};\omega).$$

[2] For obtaining these expressions, one must first use the fact that $\chi_{AB}(\mathbf{r},t,\mathbf{r}',t') = \chi_{AB}(\mathbf{r},\mathbf{r}',t-t')$ and $\chi_{ABC}(\mathbf{r},t,\mathbf{r_1},t_1,\mathbf{r_2},t_2) = \chi_{ABC}(\mathbf{r},\mathbf{r_1},\mathbf{r_2},t-t_1,t-t_2)$. Indeed, in absence of strong perturbing field, the system is stationary in time and the response depends only on the time difference between the moment of the response and the imposition of perturbation [54].

$$\mathbf{j}^{(2)}_{\text{ind}}(\mathbf{r};\omega) = -\frac{1}{2\omega_1\omega_2}\int d^3\mathbf{r_1}d^3\mathbf{r_2}\int d\omega_1 d\omega_2 \delta(\omega-\omega_1-\omega_2)\mathbf{E}^P(\mathbf{r_1};\omega_1)\mathbf{E}^P(\mathbf{r_2};\omega_2)$$
$$\times\left[\chi_{\mathbf{jjj}}(\mathbf{r},\mathbf{r_1},\mathbf{r_2};\omega_1,\omega_2) + 2\chi_{\rho\mathbf{j}}(\mathbf{r},\mathbf{r_1};\omega_1)\delta(\mathbf{r}-\mathbf{r_2}) - \frac{i\delta(\mathbf{r}-\mathbf{r_2})}{(\omega_1+\omega_2)}\frac{\partial}{\partial\mathbf{r_1}}\chi_{\mathbf{jj}}(\mathbf{r},\mathbf{r_1};\omega_1+\omega_2)\right], \quad (3.9b)$$

$$n^{(1)}_{\text{ind}}(\mathbf{r};\omega) = \frac{i}{\omega}\int d^3\mathbf{r}'\chi_{\rho\mathbf{j}}(\mathbf{r},\mathbf{r}',\omega)\mathbf{E}^P(\mathbf{r}';\omega), \quad (3.9c)$$

$$n^{(2)}_{\text{ind}}(\mathbf{r};\omega) = \frac{i}{2}\int d^3\mathbf{r_1}\int d\omega_1 d\omega_2 \frac{\delta(\omega-\omega_1-\omega_2)}{(\omega_1+\omega_2)\omega_1\omega_2}\frac{\partial}{\partial\mathbf{r_1}}\chi_{\rho\mathbf{j}}(\mathbf{r},\mathbf{r_1};\omega)\mathbf{E}^P(\mathbf{r_1};\omega_1).\mathbf{E}^P(\mathbf{r_1};\omega_2)$$
$$-\frac{1}{2}\int d^3\mathbf{r_1}d^3\mathbf{r_2}\int d\omega_1 d\omega_2 \frac{\delta(\omega-\omega_1-\omega_2)}{\omega_1\omega_2}\chi_{\rho\mathbf{jj}}(\mathbf{r},\mathbf{r_1},\mathbf{r_2};\omega_1,\omega_2)\mathbf{E}^P(\mathbf{r_1};\omega_1)\mathbf{E}^P(\mathbf{r_2};\omega_2). \quad (3.9d)$$

Only few response functions, among all possible response functions, are finally involved in the expressions of the induced current and the induced density. Indeed, the first-order responses are described only by the two response functions $\chi_{\mathbf{jj}}$ and $\chi_{\rho\mathbf{j}}$, whereas one must also include $\chi_{\mathbf{jjj}}$ and $\chi_{\rho\mathbf{jj}}$ in order to describe the second-order responses. All the other response functions can be obtained from these four ones. With these expressions, one can describe any perturbation of the system at first- and second-order.

3.2 Density-Functional Theory (DFT)

Before presenting the Density-Functional Theory, I start with the quantum description of system and a basic approximation, commonly used in quantum mechanics, the Born-Oppenheimer approximation. Then I review the basements of the Density-Functional Theory (DFT), which are the Hohenberg-Kohn theorems and the Kohn-Sham method.

3.2.1 Many-body Hamiltonian

In this thesis, the matter is quantified and the light is treated classically. The starting point of the quantum treatment of the matter is to consider a system of interacting electrons and nuclei. The system is considered to be non-magnetic. Relativistic and quantum electrodynamics effects are neglected. The static many-body Hamiltonian associated to such a system is given by

$$\hat{H}(\{\mathbf{r},\mathbf{R},\mathbf{p},\mathbf{P}\}) = \sum_i \frac{\mathbf{p_i}^2}{2m_e} - \sum_{i,I}\frac{Z_I e^2}{|\mathbf{r_i}-\mathbf{R_I}|} + \frac{1}{2}\sum_{i\neq j}\frac{e^2}{|\mathbf{r_i}-\mathbf{r_j}|} + \sum_I \frac{\mathbf{P_I}^2}{2M_I} + \frac{1}{2}\sum_{I\neq J}\frac{Z_I Z_J e^2}{|\mathbf{R_I}-\mathbf{R_J}|}, \quad (3.10)$$

where the electrons are represented by the coordinates $\mathbf{r_i}$, the momenta $\mathbf{p_i}$, and a mass m_e. Nuclei are represented by the coordinates $\mathbf{R_I}$, the momenta $\mathbf{P_I}$, and a mass M_I.
The fundamental Hamiltonian can be written as the sum of the different contributions

$$\hat{H} = \hat{T}_e + \hat{V}_{eN} + \hat{V}_{ee} + \hat{T}_N + \hat{V}_{NN}, \quad (3.11)$$

where $\hat{T}_e$ and $\hat{T}_N$ are the kinetic energies of the electrons and of the nuclei respectively, $\hat{V}_{ee}$ is the electron-electron Coulomb interaction

$$\hat{V}_{ee} = \frac{1}{2}\sum_{i\neq j}\frac{e^2}{|\mathbf{r_i}-\mathbf{r_j}|}, \tag{3.12}$$

that excludes the self-interaction term ($i \neq j$) and $\hat{V}_{eN}$ and $\hat{V}_{NN}$ are electron-nuclei and nuclei-nuclei Coulomb interactions.
The task associated with solving the many-body problem represented by Eq. (3.10) is too complicated to be treated numerically even for a small system of few ten of electrons. Therefore some approximations are required. One excellent approximation for many purposes, and especially for all the calculations of this thesis, is the well-known Born-Oppenheimer approximation [86].

Born-Oppenheimer approximation

The fundamental Hamiltonian given by Eq. (3.10) treats at the same footing electrons and nuclei. Nevertheless, they are quite different and in particular the mass of a proton ($m_p \sim 1.67.10^{-27}$kg) is about 1800 times bigger than the mass of the electron ($m_e \sim 9.31.10^{-31}$kg). The approximation introduced in 1927 by Born and Oppenheimer [86] consists in decoupling the motion of electrons and nuclei and to assume that the motion of the nuclei is slow in comparison to that of the electrons. The nuclei are thus considered to be fixed or *frozen*, giving also the name of *adiabatic approximation* for the Born-Oppenheimer approximation. As the mass of nuclei is set to infinity, the kinetic energy of nuclei is zero. The eigenvalue problem to solve, assuming the Born-Oppenheimer approximation, is given by

$$\hat{H}_e(\{\mathbf{r},\mathbf{R},\mathbf{p},\mathbf{P}\})\varphi_{\mathbf{R}}(\{\mathbf{r}\}) = E_{\mathbf{R}}\varphi_{\mathbf{R}}(\{\mathbf{r}\}), \tag{3.13}$$

where $\varphi_{\mathbf{R}}(\{\mathbf{r}\})$ are the wave-functions of the electrons assuming fix nuclei and $\hat{H}_e(\{\mathbf{r},\mathbf{R},\mathbf{p},\mathbf{P}\}) = \hat{T}_e + \hat{V}_{ee} + \hat{V}_{eN}$. This equation describes a system of interacting electrons in presence of an external potential due to the *frozen* nuclei at positions $\{\mathbf{R}\}$.
Using the Born-Oppenheimer approximation, we turn the many-body problem described by Eq. (3.10) into a many-electron problem represented by Eq. (3.13); which still represents a formidable problem to solve. In the following, I always assume the Born-Oppenheimer approximation. The nuclei positions are parameters of the calculations and the subscript $\mathbf{R}$ is now omitted for conciseness. The Hamiltonian representing the electronic problem will be written from now on as

$$\hat{H}_e(\{\mathbf{r},\mathbf{p}\}) = \sum_i \frac{\mathbf{p_i}^2}{2} + \sum_i \hat{V}_{\text{ext}}(\mathbf{r_i}) + \frac{1}{2}\sum_{i\neq j}\frac{1}{|\mathbf{r_i}-\mathbf{r_j}|}, \tag{3.14}$$

with $\hat{V}_{\text{ext}}$ the electrons-nuclei interaction potential.

3.2.2 Hohenberg-Kohn theorems

In their paper [87] published in 1964, Hohenberg and Kohn laid the foundations of the Density-Functional Theory (DFT). They proved two theorems that are presented here. The proofs of those

two theorems are not reported here but a detailed proof can be found, for instance, in Refs. [88, 89].

The density as the key quantity

The first theorem of Hohenberg and Kohn states the following: [89]
The ground-state density $n_0(\mathbf{r})$ of a bound system of interacting electrons in some external potential $\hat{V}_{ext}(\mathbf{r})$ determines this potential uniquely.
This theorem implies that the ground-state wave-function and thus the expectation value of any physical observable is a unique functional of the electron density $n(\mathbf{r})$. *Unique* means here: defined up to an additive constant. Originally this theorem has been demonstrated for non-degenerate states, then it has been extended to a wide class of systems including systems with degenerate states (Levy [90] and Leibs [91]), spin-polarised systems (spin density-function theory, Ref. [92, 93]). This theorem has also been extended to finite temperature by Mermin [94], thus proving that entropy, specific heat, etc. are functionals of the equilibrium density [88].

The functional that determines the ground-state

The second theorem, directly related to the first one, states that:
The total energy is a functional of the electronic density, which is minimized by the ground-state density.
The total energy for a given density $n(\mathbf{r})$ is

$$E_{tot}[n] = \langle\Psi|\hat{T}_e + \hat{V}_{ee} + \hat{V}_{\text{ext}}|\Psi\rangle = F_{HK}[n] + \int d^3\mathbf{r}\hat{V}_{\text{ext}}(\mathbf{r})n(\mathbf{r}), \tag{3.15}$$

where $\hat{T}_e$, $\hat{V}_{ee}$ and $\hat{V}_{\text{ext}}$ have been defined previously. Here, $F_{HK}[n]$ is a *universal functional* in the sense that it does not depends on the external potential felt by electrons. It is important to note that this second theorem does not tell us how to find the total energy. It is also remarkable to note that this theorem can be seen as an exact formulation of the semi-classical Thomas-Fermi theory, proposed in 1927, where all the properties of the system are determined only by the density [95, 96].

3.2.3 Kohn-Sham self-consistent equations

In 1965, Walter Kohn and his post-doc fellow, Lu Sham, published a fundamental paper [97], where they presented a method that became the most practical implementation of the DFT. Their idea was to apply the Hohenberg-Kohn theorem to a fictitious system of non-interacting particles exhibiting the same electronic density as the fully-interacting electronic system. The universal functional $F_{HK}[n]$ of the fully interacting system is proven to be

$$F_{HK}[n] = \langle\Psi|\hat{T}_e + \hat{V}_{ee}|\Psi\rangle = T_e^{KS}[n] + E_{\text{Hartree}}[n]|\Psi\rangle + E_{\text{xc}}[n], \tag{3.16}$$

where $T_e^{KS}[n]$ is the kinetic energy of the non-interacting, or so-called Kohn-Sham, electronic system, $E_{\text{Hartree}}[n]$ is the Hartree energy, and E_{xc} is the so-called exchange-correlation (xc) energy, defined by this equation. More importantly, the fictitious system is described by the Hamiltonian of an

independent-particle system of the form of

$$H_{e,i}(\mathbf{r_i})\phi_i(\mathbf{r_i}) = E_i\phi_i(\mathbf{r_i}), \qquad H_{e,i}(\mathbf{r_i}) = -\frac{\nabla_i^2}{2} + \hat{V}_{\text{eff}}(\mathbf{r_i}), \tag{3.17}$$

where i refer to the i-th electron, $\phi_i(\mathbf{r_i})$ being the single-particle wave-function of this latter. The effective potential is given by

$$\hat{V}_{\text{eff}}(\mathbf{r}) = \hat{V}_{\text{ext}}(\mathbf{r}) + \int d^3\mathbf{r}' \frac{n(\mathbf{r}')}{|\mathbf{r}-\mathbf{r}'|} + \hat{V}_{\text{xc}}(\mathbf{r}), \qquad \hat{V}_{\text{xc}}(\mathbf{r}) = \frac{\delta E_{\text{xc}}[n(\mathbf{r})]}{\delta n(\mathbf{r})}\Big|_{n=n_0}. \tag{3.18}$$

Here, $\hat{V}_{\text{xc}}(\mathbf{r})$ is the exchange-correlation potential. This potential enters in the self-consistent Kohn-Sham equations [97], formed by Eq. (3.18) and Eq. (3.17), which are inspired by the Hartree self-consistent equations. This exchange-correlation potential contains everything we do not know about the system and contains all the many-body effects, *e.g.*, the difference of kinetic energy between the auxiliary and the real systems, or the Pauli's exclusion principle. Together with the Hohenberg-Kohn theorems, this theorem forms the basement of the DFT in practice. Knowing the exact effective potential, the ground-state is found by solving self-consistently the Kohn-Sham equations, starting from a test density and by minimizing the total energy.
This theory is formally exact but the exchange-correlation energy is not known. Nevertheless, this object can be approximated and a lot of approximations have been so far proposed and tested on various kinds of systems. The major advantage of the Kohn-Sham approach is that the exchange-correlation energy can be approximated more easily than the kinetic energy for instance. In particular, the exchange-correlation energy is well approximated by local or semi-local functional of the density. In next section, I present one of the most common approximations for the exchange-correlation energy in condensed matter, which is the Local-Density Approximation (LDA), proposed by Kohn and Sham themselves in Ref. [97].

3.2.4 The local-density approximation (LDA)

Exchange-correlation energy E_{xc}

The exchange-correlation energy has the general form

$$E_{\text{xc}}[n] = \int d^3\mathbf{r} n(\mathbf{r}) e_{\text{xc}}[n](\mathbf{r}), \tag{3.19}$$

where $e_{\text{xc}}[n](\mathbf{r})$ is the energy per electron at the point $\mathbf{r}$ and depending upon the density at all point. The idea behind the local-density approximation is to replace the functional of the density $e_{\text{xc}}[n](\mathbf{r})$ by $e_{\text{xc}}^{\text{HEG}}(n(\mathbf{r}))$, which is exchange-correlation energy per electron of the homogeneous electron gas (HEG). Thereby, in the LDA, the exchange-correlation energy is given by

$$E_{\text{xc}}^{\text{LDA}}[n] = \int d^3\mathbf{r} n(\mathbf{r}) e_{\text{xc}}^{\text{HEG}}(n(\mathbf{r})). \tag{3.20}$$

Exchange-correlation energy $\hat{V}_{\mathbf{xc}}$

The effective potential that enters in the self-consistent Kohn-Sham equations (Eqs. (3.18) and (3.17)) requires the knowledge of the exchange-correlation potential, not of the exchange-correlation energy. The functional derivative of the exchange-correlation energy Eq. (3.19) gives the exchange-correlation potential of the form

$$\hat{V}_{\text{xc}}(\mathbf{r}) = e_{\text{xc}}[n](\mathbf{r}) + n(\mathbf{r})\frac{\delta e_{\text{xc}}[n](\mathbf{r})}{\delta n(\mathbf{r})}\Big|_{n=n_0}, \tag{3.21}$$

where $e_{\text{xc}}[n](\mathbf{r})$ is defined in (3.19).
Therefore the exchange-potential is easily obtained in the local-density approximation by replacing $e_{\text{xc}}[n](\mathbf{r})$ by $e_{\text{xc}}^{\text{HEG}}(n(\mathbf{r}))$. In that case, the functional derivative is replaced by an ordinary derivative, as $e_{\text{xc}}^{\text{HEG}}$ is a function of the density, and no more a functional.
The exchange-correlation potential in LDA reads as

$$\hat{V}_{\text{xc}}(\mathbf{r}) = \Big[e_{\text{xc}}^{\text{HEG}} + n\frac{\partial e_{\text{xc}}^{\text{HEG}}}{\partial n}\Big](\mathbf{r}). \tag{3.22}$$

The LDA exchange term is known and reads as $\hat{V}_x(\mathbf{r}) = \frac{4}{3}e_x^{\text{HEG}}(n(\mathbf{r}))$. Unfortunately, even in the simple case of the homogeneous electron gas, the correlation part is unknown and must to be fitted on quantum Monte Carlo simulations [98–100].
This approximation became, along the years, the most used functional for DFT calculations on extended systems. In particular, the LDA has been successfully applied to a wide range of systems, far beyond its expected range of validity. As an example, the bound lengths obtained within the LDA agree with experiment within a few percent.
Other functionals have also been proposed to overcome some known failures of the LDA. Among them, one finds the generalized-gradient approximations (GGA) [101–103], the optimized effective potentials (OEP) [104] which can include the exact-exchange (EXX) [105] or the hybrid functionals [106]. Nevertheless, as I will discuss later, the quality of approximation of the exchange-correlation potential is not the most important criteria for obtaining quantitative results for optical properties of extended systems. As, the LDA is more than enough for the purpose of this thesis, all the numerical DFT calculations presented in this thesis have been performed with the Teter-Pade parametrization [107] of the LDA functional.

3.3 Time-Dependent Density-Functional Theory (TDDFT)

As discussed above, the calculation of the optical properties of a system requires the knowledge of the excited states; which could not be obtained by the DFT [84]. For accessing these states, I used the Time-Dependent Density-Functional Theory, together with the time-dependent perturbation theory for describing the optical properties of the surfaces I am interested in. The framework of TDDFT has been rigorously introduced by Runge and Gross [108], where they replaced the time-independent external potential of DFT by a time-dependent one. A review of TDDFT and of the recent developments can be found in Refs. [84, 109]. In this section, I first present the Runge-Gross theorems which are the basis of TDDFT, then the time-dependent Kohn-Sham equations that allow practical

implementations of TDDFT.

3.3.1 Runge-Gross theorems

As previously mentioned, we assume the Born-Oppenheimer approximation and we reduce the many-body problem to a many-electron problem with an external potential. To this external static potential, we add a time dependent contribution, describing the external perturbation, which drives the system out of its ground state.
The evolution of a many-electron system is described by a time-dependent Schrödinger equation

$$i\frac{\partial}{\partial t}\Psi(\{\mathbf{r}\},t) = \hat{H}(\{\mathbf{r}\},t)\Psi(\{\mathbf{r}\},t), \qquad \hat{H}(\{\mathbf{r}\},t) = \sum_i \left(-\frac{\nabla^2}{2} + \hat{V}_{\text{ext}}(\mathbf{r_i},t)\right) + \frac{1}{2}\sum_{i\neq j}\frac{1}{|\mathbf{r_i}-\mathbf{r_j}|}, \quad (3.23)$$

where $\hat{V}_{\text{ext}}(\mathbf{r_i},t)$ is the time-dependent external potential.[3] The electronic density of such many-electron system is denoted $n(\mathbf{r},t)$. We consider that the external perturbation is switched on adiabatically at $t = t_0$.
For such a system, Runge and Gross proved in their paper that [108]
The time-dependent density $n(\mathbf{r},t)$ of a system of interacting electrons evolving from an initial state $|\Psi_0\rangle$ in some time-dependent external potential $\hat{V}_{ext}(\mathbf{r},t)$ which is Taylor expandable around $t = t_0$, determines this potential uniquely.
The density can be obtained by solving the Schrödinger equation and therefore, there is a one to one correspondence between the time-dependent electronic density and time-dependent external potential. This theorem plays the same role as the Hohenberg-Kohn theorem of DFT. Similarly to the Hohenberg-Kohn theorem, *unique* means here: defined up to a time-dependent additive constant.
The first Runge-Gross theorem states that any physical observable[4] of the many-electron system is a functional of the time-dependent density. The total energy is no more conserved and the search of minima of the total energy has to be replaced by the search of extrema of a quantum mechanical action, defined by analogy to the action in classical mechanics: [108]
For a given initial state $|\Psi_0\rangle$, the action $A[n]$ becomes stationary at the density $n_0(\mathbf{r},t)$ corresponding to the external potential $\hat{V}_{ext}(\mathbf{r},t)$.
Nevertheless, the action defined here is an unknown functional, and is the analogue of the total energy in static density-functional theory.

3.3.2 Time-dependent Kohn-Sham equations

In their paper, Runge and Gross suggested the use of an auxiliary system of independent particles to simplify the problem of finding the action, leading to a time-dependent version the Kohn-Sham equations (see theorem 4 of Ref. [108])
The exact time-dependent density of the system can be computed from the single-particle orbitals $\phi_j(\mathbf{r},t)$ ful-

[3] In this expression, the external potential is local, but the same equation and formalism holds for a non-local potential, as for instance within the pseudo-potential approximation. The effect of non-local potentials will be discussed in Chap. 6.
[4] depending on time, but neither on its derivatives or integrals.

filling the time-dependent Schrödinger equation

$$\Big(i\frac{\partial}{\partial t}+\frac{1}{2}\nabla^2\Big)\phi_j(\mathbf{r},t)=\hat{V}_{\mathit{eff}}[n,\Psi_0](\mathbf{r},t)\phi_j(\mathbf{r},t), \tag{3.24}$$

with an effective one-particle potential [5]

$$\hat{V}_{\text{eff}}[n,\Psi_0](\mathbf{r},t)=\hat{V}_{\text{ext}}(\mathbf{r},t)+\int d^3\mathbf{r}'\frac{n(\mathbf{r}',t)}{|\mathbf{r}-\mathbf{r}'|}+\frac{\delta A_{\text{xc}}[n,\Psi_0]}{\delta n(\mathbf{r},t)}. \tag{3.25}$$

These two equations define a self-consistent scheme, with a time-dependent effective potential, which is a generalization of the time-independent effective potential of Kohn-Sham equations (see Eq. 3.18). Here $A_{\text{xc}}[n,\Psi_0]$ is the exchange-correlation part of the action [108]. By analogy with the static case, a time-dependent exchange-correlation potential $\hat{V}_{\text{xc}}$ can be defined, as $\hat{V}_{\text{xc}}[n,\Psi_0]=\frac{\delta A_{\text{xc}}[n,\Psi_0]}{\delta n(\mathbf{r},t)}\big|_{n=n_0}$.

3.4 Perturbation theory and TDDFT

From the TDDFT, we know that the (induced) density of the fully interacting system is equal to the (induced) density of the non-interacting Kohn-Sham system. By applying the formalism of perturbation theory to the Kohn-Sham system, it is possible to obtain the induced quantities and, going further, to link the response functions of the fully-interacting system to the non-interacting response functions. In this case, the ground-state is known, from the DFT, and so the response functions of the auxiliary system are also known. One can then obtain the response functions of the real system, which then can be used to compute the measurable quantities.

Nevertheless there are few limitations to this approach. First, only the induced density and the longitudinal part of the current can be obtained.[6] Second, in TDDFT, the perturbation is described by a scalar potential. This implies that only the response to a longitudinal perturbation can be computed. Therefore, it is possible to access directly in TDDFT to only two response functions, which are the density-density response function $\chi_{\rho\rho}$ and density-density-density response function $\chi_{\rho\rho\rho}$.[7] The response functions which describe the optical properties of a system should give the induced current (which gives the polarization) from a transverse perturbation. This apparent contradiction vanishes if the perturbation is of long-wavelength, as already explained in Sec. 1.4. As within the long-wavelength approximation, the longitudinal response of the system is sufficient for describing its optical properties, the two density response functions are enough for describing the linear optics and second-harmonic generation. In this section, I show how it is possible to compute these two response functions starting from the response functions of the Kohn-Sham system.

For that, we follow the approach of Ref. [54], extended to second-order in Ref. [111], and we start by

[5] The assumption that it is possible to define such an effective potential is known as the "non-interacting v-representability" [84] and is not obvious. At least, we know that such a potential is unique, from the Runge-Gross theorem. In this thesis, we only apply TDDFT from Kohn-Sham wave-functions, obtained from DFT using a smooth approximate energy functional. This ensures that an effective potential can always be found [84].

[6] It is possible to access to the entire current, using the Time-Dependent Current Density-Functional Theory (TDCDFT) [109, 110] instead of the TDDFT, but this will not be discussed in this thesis.

[7] From these two response functions, the others or at least their longitudinal parts can be obtained, from the gauge invariance and the conservation of charges, see Ref. [44].

considering the effective potential of Eq. 3.25,

$$\hat{V}_{\text{eff}}[n](\mathbf{r},t) = \hat{V}_{\text{ext}}(\mathbf{r},t) + \int d^3\mathbf{r}' \frac{n(\mathbf{r}',t)}{|\mathbf{r}-\mathbf{r}'|} + \hat{V}_{\text{xc}}[n(\mathbf{r},t)](\mathbf{r},t). \tag{3.26}$$

The density of the system reads as

$$n(\mathbf{r},t) = n^{(0)}(\mathbf{r},t) + n^{(1)}_{\text{ind}}(\mathbf{r},t) + n^{(2)}_{\text{ind}}(\mathbf{r},t), \tag{3.27}$$

where $n^{(0)}(\mathbf{r},t)$ is the unperturbed density. Inserting this expression in Eq. (3.26), yield

$$\hat{V}_{\text{eff}}[n](\mathbf{r},t) = \hat{V}^{(0)}_{\text{eff}}(\mathbf{r},t) + \hat{V}^{(1)}_{\text{eff}}(\mathbf{r},t) + \hat{V}^{(2)}_{\text{eff}}(\mathbf{r},t), \tag{3.28}$$

where

$$\begin{aligned}
\hat{V}^{(0)}_{\text{eff}}(\mathbf{r},t) &= \hat{V}^{(0)}_{\text{xc}}(\mathbf{r},t) + \int d^3\mathbf{r}' \frac{n^{(0)}(\mathbf{r}',t)}{|\mathbf{r}-\mathbf{r}'|}, \\
\hat{V}^{(1)}_{\text{eff}}(\mathbf{r},t) &= \hat{V}^{(1)}_{\text{ext}}(\mathbf{r},t) + \hat{V}^{(1)}_{\text{xc}}(\mathbf{r},t) + \int d^3\mathbf{r}' \frac{n^{(1)}_{\text{ind}}(\mathbf{r}',t)}{|\mathbf{r}-\mathbf{r}'|}, \\
\hat{V}^{(2)}_{\text{eff}}(\mathbf{r},t) &= \hat{V}^{(2)}_{\text{ext}}(\mathbf{r},t) + \hat{V}^{(2)}_{\text{xc}}(\mathbf{r},t) + \int d^3\mathbf{r}' \frac{n^{(2)}_{\text{ind}}(\mathbf{r}',t)}{|\mathbf{r}-\mathbf{r}'|}.
\end{aligned}$$

Here the $\hat{V}^{(i)}_{\text{xc}}(\mathbf{r},t)$ are obtained by expending $\hat{V}_{\text{xc}}[n]$ around the ground-state density

$$\begin{aligned}
\hat{V}_{\text{xc}}[n](\mathbf{r},t) = \hat{V}_{\text{xc}}[n^{(0)}](\mathbf{r},t) &+ \int dt' \int d^3\mathbf{r}' f_{\text{xc}}(\mathbf{r},t,\mathbf{r}',t')\Big(n^{(1)}_{\text{ind}}(\mathbf{r}',t') + n^{(2)}_{\text{ind}}(\mathbf{r}',t')\Big) \\
&+ \int dt'dt'' \int d^3\mathbf{r}' d^3\mathbf{r}'' g_{\text{xc}}(\mathbf{r},t,\mathbf{r}',t',\mathbf{r}'',t'') n^{(1)}_{\text{ind}}(\mathbf{r}',t') n^{(1)}_{\text{ind}}(\mathbf{r}'',t''),
\end{aligned} \tag{3.30}$$

with [8]

$$f_{\text{xc}}(\mathbf{r},t,\mathbf{r}',t') = \frac{\delta \hat{V}_{\text{xc}}[n](\mathbf{r},t)}{\delta n(\mathbf{r}',t')}\Big|_{n=n_0} \tag{3.31a}$$

$$g_{\text{xc}}(\mathbf{r},t,\mathbf{r}',t',\mathbf{r}'',t'') = \frac{\delta f_{\text{xc}}[n](\mathbf{r},t,\mathbf{r}',t')}{\delta n(\mathbf{r}'',t'')}\Big|_{n=n_0} \tag{3.31b}$$

Density-density response function

Let us start with the first-order induced density. This induced density $n^{(1)}_{\text{ind}}$ is related to the first-order part of the external potential $\hat{V}^{(1)}_{\text{ext}}$ by the fully-interacting density-density response function

$$n^{(1)}_{\text{ind}}(\mathbf{r},t) = \int d^3\mathbf{r}' \int dt' \chi^{(1)}_{\rho\rho}(\mathbf{r},t,\mathbf{r}',t') \hat{V}^{(1)}_{\text{ext}}(\mathbf{r},t'). \tag{3.32}$$

[8] Here f_{xc} is causal [111, 112]. However, being a second derivative of the exchange-correlation action, it must respect Schwartz's theorem and must be symmetric on time. This is called the symmetric-causality paradox. This apparent contradiction can be solved using a Keldysh contour [113].

By analogy, the induced density of the non-interacting system is related to the first-order part of the *effective* potential $\hat{V}_{\text{eff}}^{(1)}$ by

$$n_{\text{ind}}^{(1)}(\mathbf{r},t) = \int d^3\mathbf{r}' \int dt' \chi_0^{(1)}(\mathbf{r},t,\mathbf{r}',t')\hat{V}_{\text{eff}}^{(1)}(\mathbf{r},t'). \tag{3.33}$$

To avoid unnecessary complicated equations, we introduce the four-vector notation

$$\mathbf{1} \equiv (\mathbf{r_1}, t_1), \qquad \int d\mathbf{1} \equiv \int d^3\mathbf{r_1} \int dt_1.$$

Inserting the expression of the effective potential into Eq. (3.33) gives

$$n_{\text{ind}}^{(1)}(\mathbf{1}) = \int d\mathbf{2}\chi_0^{(1)}(\mathbf{1},\mathbf{2})\hat{V}_{\text{ext}}^{(1)}(\mathbf{2}) + \int d\mathbf{2}\int d\mathbf{3}\chi_0^{(1)}(\mathbf{1},\mathbf{2})\Big(v(\mathbf{2}-\mathbf{3}) + f_{\text{xc}}(\mathbf{2},\mathbf{3})\Big)n_{\text{ind}}^{(1)}(\mathbf{3}), \tag{3.34}$$

with $v(\mathbf{2}-\mathbf{3}) = \frac{\delta(t_2-t_3)}{|\mathbf{r_2}-\mathbf{r_3}|}$.
In this expression, we have to replace $n_{\text{ind}}^{(1)}(\mathbf{3})$ by its expression given by Eq. (3.32). This leads to a second expression for $n_{\text{ind}}^{(1)}(\mathbf{1})$ (Eq. (3.32) being the first) which must be identical for all $\mathbf{r}$. This means that the argument of $\hat{V}_{\text{ext}}^{(1)}$ under the integral must be the same [54]

$$\chi_{\rho\rho}^{(1)}(\mathbf{1},\mathbf{2}) = \chi_0^{(1)}(\mathbf{1},\mathbf{2}) + \int d\mathbf{3}\int d\mathbf{4}\chi_0^{(1)}(\mathbf{1},\mathbf{3})\Big(v(\mathbf{3}-\mathbf{4}) + f_{\text{xc}}(\mathbf{3},\mathbf{4})\Big)\chi_{\rho\rho}^{(1)}(\mathbf{4},\mathbf{2}). \tag{3.35}$$

This equation links the response function of the fully-interacting system with the response of the independent-particle system. This equation is often referred in the literature as a Dyson equation. The response function $\chi_{\rho\rho}^{(1)}$ serves for computing all the measurable quantities at first-order, *e.g.*, the macroscopic dielectric function.

Density-density-density response function

The case of the second-order response function is more intricate. The second-order induced density is given by

$$\begin{aligned} n_{\text{ind}}^{(2)}(\mathbf{1}) &= \int d\mathbf{2}\int d\mathbf{3}\chi_{\rho\rho\rho}^{(2)}(\mathbf{1},\mathbf{2},\mathbf{3})\hat{V}_{\text{ext}}^{(1)}(\mathbf{2})\hat{V}_{\text{ext}}^{(1)}(\mathbf{3},) \\ &= \int d\mathbf{2}\int d\mathbf{3}\chi_0^{(2)}(\mathbf{1},\mathbf{2},\mathbf{3})\hat{V}_{\text{eff}}^{(1)}(\mathbf{2})\hat{V}_{\text{eff}}^{(1)}(\mathbf{3},) + \int d\mathbf{2}\chi_0^{(1)}(\mathbf{1},\mathbf{2})\hat{V}_{\text{eff}}^{(2)}(\mathbf{2}). \end{aligned} \tag{3.36}$$

where $\chi_{\rho\rho\rho}^{(2)}$ is the density-density-density response function and $\chi_0^{(2)}$ is the independent-particle second-order susceptibility. We insert the expression of Eqs. (3.32) and (3.36) into this equation. The

argument of $\hat{V}_{\text{ext}}^{(1)}\hat{V}_{\text{ext}}^{(1)}$ leads to the second-order Dyson equation [41,45]

$$\begin{aligned}\chi^{(2)}_{\rho\rho\rho}(\mathbf{1},\mathbf{2},\mathbf{3}) = \int d\mathbf{4}d\mathbf{5}\chi_0^{(2)}(\mathbf{1},\mathbf{4},\mathbf{5})\Big[\delta(\mathbf{4}-\mathbf{2}) + \int d\mathbf{6} f_{uxc}(\mathbf{4},\mathbf{6})\chi^{(1)}_{\rho\rho}(\mathbf{6},\mathbf{2})\Big] \\ \times\Big[\delta(\mathbf{5}-\mathbf{3}) + \int d\mathbf{7} f_{uxc}(\mathbf{5},\mathbf{7})\chi^{(1)}_{\rho\rho}(\mathbf{7},\mathbf{3})\Big] \\ + \int d\mathbf{4}d\mathbf{5}d\mathbf{6}\chi_0^{(1)}(\mathbf{1},\mathbf{4}) g_{\text{xc}}(\mathbf{4},\mathbf{5},\mathbf{6})\chi^{(1)}_{\rho\rho}(\mathbf{5},\mathbf{2})\chi^{(1)}_{\rho\rho}(\mathbf{6},\mathbf{3}) \\ + \int d\mathbf{4}d\mathbf{5}\chi_0^{(1)}(\mathbf{1},\mathbf{4}) f_{uxc}(\mathbf{4},\mathbf{5})\chi^{(2)}_{\rho\rho\rho}(\mathbf{5},\mathbf{2},\mathbf{3}).\end{aligned} \tag{3.37}$$

Here, we introduced the notation $f_{uxc}(\mathbf{1},\mathbf{2}) = v(\mathbf{1}-\mathbf{2}) + f_{\text{xc}}(\mathbf{1},\mathbf{2})$ for convenience. From $\chi^{(2)}_{\rho\rho\rho}$, we can obtain the macroscopic second-order susceptibility, as explained in Sec. 1.3, using the relation between the quasi-polarisability and the density-density-density response function, which reads in the reciprocal space as

$$\mathbf{q}.\left[\overset{\leftrightarrow}{\tilde{\alpha}}^{(2)}(\mathbf{q},\mathbf{q_1},\mathbf{q_2};\omega,\omega)\right]_{\mathbf{000}} : \mathbf{q_1}\mathbf{q_2} = \frac{-i}{2}\chi^{(2)}_{\rho\rho\rho}(\mathbf{q},\mathbf{q_1},\mathbf{q_2};\omega,\omega) \tag{3.38}$$

Notice that the knowledge of the first-order non-interacting and fully-interacting response functions $\chi_0^{(1)}$ and $\chi^{(1)}_{\rho\rho}$ is mandatory.

Exchange-correlation kernels

In order to solve the Dyson equations Eqs. (3.35) and (3.37), some approximations are needed. Indeed, the two exchange-correlation kernels f_{xc} and g_{xc} are unknown. The simplest approximation that one can imagine consists in setting to zero f_{xc} and g_{xc} and neglecting the effect of v. This removes all the interactions between the electrons, giving the name of independent-particle approximation (IPA) to this approximation.
By neglecting the exchange-correlation kernels, we obtain the so-called random-phase approximation (RPA) [41,84]

$$f_{\text{xc}}^{\text{RPA}} = g_{\text{xc}}^{\text{RPA}} = 0.$$

In this case, all the exchange and correlation effects are considered to carry a random phase, which cancel each other and only the Coulomb interaction remains in the Dyson equation [88]. This approximation includes the effect of the local field (see Chap. 1). The RPA leads to quite accurate results for numerous materials and will be used in this thesis to improve the theoretical description of generation of second-harmonic from surfaces.
As mentioned previously, the most used approximation for DFT is the LDA. One can thus insert the expression of $\hat{V}_{\text{xc}}^{\text{LDA}}$ into the definition of f_{xc}. One can then derive the local and adiabatic TDLDA exchange-correlation kernel (see Ref. [84] and references therein)

$$f_{\text{xc}}^{\text{TDLDA}}(\mathbf{r},t,\mathbf{r}',t') = \delta(\mathbf{r}-\mathbf{r}')\delta(t-t')\frac{\partial^2 e_{\text{xc}}^{\text{HEG}}(\mathbf{r})}{\partial n^2(\mathbf{r},t)}\Big|_{n=n_0}, \qquad g_{\text{xc}}^{\text{TDLDA}} = 0. \tag{3.39}$$

Other kernels can be defined from DFT kernels. A review of these kernels can be found in Refs. [84, 112] and references therein.
As a general result, it is found that the quality of the approximation of the exchange-correlation potential is really important for a correct description of optical properties of finite systems [112]. In general, the RPA and the TDLDA give reliable results for finite systems [84].
On the contrary, the most critical approximation in order to obtain reliable results for the optical properties of extended systems is the approximation of f_{xc}. TDLDA for instance is known to fail in the calculation of the optical properties of solids. This is partially explained by the fact that the TDDLA does not reproduce the correct asymptotic behaviour expected for the exchange-correlation kernel [84]. To overcome this, another approximation can be introduced, called the α-kernel. This kernel allows us accounting for the long-range contribution (LRC) of the kernel. In reciprocal space, this static LRC kernel reads as

$$f_{\text{xc}}^{\text{LRC}}(\mathbf{q}) = -\frac{\alpha}{q^2}, \qquad g_{\text{xc}}^{\text{LRC}} = 0,$$

where α is a material-dependent parameter [114].

3.5 TDDFT in practice

The DFT and TDDFT equations can be treated numerically in various ways. In this thesis, in order to treat extended systems, the numerical calculations have been performed using a plane-wave basis-set. The ground-state is determined using the ABINIT code [115] which is based on a plane-wave basis-set and uses norm-conserving pseudo-potentials. As already mentioned, I assume the local density approximation for the numerical calculations of the ground-state properties of the surfaces investigated during this thesis. The DP code [116] and 2light code [117] were used for obtaining respectively the linear optical properties and the second-harmonic generation spectra. In the following, a short introduction to some numerical details is given.

3.5.1 Plane-waves and surfaces

Thanks to Bloch's theorem, the plane-wave basis-set is perfectly suitable for 3-dimensions periodic systems. Any Bloch state [118], $|n, \mathbf{k}\rangle$, labelled by the band index n and the crystal momentum $\mathbf{k}$, reads as

$$\phi_{n\mathbf{k}}(\mathbf{r}) = \langle \hat{\mathbf{r}} | n, \mathbf{k} \rangle = u_{n\mathbf{k}}(\mathbf{r}) e^{i\mathbf{k}\mathbf{r}} = \frac{1}{\sqrt{N_{\mathbf{k}}\Omega_c}} \sum_{\mathbf{G}} u_{n\mathbf{k}}(\mathbf{G}) e^{i(\mathbf{k}+\mathbf{G})\cdot\mathbf{r}}, \tag{3.40}$$

where

$$u_{n\mathbf{k}}(\mathbf{G}) = \int_{\Omega_c} d^3\mathbf{r} e^{-i\mathbf{G}\mathbf{r}} u_{n\mathbf{k}}(\mathbf{r}), \tag{3.41}$$

and $u_{n\mathbf{k}}(\mathbf{r})$ are cell periodic. Ω_c is the volume of the unit cell and $N_{\mathbf{k}}$ is the number of $\mathbf{k}$-points considered, giving the number of repetitions of the unit-cell and thus $V = N_{\mathbf{k}}\Omega_c$ is the volume of the crystal considered. The $\mathbf{G}$-vectors are the discrete reciprocal lattice vectors of the crystal.
The treatment in a plane-wave basis is eased by the Fast Fourier Transform, which provides a very numerically efficient way to switch between real and Fourier spaces.
The number of plane-waves considered, meaning the size of the basis used, requires some cares. This

number has to be converged for obtaining the ground-state total energy but also for the response functions or any quantity of interest. In the case of the response functions, less plane-waves are in general needed than for the total energy, so one can optimize the calculation of the response functions by reducing the number of plane-waves with respect to the ground-state calculation.
The number of plane-waves is usually not given and instead one refers to a cutoff energy E_{cut} that limits the maximal number of plane-waves such as

$$\frac{(\mathbf{k}+\mathbf{G})^2}{2} < E_{\text{cut}}. \tag{3.42}$$

The main goal of this thesis being the investigation of optical properties of surfaces, the choice of plane-waves as a basis-set for treating surfaces is not obvious. Indeed a surface is periodic in 2 dimensions (the plane of the surface) and is aperiodic in the other one. The surfaces and other non-periodic systems are in fact routinely represented by means of the so-called super-cells [119]. These super-cells are cells made by the addition of atomic layers, representing the matter, with some amount of vacuum. The number of atomic layers gives the size of the thin film, or *slab*, described. If one wants to describe a single surface of a semi-infinite medium instead of a thin film, this number of layers has to be converged with respect to some surface quantities, *e.g.*, the surface total energy or some surface optical properties.
The size of the vacuum region is also quite important to converge and must be chosen wisely. The vacuum region must be large enough to isolate a system from its replicas, always present due to the periodicity; but a larger vacuum region means also a bigger number of plane-waves required for describing the system.
All the problems related to the description of surfaces by the mean of super-cells are at the heart of this thesis and will be discuss further all along the chapters of Parts II and III.

k-points and G-vectors

In the Fourier space, any vector can be expressed as a sum of a $\mathbf{q}$-vector restricted to the first Brillouin zone plus a $\mathbf{G}$-vector which is a reciprocal lattice vector, whose size is fixed by the periodicity of the system. The sampling of the first Brillouin zone is an important issue for the calculation of many quantities such as the total energy. Response functions require also to be converged in number of $\mathbf{G}$-vectors. These two parameters have to be converged carefully. In this thesis, the $\mathbf{k}$-points are distributed on a regular grid that covers the entire Brillouin zone. These $\mathbf{k}$-points can be shifted or not. The use of *shifted* $\mathbf{k}$-points can in some cases speed-up the convergence. By avoiding the high-symmetry points of the BZ, less $\mathbf{k}$-points are needed. Otherwise, high-symmetry points contribute too much to the quantity of interest, when using low-density grids. When increasing the number of $\mathbf{k}$-points, the two grids should always give the same result. These shifted $\mathbf{k}$-points are sometimes called in the literature *off-symmetry* $\mathbf{k}$-points.

3.5.2 Core electrons and pseudo-potentials

Even considering that electrons are independent and non-interacting, as it is the case for the Kohn-Sham system, numerous electrons have to be treated numerically. This is limiting for the possibilities

of numerical simulations. One can try to reduce the number of electrons to be taken into account in simulations by introducing a new kind of approximation.
The core electrons, by opposition to the valence electrons are tightly bounds to the nuclei and do not affect the chemical bonding, nor the low-energy region of optical spectra. From that simple observation originates the idea that core electrons and valence electrons can be treated separately. The spirit of the pseudo-potential approximation is to treat separately some electrons of a system. Instead of considering that electrons are affected by the true potential, some electrons are assumed to feel a *pseudo* potential which includes the effects of the ions of the crystal plus the effects of the other electrons.

There are two classes of pseudo-potentials. i) The ionic pseudo-potentials where core electrons are treated together with nuclei, as a pseudo-ion. So the electronic system is only composed of valence electrons. ii) The total pseudo-potentials where all electrons minus one are including with the nuclei and only one electron is considered. The ionic pseudo-potentials are in general more transferable and this is the kind of pseudo-potential which is implemented in the ABINIT code [115]. More precisely I used during this thesis norm-conserving, Kleinman-Bylander separable form [120], pseudo-potentials.

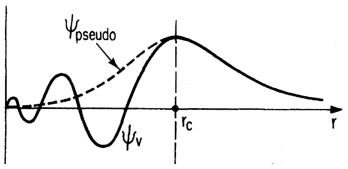

Fig. 3.1: Taken from [119].

The use of pseudo-potentials is also interesting as it allows us to reduce the number of plane-waves required for describing the system, because it replaces the real valence wave-functions, which are quickly varying close to the nuclei, by smooth pseudo wave-functions which equal the real valence wave-functions after a certain distance from the nuclei (denoted r_c in Fig. 3.1).
The price to pay when using a pseudo-potential is that the pseudo-potential contains in general a nonlocal contribution. This has some implications, *e.g.*, the electron momentum $\hat{\mathbf{p}} = -i\boldsymbol{\nabla}$ which is no more proportional to the electron velocity. Indeed, $\hat{\mathbf{v}} = i[\hat{H}, \hat{\mathbf{r}}] = \hat{\mathbf{p}} + i[\hat{V}^{nl}, \hat{\mathbf{r}}]$, where $\hat{V}^{nl}$ is the nonlocal part of the pseudo-potential.
Using the explicit separable form of Kleinman-Bylander pseudo-potential, this non-local contribution can be computed and included in the optical responses [121]. This nonlocal contribution to the surface second-harmonic spectra will be discussed widely in Chap. 6.

Summary

In this chapter, I have reviewed the density-functional theory approach for solving the many-body problem. I have first presented how from time-dependent perturbation theory, we can define the response functions, which allows us to compute the measurable quantities.
Then I have presented the density-functional theories. In both static and time-dependent cases, the electronic density of the system is the key quantity. From the density, one obtains the potential whereas from the potential, one obtains the wave-functions and thus the density.
Thanks to the TDDFT, the density response functions of the real, fully-interacting system are linked to the non-interacting density response functions of the Kohn-Sham auxiliary system. These non-interacting response functions are obtained from the ground-state; the latter being obtained by solv-

ing self-consistently the static Kohn-Sham equations of DFT.
Finally numerical details of the implementation used for solving the equations of (TD)DFT have been given.

4. Silicon and its (001) surface

Silicon is the most used semiconductor in microelectronics and merging Si-based microelectronics with photonics is required to overcome the fundamental limits reached by modern microelectronics. Lot of hybrid technologies or on-chip optical networks have been presented as possible evolutions of microelectronics. In that context, all-optical chips require nonlinear optics and in particular second-harmonic generation. Due to the inversion symmetry of the bulk silicon, only third-harmonic generation is possible in the dipole approximation, and one could not consider using bulk silicon for obtaining second-harmonic generation. By breaking this inversion symmetry, the surfaces of silicon appear as an interesting choice for obtaining SHG in nano-manufactured all-Silicon devices, where the surface-to-volume ratio increases [122].
In this chapter, I will briefly review some fundamental properties of silicon and present some applications of its surfaces in the context of second-harmonic generation. The different reconstructions of the Si(001) surface used to test the theoretical development of this thesis are then presented. Relevant experimental characteristics of bulk and surfaces are also provided here.

4.1 Silicon

Silicon is the eighth most common element in the universe by mass. The crystalline structure of silicon is diamond-like cubic structure (see Fig. 4.1). It is solid at room temperature and has a dark grey colour. From the electronic point of view, the silicon is characterized by an atomic number of 14 and an electronic shell of [Ne]$3s^2 3p^2$ leading to four covalent bonds and a sp^3 hybridation. Some of its experimental parameters are given in Tab. 4.1. Note that the spin-orbital splitting value is rather small and thus the spin effects will be neglected throughout this thesis.
For the present work, an important property of the crystalline bulk silicon is the symmetries of its structure and among all those symmetries, the inversion symmetry. As explained previously, in the dipole approximation, this symmetry prohibits the second-order processes as SHG. The major use of silicon now-a-days is obviously microelectronics, were integrated circuits are made on top of a crystalline silicon wafer. A lot of techniques have been developed for designing, producing and controlling silicon surfaces or nano-objects. From an experimental point of view, the silicon, due to its importance, has been widely investigated and numerous possible novel applications have emerged.
In the next section, I present some of the novel applications of silicon and its surfaces, showing how important Si surfaces are in those new applications.

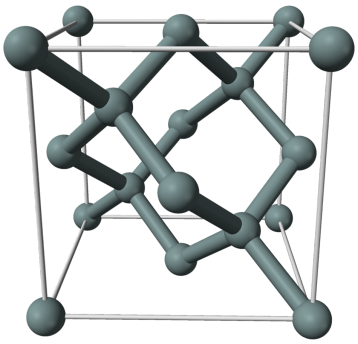

Fig. 4.1: Crystalline structure of bulk silicon. From Ref. [123].

Experimental parameters	Values (300K)	Values (0K)
Lattice parameter (Å)	5.4310[a]	5.430[g]
Indirect band-gap (eV)	1.1242[b]	1.1701[b]
Direct band-gap (eV)	3.318[c]	3.354[c]
Dielectric constant	11.7[f]	11.4[d]
Spin-orbital splitting (eV)	0.04[e], 0.044[c]	
[a]Refs. [124, 125].	[b]Ref. [126].	[c]Ref. [127].
[d]Ref. [128].	[e]Ref. [129].	[f]Ref. [130].
[g]Refs. [131, 132].		

Tab. 4.1: Some experimental constants of silicon.

4.2 The role of silicon surfaces in novel applications

Here I do not present an exhaustive list of novel applications but I show how Si surfaces have a particular importance in that novel applications.

Most of the effort devoted to novel applications using silicon is oriented toward photonics. The advantages of all-Silicon devices will not be discuss here and are out of the scope of this thesis. Nevertheless, one can keep in mind that silicon photonics appears as a natural choice for on-chip optical networks and all-optical data management, because of the high availability of silicon on earth, its low cost of fabrication and the extensive theoretical and experimental knowledge accumulated over the years.

A key point for achieving all-optical devices is the possibility of handling nonlinear second-order processes such as SHG. The second-harmonic generation in reflection from planar silicon surfaces has been widely studied from both experimental (see Ref. [32,33,133,134]) and theoretical (Ref. [135–141]) point of view. However, the new applications are more oriented toward the nano-manufacturing of the devices. New properties or the enhancement of already existing properties are often related to the enhancement of the surface-to-volume ratio in nano-objects. Therefore, the surfaces of Si appear as an crucial key for handling the silicon photonics, and in particular for the SHG on Si-based devices. Among the ways proposed in the literature for obtaining a SHG from silicon, we find nano-particles [142], micro-cavities [143], nano-pillars [122] or more recently strained silicon wave-guides [13]. In those nano-objects, the surface properties can become relatively important with respect the bulk properties, making the understanding of Si surfaces of major importance. Besides the realisation of Si-based photonic devices, Si is used in novel technologies as, for instance, the silicon nano-crystals based memory devices [144–146] or photovoltaic applications [147–150]. Note that a fine control of the characteristics of the nano-crystals is required to obtain the best performances of the nano-crystal based devices. In that context, SHG is used as a non-destructive and non-invasive probe, *e.g.*, Refs. [151, 152] where authors have applied SHG for probing the interface of Si nano-crystals embedded inside a SiO_2 matrix, which are used in the aforementioned memory devices.

4.3 The (001) surface of silicon

4.3.1 Surface notations

The different surface reconstructions are named, in Wood notations, by a letter, which can be c or p; standing respectively for *centred* or *primitive*. To that letter, one adds two numbers, *e.g.*, p(2×1), where the two numbers indicate how many times the bulk-like unit-cell is repeated along the two in-plane lattice vectors for obtaining the unit-cell associated to the reconstruction. The more atoms are involved, the bigger the reconstructed unit-cell is. In the case of the p(2×1) reconstruction, the cell is twice longer in the first in-plane direction than in the second. If no letter is present, the reader has to understand that it as a primitive cell, because the p letter is sometimes omitted. More information concerning Wood notations can be found in Ref. [153].

4.3.2 The (001) surface of silicon

In this thesis, I was interested in the some specific silicon surfaces. I have chosen to apply my theoretical developments to the (001) surfaces of Silicon for two main reasons. First, most of the electronic devices are grown on top of wafers with a cubic cleavage on the (001) plane, making this surface of main interest from the point of view of industrial applications. Among that industrial applications, one find the micro-fabrication process steps such as the doping or the ion implantation, the photo-lithographic patterning, the etching, the deposition of various materials and the laser ablation. Second, this surface exhibits simple reconstructions, making possible a study by means of *ab initio* methods. By simple reconstructions, one has to understand 1×1 or 2×1 reconstructions, keeping in mind that a 2×1 reconstruction obliges us already to double the number of atoms used for a calculation, increasing the already impressive burden associated with the *ab initio* calculation of SHG from surfaces.

The smallest reconstructions of the clean (001) surfaces are presented in Fig. 4.2. Fig. 4.2 (a) represents the ideal surface, referred also as the bulk-terminated surface. In that bulk-terminated surface, the top-most atoms are missing two neighbouring Si atoms, thus two covalent bounds, leading to what is called two "dangling" bonds per Si surface atoms. Due to the dangling bonds, this surface is not favourable in energy and, depending on the temperature and on the experimental conditions, the atoms reconstruct into different structures as the p(2×1) with asymmetric dimers (Fig. 4.2(b)), the p(2×2) with alternated dimers (Fig. 4.2(c)) or the c(4×2) structure (Fig. 4.2(d)). A careful study of the energy associated with these different reconstructions can be found in Ref. [154]. As a summary, the p(2×1) is the most favourable structure at room temperature, whereas the c(4×2) is the most stable reconstruction at low temperature [153]. The phase transition p(2×1)→ c(4×2) takes place around 200K [155]. Due to its simplicity and the fact that at room temperature, the p(2×1) surface is the most stable, I have decided to choose this surface reconstruction for representing the clean surface of Si(001). Details concerning the asymmetric dimers are given in the following section.

Finally, it is important to mention that the Si(001) surface exhibits vicinal surfaces, which have been extensively studied [156–158]. Such surfaces are Si(001) surfaces with a small miscut (of few degrees) towards the crystallographic directions [110] or [111]. Nevertheless these surfaces require a study in

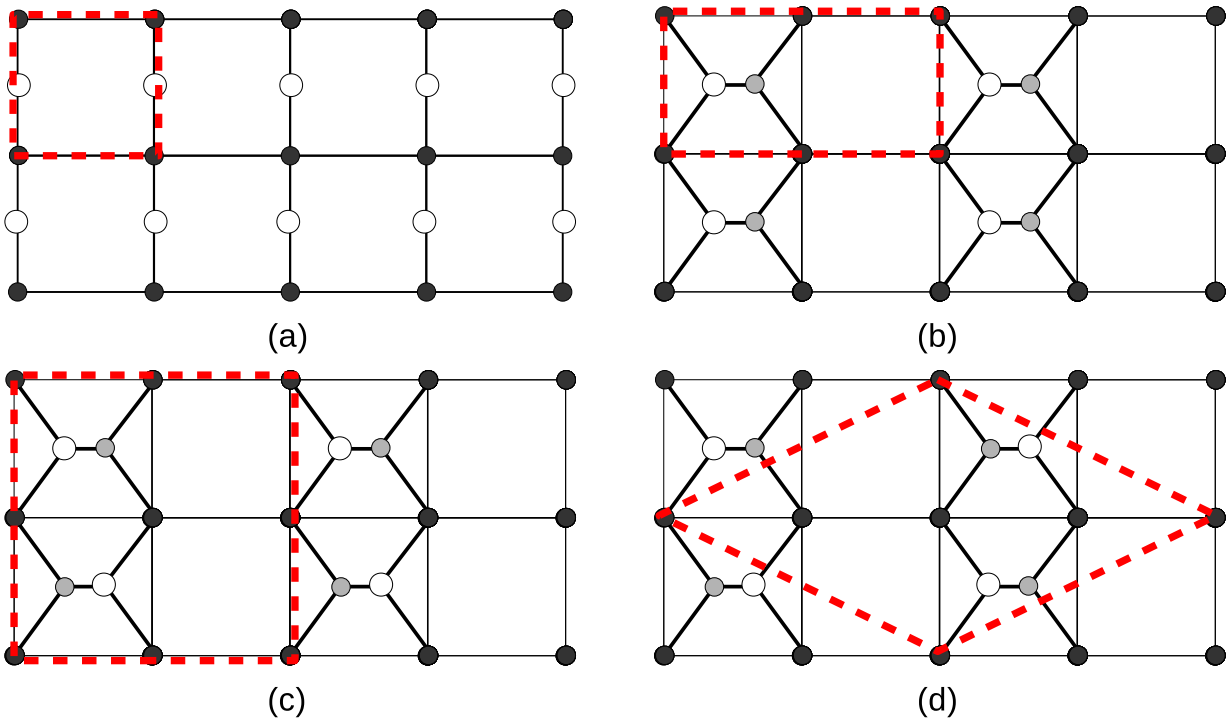

Fig. 4.2: Top view of different possible reconstructions of the Si(001) surface. (a) Ideal surface. (b) The p(2×1) reconstruction with asymmetric dimers. (c) The p(2×2) reconstruction with alternated asymmetric dimers. (d) The c(4×2) reconstruction. Details concerning these surfaces are given in the text. The top-most atoms are displayed in white. Red dashed lines correspond to the smallest cell needed for mapping the entire surface.

themselves and will not be investigated in this present thesis.
In next section, the reconstructions used latter in this thesis are presented more in details.

4.4 Geometries and reconstructions

During this thesis, I have investigated three specific reconstructions of the silicon surface, along the cleavage direction (001). Most of the effort has been devoted to the clean Si(001)2×1 surface. Two other surfaces, obtained by the adsorption of hydrogen, namely the monohydride and the dihydride surfaces, have been also investigated and are presented in that section.

4.4.1 Asymmetric dimers vs. Symmetric dimers

The 2×1 reconstruction of the clean Si(001) surface is known to be the most stable reconstruction at room temperature [153]. This reconstruction arises from the dimerization of Si top-most surface atoms, halving the number of dangling bonds (see Fig. 4.3(a) and (b)). It has been proposed two models for the dimers, the symmetric dimers model where the dimers are parallel to the surface and the asymmetric dimers model where dimers are buckled. The idea of the asymmetric dimers originates from Chadi [159], who found from tight-binding calculations that the Si(001)2×1 surface with symmetric dimers was metallic, in disagreement with experimental results published the same year,

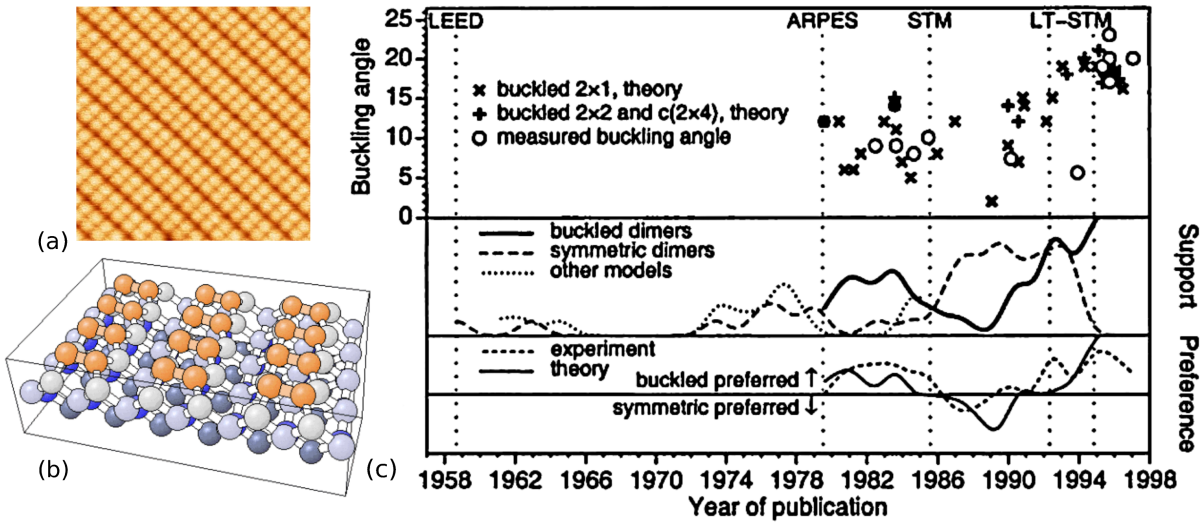

Fig. 4.3: (a) Atomic Force Microscope (AFM) image of the clean Si(001)2×1 surface, from Ref. [162]. (b) Schematic view of the Si(001)2×1 surface. Picture from NIST Surface Structure Database. (c) Evolution of opinions about the structure of clean Si(001) surface, taken from Ref. [163]. Symmetric dimers dominates between the first observation of mostly symmetric dimers at room temperature (1985) and first observation of mostly buckled dimers at low temperature (1992). In the upper panel, the value of the buckling angle obtained from theoretical and experimental studies is reported, with a clear correlation. The middle panel report the support for each model, measured by the number of published papers. The theoretical and experimental preference (lower panel) is measured by the difference between the number of papers supporting either model.

obtained by angle-resolved photo-emission spectroscopy (ARPES) [160].
From that seminal paper, lot of effort has been devoted to investigate the character of the dimers of that surface. As a summary, one can keep in mind that the asymmetric dimers are found to be more favourable in total energy by 0.1 eV per unit cell [161], and that they give the correct semiconducting character of the surface.
One can think that the metallic character obtained by tight-binding or LDA calculations can be changed by a GW correction, which opens the underestimated band-gap of LDA calculations, but it has been shown in Ref. [161] that the GW band-structure obtained assuming symmetric dimers is also metallic. As a conclusion, one can see on Fig. 4.3(c) that it is now well admitted from both theoretical and experimental communities that dimers of the Si(001)2×1 are asymmetric.

The clean Si(001) surface used in this thesis corresponds to the Si(001)2×1 surface with asymmetric dimers. Its point group is m and the corresponding space group is $p1m1$. The dimers are along the $[1\bar{1}0]$ crystallographic direction (x-axis) and the dimer rows are along the [110] direction (y-axis). Thus the surface is invariant under only one symmetry, which is $y \to -y$. The dimers are characterized by two values, which are the dimer-bond length and the dimer buckling, as reported in Fig. 4.4. Alternatively to the buckling value, the dimers can be characterized by the buckling angle. The values of the dimer bond-length and buckling angle

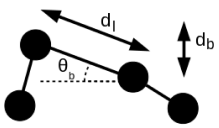

Fig. 4.4: Side view of the asymmetric dimer. d_l is the dimer length and d_b the dimer buckling. θ_b is the buckling angle.

Method	Dimer-bond length d_B (Å)	Buckling angle θ_b(°)	Ref.
LEED	2.24 ± 0.08	19 ± 2	[164]
Surface x-ray diffraction	2.37 ± 0.06	20 ± 3	[165]
X-ray diffraction	2.67 ± 0.07	20 ± 3	[166]

Tab. 4.2: Experimental values obtain from various experimental methods as Low-Energy Electron Diffraction (LEED) or (surface) X-ray diffraction. As a comparison, the bulk bond length is 2.35Å.

can be determined by a variety of methods. Results are summarized in Tab. 4.2 and the evolution in time of the measured and predicted values of the buckling angle is reported in the top panel of Fig. 4.3(c).

4.4.2 Monohydride and Dihydride surfaces

The interaction between the silicon surfaces and the hydrogen atoms is of main technological importance due to the chemical vapour deposition (CVD) growth [167] and also for the passivation of the etched silicon wafers [168]. Thus, a comprehensive understanding of the interaction of hydrogen with the silicon surfaces is essential for semiconductor growth and processing. Moreover, the hydrogen is the simplest ad-atom and it can serve as a prototype for describing the physical interaction of the Si surfaces with more complex ad-atoms.

This justifies the choice of hydrogenated surfaces for the application of theoretical developments of this thesis.

The adsorption of hydrogen on the clean Si(001)2×1 surface leads, in general [1], to two possible surfaces, depending on the amount of hydrogen used and the experimental conditions of growth.

The Si(001)2×1:H surface, also referred as the monohydride surface, has a 2×1 reconstruction, in which the Si dimers are intact and only one of the two dangling bounds of the Si dimer is H saturated. The dimers of this surface are symmetric (see Fig. 4.5 (a)), meaning that they are parallel to the surface, by opposition to the asymmetric dimers of the clean surface aforementioned. The Si-Si dimer bond-length has been found to be of 2.47 ± 0.02Å by surface x-ray diffraction [172], showing that the bond between the dimer atoms is weakened and lengthened in the monohy-

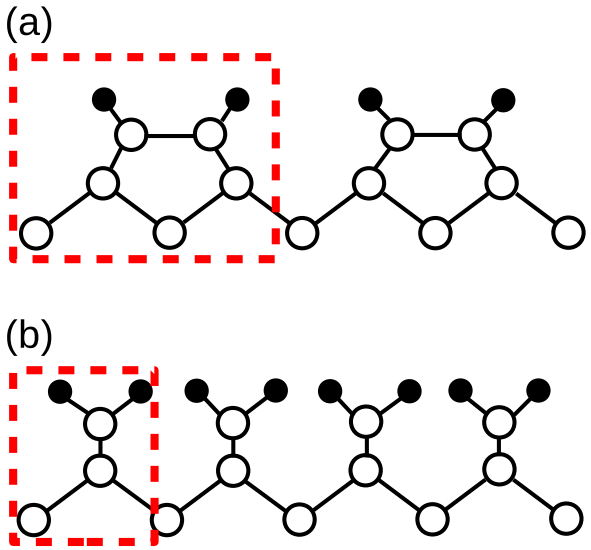

Fig. 4.5: Side view of different possible reconstructions of the hydrogenated Si(001) surface. (a) Monohydride or Si(001)2×1:H surface. (b) Dihydride or Si(001)1×1:2H surface. The H atoms are displayed in black. Red dashed lines correspond to the smallest cell needed for mapping the entire surface.

[1] A trihydride reconstruction also exists under specific conditions. [169]
Also a mixture of monohydride and dihydride can reconstruct in a 3×1 ordered reconstruction. [170, 171]

dride structure, as we compare to the clean surface using similar experimental techniques. This surface can be obtained experimentally by adsorption of hydrogen at high temperature, where the 2×1 organisation is preserved [34, 169]. This surface is also referenced as the surface with a coverage of 1 mono-layer (ML) of hydrogen.
The space group of this surface is $p2mm$. The dimers are chosen to be along the same direction as the clean surface. As the dimer are symmetric, the system is also invariant under the symmetry $x \to -x$.

The Si(001)1×1:2H surface (see Fig. 4.5(b)), also referred as the dihydride surface, is obtained by saturating all the dangling bonds of the Si(001) surface with hydrogen atoms and can be obtained experimentally if enough H (2ML) is added to the surface, so breaking dimers [34, 169]. Thus this surface preserves the bulk symmetries and the hydrogenated surface so obtained is an ideally bulk-terminated surface where hydrogen atoms saturate all the dangling bounds. The Si-H bond length is found experimentally to be 1.48Å, from the SiH_4 molecule [173]. By opposition to the two other surfaces, this surface has a 1×1 reconstruction, leading to different symmetries for the $\chi^{(2)}$ tensor; due to its space group $p4mm$.

Part II

Microscopic theory of second-harmonic generation from crystal surfaces

5. Microscopic theory of surface second-harmonic generation

Second-harmonic generation (SHG) is considered to be a versatile tool to study many kinds of surfaces [65–67], interfaces [68, 69] and nanostructures [174–176]. The theoretical description of the phenomenon is well established for bulk materials and interfaces and gives reliable results [29, 41, 177, 178], but a rigorous theoretical description of the SHG from surfaces is still missing. This can be easily understood because it is not possible to compute directly the surface second-harmonic generation by the usual *ab initio* approaches for surfaces. This is that particular problem I want to address in this chapter.

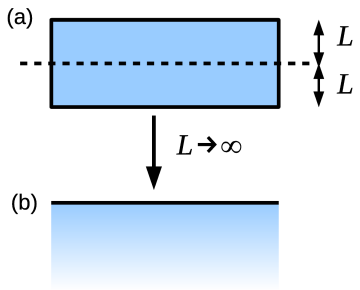

Fig. 5.1: From the slab geometry (a) to the semi-infinite medium (b).

The best model that one can imagine for representing a surface is a semi-infinite crystal that fills half of the space, say for instance z>0, with its surface parallel to the x-y plane; as sketched in Fig. 5.1(b). Unfortunately, it is difficult, if not impossible, to treat numerically a semi-infinite crystal. The standard approach, which is the one adopted in this thesis, consists in replacing the semi-infinite medium by a finite slab of matter, *i.e.*, a thin film, in order to mimic the semi-infinite crystal [119], see Fig. 5.1(a). This slab is periodic in the plane, as the surface that we want to treat. In the direction perpendicular to the plane of the surface, the slab, together with some vacuum, is repeated, in order to fill all the space. This approach is called the super-cell approach. It has been successfully applied to surfaces, for computing linear differential spectroscopies, *e.g.*, the reflectance anisotropy; leading to quantitative results [179–181].

Describing a surface by a slab of thickness $2L$ is a perfectly valid approach for representing a semi-infinite crystal, under two conditions. i) The spectra originating from one half of the slab can be obtained, independently of the other half of the slab. This means that the presence of the back surface does not affect the optical response of the front surface, and *vice versa*. ii) One is able to take the limit $L \to \infty$, as sketched in Fig. 5.1. This last point is easily done in practice, by increasing L up to the point where the surface spectroscopical quantities are converged.[1]

In the case of linear optics, the optical response of the half-slab is obtained by dividing by two the full slab response, at least within the IPA [182].

[1] Surface spectroscopical quantities means there is no contribution from the bulk part. Linear differential spectroscopies and SHG from centro-symmetric crystal surfaces are valid surface spectroscopical quantities in this context.

Problems arise when applying this technique to the calculation of the second-harmonic generation. The slab of matter being surrounded by vacuum, it exhibits two surfaces. If the slab is symmetric, as exemplified in Fig. 5.2, the full slab exhibits artificial inversion symmetry and does not yield any SHG signal.

If the slab is non-symmetric, the SHG computed is non-zero, but the spectra so obtained results from the destructive interferences between the two surface contributions.[2] It can be shown that there is no general combination of slabs and surfaces that allows us to obtain the contribution arising from a single surface, independently of the other one.
In this chapter, I present how it is possible to obtain the second-harmonic generation spectra from half of the slab, in super-cell geometry. First I present the theory behind the *extraction* procedure, which gives access to the contribution of a single surface. Then a relevant test-case is presented, showing the consistency of the method. In Sec. 5.2, the accuracy of the extraction and potential sources of errors are discussed. Finally, the spatial construction of the spectra is analysed.
In all this chapter, the second-order surface susceptibility is considered, at the level of the Independent-Particle Approximation (IPA). The local-field effects are treated later, in Chap. 7.

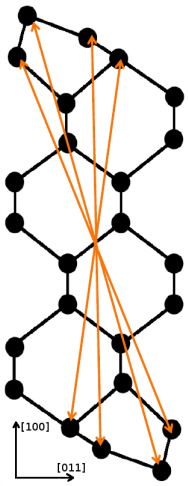

Fig. 5.2: A symmetric slab exhibits an artificial centro-symmetry

5.1 Extracting the surface second-harmonic generation spectra

In this chapter, we consider the surface of a centrosymmetric crystal, such as silicon. In this case, only the surface region contributes to the signal. The second-harmonic generation from half of the slab reduces to only the surface region. I thus refer to the extracted spectra equally as the *surface* spectra or the half-slab spectra.
The first atomistic calculations of second-harmonic generation from a surface have been performed by L. Reining *et al.* [183]. In this paper, authors assumed that the electric field of the incident light has a z dependence denoted $\mathcal{C}(z)$ and they replaced some matrix elements of the momentum, defined as $\hat{\mathbf{p}} = i[\hat{H}, \hat{\mathbf{r}}]$, by matrix elements of the modified momentum

$$\boldsymbol{\mathcal{P}} = \frac{\mathcal{C}(z)\hat{\mathbf{p}} + \hat{\mathbf{p}}\mathcal{C}(z)}{2}. \tag{5.1}$$

Then, they computed the *probability* of SHG in the velocity gauge by modifying the interaction between the electrons and the incident photons, and so introducing the modified momentum matrix elements defined by Eq. (5.1). Two matrix elements are thus modified in this approach, corresponding to the two impinging photons involved in SHG process.
Later, some authors (see Ref. [135–141]) have applied a similar technique, *i.e.*, using the same modified momentum, but for computing the IPA second-order susceptibility $\chi_0^{(2)}$ (and no more the probability of SHG). They adopted a different approach, modifying only one matrix element, arguing that

[2] This is a major difference with linear optical properties where the contributions originating from the two surfaces interfere positively.

the field corresponding to emitted photon must be modified (or equivalently to the dielectric polarization) and not the field corresponding to the two impinging photons. However the literature does not provide us with any reason for choosing one of those two methods nor a proof of one of those methods.

In this section, I will prove the second method to be the correct way for extracting the half-slab spectra; without using any phenomenological argument such as the emitted or impinging photons.

The microscopic second-order susceptibility is given, in the velocity gauge and within the independent-particle approximation by [184]

$$\chi^{(2)}_{0,\alpha\beta\gamma}(\omega,\omega) = \frac{i}{2V\omega^3}\sum_{n,n',n''}\sum_{\mathbf{k}}^{BZ}\frac{\langle n\mathbf{k}|p^\alpha|n'\mathbf{k}\rangle\Big(\langle n'\mathbf{k}|p^\beta|n''\mathbf{k}\rangle\langle n''\mathbf{k}|p^\gamma|n\mathbf{k}\rangle + \langle n'\mathbf{k}|p^\gamma|n''\mathbf{k}\rangle\langle n''\mathbf{k}|p^\beta|n\mathbf{k}\rangle\Big)}{(E_{n,\mathbf{k}} - E_{n',\mathbf{k}} + 2\omega + 2i\eta)} \times\left[\frac{f_{nn''}}{(E_{n,\mathbf{k}} - E_{n'',\mathbf{k}} + \omega + i\eta)} + \frac{f_{n'n''}}{(E_{n'',\mathbf{k}} - E_{n',\mathbf{k}} + \omega + i\eta)}\right], \tag{5.2}$$

where V is the volume of the crystal, $f_{nn''} = f_n - f_{n''}$ with f_n[3] and $E_{n,\mathbf{k}}$ being respectively the Fermi occupation number for the Bloch state n at the point $\mathbf{k}$ in the BZ, and its energy. The frequency of the impinging light is ω, and η is a small imaginary number that turns on adiabatically the electric field. Here, α, β and γ are Cartesian coordinates.

Thereby, according to all the previous references except Ref. [183], the *surface* second-order susceptibility should be computed using the formula

$$\chi^{(2)Cz1}_{0,\alpha\beta\gamma}(\omega,\omega) = \frac{i}{2V\omega^3}\sum_{n,n',n''}\sum_{\mathbf{k}}^{BZ}\frac{\langle n\mathbf{k}|\mathcal{P}^\alpha|n'\mathbf{k}\rangle\Big(\langle n'\mathbf{k}|p^\beta|n''\mathbf{k}\rangle\langle n''\mathbf{k}|p^\gamma|n\mathbf{k}\rangle + \langle n'\mathbf{k}|p^\gamma|n''\mathbf{k}\rangle\langle n''\mathbf{k}|p^\beta|n\mathbf{k}\rangle\Big)}{(E_{n,\mathbf{k}} - E_{n',\mathbf{k}} + 2\omega + 2i\eta)} \times\left[\frac{f_{nn''}}{(E_{n,\mathbf{k}} - E_{n'',\mathbf{k}} + \omega + i\eta)} + \frac{f_{n'n''}}{(E_{n'',\mathbf{k}} - E_{n',\mathbf{k}} + \omega + i\eta)}\right], \tag{5.3}$$

where $\boldsymbol{\mathcal{P}}$ is defined by Eq. (5.1).

Let us call this modification Cz1, because only one matrix element is modified in this formula. On the other hand, the susceptibility is obtained according to Ref. [183] thanks to the formula

$$\chi^{(2)Cz2}_{0,\alpha\beta\gamma}(\omega,\omega) = \frac{i}{2V\omega^3}\sum_{n,n',n''}\sum_{\mathbf{k}}^{BZ}\frac{\langle n\mathbf{k}|p^\alpha|n'\mathbf{k}\rangle\Big(\langle n'\mathbf{k}|\mathcal{P}^\beta|n''\mathbf{k}\rangle\langle n''\mathbf{k}|\mathcal{P}^\gamma|n\mathbf{k}\rangle + \langle n'\mathbf{k}|\mathcal{P}^\gamma|n''\mathbf{k}\rangle\langle n''\mathbf{k}|\mathcal{P}^\beta|n\mathbf{k}\rangle\Big)}{(E_{n,\mathbf{k}} - E_{n',\mathbf{k}} + 2\omega + 2i\eta)} \times\left[\frac{f_{nn''}}{(E_{n,\mathbf{k}} - E_{n'',\mathbf{k}} + \omega + i\eta)} + \frac{f_{n'n''}}{(E_{n'',\mathbf{k}} - E_{n',\mathbf{k}} + \omega + i\eta)}\right]. \tag{5.4}$$

This modification will be referred as Cz2, because two momentum matrix elements are modified.

Notice that the key point for the extraction of the spectra in both approaches is based on the modified momentum $\boldsymbol{\mathcal{P}}$.

With those two unproven methods, the literature does not really provide the reader with a rigorous

[3] The system is a cold semiconductor with filled band, at T=0K. The occupation numbers are thus independent of the momentum $\mathbf{k}$.

theoretical description of the second-harmonic generation from surface. Some questions have to be addressed. Is one of these two methods correct? Is there a different way to extract the spectra from half of the slab? If one of these two approaches is correct, what justifies the choice of Eq. (5.1) as a expression for $\mathcal{P}$? Answering to these different questions is the aim of this chapter and in particular of this section.
Using the argument of the gauge invariance, I will first prove that the modification denoted Cz1 allows the gauge invariant whereas this is not the case for other possible modifications of the formula. Then, in section 5.1.2, I will derive the Cz1 formula and prove that the expression of the modified momentum can be rigorously obtained, *e.g.*, from the density-matrix formalism and the perturbation theory; by integrating the microscopic current over the region of the slab limited by the aforementioned $\mathcal{C}(z)$ function.

5.1.1 Gauge invariance

The gauge invariance is an intrinsic property of the response functions [44]. This implies some properties on the $\chi_0^{(2)}$ tensor. Here I will focus on one necessary condition to be gauge invariant, which is the non-divergence of the $\chi_0^{(2)}$ tensor as ω goes to zero.
Expressed in the *velocity* gauge, as in Eq. 5.2, there is an apparent divergence as the frequency ω goes to zero. However, Sipe and co-workers proved in Ref. [185] that the formula can be expressed in a non-divergent form, in the *length* gauge, and that all the divergent terms vanish.
The natural property of the tensor to be non-divergent must be fulfilled in an exact description of microscopic surface second-harmonic generation. Therefore, the modified formula allowing us to extract half of the slab response, must respect this property. As we will see, this is not the case for all the possible modifications of the formula, and only the Cz1 formula fulfils the non-divergence condition, and therefore allows the gauge invariance.
The Sipe and co-workers gauge transformation is based on the following expansion

$$\frac{1}{\omega^3(E_{nn'}(\mathbf{k})+2\omega)}\left[\frac{f_{nn''}}{(E_{nn''}(\mathbf{k})+\omega)}+\frac{f_{n'n''}}{(E_{n''n'}(\mathbf{k})+\omega)}\right]=\frac{\mathcal{A}}{\omega^3}+\frac{\mathcal{B}}{\omega^2}+\frac{\mathcal{C}}{\omega}+\mathcal{F}(\omega), \tag{5.5}$$

where

$$\mathcal{A}=\frac{1}{E_{nn'}(\mathbf{k})}\left[\frac{f_{nn''}}{E_{nn''}(\mathbf{k})}+\frac{f_{n'n''}}{E_{n''n'}(\mathbf{k})}\right], \tag{5.6a}$$

$$\mathcal{B}=\frac{f_{nn''}}{E_{nn'}(\mathbf{k})E_{nn''}(\mathbf{k})}\left[\frac{2}{E_{n'n}(\mathbf{k})}+\frac{1}{E_{n''n}(\mathbf{k})}\right]+\frac{f_{n'n''}}{E_{nn'}(\mathbf{k})E_{n''n'}(\mathbf{k})}\left[\frac{2}{E_{n'n}(\mathbf{k})}+\frac{1}{E_{n'n''}(\mathbf{k})}\right], \tag{5.6b}$$

$$\begin{aligned}\mathcal{C}=&\frac{f_{nn''}}{E_{nn'}(\mathbf{k})E_{nn''}(\mathbf{k})}\left[\frac{4}{E_{n'n}(\mathbf{k})^2}+\frac{2}{E_{n'n}(\mathbf{k})E_{n''n}(\mathbf{k})}+\frac{1}{E_{n''n}(\mathbf{k})^2}\right]\\&+\frac{f_{n'n''}}{E_{nn'}(\mathbf{k})E_{n''n'(\mathbf{k})}}\left[\frac{4}{E_{n'n}(\mathbf{k})^2}+\frac{2}{E_{n'n}(\mathbf{k})E_{n'n''}(\mathbf{k})}+\frac{1}{E_{n'n''}(\mathbf{k})^2}\right],\end{aligned} \tag{5.6c}$$

$$\mathcal{F}(\omega)=\frac{16}{E_{n'n}^3(\mathbf{k})(E_{nn'}(\mathbf{k})+2\omega)}\left[\frac{f_{nn''}}{(E_{n'n}(\mathbf{k})-2E_{n''n}(\mathbf{k}))}+\frac{f_{n'n''}}{(E_{n'n}(\mathbf{k})-2E_{n'n''}(\mathbf{k}))}\right]$$

$$+\frac{f_{nn''}}{E^3_{n''n}(\mathbf{k})(2E_{n''n}(\mathbf{k})-E_{n'n}(\mathbf{k}))(E_{nn''}(\mathbf{k})+\omega)}+\frac{f_{n'n''}}{E^3_{n'n''}(\mathbf{k})(2E_{n'n''}(\mathbf{k})-E_{n'n}(\mathbf{k}))(E_{n''n'}(\mathbf{k})+\omega)}, \tag{5.6d}$$

where $E_{nn'}(\mathbf{k})=E_{n,\mathbf{k}}-E_{n',\mathbf{k}}$.
To be non-divergent, the terms associated with $\mathcal{A}$, $\mathcal{B}$ and $\mathcal{C}$ must be zero.
Here, I do not assume any explicit expression for $\boldsymbol{\mathcal{P}}$ and I only assume that $\hat{\mathbf{p}}$ and $\boldsymbol{\mathcal{P}}$ behave similarly under time-reversal symmetry and thus that $\langle n,-\mathbf{k}|\boldsymbol{\mathcal{P}}|n',-\mathbf{k}\rangle=-\langle n,\mathbf{k}|\boldsymbol{\mathcal{P}}|n',\mathbf{k}\rangle$.

Cz1 modification

Following Ref. [185], it is straightforward to show that the terms associated with $\mathcal{A}$ and $\mathcal{C}$ are zero, invoking the time-reversal symmetry. In order to prove that the term associated with $\mathcal{B}$ is zero, we must define the second-rank tensor

$$\overset{\leftrightarrow}{T}(\mathbf{k})=\sum_{n,n'\notin\mathcal{D}_n} f_{nn'}\frac{\langle n,\mathbf{k}|\boldsymbol{\mathcal{P}}|n',\mathbf{k}\rangle\langle n',\mathbf{k}|\mathbf{p}|n,\mathbf{k}\rangle}{E^2_{n'n}(\mathbf{k})}.$$

Using the $\mathbf{k}.\mathbf{p}$ perturbation theory, and after some algebra, we obtain

$$\begin{aligned}\frac{1}{2}\left(\frac{\partial T^{\alpha\beta}}{\partial k^\gamma}+\frac{\partial T^{\alpha\gamma}}{\partial k^\beta}\right)&=\sum_{n,n'\notin\mathcal{D}_n}\frac{f_{nn'}\tilde{\Delta}^\alpha_{nn'}(\mathbf{k})\left\{\langle n,\mathbf{k}|p^\beta|n',\mathbf{k}\rangle\langle n',\mathbf{k}|p^\gamma|n,\mathbf{k}\rangle\right\}}{E^2_{n'n}(\mathbf{k})}\\
-\sum_{n,n'}\left(\frac{3f_{nn'}\langle n,\mathbf{k}|\mathcal{P}^\alpha|n',\mathbf{k}\rangle\{\langle n',\mathbf{k}|p^\beta|n,\mathbf{k}\rangle\Delta^\gamma_{n'n}(\mathbf{k})\}}{E^3_{n'n}(\mathbf{k})}+\frac{f_{nn'}\langle n,\mathbf{k}|\mathcal{C}(z)\delta_{\alpha\gamma}|n',\mathbf{k}\rangle\langle n',\mathbf{k}|p^\beta|n,\mathbf{k}\rangle}{E^2_{n'n}(\mathbf{k})}\right)&\\
-\sum_{\substack{n,n',n''\\ n'\notin\mathcal{D}_n\\ n''\notin\{\mathcal{D}_n\mathcal{D}_{n'}\}}}\beta_{n,n',n''}(\mathbf{k})\langle n,\mathbf{k}|\mathcal{P}^\alpha|n',\mathbf{k}\rangle\{\langle n',\mathbf{k}|p^\beta|n'',\mathbf{k}\rangle\langle n'',\mathbf{k}|p^\gamma|n,\mathbf{k}\rangle\},&\end{aligned} \tag{5.7}$$

with $\tilde{\Delta}^\alpha_{nn'}(\mathbf{k})=\langle n,\mathbf{k}|\mathcal{P}^\alpha|n,\mathbf{k}\rangle-\langle n',\mathbf{k}|\mathcal{P}^\alpha|n',\mathbf{k}\rangle$, and

$$\left\{\langle n,\mathbf{k}|p^\beta|n',\mathbf{k}\rangle\langle n',\mathbf{k}|p^\gamma|n,\mathbf{k}\rangle\right\}=\frac{1}{2}\left(\langle n,\mathbf{k}|p^\beta|n',\mathbf{k}\rangle\langle n',\mathbf{k}|p^\gamma|n,\mathbf{k}\rangle+\langle n,\mathbf{k}|p^\gamma|n',\mathbf{k}\rangle\langle n',\mathbf{k}|p^\beta|n,\mathbf{k}\rangle\right).$$

In order to obtain Eq.(5.7), we have used the following sum-rule

$$\begin{aligned}\frac{\partial}{\partial k^\gamma}\langle n,\mathbf{k}|\mathcal{P}^\alpha|n',\mathbf{k}\rangle=i\sum_{m\notin\{\mathcal{D}_n\mathcal{D}_{n'}\}}&\left[\langle n,\mathbf{k}|r^\gamma|m,\mathbf{k}\rangle\langle m,\mathbf{k}\mathcal{P}^\alpha|n',\mathbf{k}\rangle-\langle n,\mathbf{k}|\mathcal{P}^\alpha|m,\mathbf{k}\rangle\langle m,\mathbf{k}|r^\gamma|n',\mathbf{k}\rangle\right]\\
&-\langle n,\mathbf{k}|\mathcal{C}(z)\delta_{\alpha\gamma}|n',\mathbf{k}\rangle+i\langle n,\mathbf{k}|r^\gamma|n',\mathbf{k}\rangle\tilde{\Delta}^\alpha_{n'n},\end{aligned} \tag{5.8}$$

that can be derived from the $\mathbf{k}.\mathbf{p}$ perturbation theory. Here $\mathcal{D}_n$ are all the possible degenerate n-states. Using the time-reversal symmetry, we obtain that

$$\frac{1}{2}\left(\frac{\partial T^{\alpha\beta}}{\partial k^\gamma}+\frac{\partial T^{\alpha\gamma}}{\partial k^\beta}\right)=-\sum_{\substack{n,n',n''\\ n'\notin\mathcal{D}_n\\ n''\notin\{\mathcal{D}_n\mathcal{D}_{n'}\}}}\beta_{n,n',n''}(\mathbf{k})\langle n,\mathbf{k}|\mathcal{P}^\alpha|n',\mathbf{k}\rangle\{\langle n',\mathbf{k}|p^\beta|n'',\mathbf{k}\rangle\langle n'',\mathbf{k}|p^\gamma|n,\mathbf{k}\rangle\}. \tag{5.9}$$

Using the fact that $\overset{\leftrightarrow}{T}(\mathbf{k})$ is a periodic function throughout the BZ, its integral over the full BZ is zero. The $\beta_{n,n',n''}(\mathbf{k})$ term corresponds to the $\mathcal{B}$ term of Eq. (5.6b); which is integrated over the full BZ. We thus prove that the term associated with $\mathcal{B}$, in the case of the formula Cz1, is zero which is a necessary condition for the formula Cz1 to be gauge invariant.

Cz2 modification

Similarly to the previous case, the terms associated to $\mathcal{A}$ and $\mathcal{C}$ are zero from time-reversal symmetry. The term associated to $\mathcal{B}$ contains two modified matrix elements. The sum-rule Eq. (5.8) yields only one modified momentum matrix element on the right-hand side. In order to allow the gauge invariance, one must define a second-rank tensor, and takes its derivative. The only possible choice for obtaining two modified momentum matrix elements from the derivative of a second-order tensor, is to define the following tensor

$$\overset{\leftrightarrow}{T}(\mathbf{k}) = \sum_{n,n\neq n'} f_{nn'} \frac{\langle n,\mathbf{k}|\boldsymbol{\mathcal{P}}|n',\mathbf{k}\rangle\langle n',\mathbf{k}|\boldsymbol{\mathcal{P}}|n,\mathbf{k}\rangle}{E^2_{n'n}(\mathbf{k})}. \tag{5.10}$$

More precisely, due to the structure of $\mathcal{B}$, only the specific combination of derivative of that tensor $\frac{1}{2}\left(\frac{\partial T^{bc}}{\partial k^a} + \frac{\partial T^{cb}}{\partial k^a}\right)$ would give the correct coordinates associated with the modified momentum matrix elements. Any other combination does not yield the correct coordinates associated with $\boldsymbol{\mathcal{P}}$. Unfortunately, it is not possible to recover the expected $\mathcal{B}$ term from this expression. The conclusion is *the formula Cz2 is not gauge invariant*, due to the fact that $\mathcal{B}$ term is non-vanishing.

Other possible modifications

We have, up to now, considered only Cz1 and Cz2 as possible modifications for the expression of the second-order susceptibility tensor. But is there any other possible modifications? One can think for instance to modify one matrix element but not the first one, or to modify two matrix elements but not the two last one. First, this is meaningless because this breaks the intrinsic permutation rule of the indices of the $\chi_0^{(2)}$ tensor, $\chi^{(2)}_{0,\alpha\beta\gamma} = \chi^{(2)}_{0,\alpha\gamma\beta}$. Second, in each cases, applying the time-reversal symmetry to the $\mathcal{A}$ and $\mathcal{C}$ terms does not make them vanish.
The last possible option could be to modify all matrix elements. In that case, due to the sum-rule Eq. (5.8), the $\mathcal{B}$ term will not be zero, because any derivative of a second-order tensor will leave, at least, one unmodified momentum matrix element.

Conclusion

To conclude, I have proven that the only modified expression of the microscopic second-order susceptibility tensor, which includes the cut-function $\mathcal{C}(z)$ while allowing gauge invariance, is the Cz1

modified quantity; which will now be denoted $\chi_0^{(2)S}$, and which is given by

$$\chi^{(2)S}_{0,\alpha\beta\gamma}(\omega,\omega) = \frac{i}{2V\omega^3}\sum_{n,n',n''}\sum_{\mathbf{k}}^{BZ}\frac{\langle n\mathbf{k}|\mathcal{P}^{\alpha}|n'\mathbf{k}\rangle\Big(\langle n'\mathbf{k}|p^{\beta}|n''\mathbf{k}\rangle\langle n''\mathbf{k}|p^{\gamma}|n\mathbf{k}\rangle + \langle n'\mathbf{k}|p^{\gamma}|n''\mathbf{k}\rangle\langle n''\mathbf{k}|p^{\beta}|n\mathbf{k}\rangle\Big)}{(E_{n,\mathbf{k}} - E_{n',\mathbf{k}} + 2\omega + 2i\eta)} \times\left[\frac{f_{nn''}}{(E_{n,\mathbf{k}} - E_{n'',\mathbf{k}} + \omega + i\eta)} + \frac{f_{n'n''}}{(E_{n'',\mathbf{k}} - E_{n',\mathbf{k}} + \omega + i\eta)}\right]$$

Nevertheless, at this stage, I do not have proven that this modified formula gives the correct second-harmonic generation spectra. Moreover, the analytical expression of the modified momentum has still not been given. The only thing that I have proven at this point is that gauge invariance imposes only one way to modify the formula. The interesting point is that this choice corresponds to the choice of the majority of authors in the literature. I will now show the expression of $\boldsymbol{\mathcal{P}}$.

5.1.2 Density-matrix formalism and perturbation theory

In Ref. [139], Mendoza *et al.* derived from a microscopic approach the modification Cz1 for the *linear optical properties*; by integrating the polarization (and therefore the microscopic current) over the surface region. Here I briefly reproduce their derivation for the linear case and I extend it to the case of the second-harmonic generation. The potential is assumed here to be local. The specificities related to non-local operators are treated in next chapter.

For a system perturbed by an external electric field, Sipe *et al.* [186] have shown, from perturbation theory, that the corrections to density matrix due to the perturbing field, denoted here $c_{mn}(\mathbf{k},t)$, are given at first- and second-order in the perturbing electric field, by

$$c^{(1)}_{mn}(\mathbf{k},t) = \int d\omega \sum_{\beta}\frac{f_{nm}r^{\beta}_{mn}(\mathbf{k})}{(E_{mn}(\mathbf{k}) - \omega - i\eta)}E^{P}_{\beta}(\omega)e^{-i(\omega+i\eta)t} \tag{5.11a}$$

$$c^{(2)}_{mn}(\mathbf{k},t) = \frac{i}{4}\int d\omega_1 d\omega_2 \sum_{\beta\gamma}\frac{1}{(E_{mn}(\mathbf{k}) - (\omega_1+\omega_2+2i\eta))}\Bigg[\frac{f_{nm}r^{\beta}_{mn;\gamma}(\mathbf{k})}{(E_{mn}(\mathbf{k}) - \omega_1 - i\eta)} - \frac{f_{nm}r^{\beta}_{mn}(\mathbf{k})\Delta^{\gamma}_{mn}(\mathbf{k})}{(E_{mn}(\mathbf{k}) - \omega_1 - i\eta)^2} - i\sum_{p}\Big(\frac{f_{np}r^{\gamma}_{mp}(\mathbf{k})r^{\beta}_{pn}(\mathbf{k})}{(E_{pn}(\mathbf{k}) - \omega_1 - i\eta)} - \frac{f_{pm}r^{\beta}_{mp}(\mathbf{k})r^{\gamma}_{pn}(\mathbf{k})}{(E_{mp}(\mathbf{k}) - \omega_1 - i\eta)}\Big) + (\beta\gamma 12 \Leftrightarrow \gamma\beta 21)\Bigg]E^{P}_{\beta}(\omega_1)E^{P}_{\gamma}(\omega_2)e^{-i(\omega_1+\omega_2+2i\eta)t} \tag{5.11b}$$

where $\mathbf{E}^P(\omega) = \int dt \mathbf{E}^P(t) exp(i\omega t)$, $\mathbf{E}^P$ being the perturbing field, see Chap. 1.

Here, $E_{mn}(\mathbf{k}) = E_{m,\mathbf{k}} - E_{n,\mathbf{k}}$ are energy differences between the bands m and n for a momentum $\mathbf{k}$ in the BZ, Δ^{γ}_{mn} is defined as $\Delta^{\gamma}_{mn}(\mathbf{k}) = p^{\gamma}_{mm}(\mathbf{k}) - p^{\gamma}_{nn}(\mathbf{k})$ and $r^{\beta}_{mn;\gamma}$ is given by

$$r^{\beta}_{mn;\gamma}(\mathbf{k}) = \frac{-[r^{\beta}_{mn}(\mathbf{k})\Delta^{\gamma}_{mn}(\mathbf{k}) + r^{\gamma}_{mn}(\mathbf{k})\Delta^{\beta}_{mn}(\mathbf{k})]}{E_{mn}(\mathbf{k})} - i\sum_{p}\frac{E_{mp}(\mathbf{k})r^{\beta}_{mp}(\mathbf{k})r^{\gamma}_{pn}(\mathbf{k}) - E_{pn}(\mathbf{k})r^{\gamma}_{mp}(\mathbf{k})r^{\beta}_{pn}(\mathbf{k})}{E_{mn}(\mathbf{k})}. \tag{5.12}$$

Even if the expression (5.11b) is general for all the second-order phenomena, I will restrict myself to the case of second-harmonic generation.

Following Ref. [139], we write the mean value of the microscopic current density integrated over the

full BZ [4]

$$< \mathbf{j}^{(1)}(\mathbf{r},t) > = \int \frac{d^3\mathbf{k}}{8\pi^3} \sum_{mn} c^{(1)}_{mn}(\mathbf{k},t)\mathbf{j}_{nm}(\mathbf{k};\mathbf{r}), \tag{5.13a}$$

$$< \mathbf{j}^{(2)}(\mathbf{r},t) > = \int \frac{d^3\mathbf{k}}{8\pi^3} \sum_{mn} c^{(2)}_{mn}(\mathbf{k},t)\mathbf{j}_{nm}(\mathbf{k};\mathbf{r}), \tag{5.13b}$$

where $\mathbf{j}_{nm}(\mathbf{k};\mathbf{r})$ is a matrix element of the microscopic current operator given by [187]

$$\mathbf{j}_{nm}(\mathbf{k};\mathbf{r}) = \frac{-i}{2}[\psi^*_{n\mathbf{k}}(\mathbf{r})\boldsymbol{\nabla}\psi_{m\mathbf{k}}(\mathbf{r}) - \psi_{m\mathbf{k}}(\mathbf{r})\boldsymbol{\nabla}\psi^*_{n\mathbf{k}}(\mathbf{r})]. \tag{5.14}$$

Rather than integrating over the full slab, we integrate over a part of the slab, defined by $\mathcal{C}(z)$. The surface microscopic induced current density $\mathbf{J}^S_{ind}$ is given at the i-th order by

$$< \mathbf{J}^{(i)S}_{ind}(t) >= \int d^3\mathbf{r}\mathcal{C}(z) < \mathbf{j}^{(i)}(\mathbf{r},t) >= \int \frac{d^3\mathbf{k}}{8\pi^3} \sum_{mn} c^{(i)}_{mn}(\mathbf{k},t) \int d^3\mathbf{r}\mathcal{C}(z)\mathbf{j}_{nm}(\mathbf{k};\mathbf{r}). \tag{5.15}$$

We now compute the last integral in Eqs. (5.15).

$$\begin{aligned}
\int d^3\mathbf{r}\mathcal{C}(z)\mathbf{j}_{nm}(\mathbf{k};\mathbf{r}) &= \frac{1}{2}\int d^3\mathbf{r}\mathcal{C}(z)[\psi^*_{n\mathbf{k}}(\mathbf{r})(-i\boldsymbol{\nabla})\psi_{m\mathbf{k}}(\mathbf{r}) + \psi_{m\mathbf{k}}(\mathbf{r})(i\boldsymbol{\nabla})\psi^*_{n\mathbf{k}}(\mathbf{r})] \\
&= \int d^3\mathbf{r}\psi^*_{n\mathbf{k}}(\mathbf{r})\frac{\mathcal{C}(z)\hat{\mathbf{p}} + \hat{\mathbf{p}}\mathcal{C}(z)}{2}\psi_{m\mathbf{k}}(\mathbf{r}) \\
&= \boldsymbol{\mathcal{P}}_{nm}(\mathbf{k}),
\end{aligned} \tag{5.16}$$

where $\hat{\mathbf{p}} = -i\boldsymbol{\nabla}$.
Here an integration by part is performed on the second term of the right-hand side of the first line. Notice that we obtain the expression of a matrix element of the modified momentum mentioned before.
The next step consists in linking explicitly $c^{(1)}_{mn}$ and $c^{(2)}_{mn}$, given by expressions (5.11a) and (5.11b), to the linear and second-order susceptibilities.

First-order response

Using Eq.(5.16) and Eq.(5.15), we obtain[5]

$$< J^{(1)S,\alpha}_{ind}(t) >= \int d\omega \sum_{\beta} \int \frac{d^3\mathbf{k}}{8\pi^3} \sum_{mn} \frac{f_{nm}\mathcal{P}^{\alpha}_{nm}(\mathbf{k})p^{\beta}_{mn}(\mathbf{k})}{E_{mn}(\mathbf{k})\left(E_{mn}(\mathbf{k}) - \omega - i\eta\right)} E^P_{\beta}(\omega)e^{-i(\omega+i\eta)t}. \tag{5.17}$$

[4] At this point of the derivation, one must not replace the integral over the Brillouin zone by a sum because an integration by part will be performed later.

[5] Position matrix elements are linked to the momentum matrix elements by the relation

$$\mathbf{r}_{nm}(\mathbf{k}) = \frac{\mathbf{p}_{nm}}{iE_{nm}(\mathbf{k})}, \qquad n \notin \mathcal{D}_m,$$

where $\mathcal{D}_m$ are all the possible degenerate m-states. The occupation numbers prevent from having $n \in \mathcal{D}_m$.

We now use the following definition, where $\chi_0^{(1)S}$ is the first-order surface susceptibility, linking the surface polarization at first order to the electric field.[6]

$$< J_{ind}^{(1)S,\alpha}(t) >= -i \int d\omega \sum_{\beta} (\omega + i\eta) \chi_{0,\alpha\beta}^{(1)S}(\omega) E_{\beta}^{P}(\omega) e^{-i(\omega+i\eta)t}.$$

After simple algebra, one obtains that

$$\chi_{0,\alpha\beta}^{(1)S}(\omega) = \frac{1}{V} \sum_{mn} \sum_{\mathbf{k}}^{BZ} \frac{f_{nm} \langle n, \mathbf{k} | \mathcal{P}^{\alpha} | m, \mathbf{k} \rangle \langle m, \mathbf{k} | p^{\beta} | n, \mathbf{k} \rangle}{E_{mn}^{2}(\mathbf{k}) \left(E_{mn}(\mathbf{k}) - \omega - i\eta \right)}, \tag{5.18}$$

where we replaced the integral over the BZ by a sum. We obtain exactly the same formula as in [188], except that the first momentum matrix element is replaced by a matrix element of the modified momentum (5.1).
Thus we showed that computing the first-order microscopic susceptibility for a surface yield the Cz1 formula Eq. (5.3). Moreover, the expression of the modification $\boldsymbol{\mathcal{P}}$, given by Eq.(5.1), is obtained analytically.

Second-harmonic generation

The case of SHG is more difficult to tackle.
Combining Eq. (5.16) and Eq. (5.15), and identifying to the surface susceptibility defined by

$$< J_{ind,\alpha}^{(2)S}(t) >= -i \int d\omega \sum_{\beta\gamma} (\omega + i\eta) \chi_{0,\alpha\beta\gamma}^{(2)S}(\omega, \omega) E_{\beta}^{P}(\omega) E_{\gamma}^{P}(\omega) e^{-2i(\omega+i\eta)t}, \tag{5.19}$$

we obtain that

$$\begin{aligned}
\chi_{0,\alpha\beta\gamma}^{(2)S}(\omega,\omega) = \frac{-i}{(\omega+i\eta)} \int \frac{d^3\mathbf{k}}{8\pi^3} \sum_{mn} \frac{1}{(E_{mn}(\mathbf{k}) - 2\omega - 2i\eta)} \Bigg[& \frac{f_{nm} \mathcal{P}_{nm}^{\alpha}(\mathbf{k}) \left[p_{mn}^{b}(\mathbf{k}) \Delta_{mn}^{c}(\mathbf{k}) + p_{mn}^{c}(\mathbf{k}) \Delta_{mn}^{b}(\mathbf{k}) \right]}{(E_{mn}(\mathbf{k}) - \omega) E_{mn}^{2}(\mathbf{k})} \\
& + \sum_{p} \frac{f_{nm} \mathcal{P}_{nm}^{\alpha}(\mathbf{k}) \left[E_{mp}(\mathbf{k}) p_{mp}^{\beta}(\mathbf{k}) p_{pn}^{c}(\mathbf{k}) - E_{pn}(\mathbf{k}) p_{mp}^{c}(\mathbf{k}) p_{pn}^{b}(\mathbf{k}) \right]}{E_{mp}(\mathbf{k}) E_{pn}(\mathbf{k}) E_{mn}(\mathbf{k}) (E_{mn}(\mathbf{k}) - \omega - i\eta)} + \frac{f_{nm} \mathcal{P}_{nm}^{\alpha}(\mathbf{k}) p_{mn}^{\beta}(\mathbf{k}) \Delta_{mn}^{c}(\mathbf{k})}{E_{mn}(\mathbf{k}) (E_{mn}(\mathbf{k}) - \omega - i\eta)^2} \\
& + \sum_{p} \Big(\frac{f_{np} \mathcal{P}_{nm}^{\alpha}(\mathbf{k}) p_{mp}^{c}(\mathbf{k}) p_{pn}^{b}(\mathbf{k})}{E_{mp}(\mathbf{k}) E_{pn}(\mathbf{k}) (E_{pn}(\mathbf{k}) - \omega - i\eta)} - \frac{f_{pm} \mathcal{P}_{nm}^{\alpha}(\mathbf{k}) p_{mp}^{b}(\mathbf{k}) p_{pn}^{c}(\mathbf{k})}{E_{mp}(\mathbf{k}) E_{pn}(\mathbf{k}) (E_{mp}(\mathbf{k}) - \omega - i\eta)} \Big) + (\beta\gamma \Leftrightarrow \gamma\beta) \Bigg].
\end{aligned} \tag{5.20}$$

This expression is divergent as $\frac{1}{(\omega+i\eta)}$, but after some tedious algebra, we obtain a non-divergent formula. The derivation proceeds as follow. The following term

$$A = \frac{-i}{2(\omega+i\eta)} \int \frac{d^3\mathbf{k}}{8\pi^3} \sum_{mn} \frac{f_{nm} \mathcal{P}_{nm}^{a}(\mathbf{k}) p_{mn}^{b}(\mathbf{k}) \Delta_{mn}^{c}(\mathbf{k})}{\omega_{mn}(\mathbf{k}) (\omega_{mn}(\mathbf{k}) - 2\omega - 2i\eta) (\omega_{mn}(\mathbf{k}) - \omega - i\eta)^2},$$

is not satisfactory because it contains a term with $(\omega_{mn}(\mathbf{k}) - \omega - i\eta)^{-2}$. In order to overcome this term, we expand A into partial fraction and we use a relation given by Sipe and co-workers in Ref. [186]

[6] The total electric field and the perturbing electric field are equals in the independent-particle approximation.

for any function g

$$\frac{\partial g(\omega_{mn})}{\partial k^a} = \frac{\partial \omega_{mn}}{\partial k^a}\frac{\partial g(\omega_{mn})}{\partial \omega_{mn}} = \Delta^a_{mn}\frac{\partial g(\omega_{mn})}{\partial \omega_{mn}}.$$

Then after performing integration by parts, all the terms are factorized and simplified using time-reversal symmetry. The $\frac{1}{(\omega+i\eta)}$ divergence vanishes naturally when applying the time-reversal symmetry on the remaining expression. For convenience, we split this expression into two contributions, one giving the two-bands contribution, where only two bands are involved and a second one, giving the contribution which involves three bands.

$$\chi^{(2)S}_{0,\alpha\beta\gamma}(\omega,\omega) = \chi^{3bnd}_{\alpha\beta\gamma}(\omega) + \chi^{2bnd}_{\alpha\beta\gamma}(\omega), \tag{5.21}$$

with

$$\chi^{3bnd}_{\alpha\beta\gamma}(\omega) = \frac{i}{2V}\sum_{nmp}\sum_{\mathbf{k}}^{BZ}\frac{\langle n,\mathbf{k}|\mathcal{P}^\alpha|m,\mathbf{k}\rangle\left(\langle m,\mathbf{k}|p^\beta|p,\mathbf{k}\rangle\langle p,\mathbf{k}|p^\gamma|n,\mathbf{k}\rangle + \langle m,\mathbf{k}|p^\gamma|p,\mathbf{k}\rangle\langle p,\mathbf{k}|p^\beta|n,\mathbf{k}\rangle\right)}{(2E_{pn}(\mathbf{k}) - E_{mn}(\mathbf{k}))}$$
$$\times\left[\frac{16 f_{nm}}{E^3_{mn}(\mathbf{k})(E_{mn}(\mathbf{k}) - 2\omega - 2i\eta)} + \frac{f_{pn}}{E^3_{pn}(\mathbf{k})(E_{pn}(\mathbf{k}) - \omega - i\eta)} + \frac{f_{mp}}{E^3_{pm}(\mathbf{k})(E_{mp}(\mathbf{k}) - \omega - i\eta)}\right], \tag{5.22a}$$

$$\chi^{2bnd}_{\alpha\beta\gamma}(\omega) = \frac{i}{V}\sum_{nm}\sum_{\mathbf{k}}^{BZ}\frac{f_{nm}\langle n,\mathbf{k}|\mathcal{P}^\alpha|m,\mathbf{k}\rangle\left(\langle m,\mathbf{k}|p^\beta|n,\mathbf{k}\rangle\langle m,\mathbf{k}|\Delta^\gamma|n,\mathbf{k}\rangle + \langle m,\mathbf{k}|p^\gamma|n,\mathbf{k}\rangle\langle m,\mathbf{k}|\Delta^\beta|n,\mathbf{k}\rangle\right)}{\omega^4_{mn}(\mathbf{k})}$$
$$\times\left[\frac{8}{(E_{mn}(\mathbf{k}) - 2\omega - 2i\eta)} - \frac{1}{2(E_{mn}(\mathbf{k}) - \omega - i\eta)}\right]. \tag{5.22b}$$

We have replaced integral by a sum over the full BZ. We obtain a formula for $\chi^{(2)S}_0$ expressed in the length gauge similar to the expressions of $\chi^{(2)}_0$ that one can find in the literature, *e.g.*, Ref. [189]; except that the momentum matrix element associated with the Cartesian coordinate α of the polarization has been replaced here by a modified momentum matrix element.

Thereby we have derived explicitly the Cz1 expression, without any approximation on the second-order susceptibility. As in the case of linear optical properties, we recovered the analytical expression of $\boldsymbol{\mathcal{P}}$ as given by Eq.(5.1); proving thus the correctness of the approach assumed by authors in literature.

Together with the previous result, we have established a rigorous derivation of the extraction of the surface second-harmonic generation. We have proven that it exists an unique way to modify the expression of the $\chi^{(2)}_0$ tensor. Then we have proven that integrating over a region of the system defined by a cut-function $\mathcal{C}(z)$, instead of the entire system, leads to modified momentum $\boldsymbol{\mathcal{P}}$ of the literature. Next section is dedicated to the numerical validation of this approach.

5.1.3 Tight-binding results - Numerical Validation

Tight-binding

The tight-binding (TB) method, using a $sp^3d^5s^*$ basis-set, [190, 191] gives reliable results for the electronic structure and the optical properties of solids. As the qualitative effects of the extraction of

the second-harmonic generation spectra do not depend on the scheme used to calculate the energies and velocity matrix elements, I decided to use this nearest-neighbour semi-empirical tight-binding scheme to determine the electronic structure of the surfaces in this section. Thereby, we obtain very well converged spectra as a function of the size of the slab, with an easy numerical implementation of the function $\mathcal{C}(z)$. During this thesis, I have implemented a tight-binding code for computing the linear and nonlinear optical properties of bulk materials and surfaces. This code has been used to test the theory presented in the first part of this chapter. Notice that only the numerical results of this chapter are obtained with this tight-binding code, whereas the rest of this thesis contains only the result of *ab initio* calculations.

Atomic positions and numerical details

The surfaces have been studied with the experimental lattice constant of 5.43 Å. We assume that *ab initio* atomic positions can be used directly for tight-binding calculations without performing any other relaxation. Structural optimizations were performed with the ABINIT code [115]. The geometry optimizations have been carried out in slabs of 12 atomic layers where the central four layers where fixed at the bulk positions. The structures were relaxed until the Cartesian force components were less than 5 meV/Å. The energy cut-off used was 20 Ha and I used Trouiller-Martin LDA pseudopotentials. The geometry optimization for the clean surface gives a dimer buckling of 0.721 Å, and a dimer length of 2.301 Å. For the Si(001)1×1:2H dihydride surface, we have obtained a Si-H bond distance of 1.48 Å. These results are in good agreement with previous theoretical studies [192, 193], as well as experimental values (see Chap. 4).

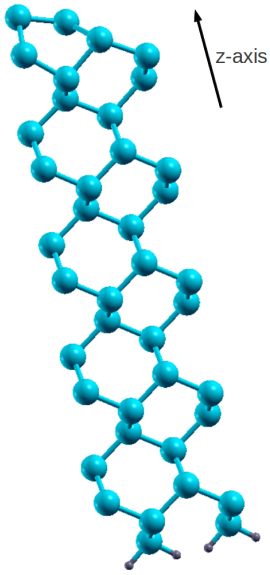

Fig. 5.3: A slab with an front clean Si(001)2×1 surface and a back dihydride surface. The dangling bonds are H (small balls) saturated. This image depicts 20 Si atomic layers with one H atomic layer.

The Si-Si parameters for the tight-binding code are taken from Ref. [194], and the H-H and Si-H parameters are taken from Ref. [195]. The parameters correspond to the values of the matrix elements of the Hamiltonian for the different orbitals of the chosen basis, at a fixed atomic distance. If the two orbitals are located on different atoms, we refer to them as inter-atomic terms. For two orbitals located on the same atom, we speak about intra-atomic terms. Intra-atomic matrix elements are important for obtaining quantitative optical properties in TB [196]. As the intra-atomic matrix elements do not exist in the literature for the $sp^3d^5s^*$ basis set, I optimised these parameters, imposing the Thomas-Reiche-Kuhn [197, 198] sum rule to be fulfilled. I also checked that for a smaller basis set (sp^3s^*), the values given in the literature for Si bulk are recovered with our approach. The values of intra-atomic matrix elements used in the surface calculations are given in Table 5.1. We checked that a slight change in the intra-atomic matrix elements does not induce any important change in the resulting optical spectra. Therefore, for the surfaces, we used the Si intra-atomic matrix elements optimized for the bulk material. Finally, to

	$\langle s\|d\|p_x\rangle$	$\langle s^*\|d\|p_x\rangle$	$\langle p_x\|d\|d_{xy}\rangle$	$\langle p_x\|d\|d_{3z^2-r^2}\rangle$	$\langle p_z\|d\|d_{3z^2-r^2}\rangle$
Si	0.636	0.247	0.309	0.203	0.258

Tab. 5.1: Intra-atomic matrix elements for bulk Si. Other intra-atomic matrix elements are obtained by symmetry.

	Non-zero components
Clean Surface	yyx=yxy xyy xxx yyz=yzy xxz=xzx zxx zyy xzz zzx=zxz zzz
Dihydride Surface	xxz=xzx yyz=yzy zxx zyy zzz

Tab. 5.2: Non-zero components for the different surfaces. Clean surface denotes a clean silicon surface with asymmetric dimers reconstruction. Dihydride surface denotes a silicon surface with 2 H atoms per Si surface atoms with the bulk in-plane symmetries preserved.

account for the deformation potential induced by the modified bond-length at the surface, we used a generalized Harrison scaling law [199], whose parameters for Si are also given in Ref. [194].
The tight-binding calculations have been performed using super-cells composed of 36 atomic layers and a 256 off-symmetry **k**-points grid has been used to sample the 2D Brillouin zone. We used the same amount of vacuum that the amount of matter in the super-cell. The results are found to be converged with those parameters. A Lorentzian broadening of 100 meV has been used.

The Clean-Dihydride slab

Here, we present a relevant test case to check the consistency of our approach. We have selected a clean Si(001) surface with a 2×1 surface reconstruction. The different silicon surfaces have already been presented in Chap. 4. The slab for such a surface could be chosen to be centrosymmetric by creating the front and back surfaces with the same 2×1 reconstruction. The fact that the clean surface has an asymmetric reconstruction breaks symmetries between x-axis (defined in crystallographic direction as $[1\bar{1}0]$) and y-axis ([110]). On the contrary, the hydrogen saturated surface is ideally bulk terminated, thus preserving the in-plane symmetries between the x and y axis. We choose to terminate one of the surfaces with hydrogen producing an ideal terminated bulk Si surface. The H atoms simply saturate the dangling bonds of the bulk-like Si atoms at the surface, as seen in Fig. 5.3. We take the z coordinate pointing out of the surface and the x direction is parallel to the dimers. The idea behind this slab configuration is that the crystalline symmetry of the H terminated surface imposes that $\chi^{2H}_{xxx} = 0$. The 2×1 surface has no such restrictions, so $\chi^{2\times1}_{xxx} \neq 0$. Therefore, the full-slab xxx component, calculation without selecting only one surface, *i.e.*, without using the $\mathcal{C}(z)$ function, equals the clean surface xxx component

$$\chi^{\text{full-slab}}_{xxx} = \chi^{2\times1}_{xxx} - \chi^{2H}_{xxx} = \chi^{2\times1}_{xxx}. \tag{5.23}$$

In total, five components can be calculated using the same technique, see Tab. 5.2. I want to stress that we are able to compute here five components of clean 2×1 surface *without any modification of the*

formula, as the full slab calculation yield in this case the interference between a zero and a non-zero signal. We can then compare these exact spectra with the extracted spectra corresponding to the half of a symmetric slab with two clean 2×1 surfaces. The result of the comparison is reported in Fig. 5.4. Our extraction perfectly reproduces the exact spectra in the low energy region. For higher energies, the two calculations present slight deviations but remain very similar. This proves the correctness of our approach, which reveals a really good agreement with exact spectra.
Small discrepancies can be attributed to convergence problems or to interferences between the front and the back surfaces. In next section, the possible sources of discrepancies are discussed.

5.2 Discussions

5.2.1 Numerical accuracy

The fact that the extraction of the spectra is possible and that it should recover the exact full-slab calculation relies on two implicit assumptions. The first assumption is that the two surfaces are independent and non-interacting. The validity of this assumption can be checked easily by computing the same component of the tensor $\chi_0^{(2)S}$ extracted from different super-cells. In Fig. 5.5, I compared the zzz component of the second-order susceptibility tensor for the clean (left panel) and dihydride (right panel) surfaces. The red curves correspond to the extraction of the spectra from a symmetric slab, *i.e.*, with two identical surfaces. The black curves correspond to the extraction from an asymmetric slab, *i.e.*, the front and the back surfaces are different. Here I chose the zzz component, because this is the biggest component in magnitude, and therefore, potential interference effects should be strengthened for this component.

The two obtained spectra for the clean and the dihydride surfaces are in a very good agreement. Indeed, the effect of the back termination on the front surface spectra is negligible. Notice that the discrepancy between the full slab and half slab spectra in Fig.5.4 is of the same order than the discrepancy between the spectra of Fig. 5.5.
The second assumption made is that the five components of Fig. 5.4 are numerically zero for the dihydride surface. The extraction of those five components for the dihydride surfaces yields as a result (not shown) a small but non-zero spectra.[7] Extracting those five components for the dihydride surface from a clean-dihydride slab, we obtain a spectra whose magnitude is three order of magnitude greater than our numerical zero.
Few reasons here can explain this result. Maybe the most reasonable reason is that the shifted **k**-point grid breaks the symmetries between the x and y axis and the number of **k**-points should be increased for improving the agreement between the different spectra. However, considering a good balance between the complexity of the calculation and the accuracy, the precision obtained by converging the number of **k**-point, conduction bands and more importantly the number of atomic layers is always more than a few percent. This is confirmed in the next section by a study of convergence of the zzz component of the clean silicon surface.
To conclude, the numerical accuracy has been investigated by analysing the possible interference ef-

[7] The numerical zero has been established for bulk systems to be at 10^{-5} atomic units for the SHG tight-binding code.

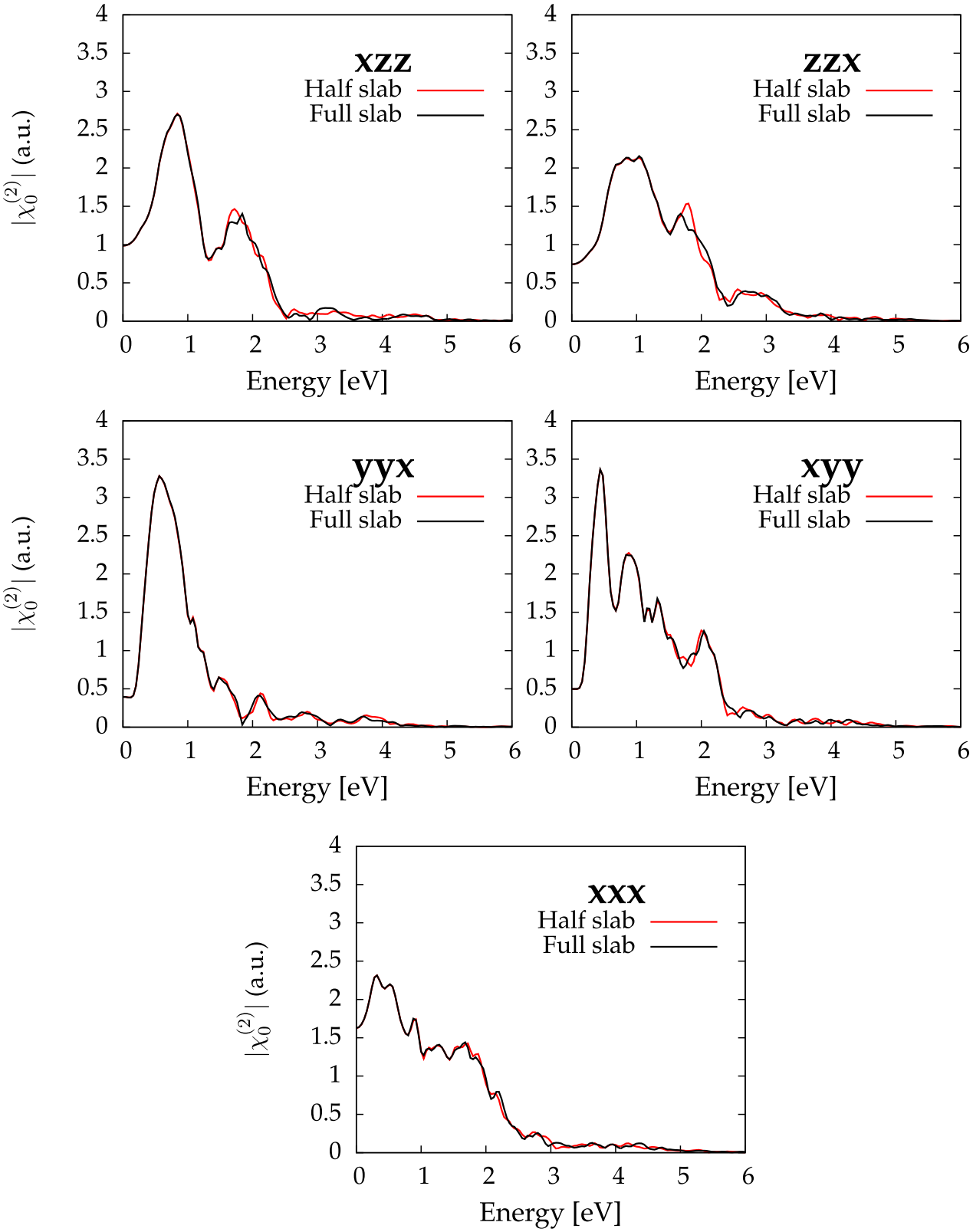

Fig. 5.4: Comparison of $|\chi_0^{(2)S}|$ for five components. Black curves: full slab calculations from a Clean-Dihydride 2x1 super-cell. Red curves: extracted half-slab calculations from a Clean-Clean symmetric super-cell.

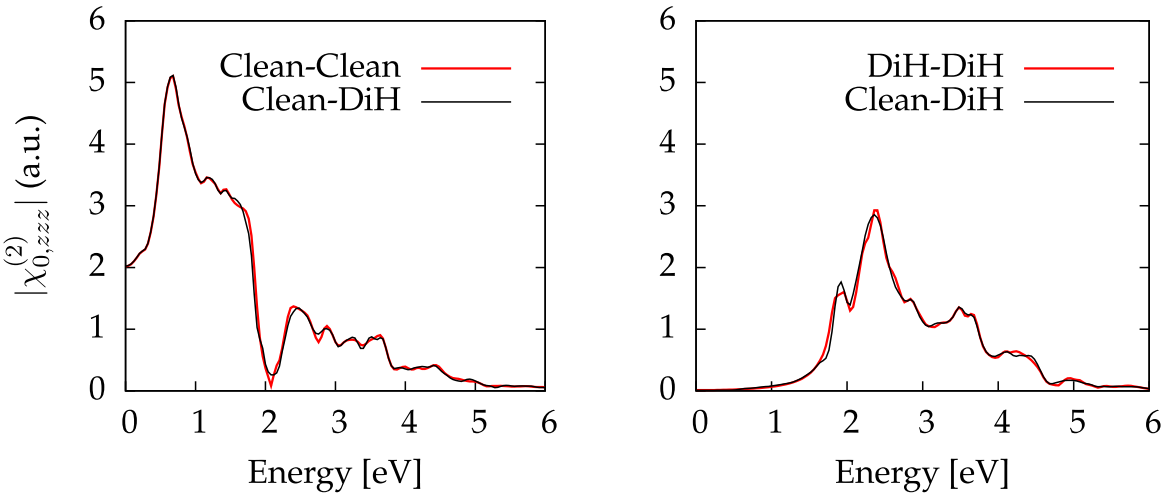

Fig. 5.5: Comparison between $|\chi^{(2)}_{0,zzz}|$ spectra for the clean (left panel) and the dihydride (right panel), extracted from a two different type of slabs. The curves are explained in the text. DiH stands for dihydride surface here.

fects between the front and back surfaces of the slab. The error introduced by the extraction (2-3%) on the spectra is rather negligible and, more importantly, smaller than the error introduced by the convergence parameters.

5.2.2 Convergence in atoms

An atomic layer is defined as a part of the slab containing atoms at the same height, or almost at the same height, in case of a surface reconstruction. For a 2×1 cell for instance, a layer is composed of 2 atoms. The slab is so divided into atomic layers. For instance, a 72 Si atoms super-cell is composed of 36 layers for the full slab or equally, 18 layers for the half-slab. Hydrogen atoms are not taken into account for layers counting and are including in the topmost layer.
The results presented up to here have always been obtained from slabs made of 36 atomic layers. Here I report the convergence in number of atomic layers for the zzz component of the clean surface. Other components are found to converge similarly in atoms and therefore are not reported here. In order to compare the spectra obtained for different number of atoms, the different spectra have been expressed in pm^2/V.

For helping the understanding of the convergence, Tab. 5.3 shows the static values of $|\chi^{(2)S}_0|$ with respect to the number of atomic layers in the half-slab. Using the criteria of less than 5% of error on static limit value, I found that the convergence is reached at 16 layers (64 atoms, ∼21.7Å); and that the spectra obtained for 12 layers (48 atoms, ∼16.3Å) is good enough to obtain quantitative results. We have checked that this result is very similar to the *ab initio* convergence in atoms, also performed during this thesis. This *ab initio* convergence can be found in Ref. [200]; where 12 atomic layers also yield a quantitative result and where 16 layers yield the converged SHG spectra.

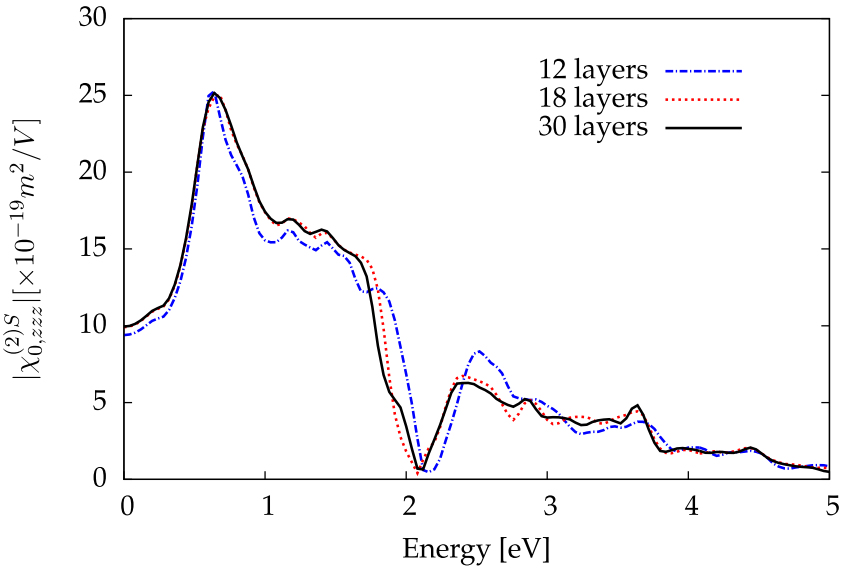

Fig. 5.6: Convergence of $|\chi^{(2)S}_{0,zzz}|$ in number of atomic layers. The numbers of layers indicated correspond to the numbers of atomic layers in half of the slab. To be converted in numbers of atoms, they have to be multiplied by 2 because the clean surface has two atoms per layer, and by another factor of 2 for the two half of the slab.

N. layers	Static value $[\times 10^{-19}$ pm^2/V]
8	7.17
10	8.70
12	9.39
14	9.07
16	9.85
18	9.91
24	9.96
30	9.95

Tab. 5.3: Static value of $|\chi^{(2)S}_{0,zzz}|$ for the clean surface.

5.2.3 Two-bands contribution

In the special case of $\alpha = \beta = \gamma$ and when the first momentum matrix element is *not* a modified momentum matrix element, the two-bands contribution, given by Eq. (5.22b), reads as

$$\chi^{2bnd}_{\alpha\alpha\alpha}(\omega) = \frac{i}{V}\sum_{nn'}\sum_{\mathbf{k}}^{BZ} \frac{f_{nm}\langle n,\mathbf{k}|p^\alpha|n',\mathbf{k}\rangle\langle n',\mathbf{k}|p^\alpha|n,\mathbf{k}\rangle\langle n',\mathbf{k}|\Delta^\alpha|n,\mathbf{k}\rangle}{E^4_{n'n}(\mathbf{k})}\left[\frac{16}{(E_{n'n}(\mathbf{k})-2\omega)} - \frac{1}{(E_{n'n}(\mathbf{k})-\omega)}\right].$$

From the time-reversal symmetry, one obtains that $\chi^{2bnd}_{\alpha\alpha\alpha}(\omega) = 0$. This property can be used in SHG codes to optimise the calculation of $\chi^{(2)}_0$ for the components such as $\alpha = \beta = \gamma$.
One could be interested by proving an equivalent result for the surface two-band contribution. In the surface case, $\langle n,\mathbf{k}|p^\alpha|n',\mathbf{k}\rangle$ is replaced by $\langle n,\mathbf{k}|\mathcal{P}^\alpha|n',\mathbf{k}\rangle$. Thus, the two momentum matrix elements are now a momentum matrix element and a modified momentum matrix element. There are no more equivalent by the time-reversal symmetry. Therefore, if we want to compute the half-slab spectra, the two-bands contribution must always be computed.

5.2.4 Symmetric or asymmetric slab

In this section, we use the fact that the half-slab and the full-slab spectra in the linear spectra differ only by a factor of 2. In Fig.5.7, a comparison between the *linear* full slab and extracted spectra of the clean Si(001) surface is reported. In the left panel, the total spectra divided by two (full slab calculation from the clean-clean slab) is compared with the extracted spectra from the clean-clean slab. In the right panel, the same total spectra divided by two is compared with the extracted spectra

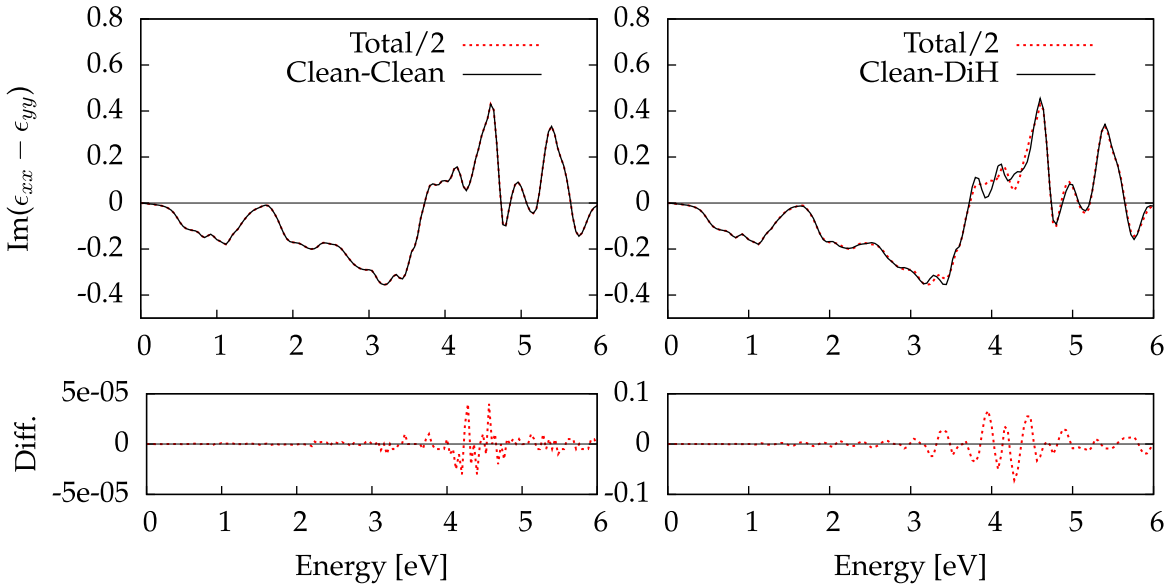

Fig. 5.7: Top panels: Comparison between linear spectra obtained from two different systems, a symmetric slab (clean-clean) and an asymmetric slab (clean-dihydride), using the tight-binding code. Total refers to full slab calculation from the clean-clean slab. Bottom panels: difference between full slab over two and half slab calculations.

from a clean-dihydride slab. The quantity reported is $Im(\epsilon_{xx} - \epsilon_{yy})$, in order to overcome the bulk contribution. The bulk being isotropic, this allows us to discuss only about the surface contribution. Notice that this quantity is close to the reflectance anisotropy spectroscopy (RAS).
In the linear case, if the spectrum is computed from a symmetric slab, *i.e.*, front and back surfaces being identical; we obtain exactly, by extraction, one half of the total spectra. This is verified in the lower left panel, showing the difference of the two spectra. This has already been pointed out, see, for instance Ref. [182]. On the contrary, if the spectrum is extracted from an asymmetric slab, there is a small but visible discrepancy between the two spectra.
Even if it is not possible to access as easily to the SHG surface spectra, we expect that using a symmetric slab leads to better results in SHG too. In Chap. 7, it is proven analytically that the slab must be chosen symmetric if one wants to be able to compute the macroscopic second-harmonic generation.

5.2.5 Tight-binding picture of Cz1

Let us consider a basis of orbitals, localized on atoms. This basis-set of orbitals is assumed to be orthogonal. Any Bloch state can be expressed in this basis as

$$|n, \mathbf{k}\rangle = \sum_i \sum_{\alpha_i} c^n_{\alpha_i}(\mathbf{k}) |\alpha, i\rangle,$$

where i refers to the atoms and α_i is the orbitals α attached to the atom i, and $c^n_{\alpha_i}(\mathbf{k})$ are the coefficients of the Bloch state $|n, \mathbf{k}\rangle$, in the orbital basis.

In this basis, a matrix element of the momentum can be written as [201, 202]

$$\langle n, \mathbf{k}|\hat{\mathbf{p}}|n', \mathbf{k}\rangle = \sum_{i,j} \sum_{\alpha_i,\beta_j} c^{n\dagger}_{\alpha_i}(\mathbf{k}) c^{n'}_{\beta_j}(\mathbf{k}) \boldsymbol{\nabla}_{\alpha_i,\beta_j}. \tag{5.24}$$

Starting from (5.3), it is possible to rewrite that formula as

$$\begin{aligned} \chi^{(2)S}_{0,abc}(\omega) &= -\frac{1}{2V\omega^3} \sum_{n,n',n'',\mathbf{k}} \frac{Im(\mathcal{P}^{Part,a}_{n,n'}(\mathbf{k})(p^b_{n',n''}(\mathbf{k})p^c_{n'',n}(\mathbf{k}) + p^c_{n',n''}(\mathbf{k})p^b_{n'',n}(\mathbf{k})))}{E_{n,\mathbf{k}} - E_{n',\mathbf{k}} + 2\omega + 2i\eta} \\ &\left[\frac{f_{nn''}}{E_{n,\mathbf{k}} - E_{n'',\mathbf{k}} + \omega + i\eta} + \frac{f_{n'n''}}{E_{n'',\mathbf{k}} - E_{n',\mathbf{k}} + \omega + i\eta}\right], \end{aligned} \tag{5.25}$$

with

$$\boldsymbol{\mathcal{P}}^{Part}_{n,n'}(\mathbf{k}) = \langle n\mathbf{k}|\mathcal{C}(z)\hat{\mathbf{p}}|n'\mathbf{k}\rangle = \sum_{i,j} C(z_i) \sum_{\alpha_i,\beta_j} c^{n\dagger}_{\alpha_i}(\mathbf{k}) c^{n'}_{\beta_j}(\mathbf{k}) \boldsymbol{\nabla}_{\alpha_i,\beta_j},$$

where $\mathcal{C}(z_i)$ is 1 if the atom i, located at the height z_i, is inside the half-slab defined by $\mathcal{C}(z)$. Here we defined $\boldsymbol{\nabla}_{\alpha_i,\beta_j} = \langle \alpha, i|\boldsymbol{\nabla}\hat{H}_0|\beta, j\rangle$. For obtaining this expression, we explicitly used the tight-binding expression of the matrix elements given by Eq. (5.24); and therefore Eq. (5.25) is only valid in the tight-binding limit.
We can now write more explicitly $\mathcal{P}^{Part,a}_{n,n'}(\mathbf{k})(v^b_{n',n''}(\mathbf{k})v^c_{n'',n}(\mathbf{k}) + v^c_{n',n''}(\mathbf{k})v^b_{n'',n}(\mathbf{k}))$ in the tight-binding formalism.
So putting all together, we get

$$\mathcal{P}^{Part,a}_{n,n'}(v^b_{n',n''}v^c_{n'',n} + v^c_{n',n''}v^b_{n'',n}) = \sum_i \mathcal{C}(z_i) \sum_j \sum_{\alpha_i\beta_j} c^{n\dagger}_{\alpha_i} c^{n'}_{\beta_j} \nabla^a_{\alpha_i\beta_j}(v^b_{n',n''}v^c_{n'',n} + v^c_{n',n''}v^b_{n'',n}). \tag{5.26}$$

Inserting Eq. (5.26) into Eq. (5.25), we obtain a formula where it appears explicitly a sum over the atoms in front of the expression, weighted by the cut-function $\mathcal{C}(z)$ evaluated at the height z_i of the atoms. Therefore $\chi^{(2)S}_0$ is constructed by adding the individual contributions of each atom. Each atom playing an independent role, we can decide how to construct a spectra. For instance, the half-slab spectra can be computed choosing $\mathcal{C}(z)$ as the indicator function of the half-slab. Or it can be constructed by adding the individual contributions of the atomic layers forming the half-slab, computed separately. Mathematically, this function $\mathcal{C}(z)$ describes a *partition over the atoms*. A direct consequence is the possibility to perform a layer-by-layer analysis of the surface second-harmonic generation spectra. Therefore in next section, I exploit this result to analyse the spatial construction of the second-harmonic spectra.

5.2.6 Spatial construction of the SHG spectra

As mentioned above, the extraction procedure results to be a partition over the atoms, and each layer can be computed and analysed separately. The main motivation of this section is the understanding of the spatial construction of the SHG spectra.

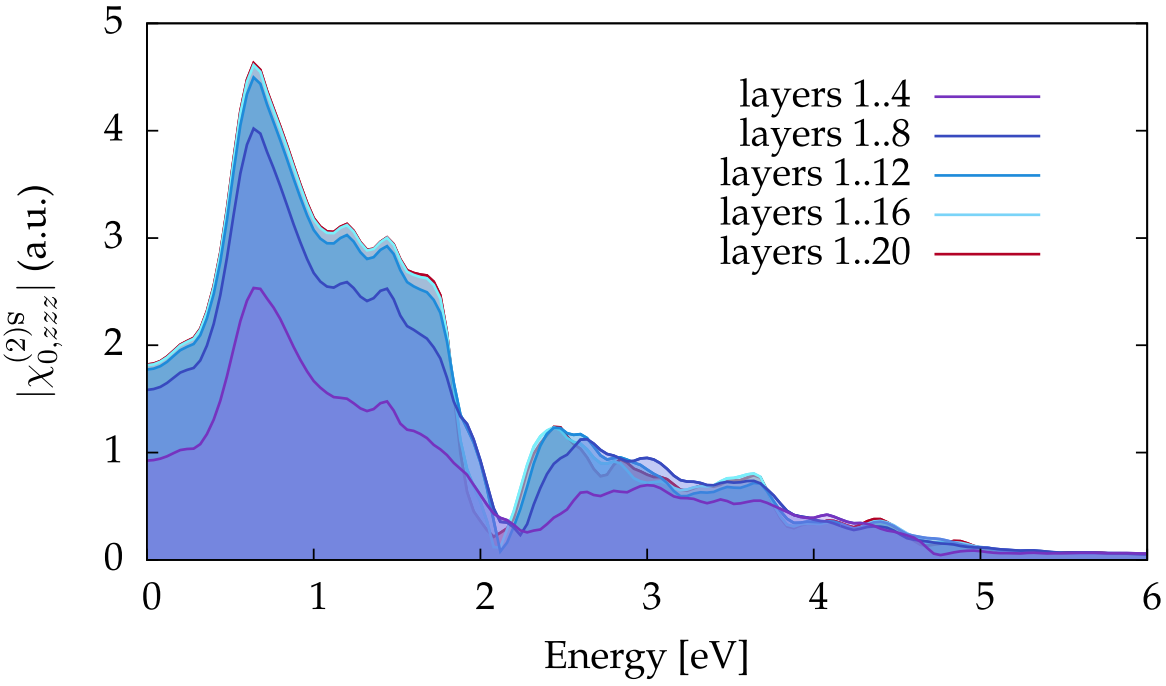

Fig. 5.8: Layer-by-layer analysis of the $|\chi^{(2)S}_{0,zzz}|$ for the clean Si(001)2×1 surface.

In Fig. 5.8, we present our layer-by-layer analysis of $|\chi^{(2)S}_{0,zzz}|$, computed for the clean silicon surface. In fact we analysed the spatial construction of the spectra. For a fixed size of the slab, we increase the number of layers contributing to the spectra, up to the half-slab. This analysis is performed on a slab containing 40 atomic layers in total. Here only blocks of 4 layers are considered, because we want to consider only block of centro-symmetric matter, to avoid possible spurious effects. This is another difference with linear case where each layer can be analysed separately (see, for instance, Ref. [192]). The spectrum quickly converges inside the material. The contribution of the atomic layers decays while going deeper in the slab, as one can expect for a spectra that originates only from the surface. The first 8 atomic layers yield already a qualitative result. Moreover, we found that the discrepancy between this spectrum and the half-slab ("layers 1..20") originates from the layers 8 to 12. The surface SHG spectrum originates mostly from the first 12 topmost layers, which corresponds to a surface region of ∼16.3Å.

The number of atoms is a major concern for atomistic simulations. Thus it is important to understand why the convergence requires so much atomic layers. Two possible reasons can explain that slow convergence in atoms. The first possibility is that the surface wave-functions spread over a wide region and this region determines the size of the slab to use in the simulations. Alternatively, the region contributing to the spectra can be wider than the extension of the surface wave-functions; due to the non-locality of the surface optical properties that allows surface-states bulk-states transitions to occur with bulk states located far from the surface. A detailed discussion on surface-bulk contributions can be found, for instance, in Ref. [203].

In order to determine which statement is correct, I have calculated the size of the region where the slab density and bulk density are different. In the vocabulary of Ref. [204], this region is called the

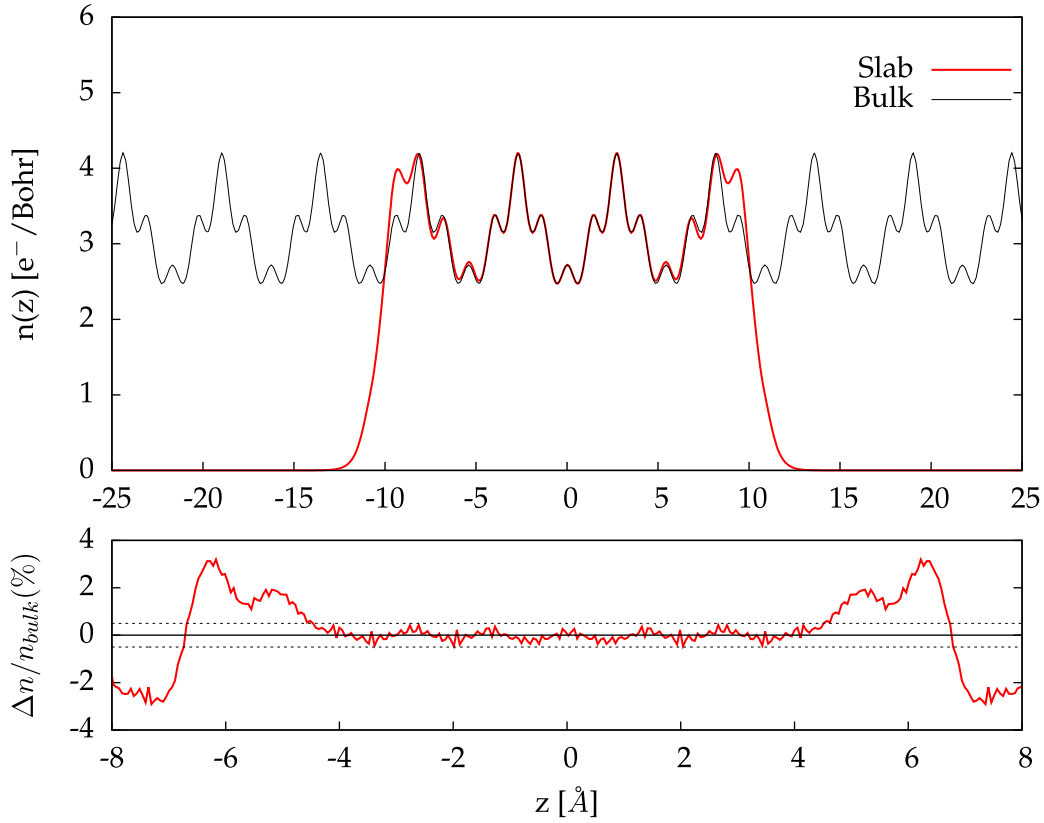

Fig. 5.9: Top panel: Variation of the number of electrons par Bohr along the z direction. This value is obtained by averaging the electronic density in the $x-y$ plan for the entire cell. Bottom panel: relative differences between the bulk and the slab densities of the above panel. Note the change in the scale. The slab is composed of 16 atomic layers in total, with asymmetric dimers as surface reconstruction on both sides.

density surface region; by opposition to the *optical* surface region, where the optical properties of the surface are different from bulk optical properties.

Using the density obtained from an *ab initio* DFT calculation, it is possible to determine the depth of the *density* surface region. In order to present quantitative results, the density has been averaged in the plane perpendicular to the surface normal. The resulting quantity is shown in Fig. 5.9. The density of the upper-most layers differs slightly from the value in the deeper layers and quickly recovers the bulk density in the deeper layers. Using as a criteria that the slab and the bulk density are identical if the relative difference is smaller than 0.5% (black dashed line, lower panel), I found that the density surface region is about 8.5 Å.[8]

By comparing this value to the *optical* surface region size (estimated above to be ∼16.3Å), we directly obtain that the *optical* surface region is wider than the *density* surface region; as already found in Ref. [205] for the semi-classical infinite barrier model. Physically, this originates from the fact that the optical properties of surfaces are non-local and by consequence, the optical response lives on a wider region than the density surface region. This allows the aforementioned bulk-states surface-states

[8]This value of 0.5% is here fixed by the numerical noise on the signal and under this value, the two signals can be considered as equal.

transitions to occur deeper inside the material than the *density* surface region. Even if the changes of the density induced by the presence of the surface (and therefore the surface wave-functions) are well described, the correct description of the optical properties of surfaces requires more layers to be converged.

Conclusions

In this chapter, I have investigated the theory behind the calculation of the surface second-harmonic generation within the super-cell approach. More precisely, we have seen how it is possible to extract the spectrum containing only the contribution of a single surface, within the independent-particle approximation.
We have first analysed the different choices offered by the literature in order to access the SHG spectra in super-cell geometry. Invoking the gauge invariance, we have reduced to one the number of possible formulae for extracting the spectra. This formula have then been derived by integrating the microscopic current over half of the slab. In the case of clean Si(001) surface, we found that when it is possible to access to the exact spectra, our method reproduce surprisingly well the correct spectra, thus validating our approach. Interestingly, we have recovered the formula adopted by the majority of the literature, validating their choice.
I have also discussed about numerical accuracy of the extraction procedure, showing that a small error of 2-3% is expected. It has been verified by tight-binding calculations on silicon surfaces that the two surfaces of a finite slab are independent. Using the fact that our approach turns to be a partition over the atoms in the tight-binding limit, we have analysed the spatial construction of the spectra, performing a layer-by-layer analysis. The calculations show that surface spectra originates from the top-most atomic layers and that the contribution decays when going far from the surface. More precisely, I found that the spectra mainly originates from the 12 topmost layers. Going further I explained that the number of atomic layers required for a converged calculation is governed by the non-locality of the response function $\chi_0^{(2)S}$ and not by the spatial extension of the surface wave-functions.

To conclude, the calculation of the surface second-harmonic generation is now based on a solid theoretical ground. Nevertheless, only the microscopic response can be described by the theory presented in this chapter. In the next chapter, the microscopic theory is improved by the inclusion of the effects of nonlocal operators. The macroscopic theory of surface second-harmonic generation is then presented in Chapter 7.

6. Effects of nonlocal operators on surface second-harmonic generation

The most used framework for *ab initio* calculations, density-functional theory within the local-density approximation [97], underestimates the energy band gap of semiconductors. It is now well understood that solving the DFT equations using a Kohn-Sham scheme should not yield the correct band-gap [88]. In this context, the so-called GW approximation [112] is known to correct the electronic gap of most semiconductors [206]. However, this can be a very expensive calculation and thus one uses the much simpler scissors operator scheme [207–209], which is still a nonlocal operator. This allows us to "open" the DFT gap to its correct experimental or GW value for most bulk semiconductors. This approximation has already been used in the calculation of the linear optical properties of surfaces [210, 211], thus improving the agreement with the experimental results.

DFT calculations are often based on the use of pseudopotentials; and as mentioned previously, this is the case for all the *ab initio* calculations of this thesis. As it will be discussed in this chapter, the presence of a nonlocal part of the pseudopotential introduces corrections to the momentum operator of the electron that have to be included with care in the surface second-harmonic susceptibility [212]. For the bulk counterpart, see, for instance, Ref. [213]. For linear optical properties of surfaces including the cut-function $\mathcal{C}(z)$, see, for instance, Ref. [121].

Therefore, within the independent-particle approximation, the most complete approach for the calculation of the surface second-harmonic susceptibility is one which includes (i) the scissors correction, (ii) the contribution of the nonlocal part of the pseudopotential, and (iii) the cut function $\mathcal{C}(z)$ introduced in the previous chapter. Therefore the goal of this chapter is to derive a new expression within the length-gauge for the surface second-harmonic susceptibility tensor that includes the aforementioned contributions. The inclusion of these three contributions opens the possibility to study surface SHG with more versatility and to provide accurate results.

Partial account of this work has already been published in Ref. [200]. Here, I give a detailed description of the theory and the method of calculation; in particular I present the evaluation of the density surface response function using perturbation theory, starting from the second-order induced current. By opposition to Ref. [200], here I do not use the density-matrix formalism. This gives an other way for obtaining the surface second-order susceptibility, but more interestingly, it opens the way to go beyond the IPA. As explained in Chap. 3, the density-density-density response function computed within the independent-particle approximation enters as the key ingredient for computing the fully-interacting density-density-density response function.

In this chapter, I first present the relevant steps for deriving the surface second-order susceptibility tensor $\chi_0^{(2)}$. This derivation includes the addition of the terms mentioned above that have been absent in previous works. Then I compare results from before and after adding the different nonlocal contributions.

6.1 Nonlocal operators and perturbation theory

6.1.1 Nonlocal operators in TDDFT

We assume the IPA, a classical electromagnetic field, quantum-mechanical matter and we neglect local-field and excitonic effects.
The unperturbed Hamiltonian, describing the system in absence of any interaction, includes in some cases nonlocal operators. As explained in the introduction of this chapter, I focus on two nonlocal operators, one originating from the pseudo-potential approximation and the second one accounting for the screening of particles inside the materials.
This unperturbed Hamiltonian is used to solve the Kohn-Sham equations (see Chap. 3). As in this thesis I work within the local-density approximation, the Hamiltonian is labelled with the corresponding LDA superscript. Any other approximation can be used (like the generalized-gradient approximation) and the derivation remains the same.
Then,

$$\hat{H}_0^{\mathrm{LDA}}(\hat{\mathbf{r}}, \hat{\mathbf{p}}) = \frac{\hat{\mathbf{p}}^2}{2} + \hat{V}_{\mathrm{eff}}(\hat{\mathbf{r}}), \tag{6.1}$$

with $\hat{\mathbf{p}} = -i\boldsymbol{\nabla}$ its canonical momentum, and $\hat{V}_{\mathrm{eff}}$ the effective potential, where we neglect spin-orbit terms.
To be general in our derivation of $\chi_0^{(2)}$, we assume a nonlocal contribution as it is customary for most pseudopotentials, and then we replace the local effective potential $\hat{V}_{\mathrm{eff}}(\hat{\mathbf{r}})$ with

$$\hat{V}_{\mathrm{eff}}(\hat{\mathbf{r}}, \hat{\mathbf{p}}) = \hat{V}^{\mathrm{l}}(\hat{\mathbf{r}}) + \hat{V}^{\mathrm{nl}}(\hat{\mathbf{r}}, \hat{\mathbf{p}}), \tag{6.2}$$

where $\hat{V}^{\mathrm{l}}(\hat{\mathbf{r}})$ and $\hat{V}^{\mathrm{nl}}(\hat{\mathbf{r}}, \hat{\mathbf{p}})$ are the local and nonlocal parts, respectively. The argument $(\hat{\mathbf{r}}, \hat{\mathbf{p}})$ is equivalent to the explicit $(\hat{\mathbf{r}}, \hat{\mathbf{r}}')$ nonlocal notation [212]. In case of a local potential, *i.e.*, $\hat{V}_{\mathrm{eff}} = \hat{V}^{\mathrm{l}}(\hat{\mathbf{r}})$, like that of all-electron schemes, we simply omit the contribution of $\hat{V}^{\mathrm{nl}}(\hat{\mathbf{r}}, \hat{\mathbf{p}})$ from the results that we have derived.
It is well known that the use of the LDA leads to an underestimation of the band-gap. A standard procedure to correct for this is to use the "scissors approximation", where the conduction bands are rigidly shifted in energy so that the band-gap corresponds to the accepted experimental electronic band-gap [207–209]. This is often in fairly good agreement with the GW band-gap based on a more sophisticated calculation [214]. The LDA wave-functions are used since they produce band structures with dispersion relations similar to those predicted by the GW approximation. One might wonder if this approximation is still valid for the surface states. Taking the clean Si(001) surface as an example, one clearly see in Fig. 6.1 that the GW surface states exhibit the same dispersion as the LDA ones. Mathematically, the scissors operator $\hat{S}$ is a nonlocal operator which is added to the unperturbed or

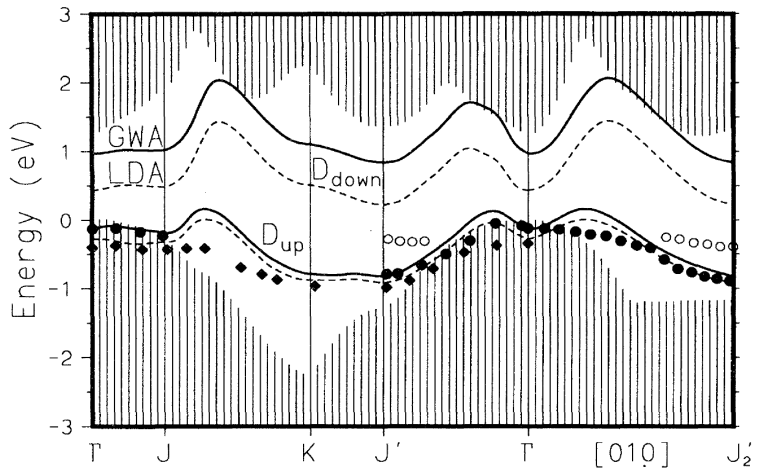

Fig. 6.1: Calculated surface states of Si(001)2×1 using LDA (dashed lines) and GW (solid lines). Symbols corresponds to photoemission experiments [215]. Reproduced from [215].

unscissored Hamiltonian H_0^{LDA},

$$\hat{H}_0^{\Sigma}(\hat{\mathbf{r}},\hat{\mathbf{p}}) = \hat{H}_0^{\mathrm{LDA}}(\hat{\mathbf{r}},\hat{\mathbf{p}}) + \hat{S}(\hat{\mathbf{r}},\hat{\mathbf{p}}), \tag{6.3}$$

where

$$\hat{S}(\hat{\mathbf{r}},\hat{\mathbf{p}}) = \Delta \sum_n \sum_{\mathbf{k}}^{BZ} (1 - f_{n,\mathbf{k}}) |n,\mathbf{k}\rangle\langle n,\mathbf{k}|, \tag{6.4}$$

with Δ the rigid ($\mathbf{k}$-independent) energy correction to be applied. The unscissored and scissored Hamiltonians satisfy

$$\begin{aligned} H_0^{\mathrm{LDA}}(\hat{\mathbf{r}},\hat{\mathbf{p}})\phi_{n,\mathbf{k}}(\hat{\mathbf{r}}) &= E_n(\mathbf{k})\phi_{n,\mathbf{k}}(\hat{\mathbf{r}}), \\ H_0^{\Sigma}(\hat{\mathbf{r}},\hat{\mathbf{p}})\phi_{n,\mathbf{k}}(\hat{\mathbf{r}}) &= E_n^{\Sigma}(\mathbf{k})\phi_{n,\mathbf{k}}(\hat{\mathbf{r}}), \end{aligned}$$

where the scissor-shifted energies $E_n^{\Sigma}(\mathbf{k})$ are given by

$$E_n^{\Sigma}(\mathbf{k}) = E_n(\mathbf{k}) + (1 - f_{n,\mathbf{k}})\Delta.$$

We emphasize that the scissored and unscissored Hamiltonians have the same eigenfunctions, where $\phi_{n,\mathbf{k}}(\hat{\mathbf{r}}) = \langle\hat{\mathbf{r}}|n,\mathbf{k}\rangle = e^{i\mathbf{k}.\hat{\mathbf{r}}}u_{n,\mathbf{k}}(\hat{\mathbf{r}})$, are the real-space representations of the Bloch states $|n,\mathbf{k}\rangle$ labelled by the band index n and the crystal momentum $\mathbf{k}$, and $u_{n,\mathbf{k}}(\hat{\mathbf{r}})$ are cell-periodic.

6.1.2 Coupling nonlocal operators to the electromagnetic field

In presence of a nonlocal operator, the treatment of the coupling to the electromagnetic field requires great care.

Let us consider the total single-electron Hamiltonian $\hat{H}(t)$ that reads as

$$\hat{H}(t) = \hat{H}_0 + \hat{H}_I(t),$$

where H_0 is the unperturbed one-particle time-independent Hamiltonian (see Eq. 6.3), and $H_I(t)$ is the time-dependent potential energy due to the interaction of the electron with the perturbing electromagnetic field.
The interaction Hamiltonian in the presence of a nonlocal potential $\hat{V}^{\rm nl}$ is given by [212]

$$\hat{H}_I(t) = \hat{\phi}^P(t) - \frac{1}{2c}\left[\hat{\mathbf{p}}\hat{\mathbf{A}}^P(t) + \hat{\mathbf{A}}^P(t)\hat{\mathbf{p}}\right] + \frac{1}{2c^2}\hat{A}^P(t)^2 + \hat{V}^A_{\rm nl}(t), \tag{6.5}$$

where ϕ^P is the scalar potential, $\mathbf{A}^P$ the vector potential, and

$$\langle \mathbf{r}|\hat{V}^A_{\rm nl}|\mathbf{r}'\rangle = V^{\rm nl}(\mathbf{r},\mathbf{r}')\sum_{k=1}^{\infty}\frac{1}{k!}\left(\frac{i}{c}\int_{\mathbf{r}'}^{\mathbf{r}}\mathbf{A}^P(\mathbf{x},t).\,d\mathbf{x}\right)^k. \tag{6.6}$$

Here, we are interested in a perturbative treatment of the interaction, therefore, the interaction Hamiltonian is expanded in power of $\mathbf{A}^P(\hat{\mathbf{r}},t)$.
First- and second-order terms, which are required to treat the linear and the second-order nonlinear optical properties, are given by

$$\begin{aligned}
H_I^{(1)}(\mathbf{r},\mathbf{r}',t) &= \phi^P(\mathbf{r},t) - \frac{1}{2c}\left[\mathbf{p}\mathbf{A}^P(\mathbf{r},t) + \mathbf{A}^P(\mathbf{r},t)\mathbf{p}\right] + V_{\rm nl}(\mathbf{r},\mathbf{r}')\frac{i}{c}\int_{\mathbf{r}'}^{\mathbf{r}}\mathbf{A}^P(\mathbf{x},t).\,d\mathbf{x},\\
H_I^{(2)}(\mathbf{r},\mathbf{r}',t) &= \frac{1}{2c^2}A^P(\mathbf{r},t)^2 - V_{\rm nl}(\mathbf{r},\mathbf{r}')\frac{1}{c^2}\left(\int_{\mathbf{r}'}^{\mathbf{r}}\mathbf{A}^P(\mathbf{x},t).\,d\mathbf{x}\right)^2.
\end{aligned}$$

To overcome integrals, I assume the long-wavelength limit; which corresponds to the replacement $\mathbf{A}^P(\mathbf{r},t) \rightarrow \mathbf{A}^P(t)$. Using the fact that $\hat{V}^{\rm nl}(\mathbf{r},\mathbf{r}')(\mathbf{r}-\mathbf{r}') = [\hat{\mathbf{r}},\hat{V}^{\rm nl}]$ and using the definition of the velocity operator $\hat{\mathbf{v}} = \hat{\mathbf{p}} - i[\hat{\mathbf{r}},\hat{V}^{\rm nl}]$, we obtain after simple algebra that

$$\begin{aligned}
\hat{H}_I^{(1)}(t) &= \phi^P(t) - \frac{1}{c}\hat{\mathbf{v}}\mathbf{A}^P(t),\\
\hat{H}_I^{(2)}(t) &= \frac{-i}{2c^2}[\mathbf{A}^P(t)\hat{\mathbf{r}},\mathbf{A}^P(t)\hat{\mathbf{v}}].
\end{aligned} \tag{6.7}$$

These two expressions are very close to the usual one, obtained in absence of nonlocal operators. Here as a result, one obtains that in presence of nonlocal operators, the momentum operator $\hat{\mathbf{p}}$ must be replaced by the velocity operator $\hat{\mathbf{v}}$ in the expression of the first- and second-order terms of the interaction Hamiltonian.
Knowing the first- and second-order interaction Hamiltonians, it is possible to derive from perturbation theory, the expression of the second-order susceptibility. This is the aim of the next section.

6.1.3 Surface second-order susceptibility

In order to derive an expression for the density-density-density response function, two ways are possible. On the one hand, it is possible to derive the surface response function from the second-order density. The formula is simple to obtain but taking analytically the long-wavelength limit is quite complicated to handle. On the other hand, it is possible to derive the expression for the surface response function from the second-order induced current. Taking the long-wavelength limit of this expression is almost straightforward but the obtained expression is apparently divergent as $\frac{1}{\omega^3}$, and must be worked out if one want to use it in practice. We know that for going beyond the IPA in the framework of TDDFT, the density response function is needed; but we also know that from gauge-invariance, the two quantities are related. Then, we decided to use the current-current-current response function as a starting point, for taking the long-wavelength limit.

The second-order induced current is related to the electric field by

$$\mathbf{j}^{(2)}_{\text{ind}}(\mathbf{r};2\omega) = -i2\omega \int d\mathbf{r}' d\mathbf{r}'' \tilde{\alpha}^{(2)}(\mathbf{r},\mathbf{r}',\mathbf{r}'';\omega,\omega)\mathbf{E}^P(\mathbf{r}';\omega)\mathbf{E}^P(\mathbf{r}'';\omega), \tag{6.8}$$

where $\tilde{\alpha}^{(2)}$ is the second-order quasi-polarisability [41]. Here $\mathbf{E}^P$ is the perturbing field as defined by Eq. (1.3). Notice that in the case of longitudinal fields, this field is exactly the external field $\mathbf{E}^{\text{ext}}$.
The *surface* induced current is obtain by replacing $\mathbf{j}^{(2)}_{\text{ind}}(\mathbf{r};2\omega)$ by $\mathcal{C}(z)\mathbf{j}^{(2)}_{\text{ind}}(\mathbf{r};2\omega)$. The surface quasipolarisability is then related, in reciprocal space and within the optical limit, to the independent-particle density-density-density response function by

$$\hat{\mathbf{q}}\tilde{\alpha}^{S(2)}(0,0,0;\omega,\omega)\hat{\mathbf{q}}_{\mathbf{1}}\hat{\mathbf{q}}_{\mathbf{2}} = \frac{-i}{4}\chi^{(0)S}_{\rho\rho\rho}(\hat{\mathbf{q}},\hat{\mathbf{q}}_{\mathbf{1}},\hat{\mathbf{q}}_{\mathbf{2}};\omega,\omega), \tag{6.9}$$

with $\mathbf{q} = \mathbf{q}_1 + \mathbf{q}_2$ and $\hat{\mathbf{q}} = \frac{\mathbf{q}}{q}$.
From perturbation theory, and using the expressions Eqs. (6.7), we obtain that

$$\begin{aligned}
\chi^{(0)S}_{\rho\rho\rho}(\hat{\mathbf{q}},\hat{\mathbf{q}}_{\mathbf{1}},\hat{\mathbf{q}}_{\mathbf{2}};\omega,\omega) = \frac{-2}{V\omega^3}\sum_{nn'n''}\sum_{\mathbf{k}}^{BZ} & \frac{\langle n,\mathbf{k}|\hat{\mathbf{q}}\mathcal{V}^{\mathbf{\Sigma}}|n',\mathbf{k}\rangle\langle n',\mathbf{k}|\hat{\mathbf{q}}_{\mathbf{1}}\hat{\mathbf{v}}^{\mathbf{\Sigma}}|n'',\mathbf{k}\rangle\langle n'',\mathbf{k}|\hat{\mathbf{q}}_{\mathbf{2}}\hat{\mathbf{v}}^{\mathbf{\Sigma}}|n,\mathbf{k}\rangle}{(E^{\Sigma}_{n,\mathbf{k}} - E^{\Sigma}_{n',\mathbf{k}} + 2\omega + 2i\eta)} \\
& \left\{ \frac{(f_{n,\mathbf{k}} - f_{n'',\mathbf{k}})}{(E^{\Sigma}_{n,\mathbf{k}} - E^{\Sigma}_{n'',\mathbf{k}} + \omega + i\eta)} + \frac{(f_{n',\mathbf{k}} - f_{n'',\mathbf{k}})}{(E^{\Sigma}_{n'',\mathbf{k}} - E^{\Sigma}_{n',\mathbf{k}} + \omega + i\eta)} \right\} \\
+\frac{2i}{V\omega^3}\sum_{nn'}\sum_{\mathbf{k}}^{BZ}(f_{n,\mathbf{k}} - f_{n',\mathbf{k}}) & \frac{\langle n,\mathbf{k}|\left[\hat{\mathbf{q}}\mathcal{R},\hat{\mathbf{q}}_{\mathbf{1}}\hat{\mathbf{v}}^{\mathbf{\Sigma}}\right]|n',\mathbf{k}\rangle\langle n',\mathbf{k}|\hat{\mathbf{q}}_{\mathbf{2}}\hat{\mathbf{v}}^{\mathbf{\Sigma}}|n,\mathbf{k}\rangle}{(E^{\Sigma}_{n,\mathbf{k}} - E^{\Sigma}_{n',\mathbf{k}} + \omega + i\eta)} \\
+\frac{i}{V\omega^3}\sum_{nn'}\sum_{\mathbf{k}}^{BZ}(f_{n,\mathbf{k}} - f_{n',\mathbf{k}}) & \frac{\langle n,\mathbf{k}|\hat{\mathbf{q}}\mathcal{V}^{\mathbf{\Sigma}}|n',\mathbf{k}\rangle\langle n',\mathbf{k}|\left[\hat{\mathbf{q}}_{\mathbf{1}}\hat{\mathbf{r}},\hat{\mathbf{q}}_{\mathbf{2}}\hat{\mathbf{v}}^{\mathbf{\Sigma}}\right]|n,\mathbf{k}\rangle}{(E^{\Sigma}_{n,\mathbf{k}} - E^{\Sigma}_{n',\mathbf{k}} + 2\omega + 2i\eta)} \\
+\frac{1}{V\omega^3}\sum_{n}\sum_{\mathbf{k}}^{BZ} & f_{n,\mathbf{k}}\langle n,\mathbf{k}|\left[\hat{\mathbf{q}}\hat{\mathbf{r}},\left[\hat{\mathbf{q}}_{\mathbf{1}}\hat{\mathbf{r}},\hat{\mathbf{q}}_{\mathbf{2}}\mathcal{V}^{\mathbf{\Sigma}}\right]\right]|n,\mathbf{k}\rangle + (\hat{\mathbf{q}}_{\mathbf{1}} \leftrightarrow \hat{\mathbf{q}}_{\mathbf{2}}),
\end{aligned} \tag{6.10}$$

where we have introduced the following definitions

$$\begin{aligned} \boldsymbol{\mathcal{V}}^{\boldsymbol{\Sigma}} &= \frac{\hat{\mathbf{v}}^{\boldsymbol{\Sigma}}\mathcal{C}(z) + \mathcal{C}(z)\hat{\mathbf{v}}^{\boldsymbol{\Sigma}}}{2}, \\ \boldsymbol{\mathcal{R}} &= \mathcal{C}(z)\hat{\mathbf{r}}. \end{aligned} \tag{6.11}$$

In presence of the nonlocal part of the pseudopotential and a scissors operator, the velocity $\hat{\mathbf{v}}^{\boldsymbol{\Sigma}}$ is given by

$$\begin{aligned} \hat{\mathbf{v}}^{\boldsymbol{\Sigma}} &= \hat{\mathbf{p}} + \hat{\mathbf{v}}^{\mathrm{nl}} + \hat{\mathbf{v}}^{\mathbf{S}} = \hat{\mathbf{v}} + \hat{\mathbf{v}}^{\mathbf{S}}, \\ \hat{\mathbf{v}}^{\mathrm{nl}} &= -i[\hat{\mathbf{r}}, \hat{V}^{\mathrm{nl}}], \\ \hat{\mathbf{v}}^{\mathbf{S}} &= -i[\hat{\mathbf{r}}, \hat{S}]. \end{aligned} \tag{6.12}$$

It is important to note first that in absence of any nonlocal operator, the Eq. (6.10) reduces to its first term only; which is the expression previously obtained (see Eq. 5.3). By opposition to the expressions of the interaction Hamiltonian, where the nonlocal operators accounts only for the replacement $\hat{\mathbf{p}} \rightarrow \hat{\mathbf{v}}^{\boldsymbol{\Sigma}}$, in the case of the surface susceptibilities, extra-terms must be including.
Even if Eq. (6.10) allows us in principle to compute the surface density-density-density response function, this expression is not satisfactory for two reasons. i) The expression Eq. (6.10) is apparently divergent as $\frac{1}{\omega^3}$; which prohibits numerical implementations. ii) This expression contains matrix elements of $\hat{\mathbf{v}}^{\boldsymbol{\Sigma}}$. This last remark comes from the fact that the matrix elements of $\hat{\mathbf{v}}$ and $\hat{\mathbf{v}}^{\boldsymbol{\Sigma}}$ (as defined by Eq. (6.12)) are related each others

$$\hat{\mathbf{r}}_{nn'}(\mathbf{k}) = \frac{\hat{\mathbf{v}}^{\boldsymbol{\Sigma}}_{nn'}}{iE^{\Sigma}_{nn'}(\mathbf{k})} = \frac{\hat{\mathbf{v}}_{nn'}}{iE_{nn'}(\mathbf{k})}, \qquad n \notin \mathcal{D}_{n'},$$

where we defined $E^{\Sigma}_{nm}(\mathbf{k}) = E^{\Sigma}_{n}(\mathbf{k}) - E^{\Sigma}_{m}(\mathbf{k})$ and $\mathcal{D}_m$ are all the possible degenerate m-states.
After tedious algebra, reported in App. E, one finally obtains a non-divergent expression of the surface second-order susceptibility, where the matrix elements of $\hat{\mathbf{v}}^{\boldsymbol{\Sigma}}$ have been analytically replaced by matrix elements of $\hat{\mathbf{v}}$. The final expression reads as

$$\chi^{(0)S}_{\rho\rho\rho} = \chi^{3bnd}_{I} + \chi^{3bnd}_{II} + \chi^{2bnd}_{l} + \chi^{2bnd}_{\mathrm{nl}}, \tag{6.13}$$

where

$$\begin{aligned} \chi^{3bnd}_{I}(\hat{\mathbf{q}}, \hat{\mathbf{q}}_{\mathbf{1}}, \hat{\mathbf{q}}_{\mathbf{2}}, \omega, \omega) = \frac{2i}{V} \sum_{n\neq n'\neq n''} \sum_{\mathbf{k}}^{BZ} &\langle n, \mathbf{k}|\hat{\mathbf{q}}\boldsymbol{\mathcal{R}}|n', \mathbf{k}\rangle\langle n', \mathbf{k}|\hat{\mathbf{q}}_{\mathbf{1}}\hat{\mathbf{r}}|n'', \mathbf{k}\rangle\langle n'', \mathbf{k}|\hat{\mathbf{q}}_{\mathbf{2}}\hat{\mathbf{r}}|n, \mathbf{k}\rangle \\ &\times \Bigg\{ \frac{(E_{n,\mathbf{k}} + E_{n',\mathbf{k}} - 2E_{n'',\mathbf{k}})}{E_{nn'}(\mathbf{k})} \frac{4(f_{n,\mathbf{k}} - f_{n',\mathbf{k}})}{E^{\Sigma}_{nn'}(\mathbf{k})(E^{\Sigma}_{nn'}(\mathbf{k}) + 2\omega + i\eta)} \\ &\quad + \frac{(2E_{n,\mathbf{k}} - E_{n',\mathbf{k}} - E_{n'',\mathbf{k}})}{E_{n''n}(\mathbf{k})} \frac{(f_{n,\mathbf{k}} - f_{n'',\mathbf{k}})}{E^{\Sigma}_{nn''}(\mathbf{k})(E^{\Sigma}_{nn''}(\mathbf{k}) + \omega + i\eta)} \\ &+ \frac{(2E_{n',\mathbf{k}} - E_{n,\mathbf{k}} - E_{n'',\mathbf{k}})}{E_{n'n''}(\mathbf{k})} \frac{(f_{n',\mathbf{k}} - f_{n'',\mathbf{k}})}{E^{\Sigma}_{n'n''}(\mathbf{k})(E^{\Sigma}_{n''n'}(\mathbf{k}) + \omega + i\eta)} \Bigg\} + (\hat{\mathbf{q}}_{\mathbf{1}} \leftrightarrow \hat{\mathbf{q}}_{\mathbf{2}}) \end{aligned} \tag{6.14a}$$

$$\chi_{II}^{3bnd}(\hat{\mathbf{q}},\hat{\mathbf{q}}_1,\hat{\mathbf{q}}_2;\omega,\omega)=\frac{4i}{V}\sum_{n\neq n'\neq n''}\sum_{\mathbf{k}}^{BZ}\frac{\langle n,\mathbf{k}|\hat{\mathbf{q}}\boldsymbol{\mathcal{R}}|n',\mathbf{k}\rangle\langle n',\mathbf{k}|\hat{\mathbf{q}}_1\hat{\mathbf{r}}|n'',\mathbf{k}\rangle\langle n'',\mathbf{k}|\hat{\mathbf{q}}_2\hat{\mathbf{r}}|n,\mathbf{k}\rangle}{(2E^{\Sigma}_{n''n}(\mathbf{k})-E^{\Sigma}_{n'n}(\mathbf{k}))}$$

$$\times\left\{\frac{2(f_{n,\mathbf{k}}-f_{n',\mathbf{k}})}{(E^{\Sigma}_{nn'}(\mathbf{k})+2\omega+2i\eta)}-\frac{(f_{n,\mathbf{k}}-f_{n'',\mathbf{k}})}{(E^{\Sigma}_{nn''}(\mathbf{k})+\omega+i\eta)}+\frac{(f_{n',\mathbf{k}}-f_{n'',\mathbf{k}})}{(E^{\Sigma}_{n''n'}(\mathbf{k})+\omega+i\eta)}\right\}+(\hat{\mathbf{q}}_1\leftrightarrow\hat{\mathbf{q}}_2) \quad (6.14b)$$

$$\chi_{l}^{2bnd}(\hat{\mathbf{q}},\hat{\mathbf{q}}_1,\hat{\mathbf{q}}_2;\omega,\omega)=\frac{-2}{V}\sum_{n\neq n'}\sum_{\mathbf{k}}^{BZ}(f_{n,\mathbf{k}}-f_{n',\mathbf{k}})\frac{\langle n,\mathbf{k}|\hat{\mathbf{q}}\boldsymbol{\mathcal{R}}|n',\mathbf{k}\rangle\langle n',\mathbf{k}|\hat{\mathbf{q}}_1\hat{\mathbf{r}}|n,\mathbf{k}\rangle\hat{\mathbf{q}}_2\boldsymbol{\Delta}_{n'n}}{E^{\Sigma}_{nn'}(\mathbf{k})^2}$$

$$\times\left\{\frac{8(E_{nn'}(\mathbf{k})+E^{\Sigma}_{nn'}(\mathbf{k}))}{E^{\Sigma}_{nn'}(\mathbf{k})(E^{\Sigma}_{nn'}(\mathbf{k})+2\omega+2i\eta)}+\frac{(2E_{nn'}(\mathbf{k})-E^{\Sigma}_{nn'}(\mathbf{k}))}{E^{\Sigma}_{nn'}(\mathbf{k})(E^{\Sigma}_{nn'}(\mathbf{k})+\omega+i\eta)}\right\}+(\hat{\mathbf{q}}_1\leftrightarrow\hat{\mathbf{q}}_2) \quad (6.14c)$$

$$\chi_{\mathrm{nl}}^{2bnd}(\hat{\mathbf{q}},\hat{\mathbf{q}}_1,\hat{\mathbf{q}}_2;\omega,\omega)=\frac{-2}{V}\sum_{nn'}\sum_{\mathbf{k}}^{BZ}\frac{(f_{n,\mathbf{k}}-f_{n',\mathbf{k}})}{E_{nn'}(\mathbf{k})E^{\Sigma}_{nn'}(\mathbf{k})}\left\{\frac{\langle n,\mathbf{k}|[\hat{\mathbf{q}}\boldsymbol{\mathcal{R}},\hat{\mathbf{q}}_1\hat{\mathbf{v}}]|n',\mathbf{k}\rangle\langle n',\mathbf{k}|\hat{\mathbf{q}}_2\hat{\mathbf{r}}|n,\mathbf{k}\rangle}{(E^{\Sigma}_{nn'}(\mathbf{k})+\omega+i\eta)}\right.$$

$$\left.+\frac{4\langle n,\mathbf{k}|\hat{\mathbf{q}}\boldsymbol{\mathcal{R}}|n',\mathbf{k}\rangle\langle n,\mathbf{k}|[\hat{\mathbf{q}}_1\hat{\mathbf{r}},\hat{\mathbf{q}}_2\hat{\mathbf{v}}]|n',\mathbf{k}\rangle}{(E^{\Sigma}_{nn'}(\mathbf{k})+2\omega+i\eta)}\right\}+(\hat{\mathbf{q}}_1\leftrightarrow\hat{\mathbf{q}}_2) \quad (6.14d)$$

where we defined $\boldsymbol{\Delta}_{n'n}=\hat{\mathbf{v}}_{n'n'}-\hat{\mathbf{v}}_{nn}$ and

$$\langle n,\mathbf{k}|\boldsymbol{\mathcal{R}}|n',\mathbf{k}\rangle=\frac{\langle n,\mathbf{k}|\boldsymbol{\mathcal{V}}|n',\mathbf{k}\rangle}{iE_{nn'}(\mathbf{k})},\qquad n\notin D_m.$$

It is interesting to note that each specific contribution incorporated in that expressions (the scissors operator, the nonlocal part of the pseudo-potential, and the cut-function $\mathcal{C}(z)$) play separate and independent roles. The cut-function $\mathcal{C}(z)$ here only affects the matrix element related to $\mathbf{q}$. The scissors operator only affects the energies and finally, the nonlocal part of the pseudo-potential is accounted for by computing matrix elements of $\hat{\mathbf{v}}$, instead of $\hat{\mathbf{p}}$.

As already pointed out in Ref. [41] for the bulk susceptibility, the scissored and unscissored energies are both present in the expression of $\chi^{(0)S}_{\rho\rho\rho}$, showing that the scissors operator is non-trivial for second-order susceptibility.

By opposition, the expression for the surface first-order density response function $\chi^{(0)S}_{\rho\rho}$ is given by

$$\chi^{(0)S}_{\rho\rho}(\hat{\mathbf{q}};\omega)=\frac{1}{V}\sum_{nn'}\sum_{\mathbf{k}}^{BZ}(f_{n,\mathbf{k}}-f_{n',\mathbf{k}})\frac{\langle n,\mathbf{k}|\hat{\mathbf{q}}\boldsymbol{\mathcal{R}}|n',\mathbf{k}\rangle\langle n',\mathbf{k}|\hat{\mathbf{q}}\hat{\mathbf{r}}|n,\mathbf{k}\rangle}{(E^{\Sigma}_{n,\mathbf{k}}-E^{\Sigma}_{n',\mathbf{k}}+\omega+i\eta)}, \quad (6.15)$$

where only scissored energies appear, resulting in a rigid shift of the spectra by Δ.

The expression of the second-order susceptibility is now satisfactory for various reasons. First, because this form is non-divergent. Second, for practical implementations, the scissors and the nonlocal part of the pseudo-potential can be easily switch on and off by replacing $E^{\Sigma}_{n}(\mathbf{k})$ by $E_n(\mathbf{k})$ in the first case and $\hat{\mathbf{v}}$ by $\hat{\mathbf{p}}$ in the second. Finally, the bulk formula is obtained by replacing $\mathcal{R}$ by $\hat{\mathbf{r}}$. Thus, by implementing only one formula, it is possible to treat easily all the possible different combinations of the three contributions. This is that expression which has been implemented in the TDDFT code 2light [117]. The analytical expression of $\boldsymbol{\mathcal{V}}$ is given in App. D.

6.2 Numerical results

The self-consistent ground-state and the Kohn-Sham states were calculated using the plane-wave ABINIT code [115]. We used Troullier-Martins pseudopotentials [216] that are fully separable nonlocal pseudopotentials in the Kleinman-Bylander form [120]. The contribution of the nonlocal part of the pseudo-potential to $\hat{\mathbf{v}}$ and $\mathcal{V}$ is carried out using the DP code [116].
The vacuum size is equivalent to one quarter the size of the slab, avoiding the effects produced by possible interaction between the replicas of the slab always present in the repeated super-cell scheme [217].
Spin-orbit, local-field, and electron-hole attraction effects on the SHG process are all neglected at this point. Although these are important factors in the optical response of a semiconductor, their efficient calculation is theoretically and numerically challenging. They will be treated later in this thesis. In order to obtain $\chi^{2bnd}_{\rm nl}$, we must evaluate the commutator of $\hat{\mathbf{r}}$ and $\hat{\mathbf{v}}^{\rm nl}$. Computing second-order derivatives of the nonlocal part of the pseudo-potential is required thus making the numerical procedure very time consuming. This adds significantly to the already lengthy time needed for the calculation of the $\hat{\mathbf{v}}^{\rm nl}$ contribution that is proportional only to the first order derivatives. Memory requirements are also increased for both $\hat{\mathbf{v}}^{\rm nl}$ and $[\hat{\mathbf{r}}, \hat{\mathbf{v}}^{\rm nl}]$. However, the contribution from $[\hat{\mathbf{r}}, \hat{\mathbf{v}}^{\rm nl}]$ is very small [218] and therefore we neglect entirely $\chi^{2bnd}_{\rm nl}$ from now on.[1]

For a given slab of 32 atomic layers, we find the converged spectra to obtain the relevant parameters. The most important of these are: an energy cutoff of 10 Ha, an equal number of conduction and valence bands, and a set of 244 $\mathbf{k}$-points. The $\mathbf{k}$-points are used for the linear analytic tetrahedron method for evaluating the 3D Brillouin-zone (BZ) integrals where special care was taken to examine the double resonances of Eq. (6.14) [219]. Note that the Brillouin zone for the slab geometry collapses to a 2D zone, with only one $\mathbf{k}$-point along the z axis. All spectra were calculated with a Gaussian smearing of 0.15 eV. The reader should note that numerical results presented here are the same results as published in Ref. [200].

6.2.1 Half-slab vs. full slab

In Fig. 6.2, we compare $\chi^{\rm fullslab}_{0,xxx}$ versus $\chi^{\rm half-slab}_{0,xxx}$ for the four different possibilities between including or not including the effects of $\hat{\mathbf{v}}^{\rm nl}$ or the scissors correction Δ. For these results, we chose Δ= 0.5 eV, that is, the GW gap reported in Refs. [215, 220]. This is justified by the fact that the surface states of the clean Si(001) surface are rigidly shifted and maintain their dispersion relation with respect to LDA according to the GW calculations of Ref. [220]. We see that for all four instances the difference between responses is quite small. Indeed, when the value $|\chi^{(2)}_{0,xxx}|$ is large, the difference between the two is very small; when the value is small the difference increases only slightly, but the spectra is so close to zero that it is negligible. These differences would decrease as the number of atomic layers increases. As already explained in the previous chapter, we remark here that 32 layers in the slab is more than enough to confirm that the extraction of the surface second-harmonic susceptibility from the 2×1 surface is readily possible using the formalism contained in Eq. (6.13).

[1] This approximation is valid for $[\hat{\mathbf{r}}, \hat{\mathbf{v}}^{\rm nl}]$ but could not be applied to $[\hat{\mathbf{r}}, \hat{\mathbf{v}}^{\mathbf{S}}]$. This is why it is important to first replace analytically $\hat{\mathbf{v}}^{\mathbf{\Sigma}}$ by $\hat{\mathbf{v}}$.

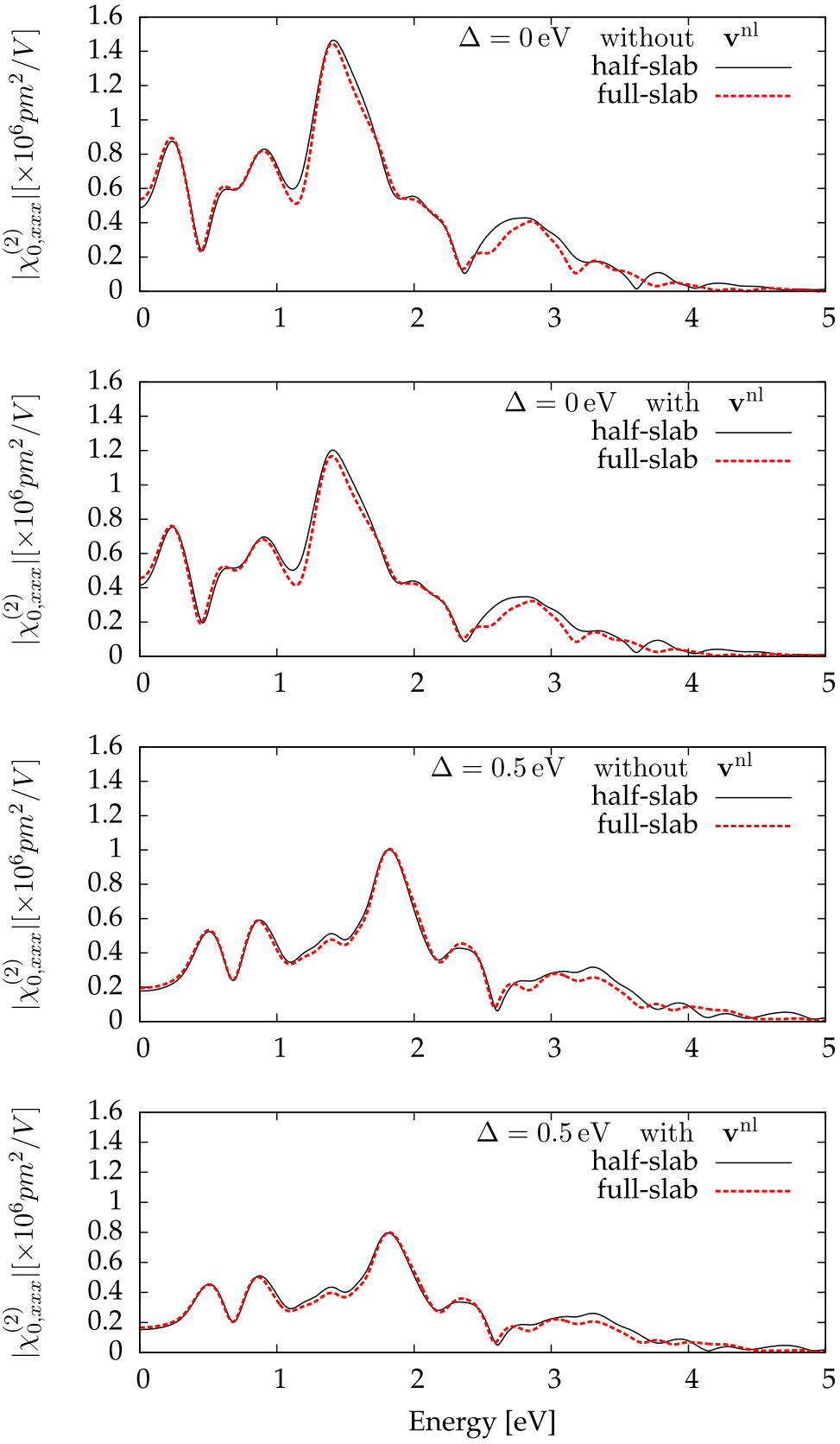

Fig. 6.2: *ab initio* spectra of $\chi^{\mathrm{fullslab}}_{0,xxx}$ and $\chi^{\mathrm{half-slab}}_{0,xxx}$ for a slab with 32 atomic Si layers plus one H layer.

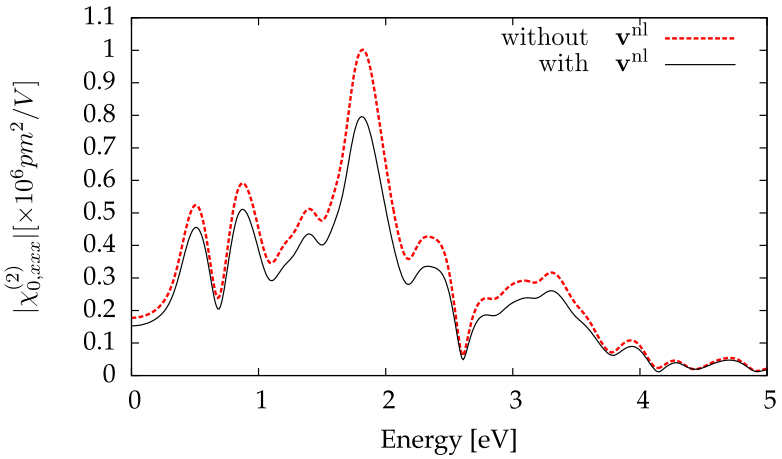

Fig. 6.3: $|\chi^{2\times1}_{0,xxx}|$ versus the photon energy for a slab with 32 atomic Si layers plus one H layer, with and without the contribution from $\hat{\mathbf{v}}^{\rm nl}$. Spectra are obtained with Δ= 0.5 eV.

6.2.2 Results for $\chi^{2\times1}_{0,xxx}$

We proceed to explain some of the features seen in $|\chi^{2\times1}_{0,xxx}|$ that are obtained by calculating $|\chi^{\rm half-slab}_{0,xxx}|$. First, from Fig. 6.2, we note a series of resonances that derive from 1ω and 2ω terms in Eq. (6.14). Notice that the 2ω resonances start below $E_g/2$ where E_g is the band gap (0.53 eV for LDA and 1.03 eV if the scissor is used with Δ= 0.5 eV). These resonances come from the electronic states of the 2×1 surface, that lie inside the bulk band gap of Si and are the well known electronic surface states [220]. In Fig. 6.3, we see that the effect of $\hat{\mathbf{v}}^{\rm nl}$ reduces the value of $|\chi^{2\times1}_{0,xxx}|$ by 15%-20% showing the importance of this contribution for a correct calculation of surface SHG, in agreement with a similar analysis for bulk semiconductors [213]. However, the inclusion of $\hat{\mathbf{v}}^{\rm nl}$ does not change the spectral shape of $|\chi^{2\times1}_{0,xxx}|$; this also can be confirmed from the cases of zero scissors correction from Fig. 6.2. To see the effect of the scissors correction, we take two different finite values for Δ. The first one with a value of Δ= 0.5 eV, used in the above results, is the "average" GW gap taken from Ref. [220] that is in agreement with Ref. [215]. The second one with a value of Δ = 0.63 eV is the "average" gap taken from Ref. [221], where more **k**-points in the Brillouin zone were used to calculate its GW value. From Fig. 6.4, we note that the scissors correction shifts the spectra from its LDA value to higher energies as expected. However, contrary to the case of linear optics [222] the shift introduced by the scissors correction is not rigid, as pointed out in Ref. [219]. This is because the second-harmonic optical response mixes 1ω and 2ω transitions (see Eq. (6.14)), and accounts for the non-rigid shift. The reduction of the spectral strength is in agreement with the previous calculations for bulk systems [41, 219, 223].

When we compare $|\chi^{2\times1}_{0,xxx}|$ for the two finite values of Δ, we see that the first two peaks are almost rigidly shifted with a small difference in height while the rest of the peaks are modified substantially. This behaviour comes from the fact that the first two peaks are almost exclusively related to the 2ω resonances of Eq. (6.14). The other peaks are a combination of 1ω and 2ω resonances and yield a more modified spectrum. We mention that for large band-gap materials, the 1ω and 2ω would be split showing a small interference effect, but still the 2ω would strongly depend on the surface

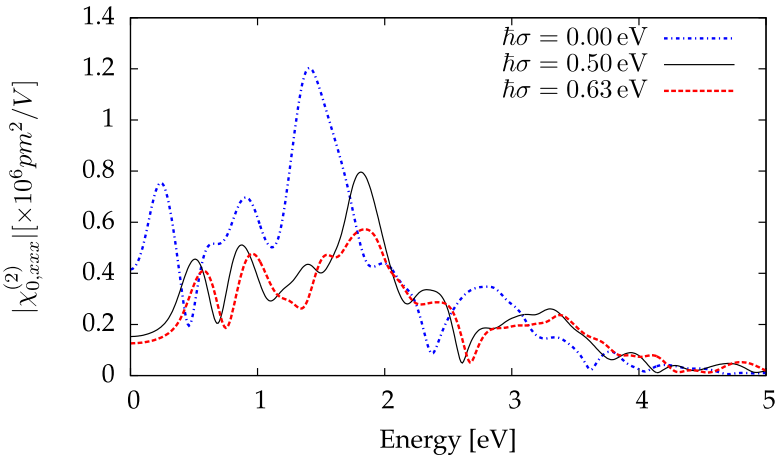

Fig. 6.4: $|\chi^{2\times1}_{0,xxx}|$ vs the photon energy for a slab with 32 atomic Si layers plus one H layer, for two different values of the scissors correction, with $\hat{\mathbf{v}}^{\mathrm{nl}}$ included.

states. This way we see that small changes in the value of the scissors shift can in general affect the surface second-harmonic generation spectrum quite dramatically. In Ref. [224], the authors already remarked that nonlinear optical response of bulk materials is more sensitive to the correction to the electronic structure of the material (GW or scissors operator correction) than the linear case. In the case of semiconducting surfaces, the problem is even more intricate due to the presence of electronic surface states. The high sensitivity of surface SHG to the energy position of surface-states, as seen in Fig. 6.4, makes surface SHG a good benchmark spectroscopical tool for testing the validity of the inclusion of many-body effects and, in particular, the quasi-particle correction to the electronic states.

Summary

I have presented in this chapter how to properly include the effects of nonlocal operators on the nonlinear susceptibility tensor of surfaces.

I have derived a formula for the second-harmonic susceptibility of surfaces including the effect of two nonlocal operators, namely the nonlocal part of the pseudo-potential and the scissors operator. The first one accounts for the non-locality of the pseudo-potential and changes the spectral weight up to 15-20%. This does not describe any new physics but allows one to make a correct use of the formula when using a pseudo-potential.

This second operator allows us to include a many-body effect due to the screening of the particles in materials, called quasi-particle correction, in its simplest form. We have demonstrated how this effect can change the line-shape of the spectra in an non-obvious way. As shown for bulk second-harmonic generation, this operator does not yield a rigid shift, by opposition to the case of linear optics. These two effects bring us a step closer to the reality.

Part III

Local-field effects in surface optical properties

7. *Ab initio* macroscopic linear and second-order optical properties of crystal surfaces: From the slab to the single surface

DON'T PANIC.

Douglas Adams, *The Hitchhiker's Guide to the Galaxy*

As we have seen, the efficient approach for computing optical properties of surfaces relies on the super-cell approach and a slab geometry. However, this approach suffers intrinsically from the fact that a slab is composed of two surfaces. The definition of a *surface* dielectric tensor (or second-order susceptibility) remains unclear and the difference between the optical response of a thin film (made of two surfaces) and the optical response of a semi-infinite system, with a single surface, has not really being investigated so far, in particular when local-field effects are included. In the linear case, the two surfaces of a slab interfere constructively, making the mapping between slab calculations and surface optical properties possible. However, as explained in Chap. 5, the direct calculation of the second-order optical properties is not possible in slab geometry, due to the destructive interferences between the two surfaces of the slab. Even at the simple level of independent-particle approximation, we have to introduce a cut-function, denoted here $\mathcal{C}(z)$, for being able to compute the second-harmonic generation from surfaces (see Chap. 5 and Chap. 6).

This chapter aims to give the theoretical background for computing the macroscopic optical properties of a single surface, from calculations performed in slab geometry.

I refer in that chapter to the optical properties of half of the slab equally as *half-slab* or *surface* optical properties. In SHG, only the surface region contributes to the signal, justifying the use of the term *surface optical properties* for the optical properties computed from half of the slab.

This chapter is organised as follows. I first present how we can obtain from the microscopic components of the polarization, the in-plane averaged dielectric tensor $\overset{\leftrightarrow}{\epsilon}_m\ (\mathbf{q}_{||}, z, z'; \omega)$, keeping explicitly the spatial fluctuations along the z direction [40]. From that expression, I give an expression for that surface macroscopic dielectric tensor in the optical limit. I thus show that the longitudinal-longitudinal part of the macroscopic dielectric tensor can be computed from Time-Dependent Den-

sity Functional Theory (TDDFT).
The second part of this chapter is dedicated to the extension of that calculation to the macroscopic surface second-order response and follows the same organisation. Some properties of those new surface response functions are finally discussed in Sec. 7.5.

7.1 Macroscopic dielectric tensor of crystal surfaces

In this section, I present in detail the derivation of the macroscopic dielectric tensor of half of a periodic system. Let us consider a system of electrons, perturbed by an external field $\mathbf{E}^{\text{ext}}$. Following the paper of R. Del Sole and E. Fiorino [38], we express the polarization as the response to a perturbing field $\mathbf{E}^{P}$, defined as

$$\mathbf{E}^{P} = \mathbf{E}^{\text{ext}} + \mathbf{E}^{\text{ind},T} = \mathbf{E} - \mathbf{E}^{\text{ind},L},$$

where $\mathbf{E}$ is the total microscopic field, and $\mathbf{E}^{\text{ind},T}$ and $\mathbf{E}^{\text{ind},L}$ are respectively, the transverse and the longitudinal components of the field induced by the external perturbation.
The polarization is related to the perturbing field via the quasi-polarisability $\overleftrightarrow{\tilde{\alpha}}$ and reads in Fourier space as [38]

$$\mathbf{P}_{\mathbf{G}}(\mathbf{q};\omega) = \sum_{\mathbf{G}'} \left[\overleftrightarrow{\tilde{\alpha}}\ (\mathbf{q};\omega)\right]_{\mathbf{G}\mathbf{G}'} \mathbf{E}^{P}_{\mathbf{G}'}(\mathbf{q};\omega), \tag{7.1}$$

where the notation $\mathbf{P}_{\mathbf{G}}(\mathbf{q})$ stands for $\mathbf{P}(\mathbf{q}+\mathbf{G})$ and $\left[\overleftrightarrow{\tilde{\alpha}}\ (\mathbf{q})\right]_{\mathbf{G}\mathbf{G}'}$ for $\overleftrightarrow{\tilde{\alpha}}\ (\mathbf{q}+\mathbf{G},\mathbf{q}+\mathbf{G}')$.
It is shown in Ref. [38], that the polarization can be expressed as a response to the total electric field using the expression

$$\mathbf{P}_{\mathbf{G}}(\mathbf{q};\omega) = \left[\overleftrightarrow{\tilde{\alpha}}\ (\mathbf{q};\omega)\right]_{\mathbf{G0}} \overleftrightarrow{A}_r\ (\mathbf{q};\omega)\mathbf{E}_{\mathbf{0}}(\mathbf{q};\omega), \tag{7.2}$$

where $\overleftrightarrow{A}_r\ (\mathbf{q};\omega) = \overleftrightarrow{1} + 4\pi \frac{\mathbf{q}}{q}\frac{\mathbf{q}}{q} \frac{\left[\overleftrightarrow{\tilde{\alpha}}(\mathbf{q};\omega)\right]_{\mathbf{00}}}{1-4\pi[\tilde{\alpha}^{LL}(\mathbf{q};\omega)]_{\mathbf{00}}}$.
This formula is the starting point of this section. It is general and perfectly valid for any periodic system.
Let us consider a super-cell, containing N atomic layers of thickness L_z and the same amount of vacuum. In order to average over a selected region of the slab, we express the polarization in a mixed-space (details can be found in App. A), where the in-plane periodicity is treated in reciprocal space and the out-of-plane direction is treated in real space.
Let us consider a function f of one variable in space. In real space, f is a function of the position vector $\mathbf{r}$ and reads $f(\mathbf{r})$. In reciprocal space, f is a function of a reciprocal vector $\mathbf{k}$, that we can split, for periodic systems as super-cells, into a vector $\mathbf{q}$ belonging to the BZ plus a reciprocal lattice vector $\mathbf{G}$, and reads $f(\mathbf{q}+\mathbf{G})$. In the mixed-space, the in-plane periodicity is treated in reciprocal space whereas the out-of-plane direction is treated in real space. Therefore a function f reads in this space $f(\mathbf{q}_{||}+\mathbf{G}_{||},z)$ or $f_{\mathbf{G}_{||}}(\mathbf{q}_{||},z)$, where $\mathbf{q}_{||}$ is a vector in the 2D BZ, $\mathbf{G}_{||}$ is an in-plane reciprocal-lattice vector and z is the coordinate in the out-of-plane direction.
The definitions of the corresponding Fourier transforms can be found in the App. A.
Using Def. A.16,

$$\mathbf{P}_{\mathbf{G}_{||}}(\mathbf{q}_{||},z;\omega) = \frac{1}{2L_z}\sum_{q_z,G_z} e^{i(q_z+G_z)z}\mathbf{P}_{\mathbf{G}}(\mathbf{q};\omega). \tag{7.3}$$

From the definition of the electric displacement, we obtain that

$$\mathbf{D}_{\mathbf{G}_{||}}(\mathbf{q}_{||},z;\omega)=\mathbf{E}_{\mathbf{G}_{||}}(\mathbf{q}_{||},z;\omega)+4\pi\mathbf{P}_{\mathbf{G}_{||}}(\mathbf{q}_{||},z;\omega). \tag{7.4}$$

Inserting Eq. (7.2) and Eq. (7.3) into Eq. (7.4), we obtain for $\mathbf{G}_{||}=0$ that

$$\begin{aligned}\mathbf{D_0}(\mathbf{q}_{||},z;\omega)&=\mathbf{E_0}(\mathbf{q}_{||},z;\omega)+\frac{4\pi}{2L_z}\sum_{q_z,G_z}e^{i(q_z+G_z)z}\Big[\overleftrightarrow{\tilde{\alpha}}\ (\mathbf{q};\omega)\Big]_{\mathbf{G_z0}}\overleftrightarrow{A}_r\ (\mathbf{q};\omega)\mathbf{E_0}(\mathbf{q};\omega)\\&=\int dz'\Bigg(\overleftrightarrow{\mathbb{1}}\ \delta(z-z')+\frac{4\pi}{2L_z}\sum_{q_z,G_z}e^{i(q_z+G_z)z}\Big[\overleftrightarrow{\tilde{\alpha}}\ (\mathbf{q};\omega)\Big]_{\mathbf{G_z0}}\overleftrightarrow{A}_r\ (\mathbf{q};\omega)e^{-iq_zz'}\Bigg)\mathbf{E_0}(\mathbf{q}_{||},z';\omega),\end{aligned} \tag{7.5}$$

where we used the relation $\mathbf{E_0}(\mathbf{q};\omega)=\int dz'e^{-iq_zz'}\mathbf{E_0}(\mathbf{q}_{||},z';\omega)$.
Therefore, the in-plane averaged macroscopic dielectric tensor, relating $\mathbf{D_0}(\mathbf{q}_{||},z;\omega)$ to $\mathbf{E_0}(\mathbf{q}_{||},z;\omega)$ is given by

$$\overleftrightarrow{\epsilon}_m\ (\mathbf{q}_{||},z,z';\omega)=\overleftrightarrow{\mathbb{1}}\ \delta(z-z')+\frac{4\pi}{2L_z}\sum_{q_z,G_z}e^{i(q_z+G_z)z}\Big[\overleftrightarrow{\tilde{\alpha}}\ (\mathbf{q};\omega)\Big]_{\mathbf{G_z0}}\overleftrightarrow{A}_r\ (\mathbf{q})e^{-iq_zz'}. \tag{7.6}$$

This quantity still contains the microscopic fluctuations along the z direction [40]. This allows us to define the *surface* macroscopic dielectric function, as the macroscopic average of the dielectric tensor over half of the system.
The surface macroscopic dielectric tensor reads as

$$\overleftrightarrow{\epsilon}^S_M\ (\mathbf{q};\omega)=\frac{1}{L_z}\int_{-L_z}^{L_z}dz\int_{-L_z}^{L_z}dz'\mathcal{C}(z)\ \overleftrightarrow{\epsilon}_m\ (\mathbf{q}_{||},z,z';\omega)e^{-iq_z(z-z')}, \tag{7.7}$$

where $\mathcal{C}(z)$ is a cut-function equal to 1 on half of the system and 0 elsewhere, as previously introduced in Chap. 5. This is illustrated in Fig. 7.1. The choice of $\mathcal{C}(z)$ will be discussed later in the chapter.
This dielectric tensor, called here surface dielectric tensor, fully accounts for all the surface-induced modification of the bulk material; at the microscopic level with the modification of the electronic structure, including possible surface states, and at a macroscopic level, including properly the (surface) local-field effects.
This result can be related to previous works on the *microscopic* optical properties of surfaces (see, for instance, Refs. [182, 192]) in which the microscopic optical properties of surfaces are defined thanks to a cut-function, weighting the polarization emitted by the system as the response to an external perturbation.
Nevertheless the present result is different by two aspects. First, we have here a macroscopic formalism. We used a macroscopic averaging for introducing $\mathcal{C}(z)$, meaning that the cut-function is introduced properly in

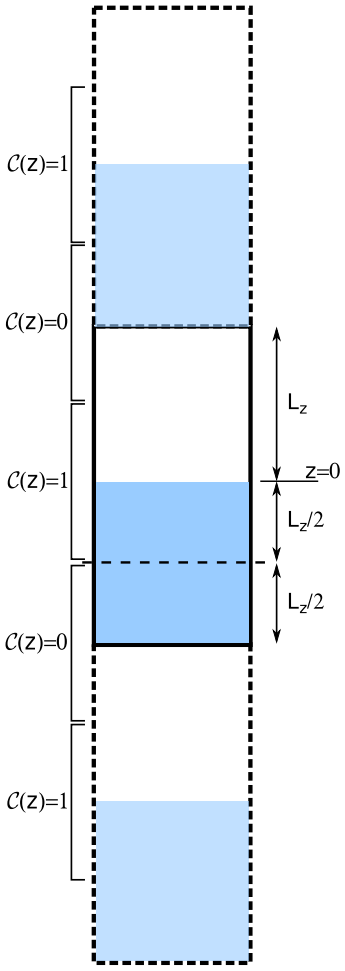

Fig. 7.1: The $\mathcal{C}(z)$ funtion.

the expression, with a clear derivation from the macroscopic Maxwell equations. The second point, more subtle, concerns the normalisation. As Eq. (7.7) is an average, we normalise there by half of the super-cell height, when averaging over half of the super-cell, leading to a well defined *surface* dielectric tensor.

Putting everything together, we obtain an expression for the macroscopic surface dielectric tensor

$$\overset{\leftrightarrow}{\epsilon}{}^{S}_{M}\,(\mathbf{q};\omega) = \overset{\leftrightarrow}{\mathbb{1}} + \frac{4\pi}{L_z}\sum_{G_z}\tilde{\mathcal{C}}(-G_z)\big[\,\overset{\leftrightarrow}{\tilde{\alpha}}\,(\mathbf{q};\omega)\big]_{\mathbf{G_z 0}}\,\overset{\leftrightarrow}{A}_r\,(\mathbf{q};\omega) = \overset{\leftrightarrow}{\mathbb{1}} + 4\pi\,\overset{\leftrightarrow}{\tilde{\alpha}}{}^{S}\,(\mathbf{q},\mathbf{q};\omega)\,\overset{\leftrightarrow}{A}_r\,(\mathbf{q};\omega), \tag{7.8}$$

where $\overset{\leftrightarrow}{\tilde{\alpha}}{}^{S}$ is defined by the last part of the equation. Using the definition of $\overset{\leftrightarrow}{A}_r$, we get directly that

$$\overset{\leftrightarrow}{\epsilon}{}^{S}_{M}\,(\mathbf{q};\omega) = \overset{\leftrightarrow}{\mathbb{1}} + 4\pi\,\overset{\leftrightarrow}{\tilde{\alpha}}{}^{S}\,(\mathbf{q},\mathbf{q};\omega) + (4\pi)^2\frac{\overset{\leftrightarrow}{\tilde{\alpha}}{}^{S}\,(\mathbf{q},\mathbf{q};\omega)\frac{\mathbf{q}}{q}\frac{\mathbf{q}}{q}\big[\,\overset{\leftrightarrow}{\tilde{\alpha}}\,(\mathbf{q};\omega)\big]_{\mathbf{00}}}{1-4\pi\big[\tilde{\alpha}^{LL}(\mathbf{q};\omega)\big]_{\mathbf{00}}}. \tag{7.9}$$

This result is very similar to Del Sole and Fiorino expression for the dielectric tensor of bulk materials (see Eq. (25) of Ref. [38]), except that we have here a surface quantity. In Ref. [38], authors also obtained an expression for the macroscopic dielectric tensor. Their expression is very similar to Eq. (7.6). Nevertheless, they obtained an expression defined thanks to an integral operator, which plays the same role as $\overset{\leftrightarrow}{A}_r$ in Eq. (7.6) (see Eq.(45) of Ref. [38]).

We also remark that not all ingredients of that formula are modified by the presence of the surface. This expression is general, in the sense that it gives access to all the components of the dielectric tensor. However, as explained in Chap. 1, it is possible to calculate the entire dielectric tensor in the optical limit only from longitudinal-longitudinal (LL) calculations. Therefore, in the following we focus only on the LL part of the surface dielectric tensor in the optical limit, as it corresponds to the scope of this chapter.

7.2 Optical limit for the surface macroscopic dielectric function

For the following, we restrict our discussion to the optical limit, which corresponds to a perturbation with a vanishing momentum. This is valid for the low-energy region of the spectra where we are precisely interested in.

The key quantity in the optical limit is the longitudinal-longitudinal part of the macroscopic dielectric function $\epsilon_M^{S,LL}$. Only this quantity can be evaluated in the framework of TDDFT, where the electronic density is the fundamental physical quantity.

From Eq. (7.9), the LL part of the surface macroscopic dielectric tensor reads as

$$\epsilon_M^{S,LL}(\hat{\mathbf{q}};\omega) = 1 + \lim_{\mathbf{q}\to\mathbf{0}}\frac{4\pi\tilde{\alpha}^{S,LL}(\mathbf{q},\mathbf{q};\omega)}{1-4\pi\big[\tilde{\alpha}^{LL}(\mathbf{q};\omega)\big]_{\mathbf{00}}}, \qquad \hat{\mathbf{q}} = \frac{\mathbf{q}}{q}. \tag{7.10}$$

Here, the quasi-polarisability $\tilde{\alpha}$ is related to response functions by [44]

$$\overset{\leftrightarrow}{\tilde{\alpha}}\,(\mathbf{r},\mathbf{r}';\omega) = -\frac{1}{\omega^2}\left(\chi^{(1)}_{\mathbf{jj}}(\mathbf{r},\mathbf{r}';\omega) - \overset{\leftrightarrow}{\mathbb{1}}\,\langle\rho\rangle\delta(\mathbf{r}-\mathbf{r}')\right),$$

where $\chi^{(1)}_{\mathbf{jj}}$ is the current-current response function and ρ is the electronic density of the system. Starting from the expression of the surface averaged quasi-polarisability, we can show easily that

$$\overset{\leftrightarrow}{\tilde{\alpha}}^{S}(\mathbf{q},\mathbf{q};\omega) = \frac{1}{L_z}\int dz_1 \int dz_2 e^{-iq_z z_1}\mathcal{C}(z_1)\big[\overset{\leftrightarrow}{\tilde{\alpha}}(\mathbf{q}_{||},z_1,z_2;\omega)\big]_{\mathbf{00}} e^{iq_z z_2}.$$

We define $\chi^{(1)S}_{\mathbf{jj}}(\mathbf{q},\mathbf{q};\omega)$ in the same way. Thus, we get

$$\overset{\leftrightarrow}{\tilde{\alpha}}^{S}(\mathbf{q},\mathbf{q};\omega) = -\frac{1}{\omega^2}\left(\chi^{(1)S}_{\mathbf{jj}}(\mathbf{q},\mathbf{q};\omega) - \overset{\leftrightarrow}{\mathbb{1}}\langle\rho^S\rangle\right).$$

From this result, we obtain an expression for the LL part of the surface macroscopic dielectric tensor expressed in terms of response functions

$$\epsilon_M^{S,LL}(\hat{\mathbf{q}};\omega) = 1 - \lim_{\mathbf{q}\to\mathbf{0}}\frac{4\pi}{\omega^2}\frac{\left(\frac{\mathbf{q}}{q}.\chi^{(1)S}_{\mathbf{jj}}(\mathbf{q},\mathbf{q};\omega).\frac{\mathbf{q}}{q} - \langle\rho^S\rangle\right)}{1+v_{\mathbf{0}}(\mathbf{q})\big[\chi^{(1)}_{\rho\rho}(\mathbf{q};\omega)\big]_{\mathbf{00}}}, \tag{7.11}$$

where we used explicitly the link between the longitudinal-longitudinal part of the quasi-polarisability and the density-density response function $\chi^{(1)}_{\rho\rho}$ [38]. Also, we have here $\langle\rho^S\rangle = \langle\rho(\mathbf{r})\mathcal{C}(z)\rangle = \frac{\langle\rho\rangle}{2}$.
As explained in App. F.1, we can show from the conservation of charges, in presence of a cut-function, and under two restrictions, that

$$\omega^2\chi^S_{\rho\rho}(\mathbf{q},\mathbf{q};\omega) = \mathbf{q}.\chi^S_{\mathbf{jj}}(\mathbf{q},\mathbf{q};\omega).\mathbf{q} - \langle\rho^S\rangle. \tag{7.12}$$

That two restrictions are i) the cut-function $\mathcal{C}(z)$ is a step function, centred at the center of the slab and ii) the slab has a mirror plan perpendicular to the z-axis. The direct consequences are that i) one must use a symmetric slab and ii) it is not possible to perform a layer-by-layer analysis. Physically, this is meaningful, because in a fully interacting system, it is not possible to define the response of an unique layer and the symmetry restriction together with the step function correspond to a case where we can only consider separately the response of the two halves of the whole slab.
I want to stress here that this choice for the cut-function is the one that most of the authors used for surface linear [182,192,225] and second-harmonic generation [139,203,226–228] calculations; with an exception for Refs. [138,183], where the cut-function has been chosen smooth.
From that, it results an expression of the LL part of the surface dielectric tensor depending only of the density-density response function of the system and its surface average

$$\boxed{\epsilon_M^{S,LL}(\hat{\mathbf{q}};\omega) = 1 - \lim_{\mathbf{q}\to\mathbf{0}}\frac{4\pi}{q^2}\frac{\chi^{(1)S}_{\rho\rho}(\mathbf{q},\mathbf{q};\omega)}{1+v_{\mathbf{0}}(\mathbf{q})\big[\chi^{(1)}_{\rho\rho}(\mathbf{q};\omega)\big]_{\mathbf{00}}} = 1 - \lim_{\mathbf{q}\to\mathbf{0}} v_{\mathbf{0}}(\mathbf{q})\frac{\chi^{(1)S}_{\rho\rho}(\mathbf{q},\mathbf{q};\omega)}{1+v_{\mathbf{0}}(\mathbf{q})\big[\chi^{(1)}_{\rho\rho}(\mathbf{q};\omega)\big]_{\mathbf{00}}}.} \tag{7.13}$$

This equation is the main result of this section. We have derived an expression for the longitudinal-longitudinal part of the surface dielectric tensor which depends only on the density-density response function and its surface average. This makes that result possible, on principle, to be evaluated within the framework of TDDFT. Nevertheless, we have introduced a new quantity $\chi^{(1)S}_{\rho\rho}$, that we do not

know how to evaluate explicitly. This is the purpose of the next session.
Notice that if we choose $\mathcal{C}(z)$ to be 1 everywhere, we recover the expression of the LL part of the dielectric function used for bulk materials [84], showing the consistency of our approach. We also note here that $\chi^{(1)S}_{\rho\rho}$ and $\chi^{(1)S}_{\mathbf{jj}}$ are not response functions; but they correspond to the surface macroscopic average of response functions.

7.3 Calculation of $\epsilon_M^{S,LL}$ in TDDFT

The last equation requires, for being evaluated, the expression of the two quantities $\chi^{(1)S}_{\rho\rho}(\mathbf{q},\mathbf{q};\omega)$ and $\chi^{(1)}_{\rho\rho}(\mathbf{q},\mathbf{q};\omega)$, in the optical limit. The latter can be computed easily in TDDFT, but not the first one. Eq. (7.13) can be rewritten as

$$\epsilon_M^{S,LL}(\hat{\mathbf{q}};\omega) = 1 - \lim_{\mathbf{q}\to\mathbf{0}} v_{\mathbf{0}}(\mathbf{q}) \frac{1}{L_z} \frac{\sum_{G_z} \tilde{\mathcal{C}}(-G_z)\left[\chi^{(1)}_{\rho\rho}(\mathbf{q};\omega)\right]_{\mathbf{G_z 0}}}{1 + v_{\mathbf{0}}(\mathbf{q})\left[\chi^{(1)}_{\rho\rho}(\mathbf{q};\omega)\right]_{\mathbf{00}}}. \tag{7.14}$$

From now on, we assume the random-phase approximation.Under this approximation, the response function of the fully interacting system $\chi^{(1)}_{\rho\rho}$ is related to the independent-particle or Kohn-Sham response function $\chi^{(0)}_{\rho\rho}$ of the (auxiliary) system by a Dyson-like equation, see Sec. 8.3.2,

$$\left[\chi^{(1)}_{\rho\rho}(\mathbf{q};\omega)\right]_{\mathbf{GG'}} = \left[\chi^{(0)}_{\rho\rho}(\mathbf{q};\omega)\right]_{\mathbf{GG'}} + \sum_{\mathbf{G_1}} \left[\chi^{(0)}_{\rho\rho}(\mathbf{q};\omega)\right]_{\mathbf{GG_1}} v_{\mathbf{G_1}}(\mathbf{q}) \left[\chi^{(1)}_{\rho\rho}(\mathbf{q};\omega)\right]_{\mathbf{G_1 G'}}. \tag{7.15}$$

Alternatively, one can introduce the response function to the total macroscopic classical potential $\bar{\chi}_{\rho\rho}$ defined by [112, 229]

$$\left[\bar{\chi}_{\rho\rho}(\mathbf{q};\omega)\right]_{\mathbf{GG'}} = \left[\chi^{(0)}_{\rho\rho}(\mathbf{q};\omega)\right]_{\mathbf{GG'}} + \sum_{\mathbf{G_1}} \left[\chi^{(0)}_{\rho\rho}(\mathbf{q};\omega)\right]_{\mathbf{GG_1}} \bar{v}_{\mathbf{G_1}}(\mathbf{q}) \left[\bar{\chi}_{\rho\rho}(\mathbf{q};\omega)\right]_{\mathbf{G_1 G'}}, \tag{7.16}$$

which implies that

$$\left[\chi^{(1)}_{\rho\rho}(\mathbf{q};\omega)\right]_{\mathbf{GG'}} = \left[\bar{\chi}_{\rho\rho}(\mathbf{q};\omega)\right]_{\mathbf{GG'}} + \left[\bar{\chi}_{\rho\rho}(\mathbf{q};\omega)\right]_{\mathbf{G0}} v_{\mathbf{0}}(\mathbf{q}) \left[\chi^{(1)}_{\rho\rho}(\mathbf{q};\omega)\right]_{\mathbf{0G'}}, \tag{7.17}$$

where $\bar{v}_{\mathbf{G}}(\mathbf{q}) = v_{\mathbf{G}}(\mathbf{q})$ if $\mathbf{G} \neq 0$ and 0 if $\mathbf{G} = 0$.
From Eq. (7.17), we obtain directly that $\bar{\chi}_{\mathbf{G0}} = \frac{\chi_{\mathbf{G0}}}{1+v_{\mathbf{0}}\chi_{\mathbf{00}}}$, leading to

$$\epsilon_M^{S,LL}(\hat{\mathbf{q}};\omega) = 1 - \lim_{\mathbf{q}\to\mathbf{0}} v_{\mathbf{0}}(\mathbf{q}) \frac{1}{L_z} \sum_{G_z} \tilde{\mathcal{C}}(-G_z)\left[\bar{\chi}_{\rho\rho}(\mathbf{q};\omega)\right]_{\mathbf{G_z 0}} = 1 - \lim_{\mathbf{q}\to\mathbf{0}} v_{\mathbf{0}}(\mathbf{q}) \bar{\chi}^S_{\rho\rho}(\mathbf{q},\mathbf{q};\omega). \tag{7.18}$$

For obtaining the quantity $\bar{\chi}^S(\mathbf{q},\mathbf{q};\omega)$, we have to solve the equation

$$\bar{\chi}^S_{\rho\rho}(\mathbf{q},\mathbf{q};\omega) = \chi^{(0)S}_{\rho\rho}(\mathbf{q},\mathbf{q};\omega) + \sum_{\mathbf{G_1}\neq\mathbf{0}} \chi^{(0)S}_{\rho\rho}(\mathbf{q},\mathbf{q}+\mathbf{G_1};\omega) \bar{v}_{\mathbf{G_1}}(\mathbf{q}) \left[\bar{\chi}_{\rho\rho}(\mathbf{q};\omega)\right]_{\mathbf{G_1 0}}, \tag{7.19}$$

which is not a matrix equation, by opposition to Eq. (7.15) or Eq. (7.16). This makes the direct resolution of this equation intricate. In order to solve that equation in a clever way, we introduce two

matrices, $\left[\bar{\chi}^S(\mathbf{q};\omega)\right]_{\mathbf{GG'}}$ and $\left[\chi^{(0)S}_{\rho\rho}(\mathbf{q};\omega)\right]_{\mathbf{GG'}}$.
We define the matrix $\left[\chi^{(0)S}_{\rho\rho}(\mathbf{q};\omega)\right]_{\mathbf{GG'}}$ as

$$\begin{aligned}\left[\chi^{(0)S}_{\rho\rho}(\mathbf{q};\omega)\right]_{\mathbf{0G'}} &= \chi^{(0)S}_{\rho\rho}(\mathbf{q},\mathbf{q}+\mathbf{G'};\omega),\\ \left[\chi^{(0)S}_{\rho\rho}(\mathbf{q};\omega)\right]_{\mathbf{GG'}} &= \left[\chi^{(0)}_{\rho\rho}(\mathbf{q};\omega)\right]_{\mathbf{GG'}}, \qquad \mathbf{G}\neq\mathbf{0}.\end{aligned} \tag{7.20}$$

This corresponds to the replacement of the first line of the matrix $\left[\chi^{(0)}_{\rho\rho}\right]_{\mathbf{GG'}}$ by $\chi^{(0)S}_{\rho\rho}(\mathbf{q},\mathbf{q}+\mathbf{G'};\omega)$. The matrix $\left[\bar{\chi}^S_{\rho\rho}(\mathbf{q};\omega)\right]_{\mathbf{GG'}}$ is defined similarly. From Eq. (7.19) and Eq. (7.16), and using the relation $\bar{v}_{\mathbf{G_1}}\left[\bar{\chi}_{\rho\rho}(\mathbf{q};\omega)\right]_{\mathbf{G_1 0}} = \bar{v}_{\mathbf{G_1}}\left[\bar{\chi}^S_{\rho\rho}(\mathbf{q};\omega)\right]_{\mathbf{G_1 0}}$, we obtain directly a matrix equation linking $\left[\bar{\chi}^S_{\rho\rho}(\mathbf{q};\omega)\right]_{\mathbf{GG'}}$ to $\left[\chi^{(0)S}_{\rho\rho}(\mathbf{q};\omega)\right]_{\mathbf{GG''}}$,

$$\left[\bar{\chi}^S_{\rho\rho}(\mathbf{q};\omega)\right]_{\mathbf{GG'}} = \left[\chi^{(0)S}_{\rho\rho}(\mathbf{q};\omega)\right]_{\mathbf{GG'}} + \sum_{\mathbf{G_1}}\left[\chi^{(0)S}_{\rho\rho}(\mathbf{q};\omega)\right]_{\mathbf{GG_1}}\bar{v}_{\mathbf{G_1}}\left[\bar{\chi}^S_{\rho\rho}(\mathbf{q};\omega)\right]_{\mathbf{G_1 G'}}. \tag{7.21}$$

Therefore, we have obtained a Dyson-like equation linking the matrix $\left[\bar{\chi}^S_{\rho\rho}\right]_{\mathbf{GG'}}$ to the matrix $\left[\chi^{(0)S}_{\rho\rho}\right]_{\mathbf{GG''}}$; the latter being obtained from time-dependent perturbation theory. From Eq. (7.18), $\left[\bar{\chi}^S_{\rho\rho}\right]_{\mathbf{00}}$ gives directly $\epsilon^{S,LL}_M$. Finally, we note that we can rework the expression of the surface macroscopic dielectric function for obtaining that

$$\boxed{\epsilon^{S,LL}_M(\hat{\mathbf{q}};\omega) = \lim_{\mathbf{q}\to 0}\frac{1}{\left(1-v(\mathbf{q})\chi^{(0)S}_{\rho\rho}(\mathbf{q},\mathbf{q};\omega)\right)^{-1}_{\mathbf{G}=\mathbf{G'}=0}}.} \tag{7.22}$$

It is worthwhile to note that this expression is very similar to the expression for bulk crystals in the RPA, except that the independent-particle response function $\chi^{(0)}_{\rho\rho}$ has been replaced by $\chi^{(0)S}_{\rho\rho}$. The expression of the full matrix $\left[\chi^{(0)S}_{\rho\rho}\right]_{\mathbf{GG'}}$ is given in App. I, together with numerical results. Let us emphasize that this result allows us to describe how a surface affects the optical response of a material; with the convenience and efficiency of a super-cell calculation, assuming that the slab is thick enough do describe correctly the surface region. It was not obvious also that the surface dielectric function is obtained by solving the same equations than for bulk materials and in particular that the only change at the end of the day is $\chi^{(0)}_{\rho\rho} \to \chi^{(0)S}_{\rho\rho}$. Also we note that $\bar{\chi}^S_{\rho\rho}$ is an auxiliary matrix and only the head of this matrix has a physical meaning.

7.4 Macroscopic second-order tensor of crystal surfaces

Let us consider now, instead of a linear polarization $\mathbf{P} = \tilde{\alpha}\mathbf{E}^P$, a polarization composed of two contributions, a linear contribution $\mathbf{P}^{(1)}$ associated to $\tilde{\alpha}^{(1)}$ plus a second-order (in the perturbing field) contribution $\mathbf{P}^{(2)}$ associated to $\tilde{\alpha}^{(2)}$. The aim of this section is to obtain an expression for the macroscopic surface second-order response function, following the approach used for the surface dielectric tensor.

7.4.1 Microscopic components of the polarization

In order to be able to extend the linear calculation to the case of the second-harmonic generation, we need all the microscopic components of the second-order polarization $\mathbf{P}^{(2)}_{\mathbf{G}}$ and not only the macroscopic one $\mathbf{P}^{(2)}_{\mathbf{0}}$. Therefore, we do not follow here the derivation of Ref. [41].
In reciprocal space, the first- and second-order polarizations are given by [41]

$$\mathbf{P}^{(1)}_{\mathbf{G}}(\mathbf{q};\omega) = \sum_{\mathbf{G_1}} \Big[\overset{\leftrightarrow}{\tilde{\alpha}}^{(1)} (\mathbf{q};\omega)\Big]_{\mathbf{G}\mathbf{G_1}} \mathbf{E}^{P}_{\mathbf{G_1}}(\mathbf{q};\omega), \tag{7.23a}$$

$$\mathbf{P}^{(2)}_{\mathbf{G}}(\mathbf{q};\omega) = \sum_{\mathbf{q_1},\mathbf{q_2}}^{BZ} \sum_{\mathbf{G_1},\mathbf{G_2}} \int d\omega_1 d\omega_2 \delta(\omega-\omega_1-\omega_2)\delta_{\mathbf{q},(\mathbf{q_1}+\mathbf{q_2})} \times \Big[\overset{\leftrightarrow}{\tilde{\alpha}}^{(2)} (\mathbf{q},\mathbf{q_1},\mathbf{q_2};\omega_1,\omega_2)\Big]_{\mathbf{G}\mathbf{G_1}\mathbf{G_2}} \mathbf{E}^{P}_{\mathbf{G_1}}(\mathbf{q_2};\omega_1)\mathbf{E}^{P}_{\mathbf{G_2}}(\mathbf{q_2};\omega_2), \tag{7.23b}$$

where $\overset{\leftrightarrow}{\tilde{\alpha}}^{(1)}$ and $\overset{\leftrightarrow}{\tilde{\alpha}}^{(2)}$ are respectively the first- and second-order quasi-polarisabilities [41,44]. In the following, we always have $\omega = \omega_1 + \omega_2$ and $\mathbf{q} = \mathbf{q_1} + \mathbf{q_2}$.
From Maxwell equations, we obtain that

$$\mathbf{E}^{P}_{\mathbf{G}}(\mathbf{q};\omega) = \mathbf{E}_{\mathbf{G}}(\mathbf{q};\omega) + 4\pi \frac{\mathbf{q}+\mathbf{G}}{|\mathbf{q}+\mathbf{G}|}\frac{\mathbf{q}+\mathbf{G}}{|\mathbf{q}+\mathbf{G}|}.\mathbf{P}_{\mathbf{G}}(\mathbf{q};\omega). \tag{7.24}$$

We note that this relation contains the first-order in polarization $\mathbf{P}^{(1)}$ but also the second-order polarization $\mathbf{P}^{(2)}$.
The perturbing field is the macroscopic applied perturbation and is of long wavelength, leading to $\mathbf{E}^{P}_{\mathbf{G}}(\mathbf{q};\omega) = \delta_{\mathbf{G0}}\mathbf{E}^{P}_{\mathbf{0}}(\mathbf{q};\omega)$.
Inserting Eq. (7.24) into the expression of $\mathbf{P}^{(1)}_{\mathbf{G}}$, we obtain that

$$\mathbf{P}^{(1)}_{\mathbf{G}}(\mathbf{q};\omega) = \Big[\overset{\leftrightarrow}{\tilde{\alpha}}^{(1)} (\mathbf{q};\omega)\Big]_{\mathbf{G0}} \mathbf{E}_{\mathbf{0}}(\mathbf{q};\omega) + 4\pi \Big[\overset{\leftrightarrow}{\tilde{\alpha}}^{(1)} (\mathbf{q};\omega)\Big]_{\mathbf{G0}} \frac{\mathbf{q}}{|\mathbf{q}|}\frac{\mathbf{q}}{|\mathbf{q}|}\Big(\mathbf{P}^{(1)}_{\mathbf{0}}(\mathbf{q};\omega) + \mathbf{P}^{(2)}_{\mathbf{0}}(\mathbf{q};\omega)\Big). \tag{7.25}$$

We can solve that equation for $\mathbf{P}^{(1)}_{\mathbf{0}}(\mathbf{q};\omega) + \mathbf{P}^{(2)}_{\mathbf{0}}(\mathbf{q};\omega)$, obtaining that

$$\mathbf{P}^{(1)}_{\mathbf{0}}(\mathbf{q};\omega) + \mathbf{P}^{(2)}_{\mathbf{0}}(\mathbf{q};\omega) = \overset{\leftrightarrow}{A_l}(\mathbf{q};\omega)\left(\Big[\overset{\leftrightarrow}{\tilde{\alpha}}^{(1)} (\mathbf{q};\omega)\Big]_{\mathbf{00}} \mathbf{E}_{\mathbf{0}}(\mathbf{q};\omega) + \mathbf{P}^{(2)}_{\mathbf{0}}(\mathbf{q};\omega)\right),$$

where we have introduced the tensor $\overset{\leftrightarrow}{A_l}$

$$\overset{\leftrightarrow}{A_l}(\mathbf{q};\omega) = \left(\overset{\leftrightarrow}{\mathbb{1}} - 4\pi \Big[\overset{\leftrightarrow}{\tilde{\alpha}}^{(1)} (\mathbf{q};\omega)\Big]_{\mathbf{00}} \frac{\mathbf{q}}{|\mathbf{q}|}\frac{\mathbf{q}}{|\mathbf{q}|}\right)^{-1} = \overset{\leftrightarrow}{1} + 4\pi \frac{\Big[\overset{\leftrightarrow}{\tilde{\alpha}}^{(1)} (\mathbf{q};\omega)\Big]_{\mathbf{00}}}{1 - 4\pi \left[\tilde{\alpha}^{(1),LL}(\mathbf{q};\omega)\right]_{\mathbf{00}}} \frac{\mathbf{q}}{|\mathbf{q}|}\frac{\mathbf{q}}{|\mathbf{q}|}.$$

Inserting the expression of $\mathbf{P}^{(1)}_{\mathbf{0}}(\mathbf{q};\omega) + \mathbf{P}^{(2)}_{\mathbf{0}}(\mathbf{q};\omega)$ into Eq. (7.25) yields

$$\mathbf{P}^{(1)}_{\mathbf{G}}(\mathbf{q};\omega) = \Big[\overset{\leftrightarrow}{\tilde{\alpha}}^{(1)} (\mathbf{q};\omega)\Big]_{\mathbf{G0}} \overset{\leftrightarrow}{A_r}(\mathbf{q};\omega)\mathbf{E}_{\mathbf{0}}(\mathbf{q};\omega) + 4\pi \Big[\overset{\leftrightarrow}{\tilde{\alpha}}^{(1)} (\mathbf{q};\omega)\Big]_{\mathbf{G0}} \frac{\mathbf{q}}{|\mathbf{q}|}\frac{\mathbf{q}}{|\mathbf{q}|} \overset{\leftrightarrow}{A_l}(\mathbf{q};\omega)\mathbf{P}^{(2)}_{\mathbf{0}}(\mathbf{q};\omega), \tag{7.26}$$

where $\overleftrightarrow{A}_r\ (\mathbf{q};\omega)$ is the tensor already defined in the Sec. 7.1.
From the first-order of Eq. (7.24), we obtain that $\mathbf{E}_{\mathbf{0}}^{P}(\mathbf{q};\omega) = \overleftrightarrow{A}_r\ (\mathbf{q};\omega)\mathbf{E_0}(\mathbf{q};\omega)$; [41] which can be combined with the expression of the second-order polarization for obtaining

$$\begin{aligned}\mathbf{P}_{\mathbf{G}}^{(2)}(\mathbf{q};\omega) = \sum_{\mathbf{q_1},\mathbf{q_2}}^{BZ}\int d\omega_1 \int d\omega_2 \delta(\omega-\omega_1-\omega_2)\delta_{\mathbf{q},(\mathbf{q_1}+\mathbf{q_2})} \\ \times\big[\ \overleftrightarrow{\tilde{\alpha}}^{(2)}\ (\mathbf{q},\mathbf{q_1},\mathbf{q_2};\omega_1,\omega_2)\big]_{\mathbf{G00}}\ \overleftrightarrow{A}_r\ (\mathbf{q_1},\omega_1)\ \overleftrightarrow{A}_r\ (\mathbf{q_2},\omega_2)\mathbf{E_0}(\mathbf{q_2};\omega_1)\mathbf{E_0}(\mathbf{q_2};\omega_2).\end{aligned} \tag{7.27}$$

Thus, we have all the ingredients for obtaining the microscopic components of the full polarization. Finally, the total polarization is given by

$$\begin{aligned}\mathbf{P_G}(\mathbf{q};\omega) = \sum_{\mathbf{q_1}\mathbf{q_2}}^{BZ}\delta_{\mathbf{q},(\mathbf{q_1}+\mathbf{q_2})}\int d\omega_1\int d\omega_2\delta(\omega-\omega_1-\omega_2) \\ \times\big[\ \overleftrightarrow{\tilde{\alpha}}^{(2)}\ (\mathbf{q},\mathbf{q_1},\mathbf{q_2};\omega_1,\omega_2)\big]_{\mathbf{G00}}\ \overleftrightarrow{A}_r\ (\mathbf{q_1};\omega_1)\ \overleftrightarrow{A}_r\ (\mathbf{q_2};\omega_2)\mathbf{E_0}(\mathbf{q_1};\omega_1)\mathbf{E_0}(\mathbf{q_2};\omega_2) \\ +\big[\ \overleftrightarrow{\tilde{\alpha}}^{(1)}\ (\mathbf{q};\omega)\big]_{\mathbf{G0}}\ \overleftrightarrow{A}_r\ (\mathbf{q};\omega)\mathbf{E_0}(\mathbf{q};\omega) + 4\pi\big[\ \overleftrightarrow{\tilde{\alpha}}^{(1)}\ (\mathbf{q};\omega)\big]_{\mathbf{G0}}\frac{\mathbf{q}}{|\mathbf{q}|}\frac{\mathbf{q}}{|\mathbf{q}|}\ \overleftrightarrow{A}_l\ (\mathbf{q};\omega)\mathbf{P}_{\mathbf{0}}^{(2)}(\mathbf{q};\omega).\end{aligned} \tag{7.28}$$

By opposition to the result of Ref. [41], we have obtained here the expression of all the microscopic components of the total polarization. This allows us to obtain the z dependence of the second-order polarization, as explained in the next section.

7.4.2 Macroscopic surface response function

Inserting the expression Eq. (7.28) into Eq. (7.4), gives the in-plane averaged dielectric tensor

$$\overleftrightarrow{\epsilon}_m\ (\mathbf{q}_{||},z,z';\omega) = \overleftrightarrow{\mathbb{1}}\ \delta(z-z') + \frac{4\pi}{2L_z}\sum_{q_z,G_z} e^{i(q_z+G_z)z}\big[\ \overleftrightarrow{\tilde{\alpha}}^{(1)}\ (\mathbf{q};\omega)\big]_{\mathbf{G_z0}}\ \overleftrightarrow{A}_r\ (\mathbf{q};\omega)e^{-iq_zz'},$$

plus the in-plane averaged second-order polarization

$$\begin{aligned}\mathbf{P}_{\mathbf{0}}^{(2)}(\mathbf{q}_{||},z;\omega) =& \frac{4\pi}{2L_z}\sum_{q_z,G_z} e^{i(q_z+G_z)z}\big[\ \overleftrightarrow{\tilde{\alpha}}^{(1)}\ (\mathbf{q};\omega)\big]_{\mathbf{G_z0}}\frac{\mathbf{q}}{|\mathbf{q}|}\frac{\mathbf{q}}{|\mathbf{q}|}\ \overleftrightarrow{A}_l\ (\mathbf{q};\omega)\mathbf{P}_{\mathbf{0}}^{(2)}(\mathbf{q};\omega) \\ &+\frac{1}{2L_z}\sum_{\mathbf{q_1},\mathbf{q_2}}^{BZ}\delta_{\mathbf{q},(\mathbf{q_1}+\mathbf{q_2})}\int d\omega_1\int d\omega_2\delta(\omega-\omega_1-\omega_2)\sum_{q_z,G_z}e^{i(q_z+G_z)z} \\ &\times\big[\ \overleftrightarrow{\tilde{\alpha}}^{(2)}\ (\mathbf{q},\mathbf{q_1},\mathbf{q_2};\omega_1,\omega_2)\big]_{\mathbf{G_z00}}\ \overleftrightarrow{A}_r\ (\mathbf{q_1};\omega_1)\ \overleftrightarrow{A}_r\ (\mathbf{q_2};\omega_2)\mathbf{E_0}(\mathbf{q_1};\omega_1)\mathbf{E_0}(\mathbf{q_2};\omega_2).\end{aligned} \tag{7.29}$$

An important point here is that Eq. (7.29) contains $\mathbf{P}_{\mathbf{0}}^{(2)}(\mathbf{q};\omega)$ on the right-hand side. The dependency in the total electric field is not explicit; and it is not straightforward, from Eq. (7.29), to identify the second-order macroscopic response function in the mixed-space.
In order to find a more suitable expression for the second-order response function in the mixed-space,

we replace $\mathbf{P_0^{(2)}}(\mathbf{q};\omega)$ by its expression, using Eq. (7.27).

$$\begin{aligned}\mathbf{P_0^{(2)}}(\mathbf{q}_{||},z;\omega) = \frac{1}{2L_z}\sum_{\mathbf{q_1},\mathbf{q_2}}^{BZ}\delta_{\mathbf{q},(\mathbf{q_1}+\mathbf{q_2})}\int d\omega_1\int d\omega_2\delta(\omega-\omega_1-\omega_2)\sum_{q_z,G_z}e^{i(q_z+G_z)z}\\ \times\Bigg(4\pi\big[\overset{\leftrightarrow}{\tilde{\alpha}}^{(1)}(\mathbf{q};\omega)\big]_{\mathbf{G0}}\frac{\mathbf{q}}{|\mathbf{q}|}\frac{\mathbf{q}}{|\mathbf{q}|}\overset{\leftrightarrow}{A}_l(\mathbf{q};\omega)\big[\overset{\leftrightarrow}{\tilde{\alpha}}^{(2)}(\mathbf{q},\mathbf{q_1},\mathbf{q_2};\omega_1,\omega_2)\big]_{\mathbf{000}}\\ +\big[\overset{\leftrightarrow}{\tilde{\alpha}}^{(2)}(\mathbf{q},\mathbf{q_1},\mathbf{q_2};\omega_1,\omega_2)\big]_{\mathbf{G00}}\Bigg)\overset{\leftrightarrow}{A}_r(\mathbf{q_1};\omega_1)\mathbf{E_0}(\mathbf{q_1};\omega_1)\overset{\leftrightarrow}{A}_r(\mathbf{q_2};\omega_2)\mathbf{E_0}(\mathbf{q_2};\omega_2).\end{aligned} \tag{7.30}$$

This approach for obtaining the second-order polarization is intricate but it avoids the problem of defining the inverse of an integral operator, as done in Ref. [38].
Simple algebra gives

$$\big[\overset{\leftrightarrow}{\tilde{\alpha}}^{(1)}(\mathbf{q};\omega)\big]_{\mathbf{G0}}\frac{\mathbf{q}}{|\mathbf{q}|}\frac{\mathbf{q}}{|\mathbf{q}|}\overset{\leftrightarrow}{A}_l(\mathbf{q};\omega) = \frac{\big[\overset{\leftrightarrow}{\tilde{\alpha}}^{(1)}(\mathbf{q};\omega)\big]_{\mathbf{G0}}\frac{\mathbf{q}}{|\mathbf{q}|}\frac{\mathbf{q}}{|\mathbf{q}|}}{1-4\pi\left[\tilde{\alpha}^{LL}(\mathbf{q};\omega)\right]_{\mathbf{00}}}. \tag{7.31}$$

By inserting the expression of the fields, and by defining the in-plane averaged second-order susceptibility tensor $\overset{\leftrightarrow}{\chi}_m^{(2)}$ by

$$\begin{aligned}\mathbf{P_0^{(2)}}(\mathbf{q}_{||},z;\omega) = \int d\omega_1\int d\omega_2\delta(\omega-\omega_1-\omega_2)\int dz_1\int dz_2\sum_{\mathbf{q_1},\mathbf{q_2}}^{BZ}\delta_{\mathbf{q},(\mathbf{q_1}+\mathbf{q_2})}\\ \overset{\leftrightarrow}{\chi}_m^{(2)}(\mathbf{q}_{||},z,\mathbf{q_1}_{||},z_1,\mathbf{q_2}_{||},z_2;\omega_1,\omega_2)\mathbf{E_0}(\mathbf{q_1}_{||},z_1;\omega_1)\mathbf{E_0}(\mathbf{q_2}_{||},z_2;\omega_2),\end{aligned} \tag{7.32}$$

we obtain that

$$\begin{aligned}\overset{\leftrightarrow}{\chi}_m^{(2)}(\mathbf{q}_{||},z,\mathbf{q_1}_{||},z_1,\mathbf{q_2}_{||},z_2;\omega_1,\omega_2) = \frac{1}{2L_z}\sum_{q_z,q_{z1},q_{z2}}\sum_{G_z}\delta_{q_z,(q_{z1}+q_{z2})}e^{i(q_z+G_z)z}\\ \times\Bigg[\frac{4\pi\big[\overset{\leftrightarrow}{\tilde{\alpha}}^{(1)}(\mathbf{q};\omega)\big]_{\mathbf{G0}}\frac{\mathbf{q}}{|\mathbf{q}|}\frac{\mathbf{q}}{|\mathbf{q}|}}{1-4\pi\left[\tilde{\alpha}^{LL}(\mathbf{q};\omega)\right]_{\mathbf{00}}}\big[\overset{\leftrightarrow}{\tilde{\alpha}}^{(2)}(\mathbf{q},\mathbf{q_1},\mathbf{q_2};\omega_1,\omega_2)\big]_{\mathbf{000}}+\big[\overset{\leftrightarrow}{\tilde{\alpha}}^{(2)}(\mathbf{q},\mathbf{q_1},\mathbf{q_2};\omega_1,\omega_2)\big]_{\mathbf{Gz00}}\Bigg]\\ \times e^{-iq_{z_1}z_1}e^{-iq_{z2}z_2}\overset{\leftrightarrow}{A}_r(\mathbf{q_1};\omega_1)\overset{\leftrightarrow}{A}_r(\mathbf{q_2};\omega_2).\end{aligned} \tag{7.33}$$

The surface macroscopic second-order response function reads as

$$\overset{\leftrightarrow}{\chi}_M^{(2)S}(\mathbf{q},\mathbf{q_1},\mathbf{q_2};\omega_1,\omega_2) = \frac{1}{2L_z^2}\int_{-L_z}^{L_z}dzdz_1dz_2e^{-iq_zz}\mathcal{C}(z)\overset{\leftrightarrow}{\chi}_m^{(2)}(\mathbf{q}_{||},z,\mathbf{q_1}_{||},z_1,\mathbf{q_2}_{||},z_2;\omega_1,\omega_2)e^{iq_{z1}z_1}e^{iq_{z2}z_2}, \tag{7.34}$$

where $\mathcal{C}(z)$ is the same cut-function as the one introduced in Sec. 7.1.
This quantity describes the second-order response of a single surface of a slab in super-cell geometry.

Putting everything together, we obtain after some algebra that

$$\overset{\leftrightarrow}{\chi}{}^{(2)S}_{M}(\mathbf{q},\mathbf{q_1},\mathbf{q_2};\omega_1,\omega_2) = \left[\frac{4\pi\,\overset{\leftrightarrow}{\tilde{\alpha}}{}^{(1)S}(\mathbf{q};\omega)}{1-4\pi\left[\tilde{\alpha}^{LL}(\mathbf{q};\omega)\right]_{\mathbf{00}}}\frac{\mathbf{q}}{|\mathbf{q}|}\frac{\mathbf{q}}{|\mathbf{q}|}\left[\,\overset{\leftrightarrow}{\tilde{\alpha}}{}^{(2)}(\mathbf{q},\mathbf{q_1},\mathbf{q_2};\omega_1,\omega_2)\right]_{\mathbf{000}} + \overset{\leftrightarrow}{\tilde{\alpha}}{}^{(2)S}(\mathbf{q},\mathbf{q_1},\mathbf{q_2};\omega_1,\omega_2)\right]\overset{\leftrightarrow}{A}_r(\mathbf{q_1};\omega_1)\,\overset{\leftrightarrow}{A}_r(\mathbf{q_2};\omega_2). \tag{7.35}$$

This equation is the equivalent of Eq. (7.9) for the second order, where both surface ($\overset{\leftrightarrow}{\tilde{\alpha}}{}^{(2)S}$) and bulk ($\overset{\leftrightarrow}{\tilde{\alpha}}{}^{(2)}$) response functions are present. Notice that if we choose $\mathcal{C}(z)=1$, we obtain $\overset{\leftrightarrow}{\chi}{}^{(2)S}_{M} = \overset{\leftrightarrow}{A}_l\overset{\leftrightarrow}{\tilde{\alpha}}{}^{(2)}\overset{\leftrightarrow}{A}_r\overset{\leftrightarrow}{A}_r$, which is the result for the bulk materials, see, Chap. 1 and Ref. [41].

7.4.3 Optical limit for the macroscopic surface second-order susceptibility

The expression Eq. (7.35) gives access to the full second-order susceptibility tensor, but it could not be computed directly in the framework of the TDDFT. For the following, we restrict our discussion to the optical limit. The key quantity at second-order in that case is the longitudinal-longitudinal-longitudinal (LLL) part of the macroscopic second-order susceptibility tensor, see Chap. 1.
In the case of surfaces, the LLL part of the macroscopic second-order susceptibility tensor reads as

$$\chi^{(2)S,LLL}_{M}(\mathbf{q},\mathbf{q_1},\mathbf{q_2};\omega_1,\omega_2) = \epsilon^{LL}_{M}(\mathbf{q_1};\omega_1)\epsilon^{LL}_{M}(\mathbf{q_2};\omega_2) \times\left[\left(\epsilon^{S,LL}_{M}(\mathbf{q};\omega)-1\right)\left[\tilde{\alpha}^{(2),LLL}(\mathbf{q},\mathbf{q_1},\mathbf{q_2};\omega_1,\omega_2)\right]_{\mathbf{000}} + \tilde{\alpha}^{(2)S,LLL}(\mathbf{q},\mathbf{q_1},\mathbf{q_2};\omega_1,\omega_2)\right], \tag{7.36}$$

where we used the expression of $\overset{\leftrightarrow}{A}_r$ and that $\epsilon^{LL}_{M}(\mathbf{q};\omega) = \frac{1}{1+v_{\mathbf{0}}(\mathbf{q})\left[\chi^{(1)}_{\rho\rho}(\mathbf{q};\omega)\right]_{\mathbf{00}}}$.
We obtain from the conservation of charges, in the presence of the cut-function, and under the two same restrictions we already introduced for the linear response, see App. F.1,

$$\tilde{\alpha}^{(2)S,LLL}(\mathbf{q},\mathbf{q_1},\mathbf{q_2};\omega_1,\omega_2) = \frac{-i}{2|\mathbf{q}||\mathbf{q_1}||\mathbf{q_2}|}\chi^{S}_{\rho\rho\rho}(\mathbf{q},\mathbf{q_1},\mathbf{q_2};\omega_1,\omega_2).$$

It results that the LLL part of the surface second-order response tensor depends only upon surface average of the density-density-density response function of the system. The LLL part of the macroscopic surface second-order susceptibility tensor reads as

$$\boxed{\chi^{(2)S,LLL}_{M}(\mathbf{q},\mathbf{q_1},\mathbf{q_2},\omega_1,\omega_2) = \frac{-i}{2|\mathbf{q}||\mathbf{q_1}||\mathbf{q_2}|}\epsilon^{LL}_{M}(\mathbf{q_1};\omega_1)\epsilon^{LL}_{M}(\mathbf{q_2};\omega_2) \times\left[-v_{\mathbf{0}}(\mathbf{q})\bar{\chi}^{S}_{\rho\rho}(\mathbf{q},\mathbf{q};\omega)\left[\chi_{\rho\rho\rho}(\mathbf{q},\mathbf{q_1},\mathbf{q_2};\omega_1,\omega_2)\right]_{\mathbf{000}} + \chi^{S}_{\rho\rho\rho}(\mathbf{q},\mathbf{q_1},\mathbf{q_2};\omega_1,\omega_2)\right],} \tag{7.37}$$

where we used the fact that within the RPA, $\epsilon^{S,LL}_{M}(\mathbf{q};\omega)-1 = -v_{\mathbf{0}}(\mathbf{q})\bar{\chi}^{S}_{\rho\rho}(\mathbf{q},\mathbf{q};\omega)$.
This equation is the main result of this section. We have derived an expression for the LLL part of the surface second-order susceptibility tensor which depends only on the density-density-density

response function and its surface average. This equation is the equivalent of Eq. (7.13) obtained for the linear case. As in the linear case, we have to find a Dyson-like equation for the second-order surface quantity. This is the aim of the next section.

7.4.4 Calculation of $\chi_M^{(2)S,LLL}$ in TDDFT

The derivation of the macroscopic surface dielectric response relies on the knowledge of one quantity, namely the response function to the total macroscopic classical potential $\bar{\chi}^S_{\rho\rho}$. In App. F.2, I obtained two Dyson equations for the second-order response function to the total macroscopic classical potential, denoted $\bar{\chi}_{\rho\rho\rho}$.
In reciprocal space, Eq. (F.11a) reads as

$$\begin{aligned}\left[\chi^{(2)}_{\rho\rho\rho}(\mathbf{q},\mathbf{q_1},\mathbf{q_2};\omega_1,\omega_2)\right]_{\mathbf{GG'G''}} &= \sum_{\mathbf{G_1G_2}} \left[\bar{\chi}_{\rho\rho\rho}(\mathbf{q},\mathbf{q_1},\mathbf{q_2};\omega_1,\omega_2)\right]_{\mathbf{GG_1G_2}} \\ \times\Big[\delta_{\mathbf{G_1,G'}}+\delta_{\mathbf{G_1},\mathbf{0}}v_{\mathbf{0}}(\mathbf{q_1})\left[\chi^{(1)}_{\rho\rho}(\mathbf{q_1};\omega_1)\right]_{\mathbf{0G'}}\Big]\Big[\delta_{\mathbf{G_2},\mathbf{G''}}+\delta_{\mathbf{G_2},\mathbf{0}}v_{\mathbf{0}}(\mathbf{q_2})\left[\chi^{(1)}_{\rho\rho}(\mathbf{q_2};\omega_2)\right]_{\mathbf{0G''}}\Big] \\ +\left[\bar{\chi}_{\rho\rho}(\mathbf{q};\omega)\right]_{\mathbf{G0}}v_{\mathbf{0}}(\mathbf{q})\left[\chi^{(2)}_{\rho\rho\rho}(\mathbf{q},\mathbf{q_1},\mathbf{q_2};\omega_1,\omega_2)\right]_{\mathbf{0G'G''}},\end{aligned} \tag{7.38}$$

and we obtain from surface macroscopic averaging that

$$\begin{aligned}\chi^{(2)S}_{\rho\rho\rho}(\mathbf{q},\mathbf{q_1},\mathbf{q_2};\omega_1,\omega_2) &= \left[\bar{\chi}_{\rho\rho}(\mathbf{q};\omega)\right]_{\mathbf{00}}v_{\mathbf{0}}(\mathbf{q})\left[\chi^{(2)}_{\rho\rho\rho}(\mathbf{q},\mathbf{q_1},\mathbf{q_2};\omega_1,\omega_2)\right]_{\mathbf{000}} \\ +\bar{\chi}^S_{\rho\rho\rho}(\mathbf{q},\mathbf{q_1},\mathbf{q_2};\omega_1,\omega_2)\Big[1+v_{\mathbf{0}}(\mathbf{q_1})\left[\chi^{(1)}_{\rho\rho}(\mathbf{q_1};\omega_1)\right]_{\mathbf{00}}\Big]\Big[1+v_{\mathbf{0}}(\mathbf{q_2})\left[\chi^{(1)}_{\rho\rho}(\mathbf{q_2};\omega_2)\right]_{\mathbf{00}}\Big].\end{aligned} \tag{7.39}$$

The quantity $\bar{\chi}^S_{\rho\rho\rho}(\mathbf{q},\mathbf{q_1},\mathbf{q_2};\omega_1,\omega_2)$ is given in RPA by (see App. F.2)

$$\begin{aligned}\bar{\chi}^S_{\rho\rho\rho}(\mathbf{q},\mathbf{q_1},\mathbf{q_2};\omega_1,\omega_2) &= \sum_{\mathbf{G4}}\left[\chi^{(0)S}_{\rho\rho}(\mathbf{q};\omega)\right]_{\mathbf{0G_4}}\bar{v}_{\mathbf{G_4}}(\mathbf{q})\left[\bar{\chi}_{\rho\rho\rho}(\mathbf{q},\mathbf{q_1},\mathbf{q_2};\omega_1,\omega_2)\right]_{\mathbf{G_400}} \\ &+\sum_{\mathbf{G_3G_1}}\chi^{(0)S}_{\rho\rho\rho}(\mathbf{q},\mathbf{q_1}+\mathbf{G_1},\mathbf{q_2}+\mathbf{G_3};\omega_1,\omega_2) \\ \times\Big[\delta_{\mathbf{G_10}}+\bar{v}_{\mathbf{G_1}}(\mathbf{q_1})\left[\bar{\chi}_{\rho\rho}(\mathbf{q_1};\omega_1)\right]_{\mathbf{G_10}}\Big]\Big[\delta_{\mathbf{G_30}}+\bar{v}_{\mathbf{G_3}}(\mathbf{q_2})\left[\bar{\chi}_{\rho\rho}(\mathbf{q_2};\omega_2)\right]_{\mathbf{G_30}}\Big].\end{aligned} \tag{7.40}$$

Inserting Eq. (7.39) into Eq. (7.37) yields

$$\chi_M^{(2)S,LLL}(\mathbf{q},\mathbf{q_1},\mathbf{q_2};\omega_1,\omega_2) = \frac{-i}{2|\mathbf{q}||\mathbf{q_1}||\mathbf{q_2}|}\bar{\chi}^S_{\rho\rho\rho}(\mathbf{q},\mathbf{q_1},\mathbf{q_2};\omega_1,\omega_2). \tag{7.41}$$

This equation is the second-order equivalent of Eq. (7.18).
Again, we found that the surface response function to the total macroscopic classical potential is naturally related to surface macroscopic quantity. This exhibits the tight relation between the macroscopic quantities and the response functions to the total macroscopic classical potential. Indeed, it was already known that the bulk linear optical properties was obtained by the response to the total potential as well as the response to the total macroscopic classical potential. Here I have generalised this result by showing that the linear and nonlinear optical properties of bulk and surfaces can be obtained from the response functions to the total macroscopic classical potential. Note that this result is new, interesting, and has never been discussed for surfaces nor nonlinear optical properties.

We have transformed the problem of computing $\chi_M^{(2)S,LLL}(\mathbf{q},\mathbf{q_1},\mathbf{q_2};\omega_1,\omega_2)$ into the problem of computing $\bar{\chi}^S_{\rho\rho\rho}(\mathbf{q},\mathbf{q_1},\mathbf{q_2};\omega_1,\omega_2)$. In order to solve the equation Eq. (7.40), we follow the approach previously used for the linear calculation, defining the matrices $\left[\bar{\chi}^S_{\rho\rho\rho}\right]_{\mathbf{GG'G''}}$ and $\left[\chi^{(0)S}_{\rho\rho\rho}\right]_{\mathbf{GG'G''}}$, where we replace the first line of the matrices $\left[\bar{\chi}_{\rho\rho\rho}\right]_{\mathbf{GG'G''}}$ and $\left[\chi^{(0)}_{\rho\rho\rho}\right]_{\mathbf{GG'G''}}$ by $\bar{\chi}^S_{\rho\rho\rho}(\mathbf{q},\mathbf{q_1}+\mathbf{G'},\mathbf{q_2}+\mathbf{G''};\omega_1,\omega_2)$ and $\chi^{(0)S}_{\rho\rho\rho}(\mathbf{q},\mathbf{q_1}+\mathbf{G'},\mathbf{q_2}+\mathbf{G''};\omega_1,\omega_2)$ respectively. From Eq. (7.38) and Eq. (7.39), we obtain that

$$\bar{\chi}^S_{\mathbf{GG'G''}} = \sum_{\mathbf{G_4}} \chi^{(0)S}_{\mathbf{GG_4}} \bar{v}_{\mathbf{G_4}} \bar{\chi}^S_{\mathbf{G_4G'G''}} + \sum_{\mathbf{G_3G_1}} \chi^{(0)S}_{\mathbf{GG_3G_1}} \left[\delta_{\mathbf{G_1G'}} + \bar{v}_{\mathbf{G_1}}\bar{\chi}_{\mathbf{G_1G'}}\right]\left[\delta_{\mathbf{G_3G''}} + \bar{v}_{\mathbf{G_3}}\bar{\chi}_{\mathbf{G_3G''}}\right], \quad (7.42)$$

that we can solve for obtaining

$$\bar{\chi}^S_{\mathbf{000}} = \sum_{\mathbf{G_4G_3G_1}} \left(Id - \chi^{(0)S}\bar{v}\right)^{-1}_{\mathbf{0G_4}} \chi^{(0)S}_{\mathbf{G_4G_3G_1}} \left[\delta_{\mathbf{G_1G'}} + \bar{v}_{\mathbf{G_1}}\bar{\chi}_{\mathbf{G_10}}\right]\left[\delta_{\mathbf{G_3G''}} + \bar{v}_{\mathbf{G_3}}\bar{\chi}_{\mathbf{G_30}}\right],$$

yielding an expression for the LLL part of the surface macroscopic second-order susceptibility tensor,

$$\boxed{\begin{aligned}\chi_M^{(2)S,LLL}(\mathbf{q},\mathbf{q_1},\mathbf{q_2};\omega_1,\omega_2) = \frac{-i}{2|\mathbf{q}||\mathbf{q_1}||\mathbf{q_2}|} \sum_{\mathbf{G_4G_3G_1}} \left[Id - \chi^{(0)S}_{\rho\rho}(\mathbf{q};\omega)\bar{v}(\mathbf{q})\right]^{-1}_{\mathbf{0G_4}} \\ \times \left[\chi^{(0)S}_{\rho\rho\rho}(\mathbf{q},\mathbf{q_1},\mathbf{q_2};\omega_1,\omega_2)\right]_{\mathbf{G_4G_3G_1}} \left[Id + \bar{v}(\mathbf{q_1})\bar{\chi}_{\rho\rho}(\mathbf{q_1};\omega_1)\right]_{\mathbf{G_10}} \left[Id + \bar{v}(\mathbf{q_2})\bar{\chi}_{\rho\rho}(\mathbf{q_2};\omega_2)\right]_{\mathbf{G_30}}.\end{aligned}} \quad (7.43)$$

This results is the main result of this chapter. It allows us to compute the macroscopic surface second-order response function in the random-phase approximation, and including the effect of local-fields. This result has been obtained without introducing any new approximation than the random-phase approximation and the long-wavelength approximation. Expressed as Eq. (7.43), this formula requires only the knowledge of the two matrices $\left[\chi^{(0)S}_{\rho\rho}\right]_{\mathbf{GG'}}$ and $\left[\chi^{(0)S}_{\rho\rho\rho}\right]_{\mathbf{GG'G''}}$, thus opening the way to simple numerical implementations.

It is worthwhile to notice that Eq. (7.43) proves that the long-range, non-analytical part of the Coulomb interaction does not affect the LLL part of the macroscopic second-order response tensor. The same conclusion is straightforwardly obtained for the bulk material, by putting $\mathcal{C}(z) = 1$. Therefore, *we shown that the macroscopic second-order susceptibility is an analytic function of* $\mathbf{q}$[1]. This remarkable result is an extension of the already known equivalent result for linear dielectric tensor of bulk materials. This analyticity has also been pointed out by Del Sole and Fiorino for the surface *linear* response in Ref. [38], but has never been reported for the case of second-order response function, neither for bulk or surface cases. Note that our result is general and is applicable to any crystal, independently of its symmetries.

The expression of the full matrix $\left[\chi^{(0)S}_{\rho\rho\rho}\right]_{\mathbf{GG'G''}}$ is reported in App. I, together with numerical calculations, presenting for the first time the effects of local-fields on the spectra of second-harmonic generation from semiconductor surfaces.

[1] To be more rigorous, we have only shown here that the function is Taylor expandable in $\mathbf{q}$.

7.5 Properties of the surface macroscopic quantities

In this section, I discuss some properties of the surface macroscopic second-order susceptibility.

A more familiar form

The expression Eq. (7.43) does not have the same form as the macroscopic second-order response function for bulk materials [41]. In particular, the role of the dielectric functions that appear in the expression of the LLL part of the macroscopic surface second-order response function is not clear from Eq. (7.43). To make it more obvious, we define the quantity

$$\begin{aligned}\left[\hat{\chi}^S(\mathbf{q},\mathbf{q_1},\mathbf{q_2};\omega_1,\omega_2)\right]_{\mathbf{GG'G''}} &= \left[\bar{\chi}^S(\mathbf{q},\mathbf{q_1},\mathbf{q_2};\omega_1,\omega_2)\right]_{\mathbf{GG'G''}} \\ \times\Big[\delta_{\mathbf{G_1},\mathbf{G'}}+\delta_{\mathbf{G_1},\mathbf{0}}v_{\mathbf{0}}(\mathbf{q_1})\left[\chi^{(1)}_{\rho\rho}(\mathbf{q_1};\omega_1)\right]_{\mathbf{0G'}}\Big]&\Big[\delta_{\mathbf{G_2},\mathbf{G''}}+\delta_{\mathbf{G_2},\mathbf{0}}v_{\mathbf{0}}(\mathbf{q_2})\left[\chi^{(1)}_{\rho\rho}(\mathbf{q_2};\omega_2)\right]_{\mathbf{0G''}}\Big] \\ &+\left[\bar{\chi}^S(\mathbf{q};\omega)\right]_{\mathbf{G0}}v_{\mathbf{0}}(\mathbf{q})\left[\hat{\chi}^S(\mathbf{q},\mathbf{q_1},\mathbf{q_2};\omega_1,\omega_2)\right]_{\mathbf{0G'G''}},\end{aligned} \tag{7.44}$$

which gives, once averaged for the surface,

$$\left[\bar{\chi}^S(\mathbf{q},\mathbf{q_1},\mathbf{q_2};\omega_1,\omega_2)\right]_{\mathbf{000}} = \epsilon_M^{S,LL}(\mathbf{q};\omega)\left[\hat{\chi}^S(\mathbf{q},\mathbf{q_1},\mathbf{q_2};\omega_1,\omega_2)\right]_{\mathbf{000}}. \tag{7.45}$$

Therefore, Eq. (7.41) can be rewritten as

$$\chi_M^{(2)S,LLL}(\mathbf{q},\mathbf{q_1},\mathbf{q_2};\omega_1,\omega_2) = \frac{-i}{2|\mathbf{q}||\mathbf{q_1}||\mathbf{q_2}|}\epsilon_M^{S,LL}(\mathbf{q};\omega)\left[\hat{\chi}^S_{\rho\rho\rho}(\mathbf{q},\mathbf{q_1},\mathbf{q_2};\omega_1,\omega_2)\right]_{\mathbf{000}}\epsilon_M^{LL}(\mathbf{q_1};\omega_1)\epsilon_M^{LL}(\mathbf{q_2};\omega_2), \tag{7.46}$$

where $\hat{\chi}^S_{\rho\rho\rho}$ is obtained by solving the matrix equation

$$\begin{aligned}\left[\hat{\chi}^S(\mathbf{q},\mathbf{q_1},\mathbf{q_2};\omega_1,\omega_2)\right]_{\mathbf{GG'G''}} &= \sum_{\mathbf{G_2G_1}}\left[\chi^{(0)S}(\mathbf{q},\mathbf{q_1},\mathbf{q_2};\omega_1,\omega_2)\right]_{\mathbf{GG_1G_3}} \\ \times\Big[\delta_{\mathbf{G_1G'}}+v_{\mathbf{G_1}}(\mathbf{q_1})\left[\chi^{(1)}_{\rho\rho}(\mathbf{q_1};\omega_1)\right]_{\mathbf{G_1G'}}\Big]&\Big[\delta_{\mathbf{G_2G''}}+v_{\mathbf{G_2}}(\mathbf{q_1})\left[\chi^{(1)}_{\rho\rho}(\mathbf{q_1};\omega_2)\right]_{\mathbf{G_2G''}}\Big] \\ &+\sum_{\mathbf{G_1}}\left[\chi^{(0)S}_{\rho\rho}(\mathbf{q};\omega)\right]_{\mathbf{GG_1}}v_{\mathbf{G_1}}(\mathbf{q})\left[\hat{\chi}^S(\mathbf{q},\mathbf{q_1},\mathbf{q_2};\omega_1,\omega_2)\right]_{\mathbf{G_1G'G''}}.\end{aligned} \tag{7.47}$$

This new expression for $\chi_M^{(2)S,LLL}$ exposes more the physical meaning of the surface averaging. The two last dielectric functions are not modified by the presence of the surface as the incoming fields are allowed to go everywhere in the system. On the contrary, the radiated field experiences only a screening from the surface dielectric function, meaning from the region where it is emitted. Notice also that this form simplifies the implementation of the formalism presented in this chapter in any TDDFT code for bulk second-harmonic generation. Finally, the formalism being valid for any ω_1 and ω_2, it is not restricted to the second-harmonic generation and can also be applied to any second-order optical process.

Independent-particle approximation

In the independent-particle approximation, *i.e.*, neglecting local-field effects, we keep only the matrix elements corresponding to $\mathbf{G} = \mathbf{0}$. In this case, the solution of Eq. (7.47) becomes trivial

$$\begin{aligned}\left[\hat{\chi}^S(\mathbf{q},\mathbf{q_1},\mathbf{q_2};\omega_1,\omega_2)\right]_{\mathbf{00}} =& \frac{\left[\chi^{(0)S}_{\rho\rho\rho}(\mathbf{q},\mathbf{q_1},\mathbf{q_2};\omega_1,\omega_2)\right]_{\mathbf{000}}}{1-\left[\chi^{(0)S}_{\rho\rho}(\mathbf{q};\omega)\right]_{\mathbf{00}} v_{\mathbf{0}}(\mathbf{q})} \\ & \times\left[1+v_{\mathbf{0}}(\mathbf{q_1})\left[\chi^{(1)}_{\rho\rho}(\mathbf{q_1};\omega_1)\right]_{\mathbf{00}}\right]\left[1+v_{\mathbf{0}}(\mathbf{q_2})\left[\chi^{(1)}_{\rho\rho}(\mathbf{q_2};\omega_2)\right]_{\mathbf{00}}\right].\end{aligned} \tag{7.48}$$

Inserting this result into the expression of the macroscopic second-order surface susceptibility gives after simple algebra

$$\chi^{(2)S,LLL}_M(\mathbf{q},\mathbf{q_1},\mathbf{q_2};\omega_1,\omega_2) = \frac{-i}{2|\mathbf{q}||\mathbf{q_1}||\mathbf{q_2}|}\left[\chi^{(0)S}_{\rho\rho\rho}(\mathbf{q},\mathbf{q_1},\mathbf{q_2};\omega_1,\omega_2)\right]_{\mathbf{000}}, \tag{7.49}$$

where $\left[\chi^{(0)S}_{\rho\rho\rho}\right]_{\mathbf{000}}$ is the surface average of the independent-particle response function, as already computed in Chap. 6. Therefore this new formalism, in addition to fully taking into account the local-fields, yields in the independent-particle approximation the previously introduced microscopic formalism (see Chap. 5 and Chap. 6).

Conclusions

In conclusion, in this chapter I have presented the detailed derivation of the *ab initio* formalism I developed for calculating the macroscopic optical response of crystal surfaces, at first- and second-order. In this formalism, only one single surface contributes to the optical responses, thanks to the formalism of the extraction of the surface spectra introduced in Chap.5.
In particular, I have presented how we can evaluate the macroscopic surface second-order susceptibility $\chi^{(2)S}_M$, and therefore include the local-field effects on the surface second-harmonic generation spectra.
This approach is based on TDDFT and is valid for any crystal surfaces represented by means of a super-cell with slab geometry. In our formalism, we first derived a relation between the macroscopic surface averaged quantities and the microscopic components of the linear and second-order response functions. Then, we considered the case of the long-wavelength limit where every quantities can be reduced to the calculation of the longitudinal response to longitudinal perturbation without loosing information (see Chap. 1). In that case, I have shown that in the random-phase approximation, the macroscopic surface quantities are expressed only in terms of microscopic components of the surface averaged independent-particle response functions $\chi^{(0)S}_{\rho\rho}$ and $\chi^{(0)S}_{\rho\rho\rho}$. Moreover, we found that the long-range non-analytical part of the Coulomb potential does not affect the macroscopic second-order susceptibility, for both bulk material and surfaces.

8. Local-field effects for linear optical properties of thin-films and surfaces

The fluctuations of the electric field at the atomic scale, the so-called local-fields (LF), play a key role in the physics of surfaces. As already explained in Chap. 1, strong effects of local-fields are expected perpendicularly to the surface plane, due to the abrupt change in the electronic density. The impact of local-fields on surface optical spectra has been discussed for years, especially in the context of the so-called intrinsic or bulk-originated effects [231,232]. Analytic expressions for the surface response have been presented, but their numerical evaluation have often been restricted to simple cases [39,40,233,234]. More recently, accurate calculations have been performed on complex surfaces [235–237], but most of the efforts have been dedicated to in-plane components.

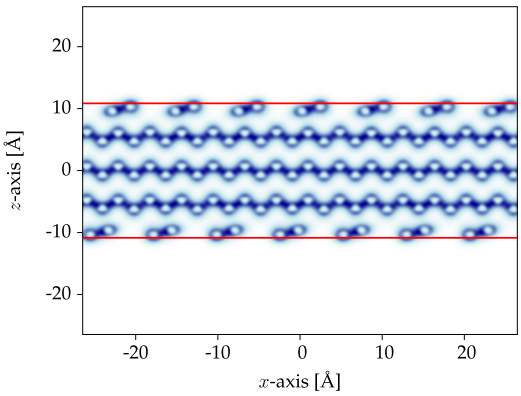

Fig. 8.1: Electronic density of a slab with two Si(001)2×1 surfaces, in the x-z plan [230].

Surprisingly, no effort has been devoted to investigate the effect of local-fields on the out-of-plane dielectric response of surfaces, $\epsilon_\perp$, while the local-field effects are expected to be stronger in the out-of-plane direction. The out-of-plane component is of particular importance for many phenomena, such as transmission or reflection at non-grazing light incidence and for all polarizations (except for the simple case of s-polarised light), when both in- and out-of-plane components mix.

In this chapter, I will show that the state-of-the-art approach for computing optical properties of surfaces in reciprocal space, namely the super-cell approach, fails to compute the *surface* optical properties when including the effect of LF. In a second part, I will present a new scheme for the evaluation of these optical properties in a surface-adapted space, where the surface is treated as an isolated system. From this approach, I will derive in the last part of this chapter, another new approach that allows us to properly account for the local-field effects on the optical properties of surfaces in reciprocal space. In this chapter, the distinction between a thin-film and a surface is discussed.

8.1 Local-field effects and super-cells

In order to investigate the LF effects on optical properties of surfaces, we have chosen a slab with two clean Si(001)2×1 surfaces as a model system. [1] The surface has been studied with the experimental lattice constant of 5.43 Å and $N = 16$ atomic layers (32 atoms), corresponding to a slab of thickness 21.72 Å. Dielectric functions have been calculated using the TDDFT code DP [116].
The optical dielectric function is given, in reciprocal space, by

$$\epsilon_M(\omega) = \lim_{\mathbf{q}\to\mathbf{0}} \frac{1}{\epsilon^{-1}_{\mathbf{G}=\mathbf{G}'=\mathbf{0}}(\mathbf{q};\omega)}. \tag{8.1}$$

Here $\mathbf{q}$ denotes a vanishing wave-vector and $\mathbf{G}$, $\mathbf{G}'$ are reciprocal lattice vectors of the crystal. The inverse of the microscopic dielectric matrix is given by $\epsilon^{-1}_{\mathbf{G}\mathbf{G}'}(\mathbf{q};\omega) = \delta_{\mathbf{G}\mathbf{G}'} + v(\mathbf{q}+\mathbf{G})\chi^{(1)}_{\mathbf{G}\mathbf{G}'}(\mathbf{q};\omega)$, where $v(\mathbf{q}+\mathbf{G}) = 4\pi/|\mathbf{q}+\mathbf{G}|^2$ is the Coulomb potential and $\chi^{(1)}$ the density response function. In frequency and reciprocal space, one has to solve a Dyson-like matrix equation for obtaining $\chi^{(1)}_{\mathbf{G}\mathbf{G}'}(\mathbf{q};\omega)$

$$\chi^{(1)}_{\mathbf{G}\mathbf{G}'}(\mathbf{q};\omega) = \chi^{(1)}_{0,\mathbf{G}\mathbf{G}'}(\mathbf{q};\omega) + \sum_{\mathbf{G}''\mathbf{G}'''} \chi^{(1)}_{0,\mathbf{G}\mathbf{G}''}(\mathbf{q};\omega) K_{\mathbf{G}''\mathbf{G}'''}(\mathbf{q};\omega)\chi^{(1)}_{\mathbf{G}'''\mathbf{G}'}(\mathbf{q};\omega). \tag{8.2}$$

In principle, the kernel K contains two terms, the Coulomb potential v and the exchange-correlation kernel f_{xc}. In the following of this chapter, we will restrict ourselves to the Random-Phase Approximation (RPA), where $f_{\text{xc}} = 0$, as we are interested only in the description of the local-fields. Nevertheless, our results are general and can be used for any kernel. $\chi^{(1)}_0$ is the independent-particle response function given in reciprocal space by

$$\chi^{(1)}_{0,\mathbf{G}\mathbf{G}'}(\mathbf{q};\omega) = \frac{2}{N_{\mathbf{k}} V_{\text{cell}}} \sum_{m,n} \sum_{\mathbf{k}}^{BZ} (f_{n,\mathbf{k}} - f_{m,\mathbf{k}+\mathbf{q}}) \frac{\langle n,\mathbf{k}|e^{-i(\mathbf{q}+\mathbf{G})\mathbf{r}}|m,\mathbf{k}+\mathbf{q}\rangle\langle m,\mathbf{k}+\mathbf{q}|e^{i(\mathbf{q}+\mathbf{G}')\mathbf{r}}|n,\mathbf{k}\rangle}{(E_{n,\mathbf{k}} - E_{m,\mathbf{k}+\mathbf{q}} + \tilde{\omega})}, \tag{8.3}$$

where $f_{n,\mathbf{k}}$ is the Fermi occupation number of the Bloch state $|n,\mathbf{k}\rangle$ with the energy $E_{n,\mathbf{k}}$. $N_{\mathbf{k}}$ is the number of $\mathbf{k}$-points and V_{cell} refers to the volume of the cell, $\tilde{\omega} = \omega + i\eta$ is the frequency with a small positive imaginary part η, that turns on adiabatically the electromagnetic field. The volume of the matter inside the cell is denoted V_{mat} in the following.

In Fig. 8.2, we present the results of the IPA calculation, where $\epsilon_M = 1 - v_{\mathbf{0}}\chi^{(1)}_{0,\mathbf{0}\mathbf{0}}$, with $\chi^{(1)}_0$ defined by Eq. (8.3), for different sizes of the vacuum slab, denoted void1 (vacuum size=21.72 Å; $V_{\text{cell}}/V_{\text{mat}} = 2$), void2 (vacuum size=43.44 Å; $V_{\text{cell}}/V_{\text{mat}} = 3$) and void3 (vacuum size=65.17 Å; $V_{\text{cell}}/V_{\text{mat}} = 4$), as schematically shown. The convergence parameters are given in Tab. 8.1. We present also the result of the renormalized super-cell calculation, using V_{mat} instead of V_{cell} for the normalization volume in Eq. (8.3). In that case, the result of the cal-

Param.	void1	void2	void3
nkpt	256	256	256
nband	300	300	400
npwwfn	1499	1499	7987
npwmat	299	391	399

Tab. 8.1: Parameters.

[1] This surface has already been presented in Chap. 4 and the numerical details such as atomic positions have been given in Sec. 5.1.3.

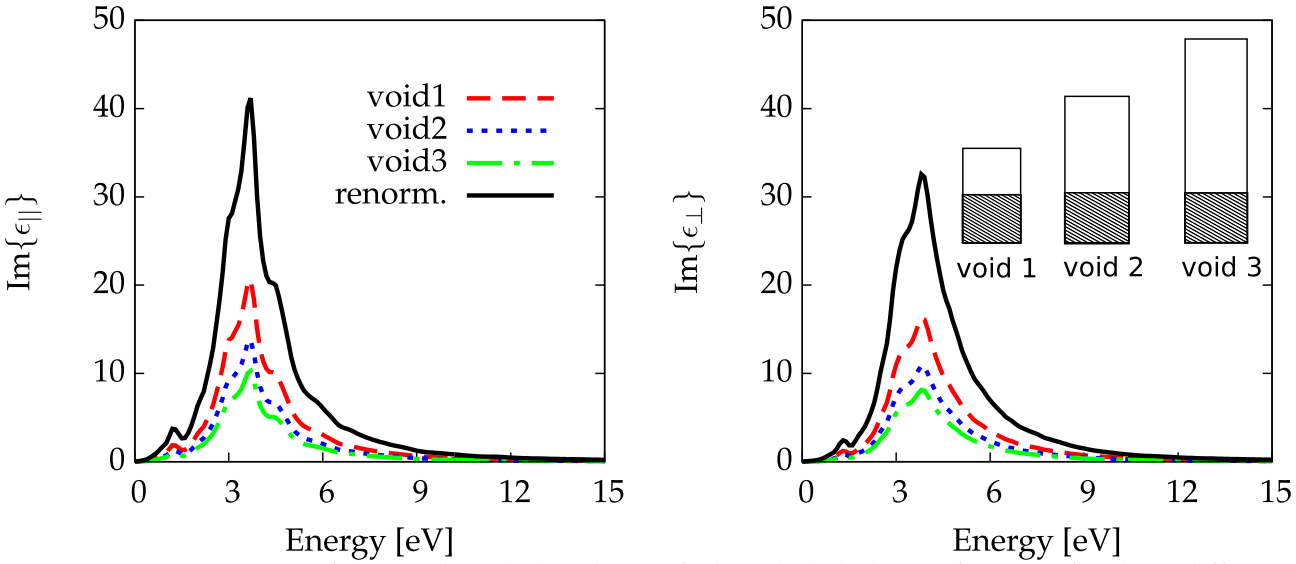

Fig. 8.2: Imaginary part of the in-plane ($\epsilon_{||}$) and out-of-plane ($\epsilon_{\perp}$) dielectric function for three different sizes of the super-cell. Local field effects are not included. The three super-cells are sketched in inset of the right panel.

culations for the different super-cells are the same, showing that the only dependence on the volume of the cell stands in the explicit prefactor volume in Eq. (8.3).

In Fig. 8.3, we report the in-plane ($\epsilon_{||}$) and out-of-plane ($\epsilon_{\perp}$) dielectric responses of the Si(001)2×1 surface in the presence of local fields (RPA), for the three different sizes of the vacuum region previously defined, as given by the code. The in-plane response (left panel) behaves similarly to the IPA results. Indeed the different calculations, including the effect of Local-Field (LF) are identical once renormalized. The peak position of the in-plane RPA result is identical to the IPA peak position, and only the spectral weight is affected by the local fields; which reduce the weight by approximatively 10% in the low-energy region. Concerning the out-of-plane dielectric response (right panel), the results strongly depend on the size of the vacuum introduced in the super-cell, in a way that cannot be attributed only to the normalization volume, since the position of the peak shifts in energy. Note also the drastic change in the peak position and amplitude, as compared to the IPA calculation (see Fig. 8.2). Note that the position of the main absorption peak of the out-of-plane dielectric function is getting closer to the plasmon peak position of bulk silicon (16.8 eV) and might converge to it.
This result obviously does not correspond to the dielectric function of a silicon surface nor a silicon thin-film, as experimental data show only a small variation of the optical gap with respect to the thickness of ultra-thin films of silicon [238, 239]. I also want to stress that the surfaces are not interacting as proved by the fact that we can renormalise the IPA results (see Fig. 8.2).

In order to understand this *a priori* unexpected result, *i.e.*, the different behaviour of the IPA and RPA responses with vacuum, we can use the so-called "effective-medium approach" [240]. This theory exhibits two limiting cases, called Wiener bounds, which correspond to no screening of the field inside the material and the maximum screening of the field inside the material [240]. Said differently, the two limiting cases correspond respectively to $\mathbf{E}$ or $\mathbf{D}$ uniform in the material. In the case of no screening, a composite material made of a bulk part and vacuum has an effective dielectric function given by $\epsilon_{\text{super-cell}} = f + (1-f)\epsilon_{\text{bulk}}$; where f refers to the amount of vacuum introduced in

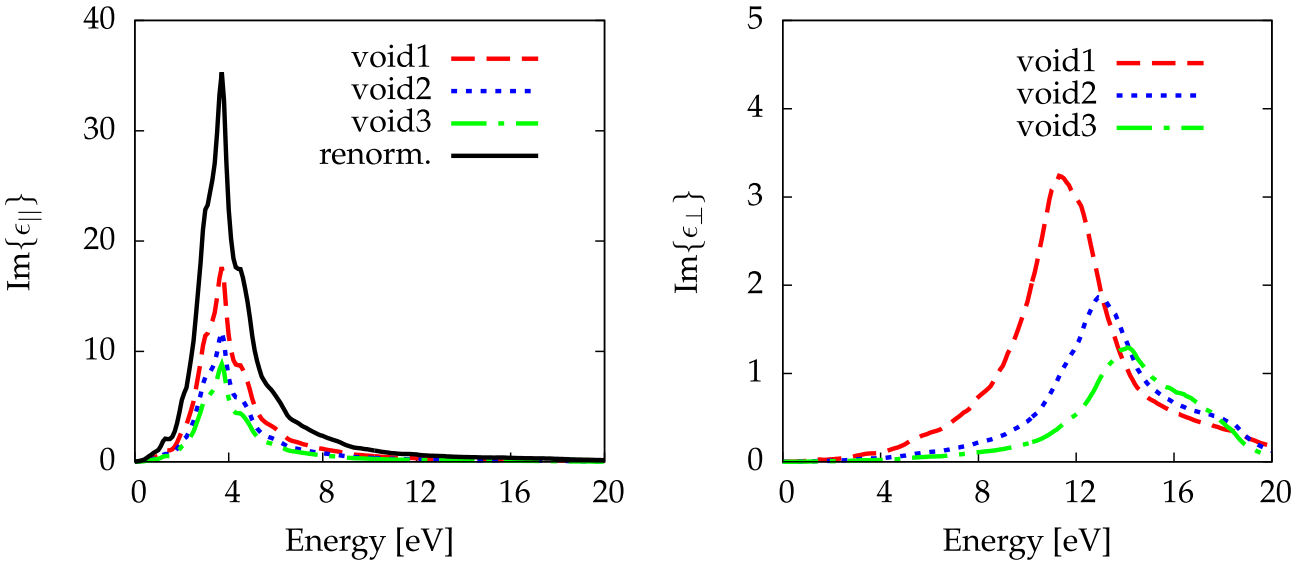

Fig. 8.3: Imaginary part of the in-plane ($\epsilon_{||}$) and out-of-plane ($\epsilon_{\perp}$) dielectric function for three different sizes of the super-cell. Local field effects are included. Note the change in the scale for the right panel.

the composite. This case corresponds to the case of the independent-particle approximation as there is no local-fields, thus explaining why all the spectra (in-plane and out-of-plane) behave similarly with vacuum.

In the case of the in-plane RPA optical responses, there is almost no local-field effects, because we are close to the no-screening case, and the corresponding formula is valid. In the out-of-plane direction, when local-field effects are included, the correct description using the effective-medium theory is the maximal screening limit. I show in Fig. 8.4 the results obtained through the effective-medium approach for maximal screening, *i.e.*, using $\epsilon^{-1}_{\text{super-cell}} = f + (1-f)\epsilon^{-1}_{\text{bulk}}$, applied to the super-cells and compared to the out-of-plane result of Fig. 8.3.

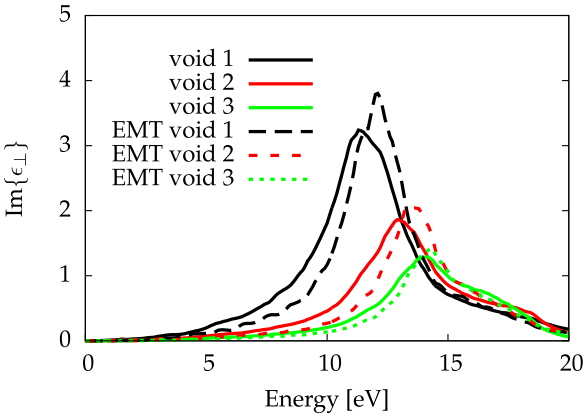

Fig. 8.4: Comparison between the super-cell and effective medium theory calculations.

This simple model reproduces quite well the TDDFT results and thus shows that the standard calculation in a super-cell approach amounts to averaging over the whole super-cell. The conclusion of this comparison is that when using super-cells in reciprocal space, only the optical properties of the entire super-cell, as an effective medium, are obtained; and the optical response of the slab is not accessible directly.

Notice that some failures of the super-cell approach have already been pointed out, *e.g.*, in Ref. [241], where authors have noticed that the screened Coulomb interaction W is "substantially influenced by the repeated-slab geometry".

8.2 Mixed-space approach

8.2.1 A surface-adapted space

The super-cell approach and the periodicity implied by this method is not perfectly adapted to the slab geometry. Indeed, the surfaces that we want to model are periodic systems in two dimensions and aperiodic in the third one. Moreover, as shown above, the super-cells do not yield the expected slab optical response.
Therefore, I chose a different approach for computing optical properties of surfaces, changing to the real space for computing the optical properties. The idea of abandoning the periodic boundary conditions and to work in real-space is not a novel idea of this thesis, and was already suggested in Ref. [241] as a possible cure for issues related to the super-cell approach. The authors decided to not investigate this approach in their paper. The real space approach for computing optical properties of surfaces has been successfully applied to surface plasmons, *e.g.*, Refs. [242,243].
The surfaces are isolated in the out-of-plane direction. Thus, in the direction perpendicular to the plane of the surface, I decided to treat the system in real space, as it is known to be efficient for isolated systems. The in-plane directions are treated in the reciprocal space, as it is customary for extended systems. In this thesis, I refer to this space as the "mixed-space".
In this mixed-space, the slab is truly isolated, because there is no out-of-plane periodicity; whereas in reciprocal space, the slab is artificially isolated by increasing the size of the vacuum region. As a consequence, we expect calculations in the mixed-space to yield directly the optical properties of the slab and not of the super-cell. Also, in the mixed-space, the size of the vacuum region is no more a convergence parameter and the vacuum serves only for describing the exponential decay of the density.
At the light of all these points, the mixed-space appears as the natural choice for working with thin-films and surfaces. Nevertheless, as it will be discussed latter, the numerical cost associated with the mixed-space is prohibitive and a new approach, also developed during this thesis should be preferred instead.

8.2.2 TDDFT and mixed-space in practice

Let us consider a super-cell containing a slab of matter and some vacuum. We denote the height of this super-cell L_z whereas L_z^{mat} refers to the thickness of the slab. The calculation of optical properties of surfaces in the mixed-space proceeds as follow:

1. The independent-particle susceptibility $\chi_0^{(1)}(\mathbf{q}_{||}, z, z'; \omega)$ is computed. Instead of writing a new TDDFT code for computing the quantity $\chi_0^{(1)}(\mathbf{q}_{||}, z, z'; \omega)$ directly, I obtained this quantity from the DP code [116]. More precisely, $\chi_0^{(1)}(\mathbf{q}_{||}, z, z'; \omega)$ is obtained by Fourier transforming the matrix $\left[\chi_0^{(1)}(\mathbf{q}; \omega)\right]_{G_z, G_z'}$, computed with the DP code. [2]

[2]The initial super-cell represents a periodic system. Nevertheless, in real space, we pad the space with zeros, thus isolating the system. Therefore we describe an isolated slab, even if the initial IPA response function has been calculated with a super-cell approach.

2. The fully interacting response function $\chi^{(1)}$ is obtained by solving the Dyson-like equation. In Ref. [242], authors have shown that neglecting the in-plane dispersion of the susceptibility gives reliable results for surface calculations. Under that approximation, *i.e.*, considering only the components of the response functions such as $\mathbf{G}_{||} = \mathbf{G'}_{||} = 0$ as in-plane reciprocal lattice vectors, the Dyson-like equation reads as[3]

$$\chi^{(1)}(\mathbf{q}_{||}, z, z'; \omega) = \chi_0^{(1)}(\mathbf{q}_{||}, z, z'; \omega) + \int_{-\infty}^{+\infty} dz_1 dz_2 \chi_0^{(1)}(\mathbf{q}_{||}, z, z_1; \omega) v(\mathbf{q}_{||}, z_1, z_2) \chi^{(1)}(\mathbf{q}_{||}, z_2, z'; \omega). \tag{8.4}$$

In practice, this equation is solved on a real space grid. On a grid, the Dyson equation Eq. (8.4) becomes a matrix equation. The solution of this matrix equation reads as

$$\chi^{(1)}(\mathbf{q}_{||}; \omega) = \frac{1}{\Delta_z} M^{-1}(\mathbf{q}_{||}; \omega) \chi_0^{(1)}(\mathbf{q}_{||}; \omega), \tag{8.5}$$

where $M(\mathbf{q}_{||}; \omega)$ is an $N_{\mathbf{G}} \times N_{\mathbf{G}}$ matrix defined by

$$M_{ij}(\mathbf{q}_{||}; \omega) = M(\mathbf{q}_{||}, z_i, z_j; \omega) = \frac{\delta_{ij}}{\Delta_z} - \sum_k \chi_0^{(1)}(\mathbf{q}_{||}, z_i, z_k; \omega) v(\mathbf{q}_{||}, z_k, z_j) \Delta_z,$$

with the 2D Fourier transform of the Coulomb potential given by

$$v(\mathbf{q}_{||}, z, z') = 2\pi e^{-|\mathbf{q}_{||}||z - z'|} / |\mathbf{q}_{||}|. \tag{8.6}$$

3. In order to compute the absorption spectra, the inverse of the microscopic dielectric matrix, defined by [244, 245]

$$\begin{aligned} \epsilon^{-1}(\mathbf{q}_{||}, z, z'; \omega) &= \delta(z, z') + \int dz_1 v(\mathbf{q}_{||}, z, z_1) \chi^{(1)}(\mathbf{q}_{||}, z_1, z'; \omega) \\ &\overset{\text{grid}}{\approx} \frac{\delta_{ij}}{\Delta_z} + \sum_{z_k} v(\mathbf{q}_{||}, z_i, z_k) \chi^{(1)}(\mathbf{q}_{||}, z_k, z_j; \omega) \Delta_z, \end{aligned} \tag{8.7}$$

is averaged, using

$$\epsilon^{-1}(\mathbf{q}; \omega) = \frac{1}{L_z} \int dz \int dz' e^{-iq_z z} \epsilon^{-1}(\mathbf{q}_{||}, z, z'; \omega) e^{iq_z z'} \overset{\text{grid}}{\approx} \sum_{z_i, z_j} e^{-iq_z(z_i - z_j)} \epsilon^{-1}(\mathbf{q}_{||}, z_i, z_j; \omega) \frac{\Delta_z^2}{L_z}. \tag{8.8}$$

Notice here that this is the *macroscopic* average [44] which is computed, *i.e.*, containing the full dependence on the momentum $\mathbf{q}$, and not a spatial average which would contain only the in-plane momentum. This allows us to compute all the components of the dielectric tensor, as explained below, and also to compare with previous results for instance.

[3] The approximation of taking only the $\mathbf{G}_{||} = \mathbf{G'}_{||} = 0$ contribution reduces drastically the burden associated with the solution of this equation, and is enough as we are using the real space approach as a test-case.

4. The macroscopic dielectric tensor is computed, using the usual expression

$$\epsilon_M(\mathbf{q};\omega) = \lim_{\mathbf{q}\to\mathbf{0}} \frac{1}{\epsilon^{-1}(\mathbf{q};\omega)}.$$

Due to the expression of the Coulomb potential in the mixed-space Eq. (8.6), some care is required for computing the zz component of the macroscopic dielectric tensor. Indeed, for obtaining the zz component, one would choose $\mathbf{q} = q_z\hat{\mathbf{e}}_\mathbf{z}$. But this leads to a divergent Coulomb potential (see Eq.(8.6)) which is prohibited for numerical simulations. This can be disappointing considering that I decided to use the mixed-space method precisely to calculate the out-of-plane component of the dielectric tensor.
This apparent problem is nevertheless solved easily using the following approach:
i) The non-interacting response function $\chi_0^{(1)}$ is evaluated for three different values of $\mathbf{q}$, which are $\mathbf{q_1} = q_{||}\hat{\mathbf{e}}_\mathbf{x}$, $\mathbf{q_2} = q_{||}\hat{\mathbf{e}}_\mathbf{x} + q_z\hat{\mathbf{e}}_\mathbf{z}$ and $\mathbf{q_3} = q_{||}\hat{\mathbf{e}}_\mathbf{x} - q_z\hat{\mathbf{e}}_\mathbf{z}$.
ii) The macroscopic dielectric tensor $\epsilon(\mathbf{q_1};\omega) = \epsilon_{xx}(\omega)$, $\epsilon(\mathbf{q_2};\omega)$ and $\epsilon(\mathbf{q_3};\omega)$ are computed according to the mixed-space scheme, as already explained.
iii) From simple algebra, using the tensorial nature of the dielectric tensor, one obtains that

$$\epsilon_{xz}(\omega) = \frac{1}{4ab}\Big(\epsilon(\mathbf{q_2};\omega) - \epsilon(\mathbf{q_3};\omega)\Big),$$
$$\epsilon_{zz}(\omega) = \frac{1}{b^2}\Big(\epsilon(\mathbf{q_2};\omega) - a^2\epsilon_{xx}(\omega) - 2ab\epsilon_{xz}(\omega)\Big),$$

where $a = \frac{q_{||}}{\sqrt{q_{||}^2+q_z^2}}$ and $b = \frac{q_z}{\sqrt{q_{||}^2+q_z^2}}$.
Some care is required in order to choose the values of $q_{||}$ and q_z. As we are interested in the optical properties, we assume the optical limit; which constrains us to the limit $\mathbf{q} \to 0$. To avoid numerical problems, we want to have non-vanishing values of $q_{||}$ and q_z, in order to have reliable numerical results when evaluating $\epsilon_{zz}(\omega)$. It is possible to satisfy these two constrains, remembering that the $\chi_0^{(1)}(\mathbf{q},\mathbf{q};\omega)$ is analytically proportional to $|\mathbf{q}|^2$ in the optical limit. Also the matrix elements $\chi_0^{(1)}(\mathbf{q},\mathbf{q}+\mathbf{G};\omega)$ and $\chi_0^{(1)}(\mathbf{q}+\mathbf{G},\mathbf{q};\omega)$ are proportional to $|\mathbf{q}|$, $\mathbf{G} \neq \mathbf{0}$. The same holds for $\chi^{(1)}$ [54]. Therefore, when calculating the matrix $\chi_0^{(1)}$ with the DP code, a vanishing value of $\mathbf{q}$ is used. Then, before performing the Fourier transform for obtaining $\chi_0^{(1)}(\mathbf{q}_{||},z_i,z_j;\omega)$, the aforementioned matrix elements are rescaled, in order to have $q_{||}, q_z \sim 1$.

8.2.3 Numerical results

During this thesis, I have implemented this numerical scheme using the software MATLAB [246]. In Fig. 8.5, I report the numerical results, obtained using the mixed-space scheme, for the clean Si(001)2×1 surface. I used 1400 G_z-vectors, corresponding to a spacing of $\Delta_z = 0.0635$ Å, in order to reach convergence. We checked that the RPA results are independent of the size of the vacuum region used in the super-cell, as expected for a mixed-space calculation. The striking point is the weak effect of local-fields on $\mathrm{Im}\{\epsilon_\perp\}$, in comparison to the previous results, presented on the right panel of Fig. 8.3. Also we obtain no effect of LF on the in-plane component (Fig. 8.3; left panel) of the dielectric tensor. Indeed, the peak positions and intensities are identical to the IPA calculation.

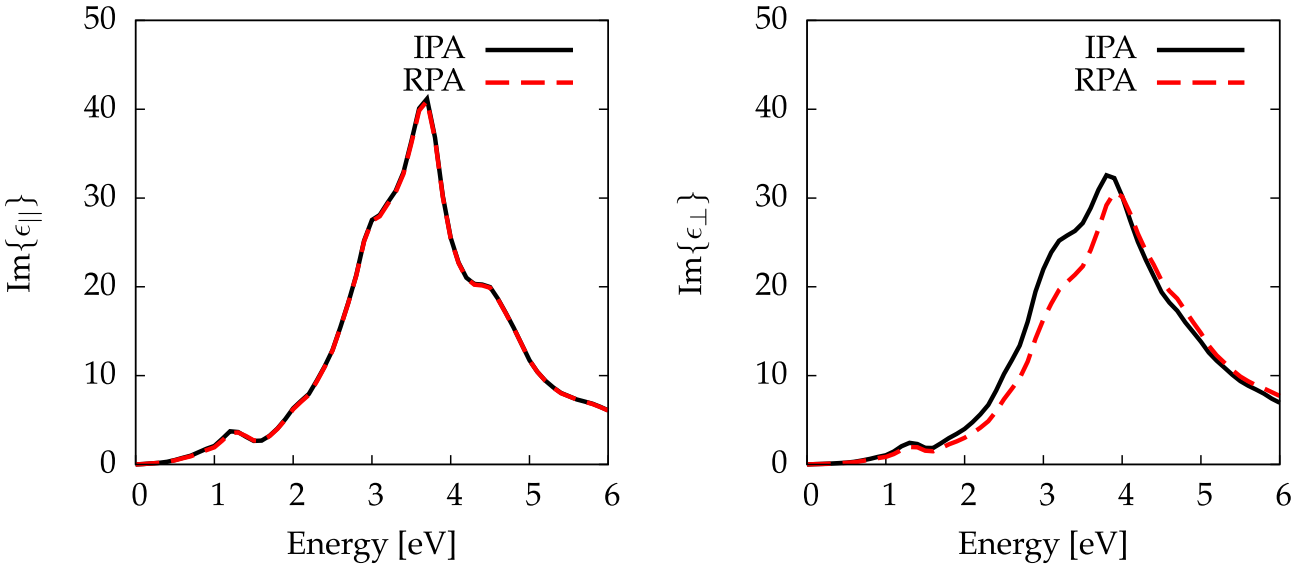

Fig. 8.5: Imaginary part of the dielectric function, computed using the mixed-space scheme. Black curves: Independent-particle approximation (IPA). Red curves: Random-phase approximation. Left panel: Imaginary part of $\epsilon_{||}$ with $\mathbf{q}$ align along the x-axis. Right panel: Imaginary part of $\epsilon_{\perp}$.

This can be attributed, as justified latter, to the approximation introduced, where we neglected the contributions of $\mathbf{G}_{||}$ in-plane vectors.

Using the mixed-space scheme, we are now able to compute all the components of the dielectric tensor, and in particular the out-of-plane component of the dielectric tensor, when including the local-field effects. Nevertheless, the price to pay is that any calculation requires three calculations of the full tensor $\chi_0^{(1)}$, for each frequency of interest and for a huge number of $\mathbf{G}$-vectors. Even with nowadays facilities, this still represents a formidable task. This is why, this method is used in this thesis only for investigation purposes. In particular, the full resolution of the Dyson equation including in-plane local-field effects ($\mathbf{G}_{||}, \mathbf{G}'_{||} \neq 0$), has not been performed in the mixed-space. Nevertheless, the numerical result obtained here serves as a reference for developing and testing a new and more efficient method, as explained in the next session.

8.3 Selected-G approach

Formally, a slab of matter can only describe the optical properties of a free-standing film. Up to now, we have not make any distinction between the optical properties of a surface and the optical properties of a thin-film. As already mentioned in the introduction of Chap. 5, a surface should be represented by a semi-infinite system.
In this section, I first give the equations for calculating the optical properties of a thin-film. Then, taking the surface limit, I obtain a new set of equations for calculating the optical properties of a surface.

8.3.1 Isolated system from periodic super-cell calculations

From the previous results, it is clear now that the periodicity induced by the super-cell approach, treated in reciprocal space, is at the origin of the failure of the super-cell approach. We must treat a thin-film as an isolated system in the out-of-plane direction in order to properly include the local-field effects in its optical properties.
Let us consider such an isolated thin-film. We introduce the following approximation: the matter, *i.e.*, the density, is localised in the z-direction between $-L_z^{\text{mat}}$ and 0. This is justify by the observation of the density of silicon slabs, as shown in Fig. 8.1. The full space has an extension in the z-direction, denoted L_z, with $L_z \to \infty$.

Considering that response functions are restricted to the matter region, the full Dyson equation, expressed in the mixed-space, reads as

$$\begin{aligned}\chi^{(1)}_{\mathbf{G}_{||}\mathbf{G}'_{||}}(\mathbf{q}_{||},z,z';\omega) = \chi^{(1)}_{0,\mathbf{G}_{||}\mathbf{G}'_{||}}(\mathbf{q}_{||},z,z';\omega) + \sum_{\mathbf{G_1}_{||}} \int_{-L_z^{\text{mat}}}^{0} dz_1 dz_2 \chi^{(1)}_{0,\mathbf{G}_{||}\mathbf{G_1}_{||}}(\mathbf{q}_{||},z,z_1;\omega) \\ \times v_{\mathbf{G_1}_{||}}(\mathbf{q}_{||},z_1,z_2)\chi^{(1)}_{\mathbf{G_1}_{||}\mathbf{G}'_{||}}(\mathbf{q}_{||},z_2,z';\omega), \qquad z,z' \in [-L_z^{\text{mat}},0].\end{aligned} \tag{8.10}$$

In contrast to Eq. (8.4), we consider here the full dependence on the in-plane $\mathbf{G}$-vectors.
Instead of solving this equation directly in the mixed-space, as already done in the previous section, we introduce here two auxiliary functions $\tilde{\chi}_0^{(1)}$ and $\tilde{\chi}^{(1)}$. These functions are respectively identical to $\chi_0^{(1)}$ and $\chi^{(1)}$ for $(z,z') \in [-L_z^{\text{mat}},0]\times[-L_z^{\text{mat}},0]$. These functions are also chosen periodic, of period L_z^{mat} [4]

$$\begin{aligned}\tilde{\chi}^{(1)}_{0,\mathbf{G}_{||}\mathbf{G}'_{||}}(\mathbf{q}_{||},z+NL_z^{\text{mat}},z'+NL_z^{\text{mat}};\omega) = \tilde{\chi}^{(1)}_{0,\mathbf{G}_{||}\mathbf{G}'_{||}}(\mathbf{q}_{||},z,z';\omega), \\ \tilde{\chi}^{(1)}_{\mathbf{G}_{||}\mathbf{G}'_{||}}(\mathbf{q}_{||},z+NL_z^{\text{mat}},z'+NL_z^{\text{mat}};\omega) = \tilde{\chi}^{(1)}_{\mathbf{G}_{||}\mathbf{G}'_{||}}(\mathbf{q}_{||},z,z';\omega).\end{aligned} \qquad N\in\mathbb{Z}$$

Note that in the standard super-cell calculations, the response functions have a periodicity of L_z instead of the periodicity of L_z^{mat} that we have here for the auxiliary response functions. These auxiliary response functions being periodic, it is possible to define their (inverse) Fourier transform

$$\tilde{\chi}_{\tilde{\mathbf{G}},\tilde{\mathbf{G}}'}(\mathbf{q};\omega) = \frac{1}{L_z^{\text{mat}}}\int_{-L_z^{\text{mat}}}^{0} dz \int_{-L_z^{\text{mat}}}^{0} dz' e^{-i(q_z+\tilde{G}_z)z}\tilde{\chi}_{\mathbf{G}_{||},\mathbf{G}'_{||}}(\mathbf{q}_{||},z,z';\omega)e^{i(q_z+\tilde{G}'_z)z'}, \tag{8.11a}$$

$$\tilde{\chi}_{\mathbf{G}_{||},\mathbf{G}'_{||}}(\mathbf{q}_{||},z,z';\omega) = \frac{1}{L_z^{\text{mat}}}\sum_{q_z}\sum_{\tilde{G}_z,\tilde{G}'_z} e^{i(q_z+\tilde{G}_z)z}\tilde{\chi}_{\tilde{\mathbf{G}},\tilde{\mathbf{G}}'}(\mathbf{q};\omega)e^{-i(q_z+\tilde{G}'_z)z'}, \quad z,z' \in [-L_z^{\text{mat}},0], \tag{8.11b}$$

with $\tilde{G}_z = N\frac{2\pi}{L_z^{\text{mat}}}$, $N\in\mathbb{Z}$.

[4] The remaining space is filled with zero.

Dyson-like equation

Using Fourier transform definitions, together with definition of delta functions (see App. A), we obtain a Dyson-like equation for the auxiliary response function $\tilde{\chi}^{(1)}$

$$\begin{aligned}\tilde{\chi}^{(1)}_{\tilde{\mathbf{G}}\tilde{\mathbf{G}}'}(\mathbf{q};\omega) &= \tilde{\chi}^{(1)}_{0,\tilde{\mathbf{G}}\tilde{\mathbf{G}}'}(\mathbf{q};\omega) + \frac{1}{L_z^{\text{mat}}}\sum_{\mathbf{G_1}_{||}}\sum_{\tilde{G}_{z1}\tilde{G}_{z2}} \tilde{\chi}^{(1)}_{0,\mathbf{G}_{||}\mathbf{G_1}_{||}}(\mathbf{q}_{||}, q_z+\tilde{G}_z, q_z+\tilde{G}_{z1};\omega) \\ \times \int_{-L_z^{\text{mat}}}^{0} dz_1 dz_2 &\left(e^{-i(q_z+\tilde{G}_{z1})z_1} v_{\mathbf{G_1}_{||}}(\mathbf{q}_{||}, z_1, z_2) e^{i(q_z+\tilde{G}_{z2})z_2} \right) \tilde{\chi}^{(1)}_{\mathbf{G_1}_{||}\mathbf{G}'_{||}}(\mathbf{q}_{||}, q_z+\tilde{G}_{z2}, q_z+\tilde{G}'_z;\omega).\end{aligned} \tag{8.12}$$

This equation can be written in a more compact way

$$\tilde{\chi}^{(1)}_{\tilde{\mathbf{G}}\tilde{\mathbf{G}}'}(\mathbf{q};\omega) = \tilde{\chi}^{(1)}_{0,\tilde{\mathbf{G}}\tilde{\mathbf{G}}'}(\mathbf{q};\omega) + \sum_{\tilde{\mathbf{G_1}}\tilde{\mathbf{G_2}}} \tilde{\chi}^{(1)}_{0,\tilde{\mathbf{G}}\tilde{\mathbf{G_1}}}(\mathbf{q};\omega)\tilde{v}_{\tilde{\mathbf{G_1}}\tilde{\mathbf{G_2}}}(\mathbf{q})\tilde{\chi}^{(1)}_{\tilde{\mathbf{G_2}}\tilde{\mathbf{G}}'}(\mathbf{q};\omega), \tag{8.13}$$

by defining

$$\tilde{v}_{\tilde{\mathbf{G_1}},\tilde{\mathbf{G_2}}}(\mathbf{q}) = \frac{1}{L_z^{\text{mat}}}\int_{-L_z^{\text{mat}}}^{0} dz_1 \int_{-L_z^{\text{mat}}}^{0} dz_2 e^{-i(q_z+\tilde{G}_{z1})z_1} v_{\mathbf{G_1}_{||}}(\mathbf{q}_{||}, z_1, z_2) e^{i(q_z+\tilde{G}_{z2})z_1} \delta_{\mathbf{G_1}_{||},\mathbf{G_2}_{||}}. \tag{8.14}$$

Using the expression of the Coulomb potential, it is possible to obtain a simplified analytical expression of $\tilde{v}_{\tilde{\mathbf{G_1}},\tilde{\mathbf{G_2}}}(\mathbf{q})$, as shown in App. G.

Dielectric response

The inverse dielectric function is given by

$$\begin{aligned}\epsilon^{-1}(\mathbf{q}_{||}, z, z';\omega) &= \delta(z,z') + \int dz_1 v(\mathbf{q}_{||}, z, z_1)\chi^{(1)}(\mathbf{q}_{||}, z_1, z';\omega) \\ &= \delta(z,z') + \int_{-L_z^{\text{mat}}}^{0} dz_1 v(\mathbf{q}_{||}, z, z_1)\tilde{\chi}^{(1)}(\mathbf{q}_{||}, z_1, z';\omega),\end{aligned} \tag{8.15}$$

where the last equation comes from the approximation that response functions are restricted to $[-L_z^{\text{mat}}, 0] \times [-L_z^{\text{mat}}, 0]$.

The macroscopic average of the inverse dielectric function Eq. (8.8), averaged over the slab, reads as

$$\begin{aligned}\epsilon^{-1}(\mathbf{q};\omega) &= \frac{1}{L_z^{\text{mat}}}\int_{-L_z^{\text{mat}}}^{0} dz \int_{-L_z^{\text{mat}}}^{0} dz' e^{-iq_z z}\epsilon^{-1}(\mathbf{q}_{||}, z, z';\omega)e^{iq_z z'} \\ &= 1 + \sum_{q'_z\tilde{G}_z\tilde{G}'_z} \tilde{v}_{\mathbf{0}\tilde{\mathbf{G}}_\mathbf{z}}(\mathbf{q}_{||}, q_z)\tilde{\chi}^{(1)}_{\tilde{\mathbf{G}}_\mathbf{z}\tilde{\mathbf{G}}'_\mathbf{z}}(\mathbf{q}_{||}, q'_z;\omega)e^{-i(q'_z-q_z+\tilde{G}'_z)\frac{L_z^{\text{mat}}}{2}}\,\text{sinc}([q'_z - q_z + \tilde{G}'_z]\frac{L_z^{\text{mat}}}{2}).\end{aligned} \tag{8.16}$$

As a result, we obtain that in order to compute the optical properties of an isolated thin-film in reciprocal space, we have to proceed in two steps. First, the Dyson equation Eq. (8.13), which links the fully interacting response function $\tilde{\chi}^{(1)}$ to the independent-particle response function $\tilde{\chi}^{(1)}_0$ is solved. In this equation, the Coulomb potential v is replaced by a modified Coulomb potential $\tilde{v}$, given by Eq. (8.14) or equally by Eq. (G.5). Then, the dielectric response of the thin-film is computed, according

to Eq. (8.16). Again, this definition contains the modified Coulomb potential $\tilde{v}$. It is important to note that this modified Coulomb potential $\tilde{v}$ is not diagonal in reciprocal space and has a complex analytical expression (see App. G), making the resolution of the Dyson equation Eq. (8.13) more intricate.

8.3.2 Selected-G approach

In order to describe the optical properties of a surface from a thin-film of thickness L_z^{mat}, we must take the limit $L_z^{\text{mat}} \to \infty$. I refer to this limit as the *surface limit*.
As shown in App. G, within the surface limit,

$$\tilde{v}_{\tilde{\mathbf{G}}_1,\tilde{\mathbf{G}}_2}(\mathbf{q}) = \frac{4\pi}{|\mathbf{q}+\tilde{\mathbf{G}}|^2}\delta_{\tilde{\mathbf{G}}_1,\tilde{\mathbf{G}}_2} = v_{\tilde{\mathbf{G}}_1}(\mathbf{q})\delta_{\tilde{\mathbf{G}}_1,\tilde{\mathbf{G}}_2}, \tag{8.17}$$

where v is the Coulomb potential. Inserting this result in Eq. (8.13) and Eq. (8.16) gives a new set of equations

$$\tilde{\chi}^{(1)}_{\tilde{\mathbf{G}}\tilde{\mathbf{G}}'}(\mathbf{q};\omega) = \tilde{\chi}^{(1)}_{0,\tilde{\mathbf{G}}\tilde{\mathbf{G}}'}(\mathbf{q};\omega) + \sum_{\tilde{\mathbf{G}}_1} \tilde{\chi}^{(1)}_{0,\tilde{\mathbf{G}}\tilde{\mathbf{G}}_1}(\mathbf{q};\omega) v_{\tilde{\mathbf{G}}_1}(\mathbf{q}) \tilde{\chi}^{(1)}_{\tilde{\mathbf{G}}_1\tilde{\mathbf{G}}'}(\mathbf{q};\omega), \tag{8.18a}$$

$$\epsilon^{-1}(\mathbf{q};\omega) = 1 + v_{\mathbf{0}}(\mathbf{q})\tilde{\chi}^{(1)}_{\mathbf{00}}(\mathbf{q};\omega). \tag{8.18b}$$

These two equations are very similar to the usual equations of the TDDFT. Only the definition of the **G**-vectors involved in is different. The equation Eq. (8.18a) contains the **G**-vectors corresponding to the material slab volume.

If we now choose the vacuum region to be an integer multiple of the height of the material slab, we obtain an easy way to construct the matrix $\tilde{\chi}_0^{(1)}$ from $\chi_0^{(1)}$. Indeed, in this case, the matrix elements of $\tilde{\chi}_0^{(1)}$ are matrix elements of $\chi_0^{(1)}$. Thus $\tilde{\chi}_0^{(1)}$ is obtained by keeping only matrix elements of $\chi_0^{(1)}$ given by the subset of the super-cell's G_z-vectors corresponding to G_z-vectors of the material slab; and by replacing the volume of normalisation V_{cell} in Eq. (8.3) by the volume of matter V_{mat}, accordingly to the definition of the Fourier transform Eq. (8.11a).

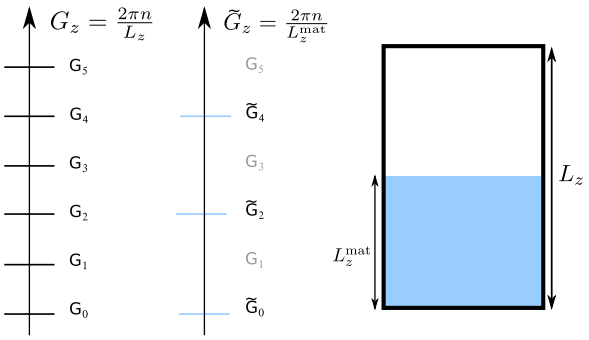

Fig. 8.6: Selected-**G** method for $L_z = 2L_z^{\text{mat}}$.

8.3.3 Numerical results

I have implemented the Selected-**G** approach in the DP code. The same parameters (see Tab. 8.1) have been used to obtain the spectra. In particular, 299 **G**-vectors have been used in total, *i.e.*, including in-plane and out-of-plane **G**-vectors. This is to be compared with the 1400 G_z-vectors needed for the mixed-space original scheme, where the in-plane dispersion is neglected. The result of this new framework, called "Selected **G**" is presented in Fig. 8.7 (red dashed line).
In the inset, we checked that solving the Dyson equation Eq. (8.18a) with slab's G_z, but keeping $\mathbf{G}_{||} =$

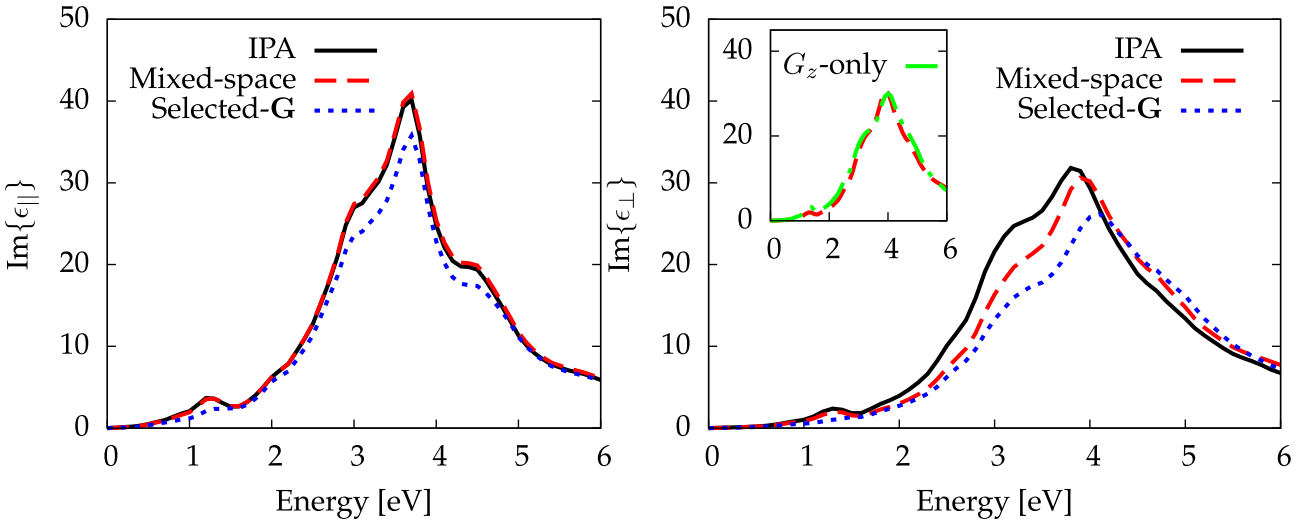

Fig. 8.7: Imaginary part of the dielectric function $\epsilon_{||}$ with $\mathbf{q}$ aligned along the x-axis (left panel) and $\epsilon_{\perp}$ (right panel). Black solid curves: Independent-particle approximation (IPA). Red dashed curves: Mixed-space calculation. Blue dotted curves: Selected-$\mathbf{G}$ calculation. Inset: Comparison between the mixed-space and the Selected-$\mathbf{G}$ method, without in-plane reciprocal vectors ("G_z-only", green dotted-dashed curve).

0, gives the same results as the mixed-space approach. The error introduced by the approximation of the strict localisation of response function between $-L_z^{\text{mat}}$ and 0 is negligible and appears *a posteriori* as a good and perfectly valid approximation. The differences with the mixed-space calculations originate then from the approximation introduced in this last approach. This allows us to understand how local fields built in, in terms of $\mathbf{G}_{||}$ and G_z.

It appears that $\epsilon_{\perp}$ depends on both $\mathbf{G}_{||}$ and G_z (right panel: blue and red curves). On the contrary, as shown in the left panel, $\epsilon_{||}$ is only influenced by $\mathbf{G}_{||}$, as the curves labelled "IPA" and "Mixed-space" are superposed. We also observe that the weak dependence of $\epsilon_{||}$ on G_z explains why the standard approach leads to a correct description of the local fields in *the plane of the surface*, although the set of G_z is not adapted to the material slab. We do not show the results for several sizes of the vacuum region as they are indistinguishable.

These results allow us to discuss for the first time the effect of the local-fields on the different components of the optical dielectric function for a surface.

We compare in Fig. 8.8 the imaginary part of $\epsilon_{\perp}$, $\epsilon_{||}^{xx}$ and $\epsilon_{||}^{yy}$ for the clean Si(001)2×1 surface to the absorption spectra silicon bulk, including local-fields in all cases.

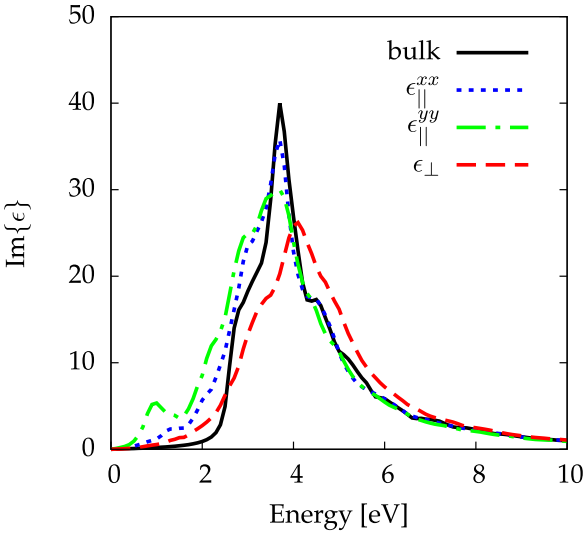

Fig. 8.8: Imaginary part of the dielectric responses of the surface and the bulk, local fields included.

The main effect is a blue shift of approximately 0.3 eV in the position of the peak for $\epsilon_{\perp}$, compared to

the bulk response, while no shift is observed for $\epsilon_{||}$. The decrease in the intensity of the main absorption peak is more pronounced for $\epsilon_{\perp}$ than for $\epsilon_{||}$. This effect was already visible in the IPA calculation (see Fig. 8.2) and for this reason, it can be attributed to the presence of the surface itself, and not to the local-fields.
For the clean Si(001)2×1 surface, the atomic relaxation at the interface with vacuum introduces states, located in the gap of the material, the so-called surface-states, which are evidenced in the IPA calculation by the appearance of a small structure around 1.3 eV, see the black curve in Fig. 8.7. With local-fields included, this structure is still clearly visible in $\epsilon_{||}$, in particular for $\epsilon_{||}^{yy}$ (see Fig. 8.8). In the case of $\epsilon_{\perp}$, the peak vanishes when all the $\mathbf{G}_{||}$ and G_z are taken into account, while it remains, in the mixed-space calculation, including the G_z only, evidencing the influence of the in-plane local fields ($\mathbf{G}_{||} \neq 0$). This also shows how local-field effects are important for the correct description of surface-induced structures.

8.4 Discussion

8.4.1 Independence of the two surfaces in a slab geometry

The two surfaces of a slab have been shown to be independent in Chap. 5, in the independent-particle approximation. Here I check the independence of the two surfaces of a slab when local-field effects are included. Due to the Coulomb interaction, which is a long-range interaction, the two surfaces of a slab of matter may potentially couple. In that case, it would not be possible to map the result of a calculation performed using a slab geometry to the semi-infinite system that we try to model, even taking the surface limit ($L_z^{\text{mat}} \to \infty$).

Let us consider the spectra of two *symmetric* slabs, one with two clean surfaces and one with two dihydride surfaces. If the surfaces of a slab are independent, the average of these two symmetric spectra should be identical to the spectrum of an *asymmetric* slab, with a front clean surface and a back dihydride surface, as depicted in Fig. 5.3. Calculations of these three slabs have been performed using the Selected-**G** method, including the local-field effects. The spectra have been computed for two different slab sizes; 12 atomic layers (top panels) and 16 atomic layers (bottom panels). Results are presented in Fig. 8.9.
The differences between the average ("Average") and the asymmetric slab ("Clean-DiH") are found to be small for the 12 atomic layers. When increasing the thickness of the slab, the differences almost vanish, showing that the surfaces become independent. I checked that the IPA results yield the same quantitative differences. Therefore these differences do not originate from the Coulomb interaction but from the size of the slab. This shows that the surfaces are numerically independent when including local-field effects.
Note that by comparing the density of a slab and the one of bulk silicon (see Sec. 5.2.6), I already found in Chap. 5.2.6 that the surface-states live in a ∼8.5Å wide region. The half-slab thicknesses are respectively here 8.15Å ("12 layers") and 10.86Å ("16 layers"). This explains that when using a slab made of 12 atomic layers, the surface-states of each side of the slab slightly overlap, resulting in small interferences. From these results, we obtain a condition of independence of the surfaces of the slabs, which is that the surface states of the two surfaces must not overlap. In the case of the clean

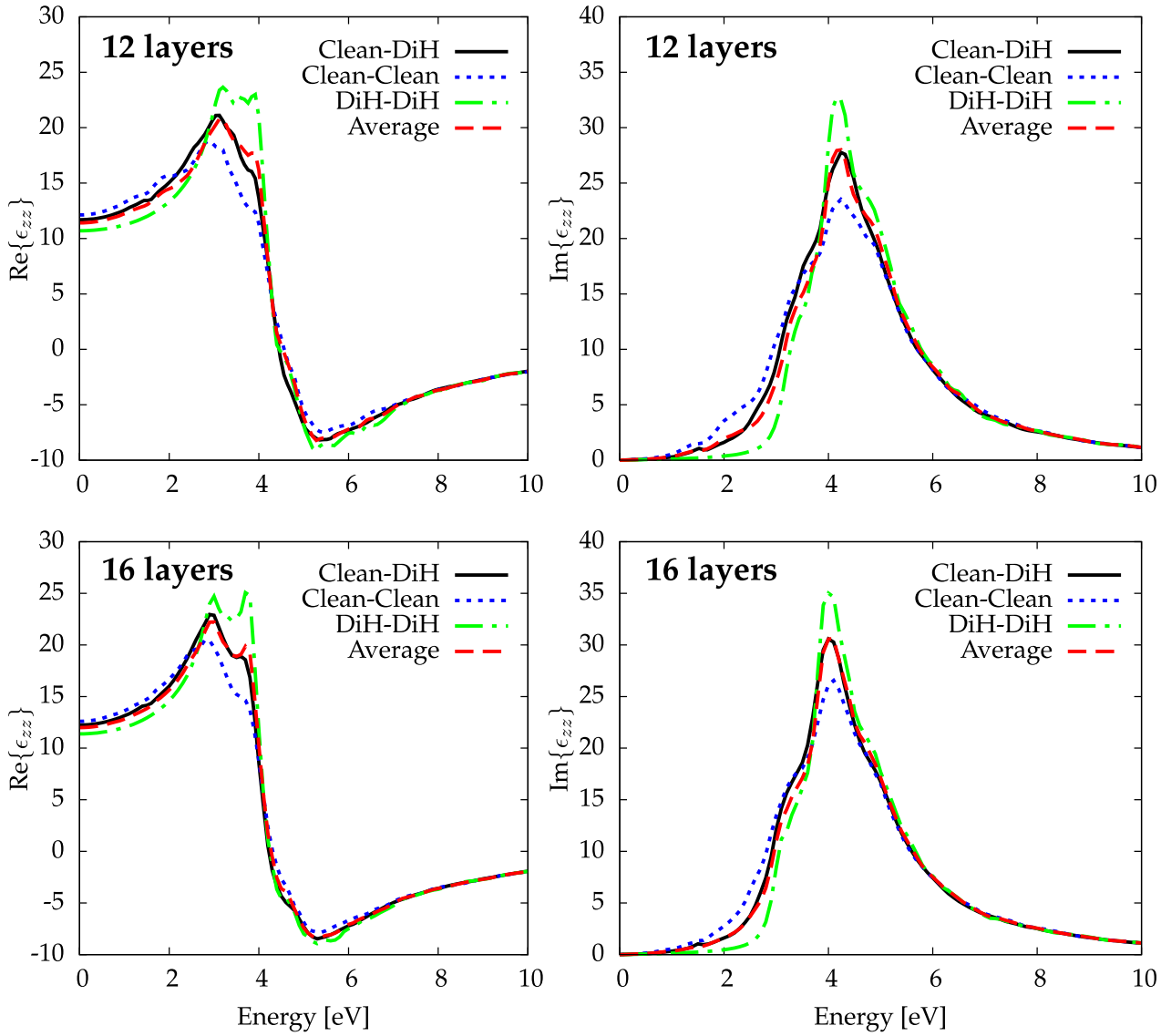

Fig. 8.9: Comparison between the real part (left panel) and imaginary part (right panel) of ϵ_{zz} computed for the asymmetric slab (Clean-DiH; solid curve), a symmetric clean slab (Clean-Clean; blue dotted curve), a symmetric dihydride slab (DiH-DiH; green dotted dashed curve) and from the average of the two symmetric slabs (Average; dashed curve). Local field effects are included.

surface, this imposes a slab to contain at least 16 layers.

8.4.2 Surface dielectric function and three-layer model

One must be careful when interpreting the optical spectra obtained from the Selected-**G** approach, especially the variation of the spectra with respect to the number of layers or atoms in the slab. Indeed, the position and amplitude of the surface spectra depend on the number of atomic layers in the slab. This is well illustrated in Fig. 8.10. We observe in Fig. 8.10 that the slab calculations slowly converge to the bulk spectra when increasing the number of atoms. In order to show that we really converge to the bulk spectra, I reported in Fig. 8.11 the evolution of the intensity of the E_2 related

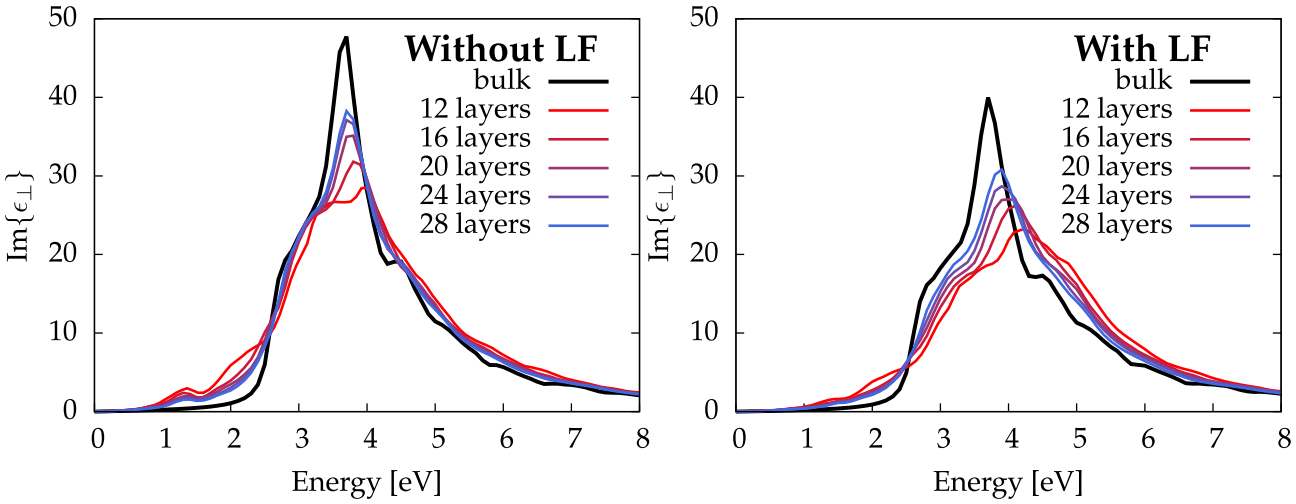

Fig. 8.10: Imaginary part of the out-of-plane component of the dielectric tensor ($\epsilon_{||}$) *versus* the number of layers in the slab, compared to the bulk silicon absorption spectra.

peak *versus* the number of layers (N) in the slab. The value at zero correspond to the bulk case. We clearly see that both IPA (black dots) and RPA (red dots) converge to the bulk values as $1/N$.
How to interpret and to extract information from these slab calculations is an intricate question.

It is common to use a three-layer model in order to extract surface quantities from a slab calculation [247, 248]. In this model, the dielectric response of the slab is given by

$$\epsilon_M^{\text{slab}}(\omega) = \frac{(N-2N_s)\epsilon_M^{\text{bulk}}(\omega) + 2N_s\epsilon^{\text{surf}}(\omega)}{N}, \tag{8.19}$$

where N and N_s are respectively the total number of layers in the slab and the effective number of surface layers where the dielectric function equals the effective surface dielectric function $\epsilon^{\text{surf}}(\omega)$. There is $(N-2N_s)$ bulk layers with a dielectric function $\epsilon_M^{\text{bulk}}(\omega)$. The factor 2 comes here from the fact that the slab has two surfaces.

Here we analyse the optical spectra obtained from the Selected-**G** method within the limits of this formula. We checked (not shown) that the surface optical region is fully contained in the slab made of 20 atomic layers of matter, as we can extract the bulk absorption spectra from the slab calculations performed with $N = 20$ layers and $N = 24$ layers.
Thereby, it is possible to extract the surface-induced spectra using Eq. (8.19) from these slabs. More precisely, as it is not possible to determine separately N_s and ϵ^{surf}, we can only determine the surface-induced quantity $N_s\big(\epsilon^{\text{surf}}(\omega) - \epsilon_M^{\text{bulk}}(\omega)\big)$, which is the only meaningful physical quantity that we can extract using Eq. (8.19).

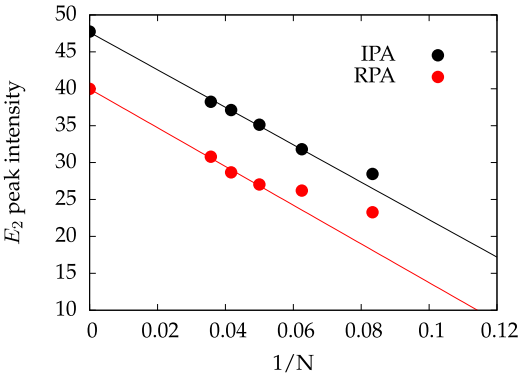

Fig. 8.11: Convergence in number of layers of the intensity of the E_2 related peak. Lines are here to guide the eyes.

The quantity $N_s\big(\epsilon_{yy}^{\text{surf}}(\omega) - \epsilon_M^{\text{bulk}}(\omega)\big)$ has been extracted from the results of a 20 atomic layer slab (black

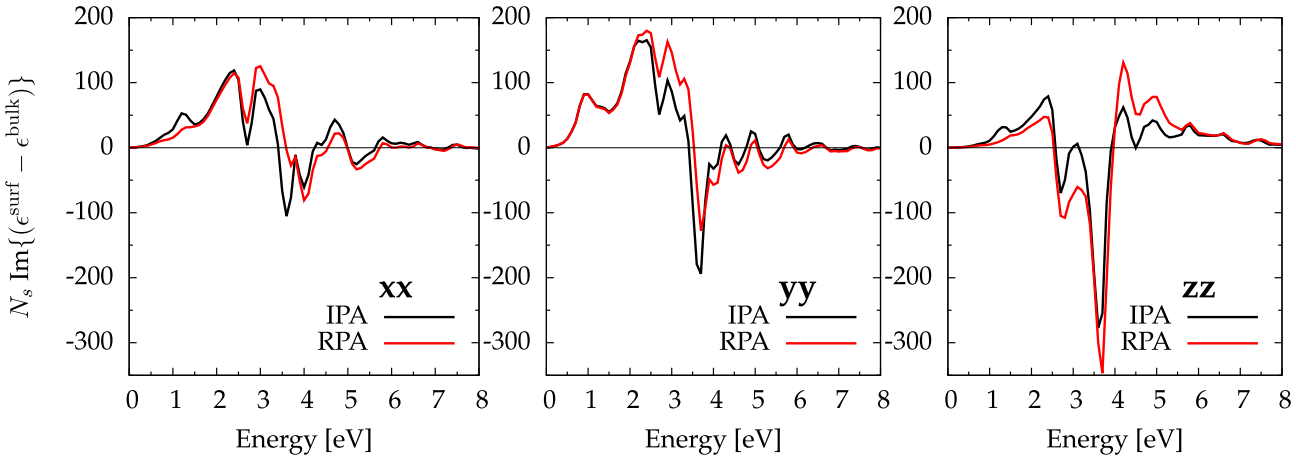

Fig. 8.13: Spectra of $N_s\big(\epsilon^{\text{surf}}(\omega) - \epsilon_M^{\text{bulk}}(\omega)\big)$ for the xx component (left panel) the yy component (middle panel) and the zz components (right panel) for the clean surface. Dashed lines are obtained without local-fields ("IPA") whereas solid lines correspond to local-field effects included ("RPA"). The spectra is obtained from the 24 atomic layer slab.

lines) and a 24 atomic layers slab (red lines), as shown in Fig. 8.12. These two slabs yield the same result, showing the reliability of the approach.

The same quantity is reported in Fig. 8.13, where the dashed lines are the results obtained without including the local-field effects ("IPA") whereas the solid lines correspond to local-field included results ("RPA").

We observe in Fig. 8.13 that the three different components of the dielectric tensor give quite different results. Nevertheless some features are common.

First, in all the spectra, there is a negative peak around 3.7 eV (corresponding to the critical point E_2 of bulk silicon) indicating a lowering of the intensity of this peak in the surface quantity. By opposition, all the spectra are positive between 0 eV and 2 eV, due to the presence of surface-states in the gap of the clean surface. The intensity of the E_1 related peak is found to be increased in the surface spectra for two in-plane components of the dielectric tensor, whereas the intensity of the same peak is reduced for the out-of-plane component. The xx component shows the smallest deviation to the bulk spectra, as already visible in Fig. 8.8.

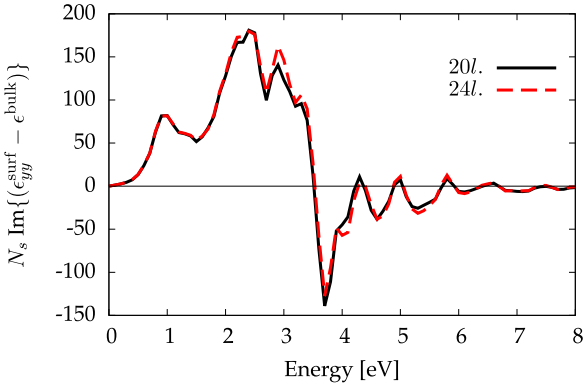

Fig. 8.12: Spectra of $N_s\big(\epsilon_{yy}^{\text{surf}}(\omega) - \epsilon_M^{\text{bulk}}(\omega)\big)$ for the clean surface, calculated for $N = 20$ layers (black solid line) and $N = 24$ layers (red dashed line).

The effects of the local fields are well evidenced in Fig. 8.13. Indeed, on the xx and the zz components, the surface-states induced structures are reduced by the local-field effects, whereas the equivalent structure on the yy component is unchanged when including local-field effects. Also the E_2 related peak intensity is closer to the bulk one when local-fields are included, for the in-plane components. For the out-of-plane components, the local-field effects induce a blue-shift of 0.1eV, whose conse-

quence is to increase the difference at the energy position of the E_2 critical point of bulk silicon.
We note that the local-field effects do not change too much the spectral shape of the quantity $N_s\big(\epsilon^{\text{surf}}(\omega) - \epsilon_M^{\text{bulk}}(\omega)\big)$, and more importantly, they do not change its sign. This means that when the surface quantity is smaller (bigger) in intensity than the bulk one, this remains true when including local-field effects. Finally, the prominent peak positions are found not to be affected by the local-field effects, expect a small blue-shift for the E_2 peak of the zz surface optical response. This means that the apparent blue-shift observed in Fig. 8.10 is mainly due to a change in the relative weight between the "surface" spectra and the bulk one.

Conclusion

In summary, I have investigated in this chapter the local-field effects on the linear optical properties of surfaces. The standard reciprocal-space based super-cell approach, has been shown to only yield the optical properties of an effective medium matter plus vacuum and to fail in the out-of-plane direction. In order to compute the optical properties of the surface and not the super-cell, I have introduced two new efficient schemes to account for local-fields in the *ab initio* description of the optical properties of surfaces, for both parallel and perpendicular components.
The two schemes are based on the resolution of TDDFT plus linear response theory equations in a mixed-space designed to be adapted to the special periodicity of the slab geometry. The first scheme corresponds to the resolution of the equations in this mixed-space directly. This approach works perfectly but an approximation has to be introduced to reduce the numerical cost of the calculation.
In order to do better, I have derived from the mixed-space equations a second scheme, still based on the super-cell approach, but which uses a selected set of reciprocal vectors. This scheme combines the correctness of the mixed-space approach, with the efficiency of a treatment in reciprocal space. Thanks to the efficiency of this scheme, we have been able to fully account for the local-field effects, removing the approximation introduced in the first scheme.
We have then demonstrated how local-field effects are important for a correct description of the out-of-plane optical properties. Comparing the two schemes, I have explained how the local-field effects construct, in terms of in-plane and out-of-plane $\mathbf{G}$-vectors. In addition, it explains why the standard calculation leads to reliable results for the in-plane components, as expected from the excellent agreement between theoretical and experimental results for Reflectance Anisotropy Spectra found in the literature.
Finally, I have checked that the two surfaces of a slab are independent, even including local-field effects, and we have extracted the surface-induced modification to the bulk spectra assuming a three-layer model.
In next chapter, I present the local-field effects for surface SHG, merging the extraction of the spectra (Chap. 5, Chap. 6 and Chap. 7) with the Selected-$\mathbf{G}$ approach for the calculation of local-field effects.

Part IV

Application to Silicon Surfaces

9. Local-field effects on second-harmonic generation from surfaces

The abrupt change in the electronic density at the surface of a dielectric material leads to a huge variation of the electric field at the interface with vacuum. As a result, strong effects of the local-fields on the optical properties of surfaces are expected; in particular in the direction perpendicular to the plane of the surface. Therefore we except the local-field effects to affect quantitatively the surface second-harmonic generation.

It is still common practice to neglect local-field effects on surface second-harmonic generation spectra, and their effects have, so far, only been estimated using models fitted on experimental data [249,250]. Understanding, by means of *ab initio* methods, how local-field effects affect the second-harmonic generation (SHG) at crystal surfaces is the aim of this chapter.

I report here a method of calculating the local-field effects in the Time-Dependent Density Functional Theory (TDDFT) framework, based on the macroscopic theory developed in Chap. 7. This macroscopic theory is used to calculate the surface second-harmonic generation of some silicon surfaces and to investigate the effect of local-fields.

The SHG from silicon surfaces has been widely studied in the literature [28, 78–80, 227, 251]; and it is found experimentally a strong influence of ad-atoms on the SHG spectra of silicon surfaces. In particular, the presence of hydrogen results in a quenching of the SHG signal [32, 33, 252–254]. Here, the local-field effects are investigated on the clean Si(001)2×1 surface, but also on two hydrogenated surfaces, namely the monohydride or Si(001)2×1:H and the dihydride or Si(001)1×1:2H surfaces; in order to shed some light on the close connection between the surface SHG, the ad-atoms and the local-field effects.

This chapter is organised as follow. First, I present the numerical results obtained at various levels of approximation, evidencing the role and the effects of the local-fields on the SHG spectra of the clean Si(001) surface. Then, the results obtained for two hydrogenated surfaces are presented and compared with available data, evidencing the importance of local-field effects for a quantitative description of surface SHG.

9.1 Local-Field Effects on the clean Si(001) SHG spectra

9.1.1 Numerical implementation

I have implemented the expressions of the $\chi^{(0)S}_{\rho\rho}$ and $\chi^{(0)S}_{\rho\rho\rho}$, as well as the Selected-**G** method in the SHG-TDDFT code known as 2light [117]. For conciseness, the expression of the full matrices $\left[\chi^{(0)S}_{\rho\rho}\right]_{\mathbf{G}\mathbf{G}'}$ and $\left[\chi^{(0)S}_{\rho\rho\rho}\right]_{\mathbf{G}\mathbf{G}'\mathbf{G}''}$ are derived and reported in App. I. Due to the impressive time required for computed the entire matrix $\chi^{(0)S}_{\rho\rho\rho}$, I have modified the parallelization of the code from an OpenMP parallelization to an hybrid OpenMP+MPI parallelization. Thanks to some optimizations of the 2light code, and to this new parallelization, I have been able to perform the calculations of surface second-harmonic generation on systems of reasonably converged size, fully taking into account local-field effects.

9.1.2 Numerical details

The self-consistent ground-state and the Kohn-Sham states were calculated using the plane-wave ABINIT code [115]. I used Troullier-Martins pseudopotentials [216] that are fully separable nonlocal pseudopotentials in the Kleinman-Bylander form [120] for Si and H atoms. The contribution of the nonlocal part of the pseudo-potential to $\mathbf{v}$ and $\boldsymbol{\mathcal{V}}$ is carried out using the 2light code [117].

The parameters of the atomic relaxation, as well as the values obtained for the dimer bond-length and buckling are the same as in Sec. 5.1.3. The convergence in number of atoms is an important issue, but the calculation of the local-field effects requires the evaluation of the entire matrix $\chi^{(0)S}_{\rho\rho\rho}$ for a big number of **G**-vectors, typically around 75-100. I found 24 atomic layers for representing the full slab to give a good trade off between quantitative results and the numerical burden associated with the inclusion of local-field effects on the surface SHG spectra.

Param.	Value
nkpt	256
npwwfn	3989
nband	220
lomo	40
npwmat	93
η	100 meV
$\Delta\omega$	100 meV

Tab. 9.1: Parameters for the clean Si(001)2×1 surface.

For this slab made of 24 atomic layers, I found the converged parameters, which are reported in Tab. 9.1 for the clean Si(001) surface. The parameter "lomo" corresponds to the index of the first valence band included in the calculation. This parameter is quite important for optimizing the computing time, as the computation of $\chi^{(0)S}_{\rho\rho\rho}$ scales as N_b^3, N_b being the number of bands considered in the simulation. Fig. 9.1 shows the effect of choosing 40 as a value for the lomo parameters ("lomo 40"; black solid line), instead of taking all the valence bands ("lomo 1"; red dotted line). As the two spectra are almost indistinguishable, we use for lomo the value of 40 in the following for the clean surface, thus almost dividing by two the number of transitions to be computed.

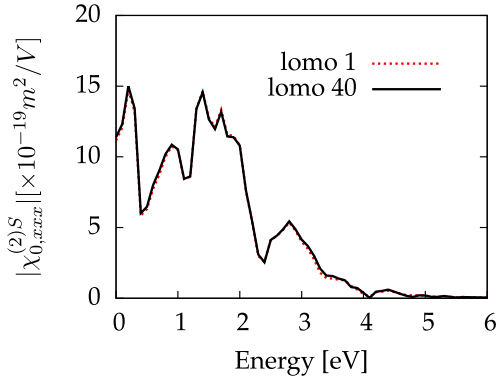

Fig. 9.1: SHG spectra $|\chi^{(2)S}_{0,xxx}|$ of the clean surface calculated. The different curves are explained in the text.

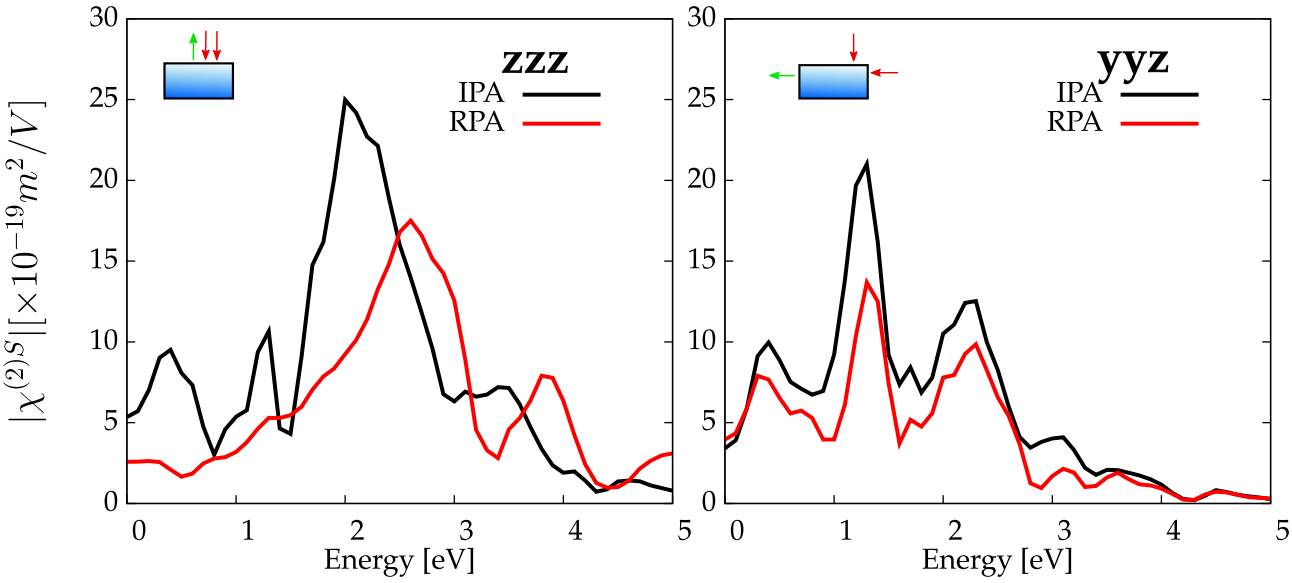

Fig. 9.2: Effect of local fields on the surface second-harmonic generation of the clean Si(001)2×1 surface. No scissors correction is included.

9.1.3 The clean Si(001)2×1 surface

As a test case, I have chosen the clean Si(001)2×1 surface to investigate the effects of local-fields on surface second-harmonic generation. The local-field effects are investigated at the level of the Random-Phase Approximation (RPA). The excitonic effects are neglected and will be treated in the next chapter. Two components of the $\chi^{(2)S}$ tensor have been selected, namely the zzz, and the yyz components, because they represent two different physical situations. The first component, zzz, corresponds to incoming electric fields and an emitted polarization perpendicular to the surface plane. Therefore, we expect this component to be more sensitive to the local-field; due to the abrupt change of the electric field at the interface with the vacuum. The yyz component corresponds to an in-plane emitted polarization, and is thus expected to be less affected by local-field effects.

The calculations of surface second-harmonic generation for these two components, with and without local-field effects, are reported in Fig. 9.2. Various effects are obtained. As a general remark, the LF are found to affect significantly the surface second-harmonic generation, and are therefore required to obtain a quantitative description of the surface second-harmonic generation. The LF are also found to reduce the spectral weight in the low-energy region. For the zzz component, the LF seem to introduce a blue-shift. Indeed, the main structure of the zzz component, around 2.0 eV seems to be shifted to 2.6eV. However, in SHG spectra, two situations can appear as a shift. One possibility is a real shift; the other possibility being a redistribution of the spectral weight from 1ω resonances to 2ω resonances or the opposite.[1] In order to investigate the nature of this apparent shift, I have compared the spectra with and without the scissors operator. The different structures which are clearly visible with and without scissors correction Δ are indicated with arrows in Fig. 9.3. As a result, we obtain that the two main structures in IPA are shifted by the inclusion of the scissors operator by

[1] This is another difference with linear optical properties where only a blue-shift can occur. No redistribution can occur as the resonances have an unique origin.

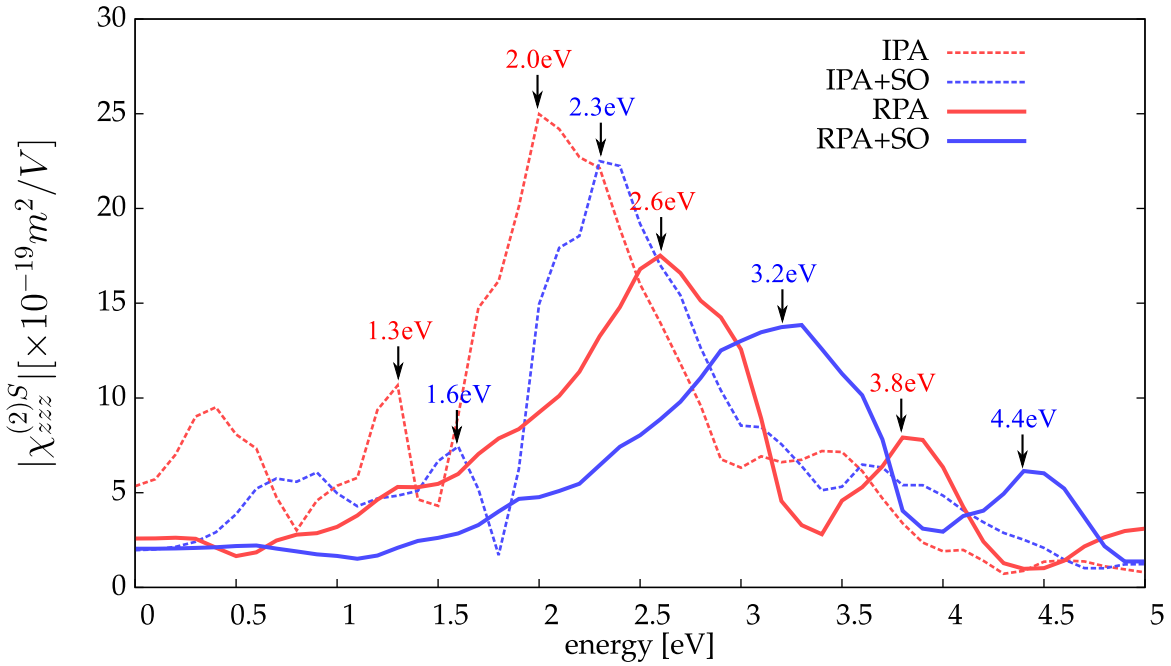

Fig. 9.3: Comparison of the effect of scissors correction on the surface second-harmonic generation of the clean Si(001)2×1 surface, with (blue curves) and without (red curves) local fields included. The scissors correction is chosen to be $\Delta = 0.6eV$. Arrows are here for indicating the positions of main structures.

$\Delta/2 = 0.3eV$ (indicating their 2ω origin) whereas the two main structures in RPA are shifted by $\Delta = 0.6eV$ (indicating their 1ω origin). Therefore the main effect of local-fields on the zzz component is *not* a blue shift but a redistribution of the spectral weight between the 2ω and the 1ω transitions. Concerning the yyz components, the LF do not alter the position of the prominent peaks, but they do reduce the spectral-weight of the main structures.

9.2 Hydrogenated surfaces and local-field effects

As explained in Chap. 4, it is possible to cover the Si(001) with adatoms and in particular with hydrogen atoms. The effect of the hydrogen on the second-harmonic generation from silicon surfaces has been widely investigated experimentally [32, 33, 252–254]; but the origin of the hydrogen-induced quenching is not well understood. In this section, I report the effects of local-fields on the spectra of two hydrogenated surfaces, the monohydride Si(001)2×1:H and the dihydride Si(001)1×1:2H surfaces.

The parameters for these calculations are given in Tab. 9.2, respectively for the dihydride ("DiH") and for the monohydride ("MonoH") surfaces. Note that due to the symmetries of the dihydride surface, twice less atoms are needed to describe the surface; lowering the requirements in terms of number of bands, and thus reducing the numerical cost of

Param.	DiH	MonoH
nkpt	288	256
npwwfn	3999	3989
nband	140	220
lomo	20	30
npwmat	73	89
η	100 meV	
$\Delta\omega$	100 meV	

Tab. 9.2: Parameters for the hydrogenated surface.

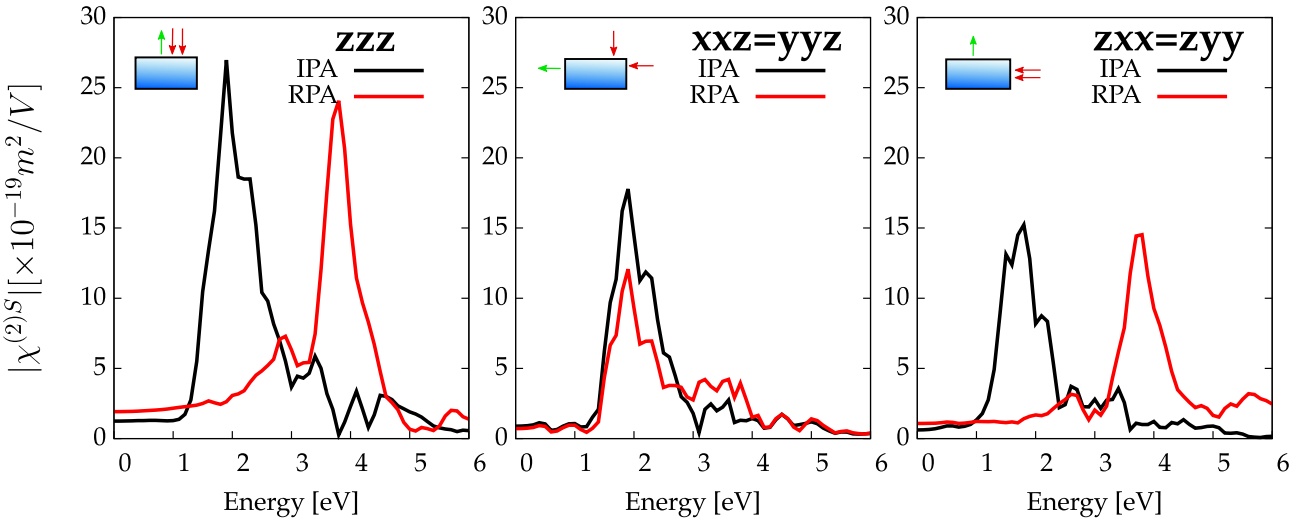

Fig. 9.4: Surface second-harmonic generation spectra of the dihydride Si(001)1×1:2H surface, for the zzz, xxz and zxx components of the $\chi^{(2)S}$ tensor. No scissors correction is included.

the calculations for the dihydride surface. In Fig. 9.4, I report the calculations of the non-zero components of the dihydride surface, with and without local-field effects included. The most striking result obtained here is the strong effect of local-fields on the SHG spectra of the dihydride surface. In particular, the zzz and the zyy components are found to be drastically affected by the LF, whereas the yyz is only slightly affected. The inclusion of the scissors correction (not shown) shows that the local-field effects redistribute the spectral weight from a structure corresponding mainly to 2ω transitions to a structure corresponding to mainly 1ω transitions, on the zzz and zyy components. Note that the structure at higher energy is sharper than the corresponding 2ω structure at low energy, due to sum-rules on the SHG spectra [255].

Interestingly, the region between 1 eV and 3 eV, which is "passivated" by local-field effects on the zzz and zyy components, corresponds to the region probed by the experiments, where it is found a quenching by the hydrogen [32, 33, 254]. However, concluding that the local-fields explain entirely the observed quenching is not obvious and requires an entire study in itself. Indeed, the quenching has been observed on the generalized reflection coefficients and each components of the $\chi^{(2)S}$ are weighted differently in the expression of these reflection coefficients (see Chap. 2 and Ref. [226]). In particular, as shown later, the R_{pp} is not affected so much by local-fields, whereas the coefficient R_{sp} is drastically reduced by the local-field effects.

We find similar conclusions for the monohydride surface second-harmonic spectra, shown in Fig. 9.5. Again we observe a big effect of local-fields on the zzz and the zyy components, whereas the yyz component is only slightly affected by local-fields and, in particular, peak positions of these components are not modified.

From the analysis of the clean, the monohydride and the dihydride surface second-harmonic spectra (corresponding to three different space-groups), it is possible to attribute to local-fields two distinct effects, depending on the kind of component concerned. If the component corresponds to an emitted polarization propagating perpendicularly to the surface plane, the spectral weight is redistributed to higher energies, by changing the weight from 2ω transitions to 1ω transitions. On the contrary, if

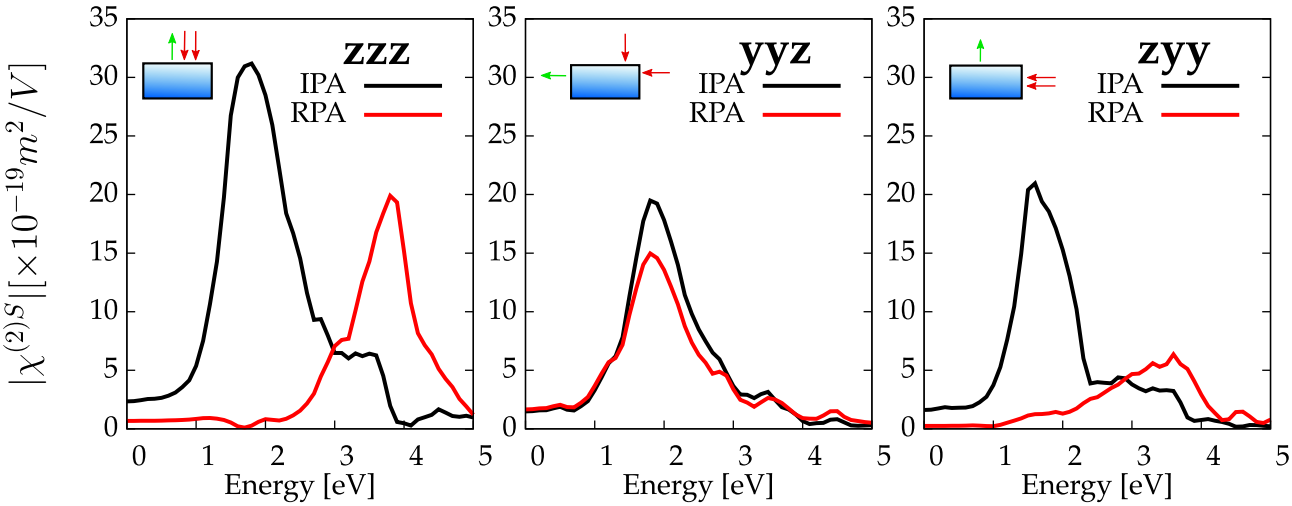

Fig. 9.5: Surface second-harmonic generation spectra of the monohydride Si(001)2×1:1H surface, for the zzz, xxz and zxx components of the $\chi^{(2)S}$ tensor. No scissors correction is included.

the polarization is propagating in the plane of the surface, the local-field effects reduce the spectral weight of the main structures but their positions are not altered.

9.3 Comparison with experimental results

In this section, we further analyse the dihydride or Si(001)1×1:2H surface. In particular, I present here two comparisons with available experimental data. First I present a comparison between experiment and theory for single components of the susceptibility tensor, and then I compare theoretical calculations of the generalized reflection coefficients with low-temperature measurements.

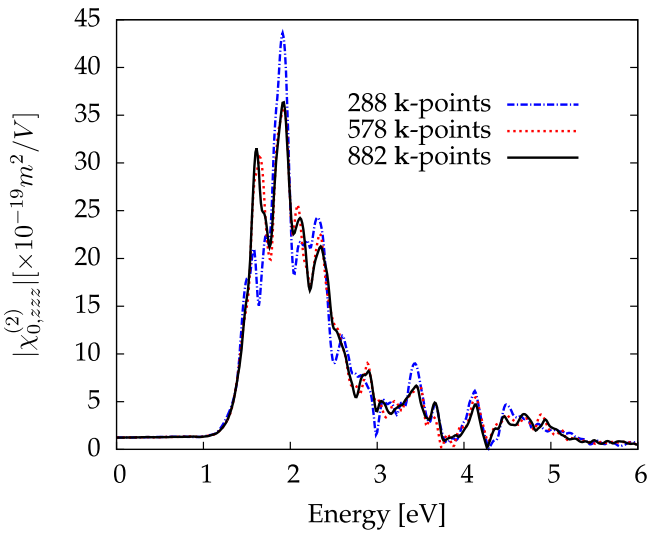

Fig. 9.6: SHG spectra $|\chi^{(2)S}_{0,zzz}|$ of the dihydride surface calculated using **k**-point grids corresponding to 288 (blue, dotted-dashed line), 578 (red, dashed line), and 882 (black solid line) points in the surface Brillouin zone.

In order to compare with the experimental data, a smaller broadening must be used. This increases the requirement in number of **k**-points. The number of **k**-points used for sampling the Brillouin zone is one of the most important criteria for the calculation of the optical properties of surfaces, as already pointed out by various authors in the literature [256–258]. Fig. 9.6 shows the SHG spectra of the dihydride surface, calculated for uniform grids of **k**-points containing respectively 288, 578 and 882 **k**-points. All the spectra are computed with a broadening of 50meV. This figure shows in particular that the grid with 578 **k**-points yield a completely converged spectra.

Therefore, in the following, this grid of **k**-point is used.

9.3.1 Components of the second-order susceptibility tensor

In experiments, the generalised reflection coefficients (see Chap. 2) result from the contributions of both surface dipolar and bulk quadrupolar terms, the latter having never being calculated, to the best of my knowledge, by means of *ab initio* methods. This makes difficult the comparison between theory and experiments. Nevertheless, when the surface dipolar contribution is isotropic, as for the dihydride surface, it is possible to exploit this isotropy to distinguish between surface dipolar and bulk quadrupolar contributions, see Refs. [78–80]. In these references, authors used rotational anisotropy to separate the anisotropic contribution, coming from the bulk quadrupolar term, and the isotropic contribution, coming from the surface. In particular, in Ref. [79], authors have been able, from their measurements, to extract the spectra of $\chi^{(2)S}_{xxz}$ and $\chi^{(2)S}_{zxx}$ for the dihydride Si(001)1×1:2H surface. Their results are not given in absolute units but the SHG spectra were normalized against the reflected SHG signal from a quartz reference [79]. Recently, it has become possible to measure experimentally the absolute amplitude of some components of the surface second-order susceptibility tensor $\chi^{(2)S}$ [78] and even the absolute phase [251]. In particular, in Ref. [78], authors found for the native-oxide covered Si(001) surface, an absolute value of $3.5 \pm 0.7 \times 10^{-19} m^2/V$ for $\chi^{(2)S}_{xxz}$, at the second-harmonic energy $2\hbar\omega = 3.1eV$. This energy is out of the resonance due to the E_1 critical point of silicon, and is found to be quite insensitive to the surface termination, as shown by the spectra of $\chi^{(2)S}_{xxz}$, extracted for three surface terminations in Ref. [79].

Using this value as a reference, we can convert the data of Ref. [79] into absolute units, as they provide us with the normalized value for the hydrogen-terminated Si(001) SHG spectra, but also with the native and thermal oxide terminated surface spectra.[2] Notice that this is only possible because the results of Ref. [251] have been normalized to a quartz crystal, as in Ref. [78].
Due to the uncertainty on the experimental absolute value of $\chi^{(2)S}_{xxz}$, there is at least 20% of error on the experimental spectra. Nevertheless, this allows us to compare the theoretical calculations with experimental data *in absolute units*, whereas theoretical calculations are usually rescaled to agree with theoretical calculations. Renormalizing by the same procedure the experimental spectrum of $|\zeta|$ given in Ref. [80] and extracted from the same experimental data as in Ref. [79], yields values in good agreement with the absolute experimental values, obtained from other references [78,251]. This shows the robustness of the approach.

The comparison between theoretical calculations and experimental data, in absolute units, is reported in Fig. 9.7. The calculation without local-fields (left panel) is found to not reproduce even qualitatively the experimental data, and in particular, we found here that $|\chi^{(2)}_{zxx}| > |\chi^{(2)}_{xxz}|$ whereas the opposite is observed experimentally, in the region probed in Ref. [79]. The local-field effects, within the RPA (right panel) improves significantly the agreement between theory and experiment. Indeed, the relative weight of the two components is now found to be consistent with the experimental data. Moreover, we obtain a good agreement for the absolute intensity, showing the importance of including local-field effects to quantitatively reproduce the experiments. Note that in a previous

[2] Some care is required when comparing the results of the different papers, due to the definition of the d matrix, which gives for instance $2d_{15} = \chi^{(2)}_{xxz}$.

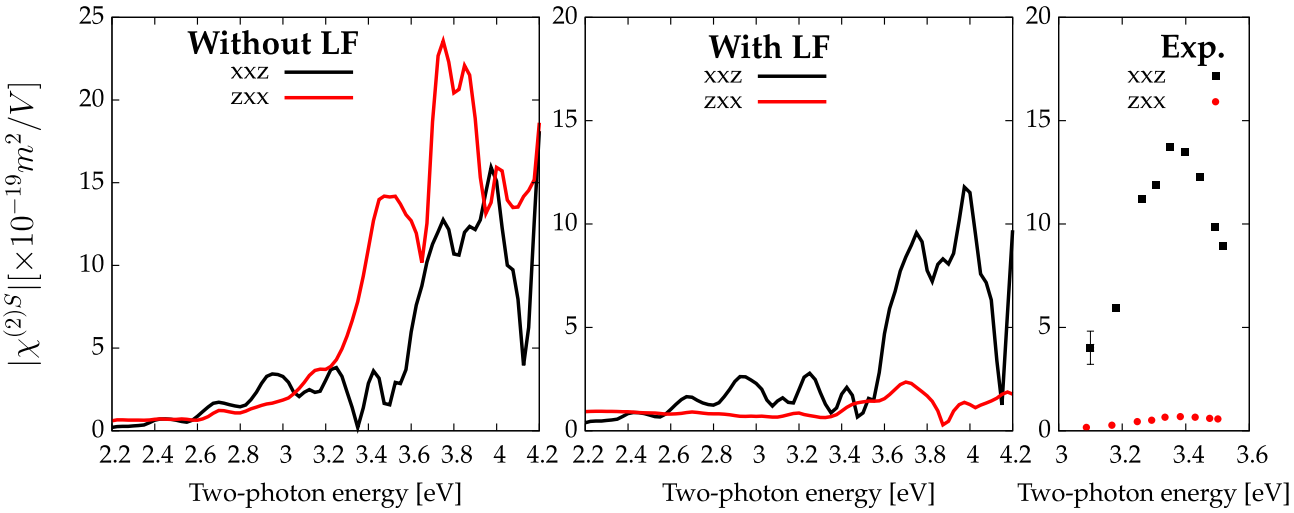

Fig. 9.7: Comparison between the theoretical calculation of $|\chi^{(2)S}_{xxz}|$ and $|\chi^{(2)S}_{zxx}|$ without local-field effects (left panel), with local-field effects (middle panel), and the experimental data, from Ref. [79] (right panel). Here we used $\Delta\omega = 0.125eV$, $\eta = 0.25eV$ and scissors correction of $\Delta = 0.6eV$.

study of surface second-harmonic generation, performed at the level of independent-particles [228], the calculated intensities were found to be respectively a factor-of-5 and a factor-of-10 larger than the experimental ones for R_{pp} and R_{ps}.

The calculated peak positions are not in good agreement with the experimental one. It has been observed that the temperature has a strong influence on the peak position of the clean and the monohydride surfaces; and that lowering the temperature induces a blue-shift of the E_1 resonance [33,253]. The experimental data presented here have been obtained from room temperature measurements. Comparing the SHG spectra of Refs. [33, 58, 259], I found that decreasing the temperature from 300K to 80K induces a blue-shift of about 0.1eV (in two-photon energy scale). Clearly, this does not explain entirely the difference in the peak positions found here of about 0.3 eV (in the two-photon energy scale). Even if we do not have a clear explanation for this discrepancy, we want to stress that state-of-the-art linear calculations, including the excitonic effects thanks to the Bethe-Salpeter equation, and with a GW correction, instead of a scissors operator, also suffer from a 0.2 eV blue-shift as compared to the experimental spectra for the dihydride surface [181]. This is consistent with the 0.3 eV of difference we obtained, in the two-photon energy scale. Possible explanations for this difference in the peak positions can be found in Ref. [181], and are therefore not repeated here. Finally, the calculation are performed here for 24 atomic layers. Calculations for thicker slabs are expected to improve the agreement with the experiment.

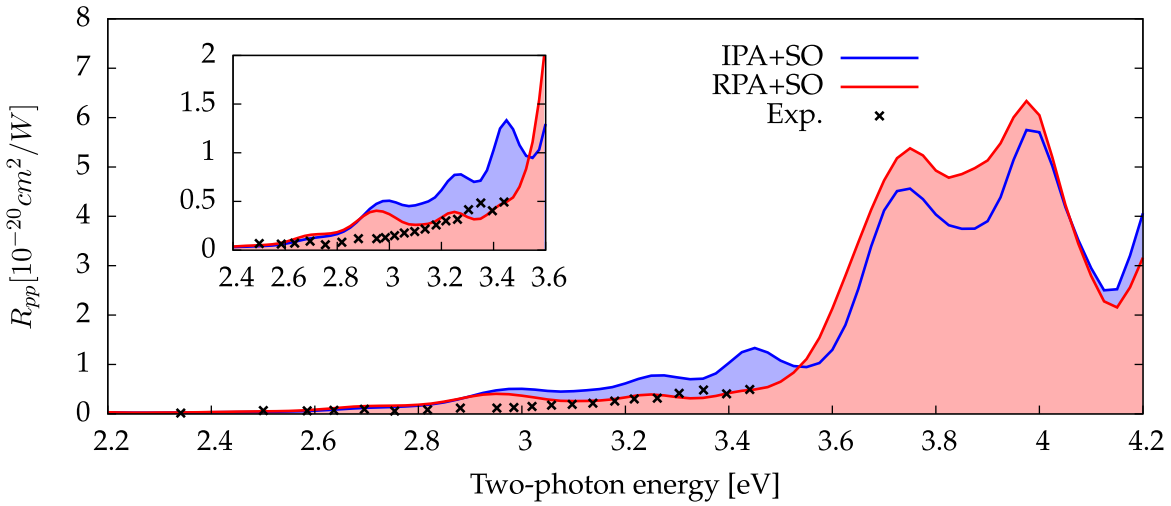

Fig. 9.8: R_{pp} *vs* the two-photon energy for the dihydride Si(001)1×1:2H surface. Blue curve: IPA+SO calculation. Red curve: RPA+SO calculation. In both cases, we used a scissors correction of $\Delta = 0.6$eV. The low-temperature experimental results (black crosses, rescaled on the vertical axis) are obtained from Ref. [259]. The angle of incidence θ=45° is the same as in the experiment. A Lorentzian broadening of 20 meV is added as a post-processing on the final R_{pp} spectra.

9.3.2 Generalized reflection coefficients

The dihydride surface exhibits a $p4mm$ symmetry. Therefore, the two non-zero reflection coefficients are given by (see Chap. 2)

$$R_{pp}(\theta,\omega) = \frac{2\omega^2\tan^2\theta}{c^3\epsilon_0}\left|\frac{t^p_{mv}(2\omega)t^p_{vm}(\omega)^2}{\sqrt{\epsilon(2\omega)}\epsilon(\omega)}\frac{q^v_\perp(2\omega)}{q^m_\perp(2\omega)}\right|^2\left|\sin^2\theta\chi^{(2)S}_{\perp\perp\perp} + \frac{c^2}{\omega^2}\left(q^m_\perp(\omega)^2\chi^{(2)S}_{\perp|||} - q^m_\perp(2\omega)q^m_\perp(\omega)\chi^{(2)S}_{|||\perp}\right)\right|^2, \tag{9.1a}$$

$$R_{sp}(\theta,\omega) = \frac{2\omega^2\tan^2\theta}{c^3\epsilon_0}\left|\frac{t^p_{mv}(2\omega)t^s_{vm}(\omega)^2}{\sqrt{\epsilon(2\omega)}}\right|^2\left|\frac{q^v_\perp(2\omega)}{q^m_\perp(2\omega)}\right|^2\left|\chi^{(2)S}_{\perp|||}\right|^2. \tag{9.1b}$$

Here θ is the angle of incidence, ω is the frequency of the incoming photon, t^i_{mv} and t^i_{vm} are the Fresnel transition coefficients, respectively describing the matter-to-vacuum and the vacuum-to-matter transmissions, for the i polarization and ϵ is the bulk dielectric function. The derivation of these coefficients is explained in Chap. 2. In Fig. 9.8, I show the reflection coefficient R_{pp}, corresponding to a p-polarized incoming light and a p-polarized outgoing photon, along with low-temperature (80K) experimental data of Ref. [259]. I used here, as for the previous comparison, a frequency spacing of $\Delta\omega = 0.125eV$ and a broadening of $\eta = 0.25eV$.

The calculations with and without local-fields are found to be of the same intensity and to agree qualitatively. This can be understood by the fact that due to the different weights in Eq. (9.1a), the component xxz is mainly responsible for the resulting line-shape of R_{pp}, as already noticed in Ref. [226]. We have already seen that the component xxz is only slightly affected by local-field effects (see Fig. 9.4), explaining the small difference between the two calculated R_{pp}. The peak around 3.4 eV, clearly visible in the calculation without local-fields included ("IPA+SO"), vanishes when these latter

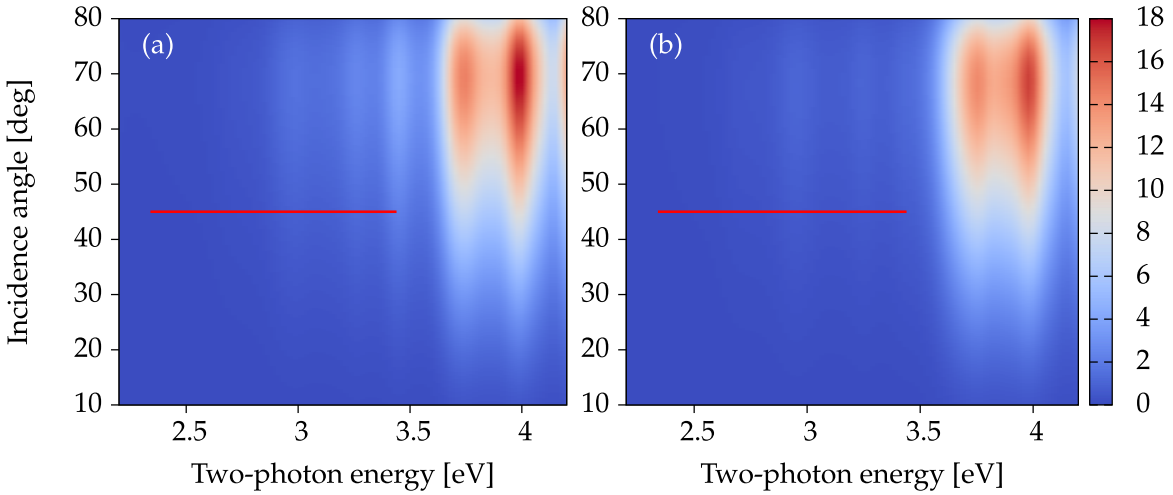

Fig. 9.9: R_{pp} spectra *versus* the incidence angle for the dihydride Si(001)1×1:2H surface. (a) Without local-field effects. (b) Local-field effects included. A Lorentzian broadening of 20 meV is added as a post-processing on the final R_{pp} spectra.

are included ("RPA+SO"). Again, we obtain that including local-field effects improve the comparison with experiments. The results suggest that more interesting features can be observed at higher energies, as shown by the big structure between 3.6 and 4.0 eV. From the results, it is also possible to obtain the evolution of the reflection coefficient *versus* the angle of incidence. This is represented in Fig. 9.9. We observe that the R_{pp} reflection coefficient has the same angular dependence with and without local-field effects, except small structures between 3.2 and 3.4 eV which are not present once local-field effects are included.

I would like to comment on the value of the angle of incidence chosen for studying the dihydride surface. The experimental measurements of Ref. [259] (shown by the red line in Fig. 9.9) were performed at 45° of incidence. Other studies of the same surface were also performed with similar angles, for instance 35° [253] and 45° [227]. However, as suggested by Fig. 9.9, the optimal value for performing measurements on the dihydride surface is around 70°, as it would yield a more intense signal. An angular value around 70° is experimentally possible, *e.g.*, Ref. [260] where authors performed their measurements with a value of 67.5° for their measurements on the clean Si(001)2×1 surface. A more complex problem is to probe the higher-energy region, even if studies have been already performed in this region [63, 228]. The absence of features in the reflection spectra from the dihydride surface is mainly due to the choice of the incidence angle, and a more optimal value of the angle of incidence would potentially reveal more details in the second-harmonic reflection spectra of the dihydride surface.

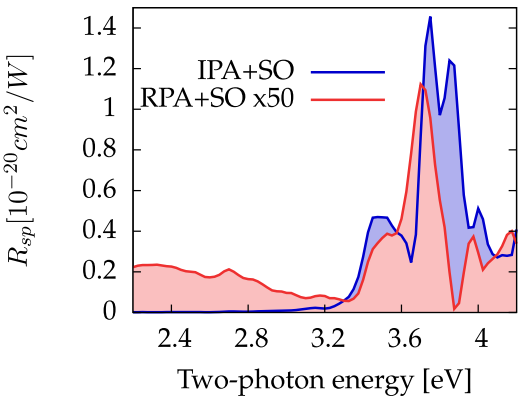

Fig. 9.10: The same as in Fig. 9.8, but for the s-in/p-out reflection coefficient R_{sp}.

In Fig. 9.8, I show the reflection coefficient R_{sp}, corresponding to an s-polarized incoming light and a p-polarized outgoing photon. By opposition to the R_{pp} reflection coefficient, the local-fields quench

completely the spectra. Note that the spectra including local-field effects ("RPA+SO") is rescaled by a factor of 50 to be compared to the spectra without local-field effects ("IPA+SO"). This is easily understood, looking at Eq. (9.1b). Indeed, the R_{sp} coefficient depends only on the square of $|\chi^{(2)}_{zyy}|$, with the component zyy being strongly affected by the local-field effects in the region between 1 eV and 2 eV, for the fundamental frequency, see Fig. 9.7. Without the local-field effects, the intensity is over-estimated by more than a factor of 50, showing how crucial it is to account for the latter.

Summary

I have presented in this chapter the local-field effects on the surface second-harmonic generation, obtained for the first time from *ab initio* calculations. The local-fields have been taken into account exactly, without assuming any model, using the theory developed in Chap. 7.

Applied to the generation of second-harmonic from silicon surfaces, I have shown how important these local-fields are for describing the components of the second-order susceptibility tensor. Through the analysis of different components of three silicon surfaces, I have shown that two main effects are possible. If the direction of the emitted polarization, *i.e.*, the first component of the $\chi^{(2)S}$ tensor, is perpendicular to the plane of the surface (z-direction), the local-field effects are found to be important and to redistribute the weight from 2ω transitions to 1ω transitions. If the outgoing polarization is in the plane of the surface, the local-field effects are found to be less important and to not affect the prominent peaks positions.

I have also investigated in this chapter the effect of ad-atoms on the spectra of surface second-harmonic generation. In particular, I found a more important effect of the local-fields on the hydrogenated surfaces. Interestingly, the major effect of local-fields, for the two hydrogenated surfaces, is to reduce the spectral weight drastically for some components of the $\chi^{(2)S}$ tensor, in the region where a quenching due to the hydrogen is found experimentally.

Comparison with available experimental data have shown that these local-field effects allows us to obtain quantitative agreement between theory and experiments. We have compared theoretical calculations and experimental data, both in absolute units; showing for the first time an agreement for the absolute intensity of surface second-harmonic generation calculated from *ab initio* methods. Also, the comparisons with low temperature reflectivity measurements have shown an improvement of the theoretical description, when including local-field effects. As a conclusion, we found that local-field effects are mandatory for a good description of surface second-harmonic generation and that the theory presented in this chapter takes us a step closer to reality.

10. Excitonic effects on second-harmonic generation from silicon surfaces

The electron-hole interaction is known to be a key ingredient for obtaining reliable results when calculating optical properties of bulk materials [261], but also surfaces [262] and nanostructures [263]. When these effects are neglected, it is generally found that the absorption spectra is underestimated in the low-energy region and overestimated the higher energy region.

The state-of-the art method for including the excitonic effects in the optical spectra, namely solving the Bethe-Salpeter equation (BSE), is still numerically challenging for surfaces, due to the big number of atoms that has to be treated. An alternative way for including excitonic effects is the time-dependent-density-functional theory (TDDFT), where these effects are obtained through the inclusion of the variations of the exchange-correlation (xc) potential. Various exchange-correlation kernels (f_{xc}) have been proposed during the twenty past years, mainly for extended systems, and only few of them have been tested on surfaces. Among these few kernels, we find the long-range contribution (LRC) kernel, or α-kernel [114], which includes the correct long-range decay of f_{xc} in momentum space as $1/q^2$. This simple kernel has been found to be sufficient to obtain the continuum exciton effects in optical spectra of bulk semiconductors, like GaAs and silicon. It has also been successfully tested against the result of the BSE for the linear optical properties of the Si(111)2×1 surface [262]. Authors of Ref. [262] found the α-kernel to be applicable to surfaces of semiconductors, with the value of α determined for the bulk material. Moreover this kernel has also been applied to the calculation of SHG spectra, thus improving the agreement with the experiment [41, 43].

In this chapter, I show that it is possible to extend the TDDFT macroscopic formalism developed in Chap. 7, in order to include the exchange-correlation kernel f_{xc} in the formalism. In the first part, I show that the effects of the LRC kernel, which is chosen to be a scalar kernel, can be included in the spectra, as a post-processing on the bulk measurable quantities, namely the macroscopic dielectric tensor, ϵ_M, and macroscopic second-order susceptibility tensor, $\chi^{(2)}_M$.

Then I extend this derivation to the case of surfaces. In particular, I present a formula allowing us to include the effects of the α-kernel on the surface second-harmonic generation spectra. Finally, this formalism is applied to the SHG spectra of silicon surfaces, to get an insight into the excitonic effects on the surface second-harmonic generation.

This chapter represents the first effort to include such excitonic effects on the nonlinear properties of surfaces.

10.1 The α-kernel as a post-processing

10.1.1 Bulk materials

Let us start by considering bulk materials. Even if this does not correspond to the scope of this chapter, the results presented in this section serves as a preliminary for the surface case.

Macroscopic dielectric tensor

We start by considering the case of the macroscopic dielectric tensor of a bulk materials. In the framework of the TDDFT, and assuming the long-wavelength limit, the longitudinal-longitudinal (LL) part of the macroscopic dielectric tensor is given, at any level of approximation, by

$$\epsilon_M^{LL}(\mathbf{q};\omega) = \frac{1}{1 + v_{\mathbf{0}}(\mathbf{q})\left[\chi^{(1)}_{\rho\rho}(\mathbf{q};\omega)\right]_{\mathbf{G}=\mathbf{G}'=\mathbf{0}}}, \tag{10.1}$$

where q is a vanishing momentum, ω the frequency of the light, $\mathbf{G}$ and $\mathbf{G}'$ are reciprocal lattice vectors, and $\chi^{(1)}_{\rho\rho}$ is the density response function of the fully interacting electronic system.
The latter quantity is obtained in reciprocal space by solving the Dyson-like equation

$$\left[\chi^{(1)}_{\rho\rho}(\mathbf{q};\omega)\right]_{\mathbf{G}\mathbf{G}'} = \left[\chi^{(0)}_{\rho\rho}(\mathbf{q};\omega)\right]_{\mathbf{G}\mathbf{G}'} + \sum_{\mathbf{G_1}\mathbf{G_2}} \left[\chi^{(0)}_{\rho\rho}(\mathbf{q};\omega)\right]_{\mathbf{G}\mathbf{G_1}} \left[v(\mathbf{q}) + f_{\text{xc}}(\mathbf{q};\omega)\right]_{\mathbf{G_1}\mathbf{G_2}} \left[\chi^{(1)}_{\rho\rho}(\mathbf{q};\omega)\right]_{\mathbf{G_2}\mathbf{G}'}, \tag{10.2}$$

where $\chi^{(0)}_{\rho\rho}$ is the density response function of the non-interacting system, v is the Coulomb interaction and f_{xc} is the exchange-correlation kernel. In order to be able to solve this equation, one has to introduce an approximation for the unknown exchange-correlation kernel. In the random-phase approximation (RPA), the exchange-correlation kernel is neglected and only the Coulomb interaction, responsible for the local-field effects, is considered (see Chap. 3). We denote $\chi^{(1)\text{RPA}}_{\rho\rho}$ the solution of Eq. (10.2) in the RPA. When the long-range contribution kernel is included, we have $\left[f^{\text{LRC}}_{\text{xc}}(\mathbf{q};\omega)\right]_{\mathbf{G_1}\mathbf{G_2}} = \alpha/q^2 \delta_{\mathbf{G_1 0}} \delta_{\mathbf{G_1}\mathbf{G_2}}$. It is straightforward to show that the solution of the Dyson equation including the long-range contribution, $\chi^{(1)}_{\rho\rho}$, is linked to the RPA response, $\chi^{(1)\text{RPA}}_{\rho\rho}$, by

$$\left[\chi^{(1)}_{\rho\rho}(\mathbf{q};\omega)\right]_{\mathbf{G}\mathbf{G}'} = \left[\chi^{(1)\text{RPA}}_{\rho\rho}(\mathbf{q};\omega)\right]_{\mathbf{G}\mathbf{G}'} + \left[\chi^{(1)\text{RPA}}_{\rho\rho}(\mathbf{q};\omega)\right]_{\mathbf{G0}} \frac{\alpha}{q^2} \left[\chi^{(1)}_{\rho\rho}(\mathbf{q};\omega)\right]_{\mathbf{0}\mathbf{G}'}. \tag{10.3}$$

From Eq. 10.3, we obtain that $\chi^{(1)}_{00}(\mathbf{q};\omega) = \frac{\chi^{(1)RPA}_{00}(\mathbf{q};\omega)}{\left(1-\chi^{(1)RPA}_{00}(\mathbf{q};\omega)\frac{\alpha}{q^2}\right)}$. Using this result, the macroscopic dielectric response including the effect of the LRC kernel, ϵ_M, can then be linked to the macroscopic RPA dielectric response, ϵ^{RPA}_M. After simple algebra, one obtains that

$$\epsilon_M^{LL}(\mathbf{q};\omega) - 1 = \frac{\epsilon_M^{LL,\text{RPA}}(\mathbf{q};\omega) - 1}{1 + \frac{\alpha}{4\pi}\left(\epsilon_M^{LL,\text{RPA}}(\mathbf{q};\omega) - 1\right)}. \tag{10.4}$$

This simple formula can be used to obtain the effect of the LRC kernel on the linear spectra, at the extremely low cost of a post-processing of the dielectric response computed in the RPA. Notice that this analytical expression is close to the contact exciton model, as already discussed in Ref. [84].

Second-order response function

The measurable quantity, playing the role of ϵ_M^{LL} at second-order is the macroscopic second-order response tensor $\chi_M^{(2)}$ given by [41]

$$\chi_M^{(2)}(\mathbf{q},\mathbf{q_1},\mathbf{q_2};\omega,\omega) = \frac{-i}{2|\mathbf{q}||\mathbf{q_1}||\mathbf{q_2}|}\left[\chi_{\rho\rho\rho}^{(2)}(\mathbf{q},\mathbf{q_1},\mathbf{q_2};\omega,\omega)\right]_{\mathbf{000}}\epsilon_M^{LL}(\mathbf{q};2\omega)\epsilon_M^{LL}(\mathbf{q_1};\omega)\epsilon_M^{LL}(\mathbf{q_2};\omega), \quad (10.5)$$

where $\chi_{\rho\rho\rho}^{(2)}$ is the second-order susceptibility of the fully interacting electronic system; which can be obtained by solving the second-order Dyson-like equation [41], see Eq. (3.37). We have defined here $\mathbf{q} = \mathbf{q_1} + \mathbf{q_2}$.

We proceed following the same idea as for the linear case, and we link the RPA density response function to the LRC density response function, *i.e.*, containing the LRC exchange-correlation kernel. Following the derivation of App. F.2, we obtain the link between the solution of the Dyson equation including the long-range contribution, $\chi_{\rho\rho\rho}^{(2)}$, and the RPA response, $\chi_{\rho\rho\rho}^{(2)\mathrm{RPA}}$, which reads in reciprocal space as

$$\begin{aligned}\left[\chi_{\rho\rho\rho}^{(2)}(\mathbf{q},\mathbf{q_1},\mathbf{q_2};\omega,\omega)\right]_{\mathbf{GG'G''}} &= \sum_{\mathbf{G_1G_2}}\left[\chi_{\rho\rho\rho}^{(2)\mathrm{RPA}}(\mathbf{q},\mathbf{q_1},\mathbf{q_2};\omega,\omega)\right]_{\mathbf{GG_1G_2}} \\ \times\left[\delta_{\mathbf{G_1G'}} + \frac{\alpha}{q_1^2}\delta_{\mathbf{G_10}}\left[\chi_{\rho\rho}^{(1)}(\mathbf{q_1};\omega)\right]_{\mathbf{G_1G'}}\right]&\left[\delta_{\mathbf{G_2G''}} + \frac{\alpha}{q_2^2}\delta_{\mathbf{G_20}}\left[\chi_{\rho\rho}^{(1)}(\mathbf{q_2};\omega)\right]_{\mathbf{G_2G''}}\right] \\ &+\left[\chi_{\rho\rho}^{(1)\mathrm{RPA}}(\mathbf{q};2\omega)\right]_{\mathbf{G0}}\frac{\alpha}{q^2}\left[\chi_{\rho\rho\rho}^{(2)}(\mathbf{q},\mathbf{q_1},\mathbf{q_2};\omega,\omega)\right]_{\mathbf{0G'G''}}.\end{aligned}$$

The solution of this equation for $\mathbf{G} = \mathbf{G'} = \mathbf{G''} = 0$ is

$$\left[\chi_{\rho\rho\rho}^{(2)}(\mathbf{q},\mathbf{q_1},\mathbf{q_2};\omega,\omega)\right]_{\mathbf{000}} = \frac{\left[\chi_{\rho\rho\rho}^{(2)\mathrm{RPA}}(\mathbf{q},\mathbf{q_1},\mathbf{q_2};\omega,\omega)\right]_{\mathbf{000}}}{\left(1-\frac{\alpha}{q^2}\left[\chi_{\rho\rho}^{(1)\mathrm{RPA}}(\mathbf{q};2\omega)\right]_{\mathbf{00}}\right)}\left[1+\frac{\alpha}{q_1^2}\left[\chi_{\rho\rho}^{(1)}(\mathbf{q_1};\omega)\right]_{\mathbf{00}}\right]\left[1+\frac{\alpha}{q_2^2}\left[\chi_{\rho\rho}^{(1)}(\mathbf{q_2};\omega)\right]_{\mathbf{00}}\right]. \quad (10.6)$$

Inserting the expressions of $\chi_{\mathbf{000}}^{(2)}$ and $\chi_{\mathbf{00}}^{(1)}$ into Eq. 10.5, we obtain directly the link between the RPA and the full macroscopic second-order susceptibilities

$$\begin{aligned}\chi_M^{(2)}(\mathbf{q},\mathbf{q_1},\mathbf{q_2};\omega,\omega) = \frac{-i}{2|\mathbf{q}||\mathbf{q_1}||\mathbf{q_2}|}&\frac{\epsilon_M^{LL}(\mathbf{q};2\omega)}{\left(1-\frac{\alpha}{4\pi}v_{\mathbf{0}}(\mathbf{q})\left[\chi_{\rho\rho}^{(1)\mathrm{RPA}}(\mathbf{q};2\omega)\right]_{\mathbf{00}}\right)}\chi_{\mathbf{000}}^{(2)\mathrm{RPA}}(\mathbf{q},\mathbf{q_1},\mathbf{q_2};\omega,\omega) \\ \times&\left[\frac{\epsilon_M^{LL}(\mathbf{q_1};\omega)}{\left(1-\frac{\alpha}{4\pi}v_{\mathbf{0}}(\mathbf{q_1})\left[\chi_{\rho\rho}^{(1)\mathrm{RPA}}(\mathbf{q_1};\omega)\right]_{\mathbf{00}}\right)}\right]\left[\frac{\epsilon_M^{LL}(\mathbf{q_2};\omega)}{\left(1-\frac{\alpha}{4\pi}v_{\mathbf{0}}(\mathbf{q_2})\left[\chi_{\rho\rho}^{(1)\mathrm{RPA}}(\mathbf{q_2};\omega)\right]_{\mathbf{00}}\right)}\right],\end{aligned}$$

where we used the fact that $\frac{\alpha}{q^2} = \frac{\alpha}{4\pi}v_{\mathbf{0}}(\mathbf{q})$.
After some algebra and using the fact that

$$\epsilon_M^{LL}(\mathbf{q};\omega) = \frac{\left(1+\frac{\alpha}{4\pi}\right)\epsilon_M^{LL,\mathrm{RPA}}(\mathbf{q};\omega) - \frac{\alpha}{4\pi}}{1+\frac{\alpha}{4\pi}\left(\epsilon_M^{LL,\mathrm{RPA}}(\mathbf{q};\omega)-1\right)}, \quad (10.7)$$

we obtain the simple result

$$\chi_M^{(2)}(\mathbf{q},\mathbf{q_1},\mathbf{q_2};\omega,\omega) = A(\mathbf{q};2\omega)\chi_M^{(2)\mathrm{RPA}}(\mathbf{q},\mathbf{q_1},\mathbf{q_2};\omega,\omega)A(\mathbf{q_1};\omega)A(\mathbf{q_2};\omega), \tag{10.8}$$

where $A(\mathbf{q};\omega) = \frac{1}{1+\frac{\alpha}{4\pi}\left(\epsilon_M^{LL,\mathrm{RPA}}(\mathbf{q};\omega)-1\right)}$.
Again we have linked the macroscopic quantity, including the long-range contribution $\chi_M^{(2)}$, to the RPA macroscopic second-order response $\chi_M^{(2)\mathrm{RPA}}$. This result allows us to include the excitonic effects on the second-harmonic spectra of bulk materials, without increasing the numerical burden associated with its calculation.

10.1.2 Surfaces

We have established that the effects of the α-kernel on the macroscopic optical responses of bulk systems can be included, at first- and second-order, as a post-processing of the macroscopic RPA optical responses. In this section, I extend this result to the case of surfaces. The calculations are more complex because of the presence, in the Dyson-like equations, of both the density response functions and surface-averaged density response functions, see Chap. 7.

Surface dielectric function

The expression of the macroscopic surface dielectric function (see Chap. 7 for the definition and the derivation) is given by

$$\epsilon_M^{S,LL}(\hat{\mathbf{q}};\omega) = 1 - \lim_{\mathbf{q}\to\mathbf{0}} v_{\mathbf{0}}(\mathbf{q})\frac{1}{L_z}\frac{\sum_{G_z}\tilde{\mathcal{C}}(-G_z)\left[\chi_{\rho\rho}^{(1)}(\mathbf{q};\omega)\right]_{\mathbf{G_z0}}}{1+v_{\mathbf{0}}(\mathbf{q})\left[\chi_{\rho\rho}^{(1)}(\mathbf{q};\omega)\right]_{\mathbf{00}}}, \tag{10.9}$$

where L_z is the thickness of half of the super-cell used to model the surface.
We introduce the quantity $\bar{\chi}^{(1)}$, defined by Eq. (7.16), which is related in the LRC approximation to the density response function of the fully interacting system, $\chi_{\rho\rho}^{(1)}$, by

$$\left[\bar{\chi}^{(1)}(\mathbf{q};\omega)\right]_{\mathbf{G0}} = \frac{\left[\chi_{\rho\rho}^{(1)}(\mathbf{q};\omega)\right]_{\mathbf{G0}}}{1+(v_{\mathbf{0}}(\mathbf{q})+\frac{\alpha}{q^2})\left[\chi_{\rho\rho}^{(1)}(\mathbf{q};\omega)\right]_{\mathbf{00}}}. \tag{10.10}$$

Inserting this relation into the expression of the macroscopic dielectric tensor, and identifying the macroscopic dielectric tensor in the RPA approximation, given by Eq. (7.18), we obtain directly that

$$\epsilon_M^{S,LL}(\mathbf{q};\omega) - 1 = \left(\epsilon_M^{S,LL,\mathrm{RPA}}(\mathbf{q};\omega) - 1\right)\frac{1+(v_{\mathbf{0}}(\mathbf{q})+\frac{\alpha}{q^2})\left[\chi_{\rho\rho}^{(1)}(\mathbf{q};\omega)\right]_{\mathbf{00}}}{1+v_{\mathbf{0}}(\mathbf{q})\left[\chi_{\rho\rho}^{(1)}(\mathbf{q};\omega)\right]_{\mathbf{00}}}.$$

Simple algebra give that

$$\frac{1+(v_{\mathbf{0}}(\mathbf{q})+\frac{\alpha}{q^2})\left[\chi_{\rho\rho}^{(1)}(\mathbf{q};\omega)\right]_{\mathbf{00}}}{1+v_{\mathbf{0}}(\mathbf{q})\left[\chi_{\rho\rho}^{(1)}(\mathbf{q};\omega)\right]_{\mathbf{00}}} = 1+\frac{\alpha}{4\pi}\frac{v_{\mathbf{0}}(\mathbf{q})\left[\chi_{\rho\rho}^{(1)}(\mathbf{q};\omega)\right]_{\mathbf{00}}}{1+v_{\mathbf{0}}(\mathbf{q})\left[\chi_{\rho\rho}^{(1)}(\mathbf{q};\omega)\right]_{\mathbf{00}}} = \frac{1}{1+\frac{\alpha}{4\pi}\left(\epsilon_M^{LL,\mathrm{RPA}}(\mathbf{q};\omega)-1\right)}.$$

Finally, we obtain that the macroscopic surface dielectric function is given by

$$\epsilon_M^{S,LL}(\hat{\mathbf{q}};\omega) - 1 = \frac{\epsilon_M^{S,LL,\mathrm{RPA}}(\hat{\mathbf{q}};\omega) - 1}{1 + \frac{\alpha}{4\pi}\big(\epsilon_M^{LL,\mathrm{RPA}}(\hat{\mathbf{q}};\omega) - 1\big)}, \tag{10.11}$$

showing that the result of Eq. (10.4) is also valid for the surface macroscopic dielectric tensor.

Surface second-order susceptibility

Now that we have established the preliminary results, we can focus on the primary interest of this chapter, which is the analytical inclusion of the effect of the LRC-kernel in the macroscopic surface second-order susceptibility.
We start from the expression of the macroscopic surface second-order susceptibility, valid for any approximation of the exchange-correlation kernel, proved in Chap. 7

$$\chi_M^{(2)S}(\mathbf{q},\mathbf{q_1},\mathbf{q_2};\omega,\omega) = \frac{-i}{2|\mathbf{q}||\mathbf{q_1}||\mathbf{q_2}|}\epsilon_M(\mathbf{q_1};\omega)\epsilon_M(\mathbf{q_2};\omega)$$
$$\times\left[\Big(\epsilon_M^{S}(\mathbf{q};2\omega) - 1\Big)\big[\chi^{(2)}_{\rho\rho\rho}(\mathbf{q},\mathbf{q_1},\mathbf{q_2};\omega,\omega)\big]_{\mathbf{000}} + \chi^{(2)S}_{\rho\rho\rho}(\mathbf{q},\mathbf{q_1},\mathbf{q_2};\omega,\omega)\right], \tag{10.12}$$

where $\chi^{(2)S}_{\rho\rho\rho}(\mathbf{q},\mathbf{q_1},\mathbf{q_2};\omega,\omega)$ is given by

$$\chi^{(2)S}_{\rho\rho\rho}(\mathbf{q},\mathbf{q_1},\mathbf{q_2};\omega,\omega) = \frac{1}{L_z}\sum_{G_z}\tilde{\mathcal{C}}(G_z)\big[\chi^{(2)}_{\rho\rho\rho}(\mathbf{q},\mathbf{q_1},\mathbf{q_2};\omega,\omega)\big]_{\mathbf{G_z00}}. \tag{10.13}$$

For conciseness, we omit here the LL superscript of the dielectric functions.
Using Eq. (10.6) and Eq. (10.11), we obtain that

$$\chi_M^{(2)S}(\mathbf{q},\mathbf{q_1},\mathbf{q_2};\omega,\omega) = \frac{-i}{2|\mathbf{q}||\mathbf{q_1}||\mathbf{q_2}|}A(\mathbf{q_1};\omega)\epsilon_M^{\mathrm{RPA}}(\mathbf{q_1};\omega)A(\mathbf{q_2};\omega)\epsilon_M^{\mathrm{RPA}}(\mathbf{q_2};\omega)$$
$$\times\left[A(\mathbf{q};2\omega)\Big(\epsilon_M^{S,\mathrm{RPA}}(\mathbf{q};2\omega) - 1\Big)\frac{\big[\chi^{(2),\mathrm{RPA}}_{\rho\rho\rho}(\mathbf{q},\mathbf{q_1},\mathbf{q_2};\omega,\omega)\big]_{\mathbf{000}}}{\Big(1 - \frac{\alpha}{4\pi}v_{\mathbf{0}}(\mathbf{q})\big[\chi^{(1)\mathrm{RPA}}_{\rho\rho}(\mathbf{q};2\omega)\big]_{\mathbf{00}}\Big)} + \chi^{(2)S,\mathrm{RPA}}_{\rho\rho\rho}(\mathbf{q},\mathbf{q_1},\mathbf{q_2};\omega,\omega)\right.$$
$$\left.+\bar{\chi}^{S}(\mathbf{q},\mathbf{q},\omega)\frac{\alpha}{q^2}\chi^{(2),\mathrm{RPA}}_{\rho\rho\rho}(\mathbf{q},\mathbf{q_1},\mathbf{q_2};\omega,\omega)\big]_{\mathbf{000}}\frac{\Big(1 + v_{\mathbf{0}}(\mathbf{q})\big[\chi^{(1)\mathrm{RPA}}_{\rho\rho}(\mathbf{q};2\omega)\big]_{\mathbf{00}}\Big)}{\Big(1 - \frac{\alpha}{4\pi}v_{\mathbf{0}}(\mathbf{q})\big[\chi^{(1)\mathrm{RPA}}_{\rho\rho}(\mathbf{q};2\omega)\big]_{\mathbf{00}}\Big)}\right]. \tag{10.14}$$

In order to simplify this expression, we first prove the following set of relations

$$\frac{1}{\big(1 - \frac{\alpha}{4\pi}v_{\mathbf{0}}(\mathbf{q})\big[\chi^{(1)\mathrm{RPA}}_{\rho\rho}(\mathbf{q};2\omega)\big]_{\mathbf{00}}\big)} = 1 + \frac{\alpha}{q^2}\big[\chi^{(1)}_{\rho\rho}(\mathbf{q};2\omega)\big]_{\mathbf{00}}, \tag{10.15a}$$

$$\frac{\Big(1 + v_{\mathbf{0}}(\mathbf{q})\big[\chi^{(1)\mathrm{RPA}}_{\rho\rho}(\mathbf{q};2\omega)\big]_{\mathbf{00}}\Big)}{\Big(1 - \frac{\alpha}{4\pi}v_{\mathbf{0}}(\mathbf{q})\big[\chi^{(1)\mathrm{RPA}}_{\rho\rho}(\mathbf{q};2\omega)\big]_{\mathbf{00}}\Big)} = 1 + (v_{\mathbf{0}}(\mathbf{q}) + \frac{\alpha}{q^2})\big[\chi^{(1)}_{\rho\rho}(\mathbf{q};2\omega)\big]_{\mathbf{00}},$$
$$= A(\mathbf{q};2\omega)\Big(1 + v_{\mathbf{0}}(\mathbf{q})\big[\chi^{(1)}_{\rho\rho}(\mathbf{q};2\omega)\big]_{\mathbf{00}}\Big), \tag{10.15b}$$

$$A(\mathbf{q};\omega)+A(\mathbf{q};\omega)\frac{\alpha}{4\pi}\Big(\epsilon_M^{\text{RPA}}(\mathbf{q};2\omega)-1\Big)=1, \tag{10.15c}$$

$$\bar{\chi}^S(\mathbf{q},\mathbf{q},\omega)\frac{\alpha}{q^2}=-\frac{\alpha}{4\pi}\Big(\epsilon_M^{S,\text{RPA}}(\mathbf{q};2\omega)-1\Big). \tag{10.15d}$$

Inserting all the ingredients above into the expression of the macroscopic surface second-order susceptibility, we obtain, after some algebra,

$$\begin{aligned}\chi_M^{(2)S}(\mathbf{q},\mathbf{q_1},\mathbf{q_2};\omega,\omega)&=\frac{-i}{2|\mathbf{q}||\mathbf{q_1}||\mathbf{q_2}|}A(\mathbf{q};2\omega)A(\mathbf{q_1};\omega)\epsilon_M^{\text{RPA}}(\mathbf{q_1};\omega)A(\mathbf{q_2};\omega)\epsilon_M^{\text{RPA}}(\mathbf{q_2};\omega)\\ \times\Bigg[\Big(\epsilon_M^{S,\text{RPA}}(\mathbf{q};2\omega)-1\Big)&\left(\left[\chi_{\rho\rho\rho}^{(2),\text{RPA}}(\mathbf{q},\mathbf{q_1},\mathbf{q_2};\omega,\omega)\right]_{\mathbf{000}}-\frac{\alpha}{4\pi}\left[\chi_{\rho\rho\rho}^{(2),\text{RPA}}(\mathbf{q},\mathbf{q_1},\mathbf{q_2};\omega,\omega)\right]_{\mathbf{000}}\right)\\ &+\chi_{\rho\rho\rho}^{(2)S,\text{RPA}}(\mathbf{q},\mathbf{q_1},\mathbf{q_2};\omega,\omega)+\frac{\alpha}{4\pi}\Big(\epsilon_M^{\text{RPA}}(\mathbf{q};2\omega)-1\Big)\chi_{\rho\rho\rho}^{(2)S,\text{RPA}}(\mathbf{q},\mathbf{q_1},\mathbf{q_2};\omega,\omega)\Bigg].\end{aligned} \tag{10.16}$$

We directly notice that if we replace the surface quantities by the bulk one, we recover the bulk expression Eq. (10.8), thus showing the consistency of the approach.
To make this more obvious, we identify Eq. (10.8) in Eq. (10.16), and we obtain

$$\begin{aligned}\chi_M^{(2)S}(\mathbf{q},\mathbf{q_1},\mathbf{q_2};\omega,\omega)&=A(\mathbf{q};2\omega)\chi_M^{(2)S,\text{RPA}}(\mathbf{q},\mathbf{q_1},\mathbf{q_2};\omega,\omega)A(\mathbf{q_1};\omega)A(\mathbf{q_2};\omega)\\ &-\frac{i}{2|\mathbf{q}||\mathbf{q_1}||\mathbf{q_2}|}\frac{\alpha}{4\pi}A(\mathbf{q};2\omega)A(\mathbf{q_1};\omega)\epsilon_M^{LL,\text{RPA}}(\mathbf{q_1};\omega)A(\mathbf{q_2};\omega)\epsilon_M^{LL,\text{RPA}}(\mathbf{q_2};\omega)\\ \times\Bigg[\Big(\epsilon_M^{LL,\text{RPA}}(\mathbf{q};2\omega)-1\Big)\chi_{\rho\rho\rho}^{(2)S,\text{RPA}}(\mathbf{q},\mathbf{q_1},\mathbf{q_2};\omega,\omega)&-\Big(\epsilon_M^{S,LL,\text{RPA}}(\mathbf{q};2\omega)-1\Big)\left[\chi_{\rho\rho\rho}^{(2),\text{RPA}}(\mathbf{q},\mathbf{q_1},\mathbf{q_2};\omega,\omega)\right]_{\mathbf{000}}\Bigg].\end{aligned} \tag{10.17}$$

The second term in this expression appears as a correction to the bulk formula, in the case of surfaces. The formalism developed in Chap. 7 is valid only for symmetric slab. We now assume that the full slab has the inversion symmetry, which is always possible to have with symmetric slab of centrosymmetric materials. This is the case for all the symmetric slab considered in this thesis. This implies that the term $\left[\chi_{\rho\rho\rho}^{(2),\text{RPA}}(\mathbf{q},\mathbf{q_1},\mathbf{q_2};\omega,\omega)\right]_{\mathbf{000}}$ is zero. In this special case, we can simplify Eq. (10.17) to obtain that

$$\boxed{\begin{aligned}\chi_M^{(2)S}(\mathbf{q},\mathbf{q_1},\mathbf{q_2};\omega,\omega)&=\frac{-i\chi_{\rho\rho\rho}^{(2)S,\text{RPA}}(\mathbf{q},\mathbf{q_1},\mathbf{q_2};\omega,\omega)}{2|\mathbf{q}||\mathbf{q_1}||\mathbf{q_2}|}\epsilon_M^{\text{RPA}}(\mathbf{q_1};\omega)\epsilon_M^{\text{RPA}}(\mathbf{q_2};\omega)A(\mathbf{q_1};\omega)A(\mathbf{q_2};\omega)\\ &=\chi_M^{(2)S,\text{RPA}}(\mathbf{q},\mathbf{q_1},\mathbf{q_2};\omega,\omega)A(\mathbf{q_1};\omega)A(\mathbf{q_2};\omega)\end{aligned}} \tag{10.18}$$

This result is the main result of this chapter. It allows us to include the effect of the α-kernel on the surface second-harmonic generation, as a post-processing on top of the RPA results. We do not have to calculate nor to diagonalize the exciton Hamiltonian and the cost of the calculation is the cost of the RPA calculation. It is worthwhile to note that the last expression is not the same as the bulk formula. Indeed, we found that the "screening" term $A(\mathbf{q};2\omega)$ is not present in Eq. (10.18), due to the symmetries of the slab, used for performing the calculation.

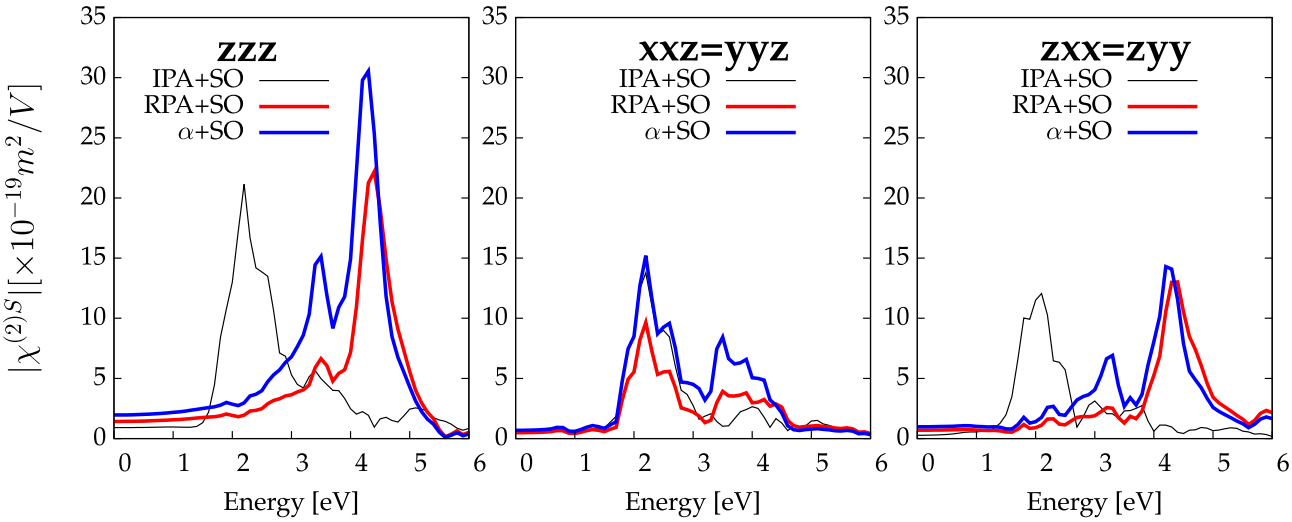

Fig. 10.1: Surface second-harmonic generation spectra of the dihydride Si(001)1×1:2H surface, for the zzz (left panel), the xxz (middle panel), and the zxx (right panel) components of the $\chi^{(2)S}$ tensor. Black lines: IPA calculations. Red lines: RPA calculations. Blue lines: excitonic calculations using the α-kernel. A scissors operator (SO) correction of $\Delta = 0.6$ eV is included in all the calculations.

10.2 Excitonic effects on the surface second-harmonic generation

10.2.1 Effects on components of the susceptibility tensor

Here we discuss the effects of the long-range contribution kernel f_{xc} on the surface second-order susceptibility spectra. The value of α used is -0.2, as it has been found to well reproduce the BSE spectra for the bulk silicon and the Si(111)2×1 surface [262].

In Fig. 10.1, we show the excitonic effects on the surface second-harmonic spectra from the dihydride surface, also including the local-field effects (blue lines), compared to the independent-particle spectra (black lines) and the spectra including only the effect of the local fields (red lines). As a general result, we find that the main effect of the α-kernel is to increase the magnitude of $|\chi_M^{(2)S}|$ in the low energy region. Notice that a similar effect has already been observed for bulk semiconductors [41, 264]. We also find that the excitonic effects almost do not change the position of the prominent peaks, by opposition to the local-field effects. Only a small red-shift of 0.1 eV is observed for the zzz and the zxx components.[1] The main effect of the α-kernel is to enhance the peak corresponding to the E_1 critical point of bulk silicon, at 3.4 eV. Also the peak corresponding to the E_2 critical point, at 4.3 eV, is enhanced for the component zzz. The corresponding peak at 2.15 eV is also enhanced for the component xxz, thus compensating almost completely the effects of the local fields on this peak. These E_1 and E_2 related peaks are located at the same energy as the bulk silicon critical points [265], as we used the same scissors correction as for bulk silicon.

The results of Fig. (10.1) show that the IPA and the RPA are not enough for describing the second-harmonic generation from surfaces, and that excitonic effects must be included for obtaining in the

[1] We checked (not shown) that this peak is a real shift, using the same approach of including or not the scissors operator, as explained in Chap. 9.

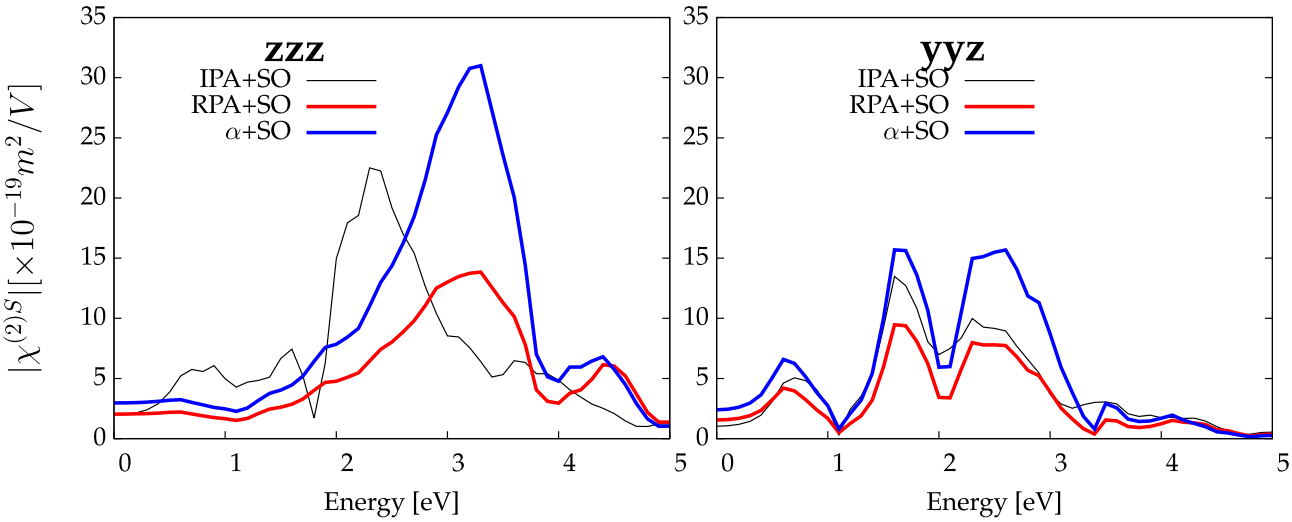

Fig. 10.2: The same as Fig. 10.1 for the clean Si(001)2×1 surface.

correct description of the surface second-harmonic generation.
We find that the same conclusions hold for the clean surface of silicon, as shown in Fig. 10.2. In particular, the effect on the E_1 related peak of the inclusion of the exciton more than double its intensity for the zzz component. For the yyz components, the two main structures, corresponding to the E_1 and E_2 critical points for 2ω transitions are enhanced, as well as the peak due to the surface-states, around 0.5 eV.

10.2.2 Effects on the reflection coefficients

It is interesting to investigate the excitonic effects on the generalized reflection coefficients. As a test case, I chose the R_{pp} coefficient of the dihydride surface. This coefficient has already been presented in Chap. 9, see Fig. 9.8. In Fig. 10.3, I reproduce the same data, adding the reflection coefficient calculated with the excitonic effects included (blue curve), as explained above. In all the calculations, I used a scissors correction of $\Delta = 0.6eV$. The low-temperature experimental results (black crosses, rescaled on the vertical axis) are obtained from Ref. [259]. The angle of incidence θ=45° is the same as in the experiment. A Lorentzian broadening of 20 meV is added as a post-processing on the final R_{pp} spectra.

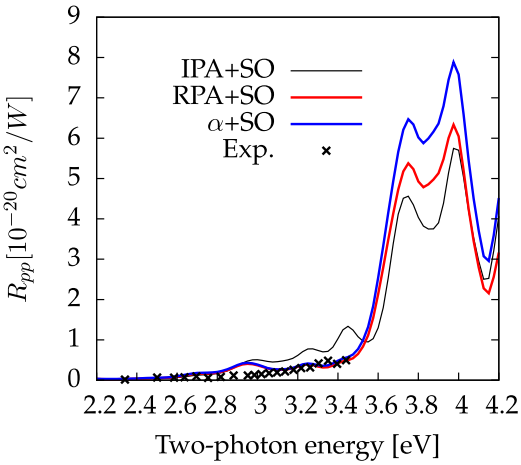

Fig. 10.3: R_{pp} vs the two-photon energy for the dihydride Si(001)1×1:2H surface. Curves are explained in the text.

We directly see that in the region probed by the experiment, there is almost no excitonic effect visible, whereas around 4.0 eV, we can see a change in the intensity, consistent with the behaviour obtain in Fig. 10.1 for the xxz component. The same conclusion hold for the R_{sp} coefficient, which is also not affected by the excitonic effects, in the region considered here.

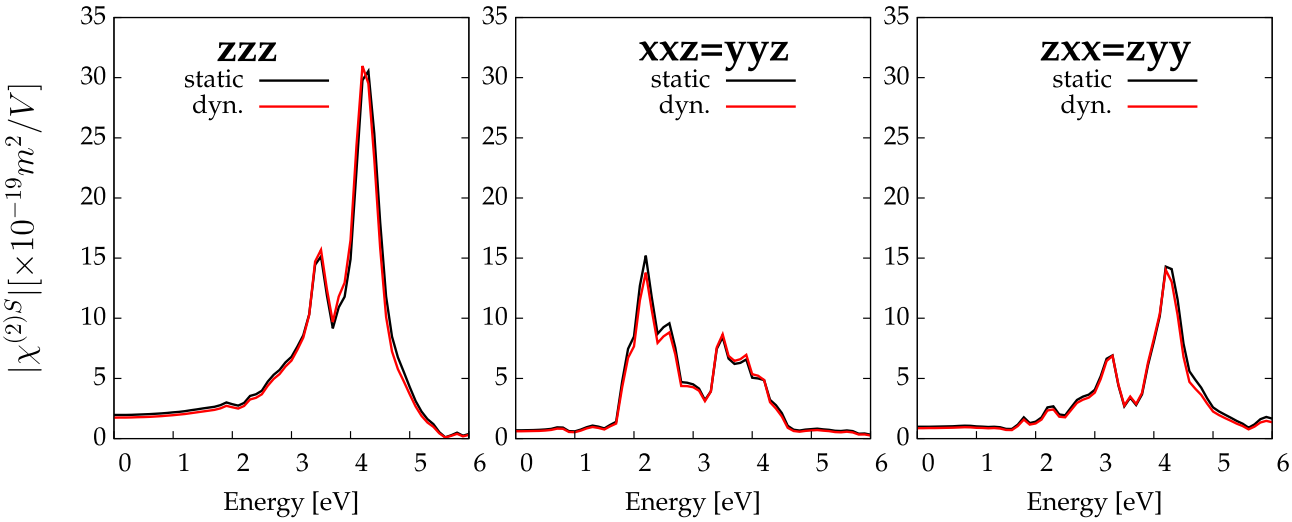

Fig. 10.4: Comparison between the effects of the static and the dynamic long-range contribution kernels on the surface second-harmonic generation of the dihydride surface. Black lines: static kernel $f_{\rm xc} = \frac{\alpha}{q^2}$, with $\alpha = -0.2$. Red lines: dynamic kernel $f_{\rm xc}^{\rm dyn} = \frac{1}{q^2}(\alpha + \beta\omega^2)$, with $\alpha = -0.13$ and $\beta = -6.35 \times 10^{-3}$ eV.

Therefore, we can conclude that the excitonic effects are less important than the local-field effects for describing the line-shape and the intensity of the reflection coefficient R_{pp}.

10.2.3 Dynamical model for the exchange-correlation kernel

In Ref. [266], authors have proposed an dynamical extension of the static α-kernel, which has the following form

$$f_{\rm xc}^{\rm dyn}(\mathbf{q};\omega) = \frac{1}{q^2}(\alpha + \beta\omega^2). \tag{10.19}$$

They have proved that including the dynamical dependency of the exchange-correlation kernel using this simple model was improving the agreement with experimental absorption spectra for wide-gap insulators, as well as for the electron energy-loss spectra for silicon. This kernel has also been tested for cluster calculations [267], molecular chains calculations [268] and bulk materials [269], yielding good agreement with the experiment or the BSE. Here I discuss the effect of the inclusion of the dynamical part of the exchange-correlation kernel on the surface second-harmonic generation spectra, with the spectra of the dihydride surface as an example. This dynamic kernel being scalar, as the static version, the formulae presented above still holds. In Fig. 10.4, I compare the spectra obtained with the static kernel, using $\alpha = -0.2$ (black lines), and with the dynamic kernel (red lines), with the values $\alpha = -0.13$ and $\beta = -6.35 \times 10^{-3}$ eV taken from Ref. [266] and obtained for bulk silicon. We obtain as a result almost no effect due to the energy-dependence of the exchange-correlation kernel, compared to the result obtained from the static α-kernel. Only the peak related to the critical point E_2 is slightly affected. Moreover, the spectral weight is almost not affected. Therefore, we conclude that the inclusion of the dynamical effects due to the exchange-correlation kernel, using the simple model of Eq. (10.19), does not really affect the surface second-harmonic

spectra in energy region we are interested in, and that dynamical effects are negligible. Note that a similar result for the absorption spectra of bulk GaAs was found in Ref. [270].

Conclusion

In this chapter, we have analysed the excitonic effects on the surface second-harmonic generation. The excitonic effects have been investigated using the α-kernel. I have proved in particular, that the effects due to this static and scalar kernel can be including by a simple post-processing of the spectra including the local-field effects and the scissors correction, calculated within the RPA.
Then we have analysed the excitonic effects on the surface second-harmonic generation spectra from two silicon surfaces. We found that the excitonic effects increase the spectra weight of $|\chi_M^{(2)S}|$, and in particular that they enhance the peak corresponding to the E_1 critical point of bulk silicon. The peak positions are almost not affected. The excitonic effects on the generalized reflection coefficient of the dihydride surface have also been investigated, showing only a small effect in the region probed by the experiments whereas an effect is observed at higher energy, around the energy of the E_2 critical point of bulk silicon. We finally investigated the effects due to the dynamical extension of the α-kernel, showing almost no effect of the dynamical version against the static α-kernel.

Concluding Remarks

This thesis has been focusing on the *ab initio* description of the second-harmonic generation from surfaces, and more generally, I have tried to improve the theoretical description and understanding of the optical properties of crystalline surfaces.
The second part of this thesis dealt with the microscopic description of the SHG from surfaces. The theory behind the calculation of the microscopic optical response of a single surface has been justified, proved and tested with tight-binding calculations. The spatial construction of the SHG spectra has been performed, showing that signal was mainly originating from the first layers and that the contribution of deeper atomic layers was decaying, as expected from a surface signal. In Chap. 6, I have presented how to improve this microscopic description by taking into account the effect of nonlocal operators, thus opening the way to more versatile and precise description of the second-harmonic generation from surfaces.
However, a microscopic description of optical properties is not enough, due to microscopic fluctuations of the electric field and of the density. These fluctuations, called local-fields, and their effects on the second-order optical properties of surfaces have been treated theoretically in Part. III. A macroscopic theory has been presented, allowing us to take into account the local-field effects on the linear and second-order optical properties of a single surface. The analyticity of the macroscopic quantity computed has been proved. Most of the effort has been devoted to the clarification between the macroscopic optical response of a super-cell, which is the numerical tool for doing the calculation, and the surface, which is the physical system that we would like to treat. In particular, the super-cell approach, due to the intrinsic periodicity induced by the approach, has been shown to fail in calculating the out-of-plane optical response of a slab of matter, when including the effects of the local fields. The real space approach, which does not suffer from this problem, has been used to calculate the correct optical response and, more importantly, to derive a new method, which merges the convenience of the super-cell approach with the correctness of the treatment in real space.
These developments have then been applied to silicon surfaces in Part. IV. The local-field effects on the surface second-harmonic generation have been analysed on three silicon surfaces, in particular shedding some light on the important role of these local fields in the surface second-harmonic generation.
Finally, the excitonic effects have also been investigated in Chap. 10.
It is clear that the developments of this thesis take us a step closer to the reality, as shown by the comparisons with experiments presented in Chap. 9.
Even if the theory seems now to be mature enough to give quantitative results, some points still need

to be addressed. Here are some of them. The excitonic effects have, so far, only been investigated by means of a simple scalar kernel. Even if these effects are found to be less important than local-field effects, as shown by the results obtained with the long-range contribution kernel, their proper inclusion must not be forgotten for a quantitative description of surface second-harmonic generation. Then, even if very interesting results have been obtained for the hydrogen as an ad-atoms on silicon surfaces, the effect of other ad-atoms like Ge or B has been experimentally well characterized but has to be understood and explained theoretically. Finally, two challenging elements are missing: the *ab initio* description of the bulk quadrupolar contribution, which should be sizeable compared to the surface dipolar contribution and the *ab initio* description of the Electric Field Induced Second-Harmonic Generation (EFISH).

To summarize, the main original results of this thesis are:

1. Justification of the formalism of the microscopic description of the Second-Harmonic Generation from surfaces, and improvement by including the effect of nonlocal operators.

2. Development of a macroscopic formalism for computing the optical response of a single surface, for linear and second-order optical properties.

3. Correct description of local-field effects on the out-of-plane optical response of surfaces.

4. First *ab initio* study of local-field effects on the second-harmonic generation spectra from clean and hydrogenated silicon surfaces.

5. Investigation of the excitonic effects, for the first time, on the second-harmonic generation spectra from silicon surfaces.

Finally, I would like to comment this often quoted citation of the famous physicist Wolfgang Pauli "God made the bulk; surfaces were invented by the devil". For Wolfgang Pauli, the diabolical nature of surfaces was coming from the fact that surface atoms, instead of being surrounded by similar atoms as in bulk materials, were interacting with the external environment. This is maybe true, but these interactions with the environment also lead to very interesting and exciting physics. I hope that this thesis is a proof of how complex but also interesting the physics of surfaces is. Therefore, if Wolfgang Pauli was right, we should probably be grateful to the devil.

Part V

Appendices

A. Fourier transforms

The definition of the Fourier transform requires some care, because authors use different conventions in the literature. In this appendix, I give the definitions of the Fourier transforms used in the thesis.

A.1 One-variable functions

Let us consider a function $f \in \mathcal{L}^2$, *i.e.*, f is *square integrable*. The Fourier transforms in time and in space for such a one-variable function f, as well as the reciprocal transformations are

$$\boxed{\begin{aligned} f(\omega) &= \int dt e^{-i\omega t} f(t), & f(t) &= \frac{1}{2\pi}\int d\omega e^{i\omega t} f(\omega), \\ f(\mathbf{r}) &= \frac{1}{(2\pi)^3}\int d^3\mathbf{k} f(\mathbf{k}) e^{i\mathbf{kr}}, & f(\mathbf{k}) &= \int d^3\mathbf{r} f(\mathbf{r}) e^{-i\mathbf{kr}}. \end{aligned}} \tag{A.1}$$

A practical application of these Fourier transforms is the definition of various Dirac's delta functions

$$\delta(t) = \frac{1}{2\pi}\int d\omega e^{i\omega t}, \qquad \delta(\omega) = \frac{1}{2\pi}\int dt e^{-i\omega t}, \tag{A.2a}$$

$$\delta(\mathbf{k}) = \frac{1}{(2\pi)^3}\int d^3\mathbf{r} e^{-i\mathbf{kr}}, \qquad \delta(\mathbf{r}) = \frac{1}{(2\pi)^3}\int d^3\mathbf{k} e^{i\mathbf{kr}}. \tag{A.2b}$$

A.2 Two-variable functions

Let us consider a two-variable functions, such as response functions.
We consider a function χ, square integrable, and two functions f and g, such that $f, g \in \mathcal{L}^2$ and

$$f(\mathbf{r}) = \int d^3\mathbf{r}' \chi(\mathbf{r}, \mathbf{r}') g(\mathbf{r}'). \tag{A.3}$$

The Fourier transform of this expression is

$$f(\mathbf{k}) = \int d^3\mathbf{k}' \chi(\mathbf{k}, \mathbf{k}') g(\mathbf{k}'). \tag{A.4}$$

Using the definitions Eqs. (A.1), we obtain by identification

$$\chi(\mathbf{r}, \mathbf{r}') = \frac{1}{(2\pi)^3}\int d^3\mathbf{k}\int d^3\mathbf{k}' e^{i\mathbf{kr}} \chi(\mathbf{k}, \mathbf{k}') e^{-i\mathbf{k}'\mathbf{r}'}, \tag{A.5a}$$

$$\chi(\mathbf{k}, \mathbf{k}') = \frac{1}{(2\pi)^3}\int d^3\mathbf{r}\int d^3\mathbf{r}' e^{-i\mathbf{kr}} \chi(\mathbf{r}, \mathbf{r}') e^{i\mathbf{k}'\mathbf{r}'}. \tag{A.5b}$$

Similarly, in time, we obtain

$$\chi(t, t') = \frac{1}{(2\pi)}\int d\omega\int d\omega' e^{i\omega t} \chi(\omega, \omega') e^{-i\omega' t'}, \tag{A.6a}$$

$$\chi(\omega,\omega') = \frac{1}{(2\pi)}\int dt \int dt' e^{-i\omega t}\chi(t,t')e^{i\omega' t'}. \tag{A.6b}$$

A.3 Crystals and Fourier Transforms

When dealing with an infinite system, such as a crystal, we can replace this infinite system by a finite system of volume V, using some periodic boundary conditions. These conditions are called *Born-von-Karman* periodic boundary conditions. The condition states that any functions of the crystal f follows

$$f(\mathbf{r} + N_i\mathbf{a_i}) = f(\mathbf{r}), \tag{A.7}$$

the $\mathbf{a_i}$ are the primitive vectors of the lattice and N_i are integers, with $i \in \{x, y, z\}$.
In a crystal of volume V, we can write [1]

$$f(\mathbf{r}) = \frac{1}{V}\sum_{\mathbf{k}} f(\mathbf{k})e^{i\mathbf{kr}}, \qquad f(\mathbf{k}) = \int_V d^3\mathbf{r} f(\mathbf{r})e^{-i\mathbf{kr}}. \tag{A.8}$$

Equations A.2b become for example

$$\delta_{\mathbf{k},\mathbf{k}'} = \frac{1}{V}\int_V d^3\mathbf{r} e^{-i(\mathbf{k}-\mathbf{k}')\mathbf{r}}, \qquad \delta(\mathbf{r}) = \frac{1}{V}\sum_{\mathbf{k}} e^{i\mathbf{kr}}. \tag{A.9}$$

The equivalent of relation A.3 in a periodic crystal is

$$f(\mathbf{k_1}) = \sum_{\mathbf{k_2}} \chi(\mathbf{k_1},\mathbf{k_2})g(\mathbf{k_2}) \tag{A.10}$$

In crystals, any reciprocal vector $\mathbf{k}$ can be expressed as the sum of a vector $\mathbf{q}$, belonging to the first BZ of the crystal and a reciprocal lattice vector $\mathbf{G}$.
Using definitions A.8 and using the fact that the integral of a periodic function u $\int_V d^3\mathbf{r} u(\mathbf{r})e^{-i\mathbf{kr}}$ is non zero only if $\mathbf{k}$ is a vector of reciprocal lattice $\mathbf{G}$, we get

$$\boxed{\begin{aligned}\chi_{\mathbf{G},\mathbf{G}'}(\mathbf{q}) &= \frac{1}{V}\int_V d^3\mathbf{r}\int_V d^3\mathbf{r}' e^{-i(\mathbf{q}+\mathbf{G})\mathbf{r}}\chi(\mathbf{r},\mathbf{r}')e^{i(\mathbf{q}+\mathbf{G}')\mathbf{r}'},\\ \chi(\mathbf{r},\mathbf{r}') &= \frac{1}{V}\sum_{\mathbf{q},\mathbf{G},\mathbf{G}'} e^{i(\mathbf{q}+\mathbf{G})\mathbf{r}}\chi_{\mathbf{G},\mathbf{G}'}(\mathbf{q})e^{-i(\mathbf{q}+\mathbf{G}')\mathbf{r}'},\end{aligned}} \tag{A.11}$$

where $\chi_{\mathbf{G},\mathbf{G}'}(\mathbf{q})$ stands for $\chi(\mathbf{q}+\mathbf{G},\mathbf{q}+\mathbf{G}')$, $\mathbf{q}$ is a vector in the first Brillouin zone and $\mathbf{G}$, $\mathbf{G}'$ are vectors of the reciprocal lattice.

[1] Here the factor V is chosen to be on the inverse transform for not having volumes in Dyson-like equations and for having a Coulomb potential defined as $\frac{4\pi}{q^2}$ and not $\frac{4\pi}{\sqrt{V}q^2}$ or $\frac{4\pi}{Vq^2}$

A.4 Fourier transform in the mixed-space

In Chap. 7, I defined the mixed-space. Here I give the different Fourier transforms, that link the mixed-space with the real space and the reciprocal space. Let us consider the 2D Fourier transform, defined by

$$f(\mathbf{k}_{||}, z) = \int dx \int dy e^{-i(k_x x + k_y y)} f(x, y, z). \tag{A.12}$$

Using this definition, we obtain the following relations

$$f(\mathbf{k}) = \int dz e^{-ik_z z} f(\mathbf{k}_{||}, z), \tag{A.13a}$$

$$f(\mathbf{k}_{||}, z) = \frac{1}{2\pi} \int dq_z e^{ik_z z} f(\mathbf{k}). \tag{A.13b}$$

We consider a two-variable function χ as the function describing the response f to a perturbation g. We have

$$f(\mathbf{k}_{||}, \mathbf{z}) = \int d^2\mathbf{k}'_{||} \int dz' \chi(\mathbf{k}_{||}, z, \mathbf{k}'_{||}, z') g(\mathbf{k}'_{||}, z'). \tag{A.14}$$

Hence,

$$\chi(\mathbf{k}, \mathbf{k}') = \frac{1}{2\pi} \int dz \int dz' e^{-ik_z z} \chi(\mathbf{k}_{||}, z, \mathbf{k}'_{||}, z') e^{ik'_z z'}, \tag{A.15a}$$

$$\chi(\mathbf{k}_{||}, \mathbf{k}'_{||}, z_1, z_2) = \frac{1}{2\pi} \int dk_z \int dk'_z e^{ik_z z} \chi(\mathbf{k}, \mathbf{k}') e^{-ik_{z'} z'}. \tag{A.15b}$$

A.4.1 Periodic crystals

Considering that the system is periodic, one gets that

$$f(\mathbf{q} + \mathbf{G}) = \int dz e^{-i(q_z + G_z)z} f(\mathbf{q}_{||} + \mathbf{G}_{||}, z), \tag{A.16a}$$

$$f(\mathbf{q}_{||} + \mathbf{G}_{||}, z) = \frac{1}{Lz} \sum_{q_z, G_z} e^{i(q_z + G_z)z} f(\mathbf{q} + \mathbf{G}), \tag{A.16b}$$

where $\mathbf{q}$ is a vector in the first Brillouin zone, $\mathbf{G}$ is a reciprocal lattice vector, $\mathbf{q} = \mathbf{q}_{||} + q_z \hat{\mathbf{z}}$ and $\mathbf{G} = \mathbf{G}_{||} + G_z \hat{\mathbf{z}}$. Here L_z is the size of the cell along the z-axis, which is then repeated to fill the space. We obtain for delta functions

$$\delta_{\mathbf{k_z}\mathbf{k}'_\mathbf{z}} = \frac{1}{L_z} \int dz e^{-i(\mathbf{k_z} - \mathbf{k}'_\mathbf{z})z}, \tag{A.17a}$$

$$\delta(z) = \frac{1}{L_z} \sum_{k_z} e^{ik_z z}. \tag{A.17b}$$

One easily extend the definitions of the Fourier transforms to two-variable response functions

$$\chi_{\mathbf{G}_{||\mathbf{1}}, \mathbf{G}_{||\mathbf{2}}}(\mathbf{q}_{||}, z_1, z_2) = \frac{1}{L_z} \sum_{q_z}^{BZ} \sum_{G_{z1}, G_{z2}} e^{i(q_z + G_{z1})z_1} \chi_{\mathbf{G_1}, \mathbf{G_2}}(\mathbf{q}) e^{-i(q_z + G_{z2})z_2}, \tag{A.18a}$$

$$\chi_{\mathbf{G_1},\mathbf{G_2}}(\mathbf{q}) = \frac{1}{L_z}\int dz_1 dz_2 e^{-i(q_z+G_{z1})z_1}\chi_{\mathbf{G}_{||\mathbf{1}},\mathbf{G}_{||\mathbf{2}}}(\mathbf{q}_{||},z_1,z_2)e^{i(q_z+G_{z2})z_2}, \tag{A.18b}$$

$$\chi_{\mathbf{G}_{||\mathbf{1}},\mathbf{G}_{||\mathbf{2}}}(\mathbf{q}_{||},z_1,z_2) = \frac{1}{A}\int d^2\mathbf{r}_{||\mathbf{1}} d^2\mathbf{r}_{||\mathbf{2}} e^{-i(q_{||}+G_{||1})r_{||1}}\chi(\mathbf{r_1},\mathbf{r_2})e^{i(q_{||}+G_{||2})r_{||2}}, \tag{A.18c}$$

$$\chi(\mathbf{r_1},\mathbf{r_2}) = \frac{1}{A}\sum_{q_{||}}^{BZ}\sum_{G_{||1},G_{||2}} e^{i(q_{||}+G_{||1})r_{||1}}\chi_{\mathbf{G}_{||\mathbf{1}},\mathbf{G}_{||\mathbf{2}}}(\mathbf{q}_{||},z_1,z_2)e^{-i(q_{||}+G_{||2})r_{||2}}, \tag{A.18d}$$

where the A is the system area.
For three-variable response functions, we obtain similarly,

$$\chi_{\mathbf{G_{1||}},\mathbf{G_{2||}},\mathbf{G_{3||}}}(\mathbf{q}_{||},z_1,z_2,z_3) = \frac{1}{A}\int d^2\mathbf{r_{1||}} d^2\mathbf{r_{2||}} d^2\mathbf{r_{3||}} e^{-i(\mathbf{q}_{||}+\mathbf{G_{1||}})\mathbf{r_{1||}}}\chi(\mathbf{r_1},\mathbf{r_2},\mathbf{r_3}) \times e^{i(\mathbf{q}_{||}+\mathbf{G_{2||}})\mathbf{r_{2||}}}e^{i(\mathbf{q}_{||}+\mathbf{G_{3||}})\mathbf{r_{3||}}} \tag{A.19a}$$

$$\chi(\mathbf{r_1},\mathbf{r_2},\mathbf{r_3}) = \frac{1}{A^2}\sum_{\mathbf{q}_{||}}^{BZ}\sum_{\mathbf{G_{1||}}\mathbf{G_{2||}}\mathbf{G_{3||}}} e^{i(\mathbf{q}_{||}+\mathbf{G_{1||}})\mathbf{r_{1||}}}\chi_{\mathbf{G_{1||}},\mathbf{G_{2||}},\mathbf{G_{3||}}}(\mathbf{q}_{||},z_1,z_2,z_3) \times e^{-i(\mathbf{q}_{||}+\mathbf{G_{2||}})\mathbf{r_{2||}}}e^{-i(\mathbf{q}_{||}+\mathbf{G_{3||}})\mathbf{r_{3||}}} \tag{A.19b}$$

B. Maxwell's equations

> From a long view of the history of mankind — seen from, say, ten thousand years from now — there can be little doubt that the most significant event of the nineteenth century will be judged as Maxwell's discovery of the laws of electrodynamics.
>
> Richard Feynman, in The Feynman Lectures on Physics (1964) Volume II, 1-6

In this thesis, all the fields are treated in a purely classical way whereas the mater is described by response functions computed quantum-mechanically. This corresponds to the framework of the semi-classical dielectric theory. The Maxwell equations are given here in a medium, not in the vacuum.

B.1 Microscopic Maxwell's equations

If one considers the matter at atomistic level, microscopic Maxwell equations are

$$\boxed{\begin{aligned} \boldsymbol{\nabla}.\mathbf{E}(\mathbf{r},t) &= 4\pi\eta(\mathbf{r},t), & \boldsymbol{\nabla}\times\mathbf{B}(\mathbf{r},t) - \frac{1}{c}\frac{\partial\mathbf{E}}{\partial t}(\mathbf{r},t) &= \frac{4\pi}{c}\mathbf{j}(\mathbf{r},t), \\ \boldsymbol{\nabla}.\mathbf{B}(\mathbf{r},t) &= 0, & \boldsymbol{\nabla}\times\mathbf{E}(\mathbf{r},t) + \frac{1}{c}\frac{\partial\mathbf{B}}{\partial t}(\mathbf{r},t) &= 0, \end{aligned}} \tag{B.1}$$

where $\mathbf{E}$ and $\mathbf{B}$ are the microscopic electric and magnetic field quantities, η and $\mathbf{j}$ are the microscopic charge and current densities, respectively [1].
These two last quantities are connected by the continuity equation for charge and current

$$\boldsymbol{\nabla}.\mathbf{j}(\mathbf{r},t) + \frac{\partial\eta}{\partial t}(\mathbf{r},t) = 0. \tag{B.2}$$

B.1.1 Separation of different contributions

When dealing with microscopic fields, one has to take care about which field is considered. Indeed the fields that appear in equations (B.1) are total fields, not external fields.
We denote by $\mathbf{E}$ the *total* field that can be separated into an *external* field $\mathbf{E}^{\text{ext}}$ and an *induced* field $\mathbf{E}^{\text{ind}}$. By linearity, Maxwell equations hold for total fields or external fields and induced fields separately. The same separation is applied to charge density and current density.
This leads to the definition of the electric polarization $\mathbf{P}$ and the magnetization $\mathbf{M}$ such that

$$\eta^{\text{ind}}(\mathbf{r},t) = -\boldsymbol{\nabla}\mathbf{P}(\mathbf{r},t), \qquad \mathbf{j}^{\text{ind}}(\mathbf{r},t) = \frac{\partial\mathbf{P}}{\partial t}(\mathbf{r},t) + \boldsymbol{\nabla}\times\mathbf{M}(\mathbf{r},t). \tag{B.3}$$

[1] There is no $\mathbf{D}$ and $\mathbf{H}$ fields because all of the charges are included in η and $\mathbf{j}$. [37].

B.2 Macroscopic Maxwell's equations

The question of averaging must be treated carefully. According to [37], only spatial averaging is necessary. *Macroscopic quantities* can be understand as quantities that vary slowly with respect to the characteristic size of the considered medium. In the case of a crystal, the characteristic size is the size of the unit cell. These macroscopic quantities result from the averaging of the microscopic one, over regions large compared to atomic separation but small compared to the wavelength of the perturbation [44]. The definition of the averaging procedure requires great cares. In Ref. [39], Mochán and Barrera defined a general averaging procedure, which then can be chosen to be an ensemble-average, a spatial average or a wave-vector average. As an example, the spatial average of a function $F(\mathbf{r},t)$ with respect to a test function $f(\mathbf{r})$ is defined by

$$\langle F(\mathbf{r},t)\rangle = \int d^3\mathbf{r}' f(\mathbf{r}')F(\mathbf{r}-\mathbf{r}',t), \tag{B.4}$$

with $f(\mathbf{r})$ a real function, non-zero in some neighbourhood of $\mathbf{r}=0$ and normalized over all space. The test function does not need to be defined but must only requires continuity and smoothness properties [39]. We can show easily that space and time derivatives, that enter in the equations, commute with the averaging operation.

$$\frac{\partial}{\partial r_i}\langle F(\mathbf{r},t)\rangle = \int d^3\mathbf{r}' f(\mathbf{r}')\frac{\partial F}{\partial r_i}(\mathbf{r}-\mathbf{r}',t) = \left\langle \frac{\partial F(\mathbf{r},t)}{\partial r_i}\right\rangle, \tag{B.5}$$

and

$$\frac{\partial}{\partial t}\langle F(\mathbf{r},t)\rangle = \int d^3\mathbf{r}' f(\mathbf{r}')\frac{\partial F}{\partial t}(\mathbf{r}-\mathbf{r}',t) = \left\langle \frac{\partial F(\mathbf{r},t)}{\partial t}\right\rangle. \tag{B.6}$$

The definition of the wave-vector truncation has been already given in Chap. 1 and is not reported here again.

Without restricting ourself to any specific averaging procedure, we define the macroscopic fields $\mathbf{E}_M = \langle\mathbf{E}\rangle$ and $\mathbf{B}_M = \langle\mathbf{B}\rangle$. From Eqs. (B.1), we obtain

$$\boldsymbol{\nabla}.\mathbf{E} = 4\pi\langle\eta\rangle, \qquad \boldsymbol{\nabla}\times\mathbf{B} - \frac{1}{c}\frac{\partial\mathbf{E}}{\partial t} = \frac{4\pi}{c}\langle\mathbf{j}\rangle, \tag{B.7a}$$

$$\boldsymbol{\nabla}.\mathbf{B} = 0, \qquad \boldsymbol{\nabla}\times\mathbf{E} + \frac{1}{c}\frac{\partial\mathbf{B}}{\partial t} = 0. \tag{B.7b}$$

In order to obtain the macroscopic Maxwell equations, we must use the following results (that are proved in [37], under dipole approximation)

$$\langle\eta\rangle = \rho - \boldsymbol{\nabla}\mathbf{P}, \qquad \langle\mathbf{j}\rangle = \mathbf{J} + \frac{\partial\mathbf{P}}{\partial t} + c\boldsymbol{\nabla}\times\mathbf{M}. \tag{B.8}$$

Here, ρ and $\mathbf{J}$ are the macroscopic averaged free charge and free current densities (see Eq. (B.3)). There is nevertheless a limit to that approach, when the external fields are not macroscopic, because it is not possible to define macroscopic quantities, *e.g.*, in the case of X-ray spectroscopy where the wavelength is very short.

The *macroscopic* Maxwell equations reads in real space by [37]

$$\boxed{\begin{aligned} &\boldsymbol{\nabla}.\mathbf{D}_M(\mathbf{r},t) = 4\pi\rho(\mathbf{r},t), && \boldsymbol{\nabla}\times\mathbf{H}_M(\mathbf{r},t) - \frac{1}{c}\frac{\partial\mathbf{D}_M}{\partial t}(\mathbf{r},t) = \frac{4\pi}{c}\mathbf{J}(\mathbf{r},t),\\ &\boldsymbol{\nabla}.\mathbf{B}_M(\mathbf{r},t) = 0, && \boldsymbol{\nabla}\times\mathbf{E}_M(\mathbf{r},t) + \frac{1}{c}\frac{\partial\mathbf{B}_M}{\partial t}(\mathbf{r},t) = 0, \end{aligned}} \tag{B.9}$$

where $\mathbf{D}_M$ and $\mathbf{H}_M$ are respectively the macroscopic electric displacement and macroscopic magnetic field.
This macroscopic current and charge densities are connected by the continuity equation for charge and current

$$\boldsymbol{\nabla}\mathbf{J}(\mathbf{r},t) + \frac{\partial\rho}{\partial t}(\mathbf{r},t) = 0. \tag{B.10}$$

For the reader more at home with SI-notation, the preceding equations are in SI notation:

$$\boxed{\begin{aligned} &\boldsymbol{\nabla}.\mathbf{D}_M(\mathbf{r},t) = \rho(\mathbf{r},t), && \boldsymbol{\nabla}\times\mathbf{H}_M(\mathbf{r},t) - \frac{\partial\mathbf{D}}{\partial t}(\mathbf{r},t) = \mathbf{J}(\mathbf{r},t),\\ &\boldsymbol{\nabla}.\mathbf{B}_M(\mathbf{r},t) = 0, && \boldsymbol{\nabla}\times\mathbf{E}_M(\mathbf{r},t) + \frac{\partial\mathbf{B}_M}{\partial t}(\mathbf{r},t) = 0. \end{aligned}} \tag{B.11}$$

B.2.1 Separation of charges

The main problem when working with $\mathbf{P}$ and $\mathbf{M}$ is that these quantities are not uniquely defined and one has to choose a convention to define them. In this thesis, we chose the separation of charges that writes

$$\mathbf{D}(\mathbf{r},t) = \mathbf{E}^{\text{ext}}(\mathbf{r},t). \tag{B.12}$$

As consequences, we get

$$4\pi\mathbf{P} = -\mathbf{E}^{\text{ind}}, \qquad \frac{4\pi}{c}\mathbf{M} = \mathbf{B}^{\text{ind}}. \tag{B.13}$$

Using the definition of the *microscopic dielectric function* ϵ

$$\mathbf{D}(\mathbf{r},t) = \int d^3\mathbf{r}' \int dt \overset{\leftrightarrow}{\epsilon}(\mathbf{r},\mathbf{r}',t-t')\mathbf{E}(\mathbf{r}',t'), \tag{B.14}$$

we get that

$$\mathbf{E}^{\text{ext}}(\mathbf{r},t) = \int d^3\mathbf{r}' \int dt \overset{\leftrightarrow}{\epsilon}(\mathbf{r},\mathbf{r}',t-t')\mathbf{E}(\mathbf{r}',t') \qquad \text{or} \qquad \mathbf{E}(\mathbf{r},t) = \overset{\leftrightarrow}{\epsilon}^{-1}(\mathbf{r},\mathbf{r}',t-t')\mathbf{E}^{\text{ext}}(\mathbf{r}',t'). \tag{B.15}$$

Here $\overset{\leftrightarrow}{\epsilon}^{-1}$ is the inverse of the dielectric tensor $\overset{\leftrightarrow}{\epsilon}$. In this thesis, I assume that $\overset{\leftrightarrow}{\epsilon}$ is always invertible. The constitutive relations connecting $\mathbf{E}_M$ and $\mathbf{B}_M$ to $\mathbf{D}_M$ and $\mathbf{H}_M$ are giving by equations (B.16):

$$\mathbf{D}_M(\mathbf{r},t) = \mathbf{E}_M(\mathbf{r},t) + 4\pi\mathbf{P}_M(\mathbf{r},t), \qquad \mathbf{H}_M(\mathbf{r},t) = \mathbf{B}_M(\mathbf{r},t) - 4\pi\mathbf{M}_M(\mathbf{r},t), \tag{B.16}$$

where $\mathbf{P}_M$ and $\mathbf{M}_M$ are respectively the macroscopic *polarization* and *magnetization*.

B.3 Longitudinal and Transverse Fields

In reciprocal space, the Maxwell equations Eqs. (B.9) reads as

$$\begin{aligned} i\mathbf{k}.\mathbf{D}(\mathbf{k};\omega) &= 4\pi\rho(\mathbf{k};\omega), & i\mathbf{k}\times\mathbf{H}(\mathbf{k};\omega) - \frac{i\omega}{c}\mathbf{D}(\mathbf{k};\omega) &= \frac{4\pi}{c}\mathbf{J}(\mathbf{k};\omega), \\ i\mathbf{k}.\mathbf{B}(\mathbf{k};\omega) &= 0, & i\mathbf{k}\times\mathbf{E}(\mathbf{k};\omega) + \frac{i\omega}{c}\mathbf{B}(\mathbf{k};\omega) &= 0. \end{aligned} \tag{B.17}$$

Due to the structure of these equations, it is natural to divide the fields into *longitudinal* and *transverse* fields. For a field $\mathbf{E}$, the longitudinal part $\mathbf{E}^L$ and transverse part $\mathbf{E}^T$ are defined in reciprocal space as[2]

$$\mathbf{E}^L(\mathbf{k};\omega) = \frac{\mathbf{k}}{k}\left(\mathbf{E}(\mathbf{k};\omega).\frac{\mathbf{k}}{k}\right), \qquad \mathbf{E}^T(\mathbf{k};\omega) = \mathbf{E}(\mathbf{k};\omega) - \mathbf{E}^L(\mathbf{k};\omega) = -\frac{\mathbf{k}}{k}\times\left(\frac{\mathbf{k}}{k}\times\mathbf{E}(\mathbf{k};\omega)\right). \tag{B.18}$$

Therefore the Maxwell equations become

$$\boxed{\begin{aligned} \mathbf{D}^L(\mathbf{k};\omega) &= \frac{4\pi\rho(\mathbf{k};\omega)}{k^2}\mathbf{k}, & i\frac{\mathbf{k}}{k}\times\mathbf{H}^T(\mathbf{k};\omega) - \frac{i\omega}{c}\mathbf{D}^T(\mathbf{k};\omega) &= \frac{4\pi}{c}\mathbf{J}^T(\mathbf{k};\omega), \\ \mathbf{B}^L(\mathbf{k};\omega) &= 0, & \mathbf{k}\times\mathbf{E}^T(\mathbf{k};\omega) + \frac{\omega k}{c}\mathbf{B}^T(\mathbf{k};\omega) &= 0. \end{aligned}} \tag{B.19}$$

And the continuity equation becomes $J^L(\mathbf{k};\omega) + \omega\rho(\mathbf{k};\omega) = 0$.

[2] In 1858, Helmholtz proved that any vector field $\mathbf{E}$ can be decomposed into a longitudinal and a transverse part [271], $\mathbf{E} = \mathbf{E}^L + \mathbf{E}^T$, where $\mathbf{E}^L$ and $\mathbf{E}^T$ are defined, in real space, by $\nabla\times\mathbf{E}^L = 0$, and $\nabla.\,\mathbf{E}^T = 0$.
This is known as the Helmholtz decomposition.

C. Second-harmonic reflection coefficients for some symmetries

In chapter 2, I have presented the expressions of the four reflection coefficients R_{pp}, R_{ps}, R_{sp} and R_{ss} for the $p4mm$ symmetry. Here I report the expressions of these reflection coefficients in the general case, meaning when no symmetry is assumed for reducing the number of components. I also give the simplified expressions in the case of the m symmetry corresponding to a single domain of the clean Si(001)2×1 surface, the $p2mm$ symmetry corresponding to a single domain of the monohydride Si(001)2×1:H surface and the $3m$ symmetry corresponding to the Si(111)1×1:H surface.

C.1 Reflection coefficients in the general case

Here we give the expression of the four reflection coefficients assuming no symmetry. In the general case, the $\chi^{(2)S}$ tensor has 18 independent components in the case of the second-harmonic generation, due to the intrinsic symmetry property of the crystal which gives $\chi^{(2)S}_{ijk} = \chi^{(2)S}_{ikj}$.

$$
\begin{aligned}
R_{pp}(\theta,\phi,\omega) = {} & \frac{\omega^2}{2c^3\epsilon_0}\frac{1}{\cos^2\theta}\left|\frac{t^p_{mv}(2\omega)t^p_{vm}(\omega)^2}{\sqrt{\epsilon(2\omega)}\epsilon(\omega)}\right|^2\left|\frac{q^v_\perp(2\omega)}{q^m_\perp(2\omega)}\right|^2 \\
& \times\Bigg|\sin^3\theta\chi^{(2)S}_{zzz} + \frac{2c}{\omega}q^m_\perp(\omega)\sin^2\theta\left[\cos\phi\chi^{(2)S}_{zzx} + \sin\phi\chi^{(2)S}_{zzy}\right] \\
& + \frac{c^2}{\omega^2}\sin\theta q^m_\perp(\omega)^2\left[\cos^2\phi\chi^{(2)S}_{zxx} + 2\cos\phi\sin\phi\chi^{(2)S}_{zxy} + \sin^2\phi\chi^{(2)S}_{zyy}\right] \\
& - \frac{c}{2\omega}\sin^2\theta q^m_\perp(2\omega)\left[\cos\phi\chi^{(2)S}_{xzz} + \sin\phi\chi^{(2)S}_{yzz}\right] \\
& - \frac{c^2}{\omega^2}\sin\theta q^m_\perp(\omega)q^m_\perp(2\omega)\left[\cos^2\phi\chi^{(2)S}_{xxz} + \cos\phi\sin\phi(\chi^{(2)S}_{xyz} + \chi^{(2)S}_{yxz}) + \sin^2\phi\chi^{(2)S}_{yyz}\right] \\
& - \frac{c^3}{2\omega^3}q^m_\perp(\omega)^2q^m_\perp(2\omega)\cos\phi\big[\cos^2\phi\chi^{(2)S}_{xxx} + \sin(2\phi)\chi^{(2)S}_{xxy} + \sin^2\phi\chi^{(2)S}_{xyy}\big] \\
& - \frac{c^3}{2\omega^3}q^m_\perp(\omega)^2q^m_\perp(2\omega)\sin\phi\big[\cos^2\phi\chi^{(2)S}_{yxx} + \sin(2\phi)\chi^{(2)S}_{yyx} + \sin^2\phi\chi^{(2)S}_{yyy}\big]\Bigg|^2,
\end{aligned}
\tag{C.1a}
$$

$$
\begin{aligned}
R_{ps}(\theta,\phi,\omega) = {} & \frac{\omega^2}{2c^3\epsilon_0}\frac{1}{\cos^2\theta}\left|\frac{t^s_{mv}(2\omega)t^p_{vm}(\omega)^2}{\epsilon(\omega)}\right|^2\left|\frac{q^v_\perp(2\omega)}{q^m_\perp(2\omega)}\right|^2 \\
& \times\Bigg|\sin^2\theta\left(\sin\phi\chi^{(2)S}_{xzz} - \cos\phi\chi^{(2)S}_{yzz}\right) \\
& + \frac{2c}{\omega}\sin\theta q^m_\perp(\omega)\left[\sin^2\phi\chi^{(2)S}_{xyz} + \cos\phi\sin\phi(\chi^{(2)S}_{xxz} - \chi^{(2)S}_{yyz}) - \cos^2\phi\chi^{(2)S}_{yzx}\right] \\
& + \frac{c^2}{\omega^2}q^m_\perp(\omega)^2\sin\phi\big[\sin^2\phi\chi^{(2)S}_{xyy} + \sin(2\phi)\chi^{(2)S}_{xxy} + \cos^2\phi\chi^{(2)S}_{xxx}\big] \\
& - \frac{c^2}{\omega^2}q^m_\perp(\omega)^2\cos\phi\big[\sin^2\phi\chi^{(2)S}_{yyy} + \sin(2\phi)\chi^{(2)S}_{yyx} + \cos^2\phi\chi^{(2)S}_{yxx}\big]\Bigg|^2,
\end{aligned}
\tag{C.1b}
$$

$$R_{sp}(\theta,\phi,\omega) = \frac{\omega^2}{2c^3\epsilon_0}\frac{1}{\cos^2\theta}\left|\frac{t^p_{mv}(2\omega)t^s_{vm}(\omega)^2}{\sqrt{\epsilon(2\omega)}}\right|^2\left|\frac{q^v_\perp(2\omega)}{q^m_\perp(2\omega)}\right|^2$$
$$\times\Bigg|\sin\theta\left[\cos^2\phi\chi^{(2)S}_{zyy}-\sin(2\phi)\chi^{(2)S}_{zyx}+\sin^2\phi\chi^{(2)S}_{zxx}\right]$$
$$-\frac{c}{2\omega}q^m_\perp(2\omega)\sin\phi\left[\cos^2\phi\chi^{(2)S}_{yyy}-\sin(2\phi)\chi^{(2)S}_{yyx}+\sin^2\phi\chi^{(2)S}_{yxx}\right]$$
$$-\frac{c}{2\omega}q^m_\perp(2\omega)\cos\phi\left[\cos^2\phi\chi^{(2)S}_{xyy}-\sin(2\phi)\chi^{(2)S}_{xxy}+\sin^2\phi\chi^{(2)S}_{xxx}\right]\Bigg|^2, \tag{C.1c}$$

$$R_{ss}(\theta,\phi,\omega) = \frac{\omega^2}{2c^3\epsilon_0}\frac{1}{\cos^2\theta}\left|t^s_{mv}(2\omega)t^s_{vm}(\omega)^2\right|^2\left|\frac{q^v_\perp(2\omega)}{q^m_\perp(2\omega)}\right|^2$$
$$\times\left|\sin^3\phi\chi^{(2)S}_{xxx}-\cos\phi\sin^2\phi\left(\chi^{(2)S}_{yxx}+2\chi^{(2)S}_{xxy}\right)+\cos^2\phi\sin\phi\left(\chi^{(2)S}_{xyy}+2\chi^{(2)S}_{yyx}\right)-\cos^3\phi\chi^{(2)S}_{yyy}\right|^2. \tag{C.1d}$$

C.2 Reflection coefficients for the m symmetry

We give here the expression for a m symmetry, where the only non-zero components of the $\chi^{(2)S}$ tensor are $\chi^{(2)S}_{yyx}, \chi^{(2)S}_{xyy}, \chi^{(2)S}_{xxx}, \chi^{(2)S}_{yyz}, \chi^{(2)S}_{xxz}, \chi^{(2)S}_{zxx}, \chi^{(2)S}_{zyy}, \chi^{(2)S}_{xzz}, \chi^{(2)S}_{zzx}, \chi^{(2)S}_{zzz}$ (The mirror plan is perpendicular to $\hat{\mathbf{e}}_\mathbf{y}$).

This symmetry corresponds for instance to a single domain of the clean Si(001)2x1 surface.

$$R_{pp}(\theta,\phi,\omega) = \frac{\omega^2}{2c^3\epsilon_0}\frac{1}{\cos^2\theta}\left|\frac{t^p_{mv}(2\omega)t^p_{vm}(\omega)^2}{\sqrt{\epsilon(2\omega)}\epsilon(\omega)}\right|^2\left|\frac{q^v_\perp(2\omega)}{q^m_\perp(2\omega)}\right|^2$$
$$\times\Bigg|\sin^3\theta\chi^{(2)S}_{zzz}+\frac{2c}{\omega}q^m_\perp(\omega)\sin^2\theta\cos\phi\chi^{(2)S}_{zzx}+\frac{c^2}{\omega^2}\sin\theta q^m_\perp(\omega)^2\left[\cos^2\phi\chi^{(2)S}_{zxx}+\sin^2\phi\chi^{(2)S}_{zyy}\right]$$
$$-\frac{c}{2\omega}\sin\theta q^m_\perp(2\omega)\left(\sin\theta\cos\phi\chi^{(2)S}_{xzz}+\frac{2c}{\omega}q^m_\perp(\omega)\left[\cos^2\phi\chi^{(2)S}_{xxz}+\sin^2\phi\chi^{(2)S}_{yyz}\right]\right)$$
$$-\frac{c^3}{2\omega^3}q^m_\perp(\omega)^2q^m_\perp(2\omega)\cos\phi\big[\cos^2\phi\chi^{(2)S}_{xxx}+\sin^2\phi(\chi^{(2)S}_{xyy}+2\chi^{(2)S}_{yyx})\big]\Bigg|^2, \tag{C.2a}$$

$$R_{ps}(\theta,\phi,\omega) = \frac{\omega^2}{2c^3\epsilon_0}\frac{\sin^2\phi}{\cos^2\theta}\left|\frac{t^s_{mv}(2\omega)t^p_{vm}(\omega)^2}{\epsilon(\omega)}\right|^2\left|\frac{q^v_\perp(2\omega)}{q^m_\perp(2\omega)}\right|^2\left|\sin\theta\left(\chi^{(2)S}_{xzz}+\frac{2c}{\omega}q^m_\perp(\omega)\cos\phi(\chi^{(2)S}_{xxz}-\chi^{(2)S}_{yyz})\right)\right.$$
$$\left.+\frac{c^2}{\omega^2}q^m_\perp(\omega)^2\big[\sin^2\phi\chi^{(2)S}_{xyy}+\cos^2\phi(\chi^{(2)S}_{xxx}-2\chi^{(2)S}_{yyx})\big]\right|^2, \tag{C.2b}$$

$$R_{sp}(\theta,\phi,\omega) = \frac{\omega^2}{2c^3\epsilon_0}\frac{1}{\cos^2\theta}\left|\frac{t^p_{mv}(2\omega)t^s_{vm}(\omega)^2}{\sqrt{\epsilon(2\omega)}}\right|^2\left|\frac{q^v_\perp(2\omega)}{q^m_\perp(2\omega)}\right|^2$$
$$\times\left|\sin\theta\left[\cos^2\phi\chi^{(2)S}_{zyy}+\sin^2\phi\chi^{(2)S}_{zxx}\right]-\frac{c}{2\omega}q^m_\perp(2\omega)\cos\phi\left[\cos^2\phi\chi^{(2)S}_{xyy}+\sin^2\phi(\chi^{(2)S}_{xxx}-2\chi^{(2)S}_{yyx})\right]\right|^2, \tag{C.2c}$$

$$R_{ss}(\theta,\phi,\omega) = \frac{\omega^2}{2c^3\epsilon_0}\frac{\sin^2\phi}{\cos^2\theta}\left|t^s_{mv}(2\omega)t^s_{vm}(\omega)^2\right|^2\left|\frac{q^v_\perp(2\omega)}{q^m_\perp(2\omega)}\right|^2\left|\sin^2\phi\chi^{(2)S}_{xxx}+\cos^2\phi\left(\chi^{(2)S}_{xyy}+2\chi^{(2)S}_{yyx}\right)\right|^2. \tag{C.2d}$$

C.3 Reflection coefficients for the $mm2$ symmetry

We give here the expression for a $mm2$ symmetry, where the only non-zero components of the $\chi^{(2)S}$ tensor are $\chi^{(2)S}_{yyz}$, $\chi^{(2)S}_{xxz}$, $\chi^{(2)S}_{zxx}$, $\chi^{(2)S}_{zyy}$, $\chi^{(2)S}_{zzz}$. This symmetry corresponds for instance to a single domain of the monohydride Si(001)2x1:H surface.

$$R_{pp}(\theta,\phi,\omega) = \frac{\omega^2}{2c^3\epsilon_0}\tan^2\theta\left|\frac{t^p_{mv}(2\omega)t^p_{vm}(\omega)^2}{\sqrt{\epsilon(2\omega)}\epsilon(\omega)}\right|^2\left|\frac{q^v_\perp(2\omega)}{q^m_\perp(2\omega)}\right|^2\Big|\sin^2\theta\chi^{(2)S}_{zzz} + \frac{c^2}{\omega^2}q^m_\perp(\omega)^2\left[\cos^2\phi\chi^{(2)S}_{zxx}+\sin^2\phi\chi^{(2)S}_{zyy}\right] - \frac{c^2}{\omega^2}q^m_\perp(2\omega)q^m_\perp(\omega)\left[\cos^2\phi\chi^{(2)S}_{xxz}+\sin^2\phi\chi^{(2)S}_{yyz}\right]\Big|^2, \tag{C.3a}$$

$$R_{ps}(\theta,\phi,\omega) = \frac{1}{2c\epsilon_0}\sin^2(2\phi)\tan^2\theta\left|\frac{t^s_{mv}(2\omega)t^p_{vm}(\omega)^2}{\epsilon(\omega)}\right|^2\left|\frac{q^v_\perp(2\omega)q^m_\perp(\omega)}{q^m_\perp(2\omega)}\right|^2\left|\chi^{(2)S}_{xxz}-\chi^{(2)S}_{yyz}\right|^2, \tag{C.3b}$$

$$R_{sp}(\theta,\phi,\omega) = \frac{\omega^2}{2c^3\epsilon_0}\tan^2\theta\left|\frac{t^p_{mv}(2\omega)t^s_{vm}(\omega)^2}{\sqrt{\epsilon(2\omega)}}\right|^2\left|\frac{q^v_\perp(2\omega)}{q^m_\perp(2\omega)}\right|^2\left|\cos^2\phi\chi^{(2)S}_{zyy}+\sin^2\phi\chi^{(2)S}_{zxx}\right|^2, \tag{C.3c}$$

$$R_{ss}(\omega) = 0. \tag{C.3d}$$

C.4 Reflection coefficients for the $3m$ symmetry

We give here the expression for a $3m$ symmetry, where the only non-zero components of the $\chi^{(2)S}$ tensor are $\chi^{(2)S}_{zzz} = \chi_{\perp\perp\perp}, \chi^{(2)S}_{xxz} = \chi^{(2)S}_{yyz} = \chi^{(2)S}_{\parallel\parallel\perp}, \chi^{(2)S}_{zxx} = \chi^{(2)S}_{zyy} = \chi^{(2)S}_{\perp\parallel\parallel}, \chi^{(2)S}_{xxx} = -\chi^{(2)S}_{xyy} = -\chi^{(2)S}_{yyx} = \chi^{(2)S}_{\parallel\parallel\parallel}$ (The mirror plan is perpendicular to $\hat{\mathbf{e}}_\mathbf{y}$). This symmetry corresponds for instance to the Si(1111)1x1:H surface.

$$R_{pp}(\theta,\phi,\omega) = \frac{\omega^2}{2c^3\epsilon_0}\frac{1}{\cos^2\theta}\left|\frac{t^p_{mv}(2\omega)t^p_{vm}(\omega)^2}{\sqrt{\epsilon(2\omega)}\epsilon(\omega)}\right|^2\left|\frac{q^v_\perp(2\omega)}{q^m_\perp(2\omega)}\right|^2\Big|\sin^3\theta\chi^{(2)S}_{\perp\perp\perp} + \frac{c^2}{\omega^2}\sin\theta\Big(q^m_\perp(\omega)^2\chi^{(2)S}_{\perp\parallel\parallel} - q^m_\perp(\omega)q^m_\perp(2\omega)\chi^{(2)S}_{\parallel\parallel\perp}\Big) - \frac{c^3}{2\omega^3}q^m_\perp(\omega)^2q^m_\perp(2\omega)\cos(3\phi)\chi^{(2)S}_{\parallel\parallel\parallel}\Big|^2, \tag{C.4a}$$

$$R_{ps}(\theta,\phi,\omega) = \frac{c}{2\omega^2\epsilon_0}\frac{\sin^2(3\phi)}{\cos^2\theta}\left|\frac{t^s_{mv}(2\omega)t^p_{vm}(\omega)^2}{\epsilon(\omega)}\right|^2\left|\frac{q^v_\perp(2\omega)q^m_\perp(\omega)^2}{q^m_\perp(2\omega)}\right|^2\left|\chi^{(2)S}_{\parallel\parallel\parallel}\right|^2, \tag{C.4b}$$

$$R_{sp}(\theta,\phi,\omega) = \frac{\omega^2}{2c^3\epsilon_0}\frac{1}{\cos^2\theta}\left|\frac{t^p_{mv}(2\omega)t^s_{vm}(\omega)^2}{\sqrt{\epsilon(2\omega)}}\right|^2\left|\frac{q^v_\perp(2\omega)}{q^m_\perp(2\omega)}\right|^2\left|\sin\theta\chi^{(2)S}_{\perp\parallel\parallel} + \frac{c}{2\omega}q^m_\perp(2\omega)\cos(3\phi)\chi^{(2)S}_{\parallel\parallel\parallel}\right|^2, \tag{C.4c}$$

$$R_{ss}(\theta,\phi,\omega) = \frac{\omega^2}{2c^3\epsilon_0}\frac{\sin^2(3\phi)}{\cos^2\theta}\left|t^s_{mv}(2\omega)t^s_{vm}(\omega)^2\right|^2\left|\frac{q^v_\perp(2\omega)}{q^m_\perp(2\omega)}\right|^2\left|\chi^{(2)S}_{\parallel\parallel\parallel}\right|^2. \tag{C.4d}$$

C.5 Reflection coefficients for a cubic non-centrosymmetric bulk

From Eq. (2.29) we get directly the four usual reflection coefficients

$$R_{pp}(\theta,\phi,\omega) = \frac{c}{2\omega^2\epsilon_0}\tan^2(\theta)\sin^2(2\phi)\left|\frac{q_\perp^v(2\omega)q_\perp^m(\omega)}{q_\perp^m(2\omega)}\frac{t_{mv}^p(2\omega)t_{vm}^p(\omega)^2}{\sqrt{\epsilon(2\omega)}\epsilon(\omega)}\frac{q_\perp^m(\omega)-q_\perp^m(2\omega)}{q_\perp^m(2\omega)+2q_\perp^m(\omega)}\right|^2\left|\chi_{xyz}^{(2)}\right|^2, \tag{C.5a}$$

$$R_{ps}(\theta,\phi,\omega) = \frac{2}{c\epsilon_0}\tan^2(\theta)\cos^2(2\phi)\left|\frac{q_\perp^v(2\omega)}{q_\perp^m(2\omega)}\frac{t_{mv}^s(2\omega)t_{vm}^p(\omega)^2}{\epsilon(\omega)}\frac{q_\perp^m(\omega)}{[q_\perp^m(2\omega)+2q_\perp^m(\omega)]}\right|^2\left|\chi_{xyz}^{(2)}\right|^2, \tag{C.5b}$$

$$R_{sp}(\theta,\phi,\omega) = \frac{\omega^2}{2c^3\epsilon_0}\tan^2(\theta)\sin^2(2\phi)\left|\frac{t_{mv}^p(2\omega)t_{vm}^s(\omega)^2}{\sqrt{\epsilon(2\omega)}}\right|^2\left|\frac{q_\perp^v(2\omega)}{q_\perp^m(2\omega)[q_\perp^m(2\omega)+2q_\perp^m(\omega)]}\right|^2\left|\chi_{xyz}^{(2)}\right|^2, \tag{C.5c}$$

$$R_{ss}(\omega) = 0. \tag{C.5d}$$

Notice here that these reflection coefficients depend on both the incident and the azimuthal angles.

D. Matrix elements of $\mathcal{V}$ in a plane-waves basis

The inclusion of the nonlocal part of the pseudo-potential requires the evaluation of the matrix elements of the modified velocity, as defined by Eq. (6.11). More precisely, we want to compute

$$\langle n,\mathbf{k}|\mathbf{q}.\,\boldsymbol{\mathcal{V}}|n',\mathbf{k}\rangle = \langle n,\mathbf{k}|\frac{\mathcal{C}(z)\mathbf{q}.\,\hat{\mathbf{v}}+\mathbf{q}.\,\hat{\mathbf{v}}\mathcal{C}(z)}{2}|n',\mathbf{k}\rangle, \tag{D.1}$$

with $\hat{\mathbf{v}} = \hat{\mathbf{p}} + i[\hat{V}^{\mathrm{nl}},\hat{\mathbf{r}}]$. Two contributions have to be computed separately: $\langle n,\mathbf{k}|\frac{\mathcal{C}(z)\mathbf{q}.\hat{\mathbf{p}}+\mathbf{q}.\hat{\mathbf{p}}\mathcal{C}(z)}{2}|n',\mathbf{k}\rangle$ and $\langle n,\mathbf{k}|\frac{\mathcal{C}(z)[\hat{V}^{\mathrm{nl}},i\mathbf{q}.\hat{\mathbf{r}}]+[\hat{V}^{\mathrm{nl}},i\mathbf{q}.\hat{\mathbf{r}}]\mathcal{C}(z)}{2}|n',\mathbf{k}\rangle$. Using the definition of the Bloch states Eq. (3.40), the first term is easily obtained

$$\begin{aligned}\langle n,\mathbf{k}|\frac{\mathcal{C}(z)\hat{\mathbf{p}}+\hat{\mathbf{p}}\mathcal{C}(z)}{2}|n',\mathbf{k}\rangle &= \frac{-i}{2V}\sum_{\mathbf{G},\mathbf{G}'} c^*_{n,\mathbf{k}}(\mathbf{G})c_{n',\mathbf{k}}(\mathbf{G}')\\ \times\int d^3\mathbf{r}\Big[e^{-i(\mathbf{k}+\mathbf{G}).\mathbf{r}}\mathcal{C}(z)\boldsymbol{\nabla}_{\mathbf{r}}(e^{i(\mathbf{k}+\mathbf{G}').\mathbf{r}}) - \boldsymbol{\nabla}_{\mathbf{r}}(e^{-i(\mathbf{k}+\mathbf{G}).\mathbf{r}})\mathcal{C}(z)e^{i(\mathbf{k}+\mathbf{G}').\mathbf{r}}\Big]&\\ = \frac{1}{2}\sum_{\mathbf{G},\mathbf{G}'} c^*_{n,\mathbf{k}}(\mathbf{G})c_{n',\mathbf{k}}(\mathbf{G}')\left[2\mathbf{k}+\mathbf{G}+\mathbf{G}'\right]\delta_{\mathbf{G}_{||}\mathbf{G}'_{||}}F(G_z-G'_z),&\end{aligned} \tag{D.2}$$

where we have defined $F(G_z) = \frac{1}{2L_z}\int dz e^{-iG_z z}\mathcal{C}(z)$, with $2L_z$ the height of the super-cell.
In order to compute the term containing the commutator, we introduce the unity operator

$$\langle n,\mathbf{k}|\mathcal{C}(z)[\hat{V}^{\mathrm{nl}},i\mathbf{q}.\,\hat{\mathbf{r}}]|n',\mathbf{k}\rangle = \sum_{\mathbf{G}''}\langle n,\mathbf{k}|\mathcal{C}(z)|\mathbf{k}+\mathbf{G}''\rangle\langle\mathbf{k}+\mathbf{G}''|[\hat{V}^{\mathrm{nl}},i\mathbf{q}.\,\hat{\mathbf{r}}]|n',\mathbf{k}\rangle,$$

where $\langle\mathbf{r}|\mathbf{k}+\mathbf{G}\rangle = e^{i(\mathbf{k}+\mathbf{G}).\mathbf{r}}/\sqrt{V}$, V being the volume of the super-cell.
Using the definition of Bloch states Eq. 3.40, we obtain that

$$\begin{aligned}\langle n,\mathbf{k}|\mathcal{C}(z)|\mathbf{k}+\mathbf{G}''\rangle &= \frac{1}{\sqrt{V}}\sum_{G} c^*_{n,\mathbf{k}}(\mathbf{G})\int d^3\mathbf{r}e^{-i(\mathbf{G}-\mathbf{G}'').\mathbf{r}}\mathcal{C}(z),\\ \langle\mathbf{k}+\mathbf{G}''|[\hat{V}^{\mathrm{nl}},i\mathbf{q}.\,\hat{\mathbf{r}}]|n',\mathbf{k}\rangle &= \frac{1}{\sqrt{V}}\sum_{G'} c_{n',\mathbf{k}}(\mathbf{G}')\langle\mathbf{k}+\mathbf{G}''|[\hat{V}^{\mathrm{nl}},i\mathbf{q}.\,\hat{\mathbf{r}}]|\mathbf{k}+\mathbf{G}'\rangle.\end{aligned}$$

Putting everything together yields

$$\begin{aligned}\langle n,\mathbf{k}|\frac{\mathcal{C}(z)[\hat{V}^{\mathrm{nl}},i\mathbf{q}.\,\hat{\mathbf{r}}]+[\hat{V}^{\mathrm{nl}},i\mathbf{q}.\,\hat{\mathbf{r}}]\mathcal{C}(z)}{2}|n',\mathbf{k}\rangle &= \frac{1}{2}\sum_{\mathbf{G},\mathbf{G}',\mathbf{G}''} c^*_{n,\mathbf{k}}(\mathbf{G})c_{n',\mathbf{k}}(\mathbf{G}')\\ \times\Big[\langle\mathbf{k}+\mathbf{G}''|[\hat{V}^{\mathrm{nl}},i\mathbf{q}.\,\hat{\mathbf{r}}]|\mathbf{k}+\mathbf{G}'\rangle\delta_{\mathbf{G}_{||}\mathbf{G}''_{||}}F(G_z-G''_z) + \langle\mathbf{k}+\mathbf{G}|[\hat{V}^{\mathrm{nl}},i\mathbf{q}.\,\hat{\mathbf{r}}]|\mathbf{k}+\mathbf{G}''\rangle\delta_{\mathbf{G}'_{||}\mathbf{G}''_{||}}F(G''_z-G'_z)\Big]&.\end{aligned}$$

Using the notation $\mathbf{K} = \mathbf{k} + \mathbf{G}$ and in case of a Kleinman-Bylander separable-form pseudo-potential, we have [120] (see Ref. [121] for the notations)

$$\langle \mathbf{K}|\hat{V}^{\rm nl}|\mathbf{K}'\rangle = \sum_s e^{i(\mathbf{K}-\mathbf{K}').\boldsymbol{\tau_s}} \sum_{l=0}^{l_s}\sum_{m=-l}^{l} E_l F_{lm}^s(\mathbf{K}) F_{lm}^{s*}(\mathbf{K}'), \qquad F_{lm}^s(\mathbf{K}) = \int d^3\mathbf{r} e^{i\mathbf{K}.\mathbf{r}} \delta V_l^s(\mathbf{r}) \Phi_{lm}^{ps}(\mathbf{r}).$$

Using the relation $i\langle \mathbf{K}|[\hat{V}^{\rm nl}, \hat{\mathbf{r}}]|\mathbf{K}'\rangle = (\nabla_{\mathbf{K}} + \nabla_{\mathbf{K}'})\langle \mathbf{K}|\hat{V}^{\rm nl}|\mathbf{K}'\rangle$, shown in Ref. [121], we obtain the nonlocal contribution to the velocity operator, as already implemented in DP [116] and 2light [117] codes

$$\begin{aligned}\langle n,\mathbf{k}|[\hat{V}^{\rm nl}, i\hat{\mathbf{r}}]|n',\mathbf{k}\rangle = \sum_s \sum_{l=0}^{l_s}\sum_{m=-l}^{l} E_l \Bigg\{ \Bigg[\sum_{\mathbf{G}} c_{n,\mathbf{k}}^*(\mathbf{G}) e^{i\mathbf{G}.\boldsymbol{\tau_s}} \nabla_{\mathbf{G}} F_{lm}^s(\mathbf{K})\Bigg]\Bigg[\sum_{\mathbf{G}'} c_{n',\mathbf{k}}(\mathbf{G}') e^{-i\mathbf{G}'.\boldsymbol{\tau_s}} F_{lm}^{s*}(\mathbf{K}')\Bigg] \\ + \Bigg[\sum_{\mathbf{G}} c_{n,\mathbf{k}}^*(\mathbf{G}) e^{i\mathbf{G}.\boldsymbol{\tau_s}} F_{lm}^s(\mathbf{K})\Bigg]\Bigg[\sum_{\mathbf{G}'} c_{n',\mathbf{k}}(\mathbf{G}') e^{-i\mathbf{G}'.\boldsymbol{\tau_s}} \nabla_{\mathbf{G}'} F_{lm}^{s*}(\mathbf{K}')\Bigg]\Bigg\}.\end{aligned} \tag{D.4}$$

The nonlocal part of the modified velocity, *i.e.*, containing the contribution of the commutator, is given by

$$\begin{aligned}\langle n,\mathbf{k}|\frac{\mathcal{C}(z)[\hat{V}^{\rm nl}, i\mathbf{q}.\hat{\mathbf{r}}] + [\hat{V}^{\rm nl}, i\mathbf{q}.\hat{\mathbf{r}}]\mathcal{C}(z)}{2}|n',\mathbf{k}\rangle = \frac{1}{2}\sum_{\mathbf{G},\mathbf{G}',\mathbf{G}''} c_{n,\mathbf{k}}^*(\mathbf{G}) c_{n',\mathbf{k}}(\mathbf{G}') \\ \times\Big[(\nabla_{\mathbf{K}''} + \nabla_{\mathbf{K}'})\langle \mathbf{K}''|\hat{V}^{\rm nl}|\mathbf{K}'\rangle \delta_{\mathbf{G}_{||}\mathbf{G}''_{||}} F(G_z - G_z'') + (\nabla_{\mathbf{K}} + \nabla_{\mathbf{K}''})\langle \mathbf{K}|\hat{V}^{\rm nl}|\mathbf{K}''\rangle \delta_{\mathbf{G}'_{||}\mathbf{G}''_{||}} F(G_z'' - G_z')\Big].\end{aligned}$$

After some algebra, we obtain the expression of the nonlocal contribution to the modified velocity matrix elements

$$\begin{aligned}\langle n,\mathbf{k}|\frac{\mathcal{C}(z)[\hat{V}^{\rm nl}, i\mathbf{q}.\hat{\mathbf{r}}] + [\hat{V}^{\rm nl}, i\mathbf{q}.\hat{\mathbf{r}}]\mathcal{C}(z)}{2}|n',\mathbf{k}\rangle = \frac{1}{2}\sum_s \sum_{l=0}^{l_s}\sum_{m=-l}^{l} E_l \\ \Bigg\{\Bigg(\sum_{\mathbf{G}''} e^{i\mathbf{G}''.\boldsymbol{\tau_s}} \nabla_{\mathbf{K}''} F_{lm}^s(\mathbf{K}'') \sum_{\mathbf{G}} c_{n,\mathbf{k}}^*(\mathbf{G}) \delta_{\mathbf{G}_{||}\mathbf{G}''_{||}} F(G_z - G_z'')\Bigg)\Bigg(\sum_{\mathbf{G}'} c_{n',\mathbf{k}}(\mathbf{G}') e^{-i\mathbf{G}'.\boldsymbol{\tau_s}} F_{lm}^{s*}(\mathbf{K}')\Bigg) \\ + \Bigg(\sum_{\mathbf{G}''} e^{i\mathbf{G}''.\boldsymbol{\tau_s}} F_{lm}^s(\mathbf{K}'') \sum_{\mathbf{G}} c_{n,\mathbf{k}}^*(\mathbf{G}) \delta_{\mathbf{G}_{||}\mathbf{G}''_{||}} F(G_z - G_z'')\Bigg)\Bigg(\sum_{\mathbf{G}'} c_{n',\mathbf{k}}(\mathbf{G}') e^{-i\mathbf{G}'.\boldsymbol{\tau_s}} \nabla_{\mathbf{K}'} F_{lm}^{s*}(\mathbf{K}')\Bigg) \\ + \Bigg(\sum_{\mathbf{G}} c_{n,\mathbf{k}}^*(\mathbf{G}) e^{i\mathbf{G}.\boldsymbol{\tau_s}} \nabla_{\mathbf{K}} F_{lm}^s(\mathbf{K})\Bigg)\Bigg(\sum_{\mathbf{G}''} e^{-i\mathbf{G}''.\boldsymbol{\tau_s}} F_{lm}^{s*}(\mathbf{K}'') \sum_{\mathbf{G}'} c_{n',\mathbf{k}}(\mathbf{G}') \delta_{\mathbf{G}'_{||}\mathbf{G}''_{||}} F(G_z'' - G_z')\Bigg) \\ + \Bigg(\sum_{\mathbf{G}} c_{n,\mathbf{k}}^*(\mathbf{G}) e^{i\mathbf{G}.\boldsymbol{\tau_s}} F_{lm}^s(\mathbf{K})\Bigg)\Bigg(\sum_{\mathbf{G}''} e^{-i\mathbf{G}''.\boldsymbol{\tau_s}} \nabla_{\mathbf{K}''} F_{lm}^{s*}(\mathbf{K}'') \sum_{\mathbf{G}'} c_{n',\mathbf{k}}(\mathbf{G}') \delta_{\mathbf{G}'_{||}\mathbf{G}''_{||}} F(G_z'' - G_z')\Bigg)\Bigg\}.\end{aligned} \tag{D.5}$$

In this last expression, a double sum over $\mathbf{G}$ vector is involved, making the calculation of the nonlocal part of the modified velocity operator more intricate and time consuming than for the bulk counterpart.

E. Divergence-free expression of $\chi^{S}_{\rho\rho\rho}$

Here I present a detailed derivation of the divergence-free expression Eqs. (6.14). The starting point is the divergent expression Eq. (6.10). We first split Eq. (6.10) into three pieces

$$\chi^{S,I}_{\rho\rho\rho}(\hat{\mathbf{q}},\hat{\mathbf{q}}_{\mathbf{1}},\hat{\mathbf{q}}_{\mathbf{2}},\omega) = \frac{-2}{V\omega^3}\sum_{nn'n''}\sum_{\mathbf{k}}^{BZ}\frac{\langle n,\mathbf{k}|\hat{\mathbf{q}}\mathcal{V}^{\mathbf{\Sigma}}|n',\mathbf{k}\rangle\langle n',\mathbf{k}|\hat{\mathbf{q}}_{\mathbf{1}}\hat{\mathbf{v}}^{\mathbf{\Sigma}}|n'',\mathbf{k}\rangle\langle n'',\mathbf{k}|\hat{\mathbf{q}}_{\mathbf{2}}\hat{\mathbf{v}}^{\mathbf{\Sigma}}|n,\mathbf{k}\rangle}{(E^{\Sigma}_{n\mathbf{k}}-E^{\Sigma}_{n'\mathbf{k}}+2\omega+2i\eta)}$$
$$\left\{\frac{(f_{n\mathbf{k}}-f_{n''\mathbf{k}})}{(E^{\Sigma}_{n\mathbf{k}}-E^{\Sigma}_{n''\mathbf{k}}+\omega+i\eta)}+\frac{(f_{n'\mathbf{k}}-f_{n''\mathbf{k}})}{(E^{\Sigma}_{n''\mathbf{k}}-E^{\Sigma}_{n'\mathbf{k}}+\omega+i\eta)}\right\}+(\hat{\mathbf{q}}_{\mathbf{1}}\leftrightarrow\hat{\mathbf{q}}_{\mathbf{2}}), \tag{E.1a}$$

$$\chi^{S,II}_{\rho\rho\rho}(\hat{\mathbf{q}},\hat{\mathbf{q}}_{\mathbf{1}},\hat{\mathbf{q}}_{\mathbf{2}},\omega) = \frac{i}{V\omega^3}\sum_{nn'}\sum_{\mathbf{k}}^{BZ}(f_{n\mathbf{k}}-f_{n'\mathbf{k}})\left\{\frac{2\langle n,\mathbf{k}|\left[\hat{\mathbf{q}}\mathcal{R},\hat{\mathbf{q}}_{\mathbf{1}}\hat{\mathbf{v}}^{\mathbf{\Sigma}}\right]|n',\mathbf{k}\rangle\langle n',\mathbf{k}|\hat{\mathbf{q}}_{\mathbf{2}}\hat{\mathbf{v}}^{\mathbf{\Sigma}}|n,\mathbf{k}\rangle}{(E^{\Sigma}_{n\mathbf{k}}-E^{\Sigma}_{n'\mathbf{k}}+\omega+i\eta)}\right.$$
$$\left.+\frac{\langle n,\mathbf{k}|\hat{\mathbf{q}}\mathcal{V}^{\mathbf{\Sigma}}|n',\mathbf{k}\rangle\langle n',\mathbf{k}|\left[\hat{\mathbf{q}}_{\mathbf{1}}\hat{\mathbf{r}},\hat{\mathbf{q}}_{\mathbf{2}}\hat{\mathbf{v}}^{\mathbf{\Sigma}}\right]|n,\mathbf{k}\rangle}{(E^{\Sigma}_{n\mathbf{k}}-E^{\Sigma}_{n'\mathbf{k}}+2\omega+2i\eta)}\right\}+(\hat{\mathbf{q}}_{\mathbf{1}}\leftrightarrow\hat{\mathbf{q}}_{\mathbf{2}}), \tag{E.1b}$$

$$\chi^{S,III}_{\rho\rho\rho}(\hat{\mathbf{q}},\hat{\mathbf{q}}_{\mathbf{1}},\hat{\mathbf{q}}_{\mathbf{2}},\omega) = \frac{1}{V\omega^3}\sum_{n}\sum_{\mathbf{k}}^{BZ}f_{n\mathbf{k}}\langle n,\mathbf{k}|\left[\hat{\mathbf{q}}\mathbf{r},\left[\hat{\mathbf{q}}_{\mathbf{1}}\hat{\mathbf{r}},\hat{\mathbf{q}}_{\mathbf{2}}\mathcal{V}^{\mathbf{\Sigma}}\right]\right]|n,\mathbf{k}\rangle+(\hat{\mathbf{q}}_{\mathbf{1}}\leftrightarrow\hat{\mathbf{q}}_{\mathbf{2}}). \tag{E.1c}$$

The last term vanishes from time-reversal symmetry.
In order to be able to apply Sipe and coworkers transformation [185], we first show that the term $n=n'$ is zero in $\chi^{S,I}_{\rho\rho\rho}$

$$\chi^{S,I,n=n'}_{\rho\rho\rho}(\hat{\mathbf{q}},\hat{\mathbf{q}}_{\mathbf{1}},\hat{\mathbf{q}}_{\mathbf{2}},\omega) = \frac{-2}{V\omega^3}\sum_{n=n'n''}\sum_{\mathbf{k}}^{BZ}\frac{\langle n,\mathbf{k}|\hat{\mathbf{q}}\mathcal{V}^{\mathbf{\Sigma}}|n,\mathbf{k}\rangle\langle n,\mathbf{k}|\hat{\mathbf{q}}_{\mathbf{1}}\hat{\mathbf{v}}^{\mathbf{\Sigma}}|n'',\mathbf{k}\rangle\langle n'',\mathbf{k}|\hat{\mathbf{q}}_{\mathbf{2}}\hat{\mathbf{v}}^{\mathbf{\Sigma}}|n,\mathbf{k}\rangle}{(E^{\Sigma}_{n\mathbf{k}}-E^{\Sigma}_{n'\mathbf{k}}+2\omega+2i\eta)}$$
$$\left\{\frac{(f_{n\mathbf{k}}-f_{n''\mathbf{k}})}{(E^{\Sigma}_{n\mathbf{k}}-E^{\Sigma}_{n''\mathbf{k}}+\omega+i\eta)}+\frac{(f_{n\mathbf{k}}-f_{n''\mathbf{k}})}{(E^{\Sigma}_{n''\mathbf{k}}-E^{\Sigma}_{n\mathbf{k}}+\omega+i\eta)}+(\hat{\mathbf{q}}_{\mathbf{1}}\leftrightarrow\hat{\mathbf{q}}_{\mathbf{2}})\right\}. \tag{E.2}$$

Using $\mathbf{k}\rightarrow-\mathbf{k}$, we obtain directly that the contribution $n=n'$ to $\chi^{(2)I}_{abc}(\omega)$ is zero. It is therefore possible to follow Sipe and coworkers demonstration and to write that

$$\frac{1}{\omega^3(E^{\Sigma}_{n\mathbf{k}}-E^{\Sigma}_{n'\mathbf{k}}+2\omega+2i\eta)}\left\{\frac{(f_{n\mathbf{k}}-f_{n''\mathbf{k}})}{(E^{\Sigma}_{n\mathbf{k}}-E^{\Sigma}_{n''\mathbf{k}}+\omega+i\eta)}+\frac{(f_{n'\mathbf{k}}-f_{n''\mathbf{k}})}{(E^{\Sigma}_{n''\mathbf{k}}-E^{\Sigma}_{n'\mathbf{k}}+\omega+i\eta)}\right\}=\frac{\mathcal{A}}{\omega^3}+\frac{\mathcal{B}}{\omega^2}+\frac{\mathcal{C}}{\omega}+\mathcal{F}(\omega).$$

As in Ref. [185], terms associated to $\mathcal{A}$ and $\mathcal{C}$ are zero thanks to time-reversal symmetry. We have to shown that the term associated with $\mathcal{B}$ is zero.

$$\mathcal{B}(\omega)=\frac{(f_{n\mathbf{k}}-f_{n''\mathbf{k}})}{(E^{\Sigma}_{n'\mathbf{k}}-E^{\Sigma}_{n\mathbf{k}})(E^{\Sigma}_{n''\mathbf{k}}-E^{\Sigma}_{n\mathbf{k}})}\left[\frac{2}{(E^{\Sigma}_{n'\mathbf{k}}-E^{\Sigma}_{n\mathbf{k}})}+\frac{1}{(E^{\Sigma}_{n''\mathbf{k}}-E^{\Sigma}_{n\mathbf{k}})}\right]$$
$$+\frac{(f_{n'\mathbf{k}}-f_{n''\mathbf{k}})}{(E^{\Sigma}_{n'\mathbf{k}}-E^{\Sigma}_{n\mathbf{k}})(E^{\Sigma}_{n'\mathbf{k}}-E^{\Sigma}_{n''\mathbf{k}})}\left[\frac{2}{(E^{\Sigma}_{n'\mathbf{k}}-E^{\Sigma}_{n\mathbf{k}})}+\frac{1}{(E^{\Sigma}_{n'\mathbf{k}}-E^{\Sigma}_{n''\mathbf{k}})}\right]. \tag{E.3}$$

Using the following definitions, derived from $\mathbf{k}\cdot\mathbf{p}$ theory,[1]

$$\frac{\partial \hat{\mathbf{v}}^{\mathbf{\Sigma}}_{nn'}}{\partial \mathbf{k}} = i \sum_{n'' \notin \mathcal{D}_n, \mathcal{D}_{n'}} \left[\hat{\mathbf{r}}_{nn''}\hat{\mathbf{v}}^{\mathbf{\Sigma}}_{n''n'} - \hat{\mathbf{v}}^{\mathbf{\Sigma}}_{nn''}\hat{\mathbf{r}}_{n''n'}\right] + i[\hat{\mathbf{v}}^{\mathbf{\Sigma}}, \hat{\mathbf{r}}]_{nn'} + i\mathbf{\Delta}_{n'n}\hat{\mathbf{r}}_{nn'}, \tag{E.4a}$$

$$\frac{\partial \boldsymbol{\mathcal{V}}^{\mathbf{\Sigma}}{}_{nn'}}{\partial \mathbf{k}} = i \sum_{n'' \notin \mathcal{D}_n, \mathcal{D}_{n'}} \left[\hat{\mathbf{r}}_{nn''}\boldsymbol{\mathcal{V}}^{\mathbf{\Sigma}}{}_{n''n'} - \boldsymbol{\mathcal{V}}^{\mathbf{\Sigma}}{}_{nn''}\hat{\mathbf{r}}_{n''n'}\right] + i[\boldsymbol{\mathcal{V}}^{\mathbf{\Sigma}}, \hat{\mathbf{r}}]_{nn'} + i\hat{\mathbf{r}}_{nn'}\tilde{\mathbf{\Delta}}_{n'n}, \tag{E.4b}$$

and the tensor $\overset{\leftrightarrow}{T} = \sum_{i,j\neq i} \frac{f_{ij}\boldsymbol{\mathcal{V}}^{\mathbf{\Sigma}}{}_{ij}(\mathbf{k})\hat{\mathbf{v}}^{\mathbf{\Sigma}}_{ji}(\mathbf{k})}{E^{\Sigma}_{ij}(\mathbf{k})^2}$, we obtain after some algebra that

$$\begin{aligned}
\frac{\partial \overset{\leftrightarrow}{T}}{\partial \mathbf{k}} &= \sum_{n,n'\neq n} f_{nn'}(\mathbf{k})\left[\frac{\partial \boldsymbol{\mathcal{V}}^{\mathbf{\Sigma}}{}_{nn'}(\mathbf{k})}{\partial \mathbf{k}}\frac{\hat{\mathbf{v}}^{\mathbf{\Sigma}}_{n'n}(\mathbf{k})}{E^{\Sigma}_{nn'}(\mathbf{k})^2} + \frac{\partial \hat{\mathbf{v}}^{\mathbf{\Sigma}}_{n'n}(\mathbf{k})}{\partial \mathbf{k}}\frac{\boldsymbol{\mathcal{V}}^{\mathbf{\Sigma}}{}_{nn'}(\mathbf{k})}{E^{\Sigma}_{nn'}(\mathbf{k})^2} - 2\frac{\boldsymbol{\mathcal{V}}^{\mathbf{\Sigma}}{}_{nn'}(\mathbf{k})\hat{\mathbf{v}}^{\mathbf{\Sigma}}_{n'n}(\mathbf{k})\mathbf{\Delta}_{nn'}}{E^{\Sigma}_{nn'}(\mathbf{k})^3}\right] \\
&= -\sum_{n,n',n''}{}' \boldsymbol{\mathcal{V}}^{\mathbf{\Sigma}}{}_{nn'}\hat{\mathbf{v}}^{\mathbf{\Sigma}}_{n'n''}\hat{\mathbf{v}}^{\mathbf{\Sigma}}_{n''n}\left[\frac{f_{n'n''}}{E^{\Sigma}_{n'n}(\mathbf{k})E^{\Sigma}_{n'n''}(\mathbf{k})}\left(\frac{2}{E^{\Sigma}_{n'n}(\mathbf{k})} + \frac{1}{E^{\Sigma}_{n'n''}(\mathbf{k})}\right)\right. \\
&\left. + \frac{f_{nn''}}{E^{\Sigma}_{n'n}(\mathbf{k})E^{\Sigma}_{n''n}(\mathbf{k})}\left(\frac{2}{E^{\Sigma}_{n'n}(\mathbf{k})} + \frac{1}{E^{\Sigma}_{n''n}(\mathbf{k})}\right)\right] - \sum_{n,n'\neq n}\frac{3f_{nn'}\boldsymbol{\mathcal{V}}^{\mathbf{\Sigma}}{}_{nn'}\hat{\mathbf{v}}^{\mathbf{\Sigma}}_{n'n}\mathbf{\Delta}_{nn'}}{E^{\Sigma}_{nn'}(\mathbf{k})^3} \\
&+ \sum_{n,n'\neq n} f_{nn'}\left[\frac{\hat{\mathbf{v}}^{\mathbf{\Sigma}}_{nn'}\tilde{\mathbf{\Delta}}_{n'n}\hat{\mathbf{v}}^{\mathbf{\Sigma}}_{n'n}}{E^{\Sigma}_{nn'}(\mathbf{k})^3} + \frac{[\boldsymbol{\mathcal{V}}^{\mathbf{\Sigma}}, i\hat{\mathbf{r}}]_{nn'}\hat{\mathbf{v}}^{\mathbf{\Sigma}}_{n'n}}{E^{\Sigma}_{nn'}(\mathbf{k})^2} - \frac{\boldsymbol{\mathcal{V}}^{\mathbf{\Sigma}}{}_{nn'}[i\hat{\mathbf{r}}, \hat{\mathbf{v}}^{\mathbf{\Sigma}}]_{n'n}}{E^{\Sigma}_{nn'}(\mathbf{k})^2}\right].
\end{aligned}$$

The first three terms vanish thank to time-reversal symmetry. Invoking the same arguments as in Ref. [185], the term associated to $\mathcal{B}$ is zero. Concerning the $\mathcal{F}$ term, we get

$$\begin{aligned}
\mathcal{F}(\omega) = &\frac{16}{(E^{\Sigma}_{n'\mathbf{k}} - E^{\Sigma}_{n\mathbf{k}})^3(E^{\Sigma}_{n\mathbf{k}} - E^{\Sigma}_{n'\mathbf{k}} + 2\omega + 2i\eta)}\left[\frac{(f_{n\mathbf{k}} - f_{n''\mathbf{k}})}{E^{\Sigma}_{n'n} - 2E^{\Sigma}_{n''n}} + \frac{(f_{n'\mathbf{k}} - f_{n''\mathbf{k}})}{E^{\Sigma}_{n'n} - 2E^{\Sigma}_{n'n''}}\right] \\
&+ \frac{(f_{n\mathbf{k}} - f_{n''\mathbf{k}})}{(E^{\Sigma}_{n''\mathbf{k}} - E^{\Sigma}_{n\mathbf{k}})^3(2E^{\Sigma}_{n''n} - E^{\Sigma}_{n'n})(E^{\Sigma}_{n\mathbf{k}} - E^{\Sigma}_{n''\mathbf{k}} + \omega + i\eta)} \\
&+ \frac{(f_{n'\mathbf{k}} - f_{n''\mathbf{k}})}{(E^{\Sigma}_{n'\mathbf{k}} - E^{\Sigma}_{n''\mathbf{k}})^3(2E^{\Sigma}_{n'n''} - E^{\Sigma}_{n'n})(E^{\Sigma}_{n''\mathbf{k}} - E^{\Sigma}_{n'\mathbf{k}} + \omega + i\eta)}.
\end{aligned}$$

We thus obtain the two-band and three-band terms,

$$\begin{aligned}
\chi^{S,I3bnd}_{\rho\rho\rho}(\hat{\mathbf{q}}, \hat{\mathbf{q}}_1, \hat{\mathbf{q}}_2, \omega) = &\frac{2}{V}\sum_{n\neq n'\neq n''}\sum_{\mathbf{k}}^{BZ}\frac{\langle n, \mathbf{k}|\hat{\mathbf{q}}\boldsymbol{\mathcal{V}}^{\mathbf{\Sigma}}|n', \mathbf{k}\rangle\langle n', \mathbf{k}|\hat{\mathbf{q}}_1\hat{\mathbf{v}}^{\mathbf{\Sigma}}|n'', \mathbf{k}\rangle\langle n'', \mathbf{k}|\hat{\mathbf{q}}_2\hat{\mathbf{v}}^{\mathbf{\Sigma}}|n, \mathbf{k}\rangle}{(2E^{\Sigma}_{n''n} - E^{\Sigma}_{n'n})} \\
\times\Bigg\{&\frac{16(f_{n\mathbf{k}} - f_{n'\mathbf{k}})}{(E^{\Sigma}_{n'\mathbf{k}} - E^{\Sigma}_{n\mathbf{k}})^3(E^{\Sigma}_{n\mathbf{k}} - E^{\Sigma}_{n'\mathbf{k}} + 2\omega + 2i\eta)} - \frac{(f_{n\mathbf{k}} - f_{n''\mathbf{k}})}{(E^{\Sigma}_{n''\mathbf{k}} - E^{\Sigma}_{n\mathbf{k}})^3(E^{\Sigma}_{n\mathbf{k}} - E^{\Sigma}_{n''\mathbf{k}} + \omega + i\eta)} \\
&+ \frac{(f_{n'\mathbf{k}} - f_{n''\mathbf{k}})}{(E^{\Sigma}_{n'\mathbf{k}} - E^{\Sigma}_{n''\mathbf{k}})^3(E^{\Sigma}_{n''\mathbf{k}} - E^{\Sigma}_{n'\mathbf{k}} + \omega + i\eta)}\Bigg\} + (\hat{\mathbf{q}}_1 \leftrightarrow \hat{\mathbf{q}}_2),
\end{aligned} \tag{E.6a}$$

$$\chi^{S,I2bnd}_{\rho\rho\rho}(\hat{\mathbf{q}}, \hat{\mathbf{q}}_1, \hat{\mathbf{q}}_2, \omega) = -\frac{2}{V}\sum_{n\neq n'}\sum_{\mathbf{k}}^{BZ}(f_{n\mathbf{k}} - f_{n'\mathbf{k}})\frac{\langle n, \mathbf{k}|\hat{\mathbf{q}}\boldsymbol{\mathcal{R}}|n', \mathbf{k}\rangle\langle n', \mathbf{k}|\hat{\mathbf{q}}_1\hat{\mathbf{r}}|n, \mathbf{k}\rangle\hat{\mathbf{q}}_2\mathbf{\Delta}_{n'n}}{(E^{\Sigma}_{n\mathbf{k}} - E^{\Sigma}_{n'\mathbf{k}})^2}$$

[1] It is interesting to note here that $\mathbf{v}$ and $\boldsymbol{\mathcal{V}}$ follow the same sum-rule.

$$\times\left\{\frac{16}{(E^{\Sigma}_{n\mathbf{k}}-E^{\Sigma}_{n'\mathbf{k}}+2\omega+2i\eta)}+\frac{1}{(E^{\Sigma}_{n\mathbf{k}}-E^{\Sigma}_{n'\mathbf{k}}+\omega+i\eta)}\right\}+(\hat{\mathbf{q}}_{\mathbf{1}}\leftrightarrow\hat{\mathbf{q}}_{\mathbf{2}}). \quad \text{(E.6b)}$$

We now use partial fraction development, to simplify $\chi^{S,I3bnd}_{\rho\rho\rho}$ that we then split into χ^{3bnd}_{I} and χ^{3bnd}_{II}, such as $\chi^{S,I3bnd}_{\rho\rho\rho}(\hat{\mathbf{q}},\hat{\mathbf{q}}_{\mathbf{1}},\hat{\mathbf{q}}_{\mathbf{2}},\omega)=\chi^{3bnd}_{I}(\hat{\mathbf{q}},\hat{\mathbf{q}}_{\mathbf{1}},\hat{\mathbf{q}}_{\mathbf{2}},\omega)+\chi^{3bnd}_{II}(\hat{\mathbf{q}},\hat{\mathbf{q}}_{\mathbf{1}},\hat{\mathbf{q}}_{\mathbf{2}},\omega)$, with

$$\begin{aligned}\chi^{3bnd}_{I}(\hat{\mathbf{q}},\hat{\mathbf{q}}_{\mathbf{1}},\hat{\mathbf{q}}_{\mathbf{2}},\omega)=&\frac{2i}{V}\sum_{n\neq n'\neq n''}\sum_{\mathbf{k}}^{BZ}\langle n,\mathbf{k}|\hat{\mathbf{q}}\boldsymbol{\mathcal{R}}|n',\mathbf{k}\rangle\langle n',\mathbf{k}|\hat{\mathbf{q}}_{\mathbf{1}}\hat{\mathbf{r}}|n'',\mathbf{k}\rangle\langle n'',\mathbf{k}|\hat{\mathbf{q}}_{\mathbf{2}}\hat{\mathbf{r}}|n,\mathbf{k}\rangle\\&\left\{-\frac{(2E^{\Sigma}_{n''\mathbf{k}}-E^{\Sigma}_{n'\mathbf{k}}-E^{\Sigma}_{n\mathbf{k}})}{(E^{\Sigma}_{n'\mathbf{k}}-E^{\Sigma}_{n\mathbf{k}})^2}\frac{4(f_{n\mathbf{k}}-f_{n'\mathbf{k}})}{(E^{\Sigma}_{n\mathbf{k}}-E^{\Sigma}_{n'\mathbf{k}}+2\omega+2i\eta)}\right.\\&-\frac{(2E^{\Sigma}_{n\mathbf{k}}-E^{\Sigma}_{n'\mathbf{k}}-E^{\Sigma}_{n''\mathbf{k}})}{(E^{\Sigma}_{n''\mathbf{k}}-E^{\Sigma}_{n\mathbf{k}})^2}\frac{(f_{n\mathbf{k}}-f_{n''\mathbf{k}})}{(E^{\Sigma}_{n\mathbf{k}}-E^{\Sigma}_{n''\mathbf{k}}+\omega+i\eta)}\\&\left.+\frac{(2E^{\Sigma}_{n'\mathbf{k}}-E^{\Sigma}_{n\mathbf{k}}-E^{\Sigma}_{n''\mathbf{k}})}{(E^{\Sigma}_{n'\mathbf{k}}-E^{\Sigma}_{n''\mathbf{k}})^2}\frac{(f_{n'\mathbf{k}}-f_{n''\mathbf{k}})}{(E^{\Sigma}_{n''\mathbf{k}}-E^{\Sigma}_{n'\mathbf{k}}+\omega+i\eta)}\right\}+(\hat{\mathbf{q}}_{\mathbf{1}}\leftrightarrow\hat{\mathbf{q}}_{\mathbf{2}}),\end{aligned} \quad \text{(E.7a)}$$

$$\begin{aligned}\chi^{3bnd}_{II}(\hat{\mathbf{q}},\hat{\mathbf{q}}_{\mathbf{1}},\hat{\mathbf{q}}_{\mathbf{2}},\omega)=&\frac{4i}{V}\sum_{n\neq n'\neq n''}\sum_{\mathbf{k}}^{BZ}\frac{\langle n,\mathbf{k}|\hat{\mathbf{q}}\boldsymbol{\mathcal{R}}|n',\mathbf{k}\rangle\langle n',\mathbf{k}|\hat{\mathbf{q}}_{\mathbf{1}}\hat{\mathbf{r}}|n'',\mathbf{k}\rangle\langle n'',\mathbf{k}|\hat{\mathbf{q}}_{\mathbf{2}}\hat{\mathbf{r}}|n,\mathbf{k}\rangle}{(2E^{\Sigma}_{n''n}-E^{\Sigma}_{n'n})}\\&\left\{\frac{2(f_{n\mathbf{k}}-f_{n'\mathbf{k}})}{(E^{\Sigma}_{n\mathbf{k}}-E^{\Sigma}_{n'\mathbf{k}}+2\omega+2i\eta)}-\frac{(f_{n\mathbf{k}}-f_{n''\mathbf{k}})}{(E^{\Sigma}_{n\mathbf{k}}-E^{\Sigma}_{n''\mathbf{k}}+\omega+i\eta)}+\frac{(f_{n'\mathbf{k}}-f_{n''\mathbf{k}})}{(E^{\Sigma}_{n''\mathbf{k}}-E^{\Sigma}_{n'\mathbf{k}}+\omega+i\eta)}\right\}\\&+(\hat{\mathbf{q}}_{\mathbf{1}}\leftrightarrow\hat{\mathbf{q}}_{\mathbf{2}}).\end{aligned} \quad \text{(E.7b)}$$

Let us now consider $\chi^{S,II}_{\rho\rho\rho}$. Using the relations

$$\begin{aligned}\frac{1}{\omega^3(E^{\Sigma}_{n\mathbf{k}}-E^{\Sigma}_{n'\mathbf{k}}+\omega+i\eta)}&=\frac{1}{\omega^3(E^{\Sigma}_{n\mathbf{k}}-E^{\Sigma}_{n'\mathbf{k}})}-\frac{1}{(E^{\Sigma}_{n\mathbf{k}}-E^{\Sigma}_{n'\mathbf{k}})^3(E^{\Sigma}_{n\mathbf{k}}-E^{\Sigma}_{n'\mathbf{k}}+\omega+i\eta)},\\\frac{1}{\omega^3(E^{\Sigma}_{n\mathbf{k}}-E^{\Sigma}_{n'\mathbf{k}}+2\omega+i\eta)}&=\frac{1}{\omega^3(E^{\Sigma}_{n\mathbf{k}}-E^{\Sigma}_{n'\mathbf{k}})}-\frac{8}{(E^{\Sigma}_{n\mathbf{k}}-E^{\Sigma}_{n'\mathbf{k}})^3(E^{\Sigma}_{n\mathbf{k}}-E^{\Sigma}_{n'\mathbf{k}}+2\omega+i\eta)},\end{aligned}$$

we obtain that

$$\begin{aligned}\chi^{S,II}_{\rho\rho\rho}(\hat{\mathbf{q}},\hat{\mathbf{q}}_{\mathbf{1}},\hat{\mathbf{q}}_{\mathbf{2}},\omega)=&\frac{2i}{V}\sum_{nn'}\sum_{\mathbf{k}}^{BZ}(f_{n\mathbf{k}}-f_{n'\mathbf{k}})\langle n,\mathbf{k}|\left[\hat{\mathbf{q}}\boldsymbol{\mathcal{R}},\hat{\mathbf{q}}_{\mathbf{1}}\hat{\mathbf{v}}^{\boldsymbol{\Sigma}}\right]|n',\mathbf{k}\rangle\langle n',\mathbf{k}|\hat{\mathbf{q}}_{\mathbf{1}}\hat{\mathbf{v}}^{\boldsymbol{\Sigma}}|n,\mathbf{k}\rangle\\&\left[\frac{1}{\omega^3(E^{\Sigma}_{n\mathbf{k}}-E^{\Sigma}_{n'\mathbf{k}})}-\frac{1}{(E^{\Sigma}_{n\mathbf{k}}-E^{\Sigma}_{n'\mathbf{k}})^3(E^{\Sigma}_{n\mathbf{k}}-E^{\Sigma}_{n'\mathbf{k}}+\omega+i\eta)}\right]+(\hat{\mathbf{q}}_{\mathbf{1}}\leftrightarrow\hat{\mathbf{q}}_{\mathbf{2}})\\&+\frac{i}{V}\sum_{nn'}\sum_{\mathbf{k}}^{BZ}(f_{n\mathbf{k}}-f_{n'\mathbf{k}})\langle n,\mathbf{k}|\hat{\mathbf{q}}\boldsymbol{\mathcal{V}}^{\boldsymbol{\Sigma}}|n',\mathbf{k}\rangle\langle n',\mathbf{k}|\left[\hat{\mathbf{q}}_{\mathbf{1}}\hat{\mathbf{r}},\hat{\mathbf{q}}_{\mathbf{2}}\hat{\mathbf{v}}^{\boldsymbol{\Sigma}}\right]|n,\mathbf{k}\rangle\\&\left[\frac{1}{\omega^3(E^{\Sigma}_{n\mathbf{k}}-E^{\Sigma}_{n'\mathbf{k}})}-\frac{8}{(E^{\Sigma}_{n\mathbf{k}}-E^{\Sigma}_{n'\mathbf{k}})^3(E^{\Sigma}_{n\mathbf{k}}-E^{\Sigma}_{n'\mathbf{k}}+2\omega+i\eta)}\right]+(\hat{\mathbf{q}}_{\mathbf{1}}\leftrightarrow\hat{\mathbf{q}}_{\mathbf{2}}).\end{aligned} \quad \text{(E.8)}$$

The term containing $\frac{1}{\omega^3}$ vanishes using $\mathbf{k} \to -\mathbf{k}$ and $n \leftrightarrow n'$. The remaining terms give

$$\begin{aligned}\chi^{S,II}_{\rho\rho\rho}(\hat{\mathbf{q}}, \hat{\mathbf{q}}_\mathbf{1}, \hat{\mathbf{q}}_\mathbf{2}, \omega) = \frac{-2}{V}\sum_{nn'}\sum_{\mathbf{k}}^{BZ}(f_{n\mathbf{k}} - f_{n'\mathbf{k}})\frac{\langle n,\mathbf{k}|\left[\hat{\mathbf{q}}\boldsymbol{\mathcal{R}}, \hat{\mathbf{q}}_\mathbf{1}\hat{\mathbf{v}}^{\boldsymbol{\Sigma}}\right]|n',\mathbf{k}\rangle\langle n',\mathbf{k}|\hat{\mathbf{q}}_\mathbf{2}\hat{\mathbf{r}}|n,\mathbf{k}\rangle}{(E^\Sigma_{n\mathbf{k}} - E^\Sigma_{n'\mathbf{k}})^2(E^\Sigma_{n\mathbf{k}} - E^\Sigma_{n'\mathbf{k}} + \omega + i\eta)} \\ -\frac{8}{V}\sum_{nn'}\sum_{\mathbf{k}}^{BZ}(f_{n\mathbf{k}} - f_{n'\mathbf{k}})\frac{\langle n,\mathbf{k}|\hat{\mathbf{q}}\boldsymbol{\mathcal{R}}|n',\mathbf{k}\rangle\langle n',\mathbf{k}|\left[\hat{\mathbf{q}}_\mathbf{1}\hat{\mathbf{r}}, \hat{\mathbf{q}}_\mathbf{2}\hat{\mathbf{v}}^{\boldsymbol{\Sigma}}\right]|n,\mathbf{k}\rangle}{(E^\Sigma_{n\mathbf{k}} - E^\Sigma_{n'\mathbf{k}})^2(E^\Sigma_{n\mathbf{k}} - E^\Sigma_{n'\mathbf{k}} + 2\omega + i\eta)} + (\hat{\mathbf{q}}_\mathbf{1} \leftrightarrow \hat{\mathbf{q}}_\mathbf{2}).\end{aligned} \tag{E.9}$$

Notice here that all energies are scissored energies. This is due to the presence of the term $[\mathbf{r}, \hat{\mathbf{v}}^{\boldsymbol{\Sigma}}]$, which is not possible to neglect. This term must be worked out in order to obtain the commutator $[\mathbf{r}, \mathbf{v}]$ that we can neglect [117]. In order to do so, we use that (with $n' \notin \mathcal{D}_n$)

$$\frac{\partial \hat{v}^{\Sigma a}_{ij}}{\partial k^c} = -i[\hat{r}^c, \hat{v}^{\Sigma a}]_{ij} - i\sum_{l\notin\mathcal{D}_i,\mathcal{D}_j}\left[\hat{v}^{\Sigma a}_{il}\hat{r}^c_{lj} - \hat{r}^c_{il}v^{\Sigma a}_{lj}\right] - i\Delta^a_{ij}\hat{r}^c_{ij}, \tag{E.10a}$$

$$\frac{\partial \hat{v}^{a}_{ij}}{\partial k^c} = -i[\hat{r}^c, \hat{v}^{a}]_{ij} - i\sum_{l\notin\mathcal{D}_i,\mathcal{D}_j}\left[\hat{v}^{a}_{il}\hat{r}^c_{lj} - \hat{r}^c_{il}\hat{v}^{a}_{lj}\right] - i\Delta^a_{ij}\hat{r}^c_{ij}. \tag{E.10b}$$

From Eq. (E.10a) we directly obtain

$$\frac{[\hat{r}^c, \hat{v}^{\Sigma a}]_{nn'}}{(E^\Sigma_{nn'})} = i\frac{\partial \hat{v}^{\Sigma a}_{nn'}}{\partial k^c}\frac{1}{(E^\Sigma_{nn'})} - \sum_{l\notin\mathcal{D}_n,\mathcal{D}_{n'}}\frac{\left[\hat{v}^{\Sigma a}_{nl}\hat{r}^c_{ln'} - \hat{r}^c_{nl}\hat{v}^{\Sigma a}_{ln'}\right]}{(E^\Sigma_{nn'})} - \frac{\Delta^a_{nn'}\hat{r}^c_{nn'}}{(E^\Sigma_{nn'})}. \tag{E.11}$$

Combining this expression with Eq. (E.10b) gives the link between the two commutators

$$\begin{aligned}\frac{[\hat{r}^c, \hat{v}^{\Sigma a}]_{nn'}}{(E^\Sigma_{nn'})} = \frac{[\hat{r}^c, \hat{v}^{a}]_{nn'}}{E_{nn'}} + \sum_{l\notin\mathcal{D}_n,\mathcal{D}_{n'}}\frac{\left[\hat{v}^{a}_{nl}\hat{r}^b_{ln'} - \hat{r}^c_{nl}\hat{v}^{a}_{ln'}\right]}{E_{nn'}} + \frac{\Delta^a_{nn'}r^c_{nn'}}{E_{nn'}} + \frac{\Delta^c_{nn'}r^a_{nn'}}{E_{nn'}} \\ - \sum_{l\notin\mathcal{D}_n,\mathcal{D}_{n'}}\frac{\left[\hat{v}^{\Sigma a}_{nl}\hat{r}^c_{ln'} - \hat{r}^c_{nl}\hat{v}^{\Sigma a}_{ln'}\right]}{E^\Sigma_{nn'}} - \frac{\Delta^a_{nn'}r^c_{nn'}}{E^\Sigma_{nn'}} - \frac{\Delta^c_{nn'}r^a_{nn'}}{E^\Sigma_{nn'}}.\end{aligned}$$

We obtain the same relations by replacing $\hat{\mathbf{v}}$ with $\boldsymbol{\mathcal{V}}$ and $\hat{\mathbf{v}}^{\boldsymbol{\Sigma}}$ with $\boldsymbol{\mathcal{V}}^{\boldsymbol{\Sigma}}$.

$$\begin{aligned}\frac{[\hat{\mathbf{q}}_\mathbf{1}\hat{\mathbf{r}}, \hat{\mathbf{q}}_\mathbf{2}\hat{\mathbf{v}}^{\boldsymbol{\Sigma}}]_{n'n}}{(E^\Sigma_{n'n})} = \frac{[\hat{\mathbf{q}}_\mathbf{1}\hat{\mathbf{r}}, \hat{\mathbf{q}}_\mathbf{2}\hat{\mathbf{v}}]_{n'n}}{E_{n'n}} + \sum_{l\notin\mathcal{D}_n,\mathcal{D}_{n'}}\frac{\left[\hat{\mathbf{q}}_\mathbf{2}\hat{\mathbf{v}}_{n'l}\hat{\mathbf{q}}_\mathbf{1}\hat{\mathbf{r}}_{ln} - \hat{\mathbf{q}}_\mathbf{1}\hat{\mathbf{r}}_{n'l}\hat{\mathbf{q}}_\mathbf{2}\hat{\mathbf{v}}_{ln}\right]}{E_{n'n}} + \frac{\hat{\mathbf{q}}_\mathbf{1}\boldsymbol{\Delta}_{n'n}\hat{\mathbf{q}}_\mathbf{2}\hat{\mathbf{r}}_{n'n}}{E_{n'n}} + \frac{\hat{\mathbf{q}}_\mathbf{2}\boldsymbol{\Delta}_{n'n}\hat{\mathbf{q}}_\mathbf{1}\hat{\mathbf{r}}_{n'n}}{E_{n'n}} \\ - \sum_{l\notin\mathcal{D}_n,\mathcal{D}_{n'}}\frac{\left[\hat{\mathbf{q}}_\mathbf{2}\hat{\mathbf{v}}^{\boldsymbol{\Sigma}}_{n'l}\hat{\mathbf{q}}_\mathbf{1}\hat{\mathbf{r}}_{ln} - \hat{\mathbf{q}}_\mathbf{1}\hat{\mathbf{r}}_{n'l}\hat{\mathbf{q}}_\mathbf{2}\hat{\mathbf{v}}^{\boldsymbol{\Sigma}}_{ln}\right]}{E^\Sigma_{n'n}} - \frac{\hat{\mathbf{q}}_\mathbf{1}\boldsymbol{\Delta}_{n'n}\hat{\mathbf{q}}_\mathbf{2}\hat{\mathbf{r}}_{n'n}}{E^\Sigma_{n'n}} - \frac{\hat{\mathbf{q}}_\mathbf{2}\boldsymbol{\Delta}_{n'n}\hat{\mathbf{q}}_\mathbf{1}\hat{\mathbf{r}}_{n'n}}{E^\Sigma_{n'n}}\end{aligned} \tag{E.13a}$$

$$\begin{aligned}\frac{[\hat{\mathbf{q}}\boldsymbol{\mathcal{R}}, \hat{\mathbf{q}}_\mathbf{1}\hat{\mathbf{v}}^{\boldsymbol{\Sigma}}]_{nn'}}{(E^\Sigma_{nn'})} = \frac{[\hat{\mathbf{q}}\boldsymbol{\mathcal{R}}, \hat{\mathbf{q}}_\mathbf{1}\hat{\mathbf{v}}]_{nn'}}{E_{nn'}} + \sum_{l\notin\mathcal{D}_n,\mathcal{D}_{n'}}\frac{\left[\hat{\mathbf{q}}_\mathbf{1}\hat{\mathbf{v}}_{nl}\hat{\mathbf{q}}\boldsymbol{\mathcal{R}}_{ln'} - \hat{\mathbf{q}}\boldsymbol{\mathcal{R}}_{nl}\hat{\mathbf{q}}_\mathbf{1}\hat{\mathbf{v}}_{ln'}\right]}{E_{nn'}} + \frac{\hat{\mathbf{q}}_\mathbf{1}\boldsymbol{\Delta}_{nn'}\hat{\mathbf{q}}\boldsymbol{\mathcal{R}}_{nn'}}{E_{nn'}} + \frac{\hat{\mathbf{q}}\tilde{\boldsymbol{\Delta}}_{nn'}\hat{\mathbf{q}}_\mathbf{1}\hat{\mathbf{v}}_{nn'}}{E_{nn'}} \\ - \sum_{l\notin\mathcal{D}_n,\mathcal{D}_{n'}}\frac{\left[\hat{\mathbf{q}}_\mathbf{1}\hat{\mathbf{v}}^{\boldsymbol{\Sigma}}_{nl}\hat{\mathbf{q}}\boldsymbol{\mathcal{R}}_{ln'} - \hat{\mathbf{q}}\boldsymbol{\mathcal{R}}_{nl}\hat{\mathbf{q}}_\mathbf{1}\hat{\mathbf{v}}_{ln'}\right]}{E^\Sigma_{nn'}} - \frac{\hat{\mathbf{q}}_\mathbf{1}\boldsymbol{\Delta}_{nn'}\hat{\mathbf{q}}\boldsymbol{\mathcal{R}}_{nn'}}{E^\Sigma_{nn'}} - \frac{\hat{\mathbf{q}}\tilde{\boldsymbol{\Delta}}_{nn'}\hat{\mathbf{q}}_\mathbf{1}\mathbf{r}_{nn'}}{E^\Sigma_{nn'}}.\end{aligned} \tag{E.13b}$$

Let us define E and F such that

$$E = \frac{-2}{V}\sum_{nn'}\sum_{\mathbf{k}}^{BZ}(f_{n\mathbf{k}} - f_{n'\mathbf{k}})\frac{\langle n,\mathbf{k}|\left[\hat{\mathbf{q}}\boldsymbol{\mathcal{R}}, \hat{\mathbf{q}}_\mathbf{1}\hat{\mathbf{v}}^{\boldsymbol{\Sigma}}\right]|n',\mathbf{k}\rangle\langle n',\mathbf{k}|\hat{\mathbf{q}}_\mathbf{2}\hat{\mathbf{r}}|n,\mathbf{k}\rangle}{(E^{\Sigma}_{n\mathbf{k}} - E^{\Sigma}_{n'\mathbf{k}})^2(E^{\Sigma}_{n\mathbf{k}} - E^{\Sigma}_{n'\mathbf{k}} + \omega + i\eta)} + (\hat{\mathbf{q}}_\mathbf{1} \leftrightarrow \hat{\mathbf{q}}_\mathbf{2}), \tag{E.14a}$$

$$F = \frac{-8}{V}\sum_{nn'}\sum_{\mathbf{k}}^{BZ}(f_{n\mathbf{k}} - f_{n'\mathbf{k}})\frac{\langle n,\mathbf{k}|\hat{\mathbf{q}}\boldsymbol{\mathcal{R}}|n',\mathbf{k}\rangle\langle n',\mathbf{k}|\left[\hat{\mathbf{q}}_\mathbf{1}\hat{\mathbf{r}}, \hat{\mathbf{q}}_\mathbf{2}\hat{\mathbf{v}}^{\boldsymbol{\Sigma}}\right]|n,\mathbf{k}\rangle}{(E^{\Sigma}_{n\mathbf{k}} - E^{\Sigma}_{n'\mathbf{k}})^2(E^{\Sigma}_{n\mathbf{k}} - E^{\Sigma}_{n'\mathbf{k}} + 2\omega + i\eta)} + (\hat{\mathbf{q}}_\mathbf{1} \leftrightarrow \hat{\mathbf{q}}_\mathbf{2}). \tag{E.14b}$$

We insert Eq. (E.13a).

$$\begin{aligned}
E = \frac{-2}{V}\sum_{nn'}\sum_{\mathbf{k}}^{BZ}(f_{n\mathbf{k}} - f_{n'\mathbf{k}})\frac{\langle n,\mathbf{k}|[\hat{\mathbf{q}}\boldsymbol{\mathcal{R}}, \hat{\mathbf{q}}_\mathbf{1}\hat{\mathbf{v}}]|n',\mathbf{k}\rangle\langle n',\mathbf{k}|\hat{\mathbf{q}}_\mathbf{2}\hat{\mathbf{r}}|n,\mathbf{k}\rangle}{(E_{n\mathbf{k}} - E_{n'\mathbf{k}})(E^{\Sigma}_{n\mathbf{k}} - E^{\Sigma}_{n'\mathbf{k}})(E^{\Sigma}_{n\mathbf{k}} - E^{\Sigma}_{n'\mathbf{k}} + \omega + i\eta)} \\
-\frac{2}{V}\sum_{nn'}\sum_{l\notin\mathcal{D}_n,\mathcal{D}_{n'}}\sum_{\mathbf{k}}^{BZ}(f_{n\mathbf{k}} - f_{n'\mathbf{k}})\frac{\langle n,\mathbf{k}|\hat{\mathbf{q}}_\mathbf{1}\hat{\mathbf{v}}|l,\mathbf{k}\rangle\langle l,\mathbf{k}|\hat{\mathbf{q}}\boldsymbol{\mathcal{R}}|n',\mathbf{k}\rangle\langle n',\mathbf{k}|\hat{\mathbf{q}}_\mathbf{2}\hat{\mathbf{r}}|n,\mathbf{k}\rangle}{(E_{n\mathbf{k}} - E_{n'\mathbf{k}})(E^{\Sigma}_{n\mathbf{k}} - E^{\Sigma}_{n'\mathbf{k}})(E^{\Sigma}_{n\mathbf{k}} - E^{\Sigma}_{n'\mathbf{k}} + \omega + i\eta)} \\
+\frac{2}{V}\sum_{nn'}\sum_{l\notin\mathcal{D}_n,\mathcal{D}_{n'}}\sum_{\mathbf{k}}^{BZ}(f_{n\mathbf{k}} - f_{n'\mathbf{k}})\frac{\langle n,\mathbf{k}|\hat{\mathbf{q}}\boldsymbol{\mathcal{R}}|l,\mathbf{k}\rangle\langle l,\mathbf{k}|\hat{\mathbf{q}}_\mathbf{1}\hat{\mathbf{v}}|n',\mathbf{k}\rangle\langle n',\mathbf{k}|\hat{\mathbf{q}}_\mathbf{2}\hat{\mathbf{r}}|n,\mathbf{k}\rangle}{(E_{n\mathbf{k}} - E_{n'\mathbf{k}})(E^{\Sigma}_{n\mathbf{k}} - E^{\Sigma}_{n'\mathbf{k}})(E^{\Sigma}_{n\mathbf{k}} - E^{\Sigma}_{n'\mathbf{k}} + \omega + i\eta)} \\
-\frac{2}{V}\sum_{nn'}\sum_{\mathbf{k}}^{BZ}(f_{n\mathbf{k}} - f_{n'\mathbf{k}})\frac{\langle n,\mathbf{k}|\hat{\mathbf{q}}_\mathbf{1}\hat{\mathbf{r}}|n',\mathbf{k}\rangle\langle n',\mathbf{k}|\hat{\mathbf{q}}_\mathbf{2}\hat{\mathbf{r}}|n,\mathbf{k}\rangle\hat{\mathbf{q}}\tilde{\boldsymbol{\Delta}}_{nn'}}{(E_{n\mathbf{k}} - E_{n'\mathbf{k}})(E^{\Sigma}_{n\mathbf{k}} - E^{\Sigma}_{n'\mathbf{k}})(E^{\Sigma}_{n\mathbf{k}} - E^{\Sigma}_{n'\mathbf{k}} + \omega + i\eta)} \\
-\frac{2}{V}\sum_{nn'}\sum_{\mathbf{k}}^{BZ}(f_{n\mathbf{k}} - f_{n'\mathbf{k}})\frac{\langle n,\mathbf{k}|\hat{\mathbf{q}}\boldsymbol{\mathcal{R}}|n',\mathbf{k}\rangle\langle n',\mathbf{k}|\hat{\mathbf{q}}_\mathbf{2}\hat{\mathbf{r}}|n,\mathbf{k}\rangle\hat{\mathbf{q}}_\mathbf{1}\boldsymbol{\Delta}_{nn'}}{(E_{n\mathbf{k}} - E_{n'\mathbf{k}})(E^{\Sigma}_{n\mathbf{k}} - E^{\Sigma}_{n'\mathbf{k}})(E^{\Sigma}_{n\mathbf{k}} - E^{\Sigma}_{n'\mathbf{k}} + \omega + i\eta)} \\
+\frac{2}{V}\sum_{nn'}\sum_{l\notin\mathcal{D}_n,\mathcal{D}_{n'}}\sum_{\mathbf{k}}^{BZ}(f_{n\mathbf{k}} - f_{n'\mathbf{k}})\frac{\langle n,\mathbf{k}|\hat{\mathbf{q}}_\mathbf{1}\hat{\mathbf{v}}^{\boldsymbol{\Sigma}}|l,\mathbf{k}\rangle\langle l,\mathbf{k}|\hat{\mathbf{q}}\boldsymbol{\mathcal{R}}|n',\mathbf{k}\rangle\langle n',\mathbf{k}|\hat{\mathbf{q}}_\mathbf{2}\hat{\mathbf{r}}|n,\mathbf{k}\rangle}{(E^{\Sigma}_{n\mathbf{k}} - E^{\Sigma}_{n'\mathbf{k}})^2(E^{\Sigma}_{n\mathbf{k}} - E^{\Sigma}_{n'\mathbf{k}} + \omega + i\eta)} \\
-\frac{2}{V}\sum_{nn'}\sum_{l\notin\mathcal{D}_n,\mathcal{D}_{n'}}\sum_{\mathbf{k}}^{BZ}(f_{n\mathbf{k}} - f_{n'\mathbf{k}})\frac{\langle n,\mathbf{k}|\hat{\mathbf{q}}\boldsymbol{\mathcal{R}}|l,\mathbf{k}\rangle\langle l,\mathbf{k}|\hat{\mathbf{q}}_\mathbf{1}\hat{\mathbf{v}}^{\boldsymbol{\Sigma}}|n',\mathbf{k}\rangle\langle n',\mathbf{k}\hat{\mathbf{q}}_\mathbf{2}\hat{\mathbf{r}}|n,\mathbf{k}\rangle}{(E^{\Sigma}_{n\mathbf{k}} - E^{\Sigma}_{n'\mathbf{k}})^2(E^{\Sigma}_{n\mathbf{k}} - E^{\Sigma}_{n'\mathbf{k}} + \omega + i\eta)} \\
+\frac{2}{V}\sum_{nn'}\sum_{\mathbf{k}}^{BZ}(f_{n\mathbf{k}} - f_{n'\mathbf{k}})\frac{\langle n,\mathbf{k}|\hat{\mathbf{q}}_\mathbf{1}\hat{\mathbf{r}}|n',\mathbf{k}\rangle\langle n',\mathbf{k}|\hat{\mathbf{q}}_\mathbf{2}\hat{\mathbf{r}}|n,\mathbf{k}\rangle\hat{\mathbf{q}}\tilde{\boldsymbol{\Delta}}_{nn'}}{(E^{\Sigma}_{n\mathbf{k}} - E^{\Sigma}_{n'\mathbf{k}})^2(E^{\Sigma}_{n\mathbf{k}} - E^{\Sigma}_{n'\mathbf{k}} + \omega + i\eta)} \\
+\frac{2}{V}\sum_{nn'}\sum_{\mathbf{k}}^{BZ}(f_{n\mathbf{k}} - f_{n'\mathbf{k}})\frac{\langle n,\mathbf{k}|\hat{\mathbf{q}}\boldsymbol{\mathcal{R}}|n',\mathbf{k}\rangle\langle n',\mathbf{k}|\hat{\mathbf{q}}_\mathbf{2}\hat{\mathbf{r}}|n,\mathbf{k}\rangle\hat{\mathbf{q}}_\mathbf{1}\boldsymbol{\Delta}_{nn'}}{(E^{\Sigma}_{n\mathbf{k}} - E^{\Sigma}_{n'\mathbf{k}})^2(E^{\Sigma}_{n\mathbf{k}} - E^{\Sigma}_{n'\mathbf{k}} + \omega + i\eta)} \\
+(\hat{\mathbf{q}}_\mathbf{1} \leftrightarrow \hat{\mathbf{q}}_\mathbf{2}).
\end{aligned} \tag{E.15}$$

We note that due to the occupation numbers and the restriction of the sum over n'', we have directly $n \notin \mathcal{D}_{n'}, \mathcal{D}_{n''}$, $n' \notin \mathcal{D}_n, \mathcal{D}_{n''}$ and $n'' \notin \mathcal{D}_n, \mathcal{D}_{n'}$. We can safely define matrix elements of the position operator for these sums. For conciseness, we introduce the notation $\sum_{nn'}\sum_{n''\notin\mathcal{D}_n,\mathcal{D}_{n'}} \rightarrow \sum'_{nn'n''}$, first introduced by Bechstedt and co-workers in Ref. [189]. By symmetrisation and using the time-reversal symmetry, we obtain a simpler expression for E, and similarly, for F. We can redefine the two-band and three-band terms, to accounts for these new terms. Two contributions are obtained for the two-band part, one local and denoted χ_l^{2bnd} that is non-zero even is the potential is local, and a

nonlocal part χ_{nl}^{2bnd} that vanishes in the case of a local potential.

$$\chi_{l}^{2bnd}(\hat{\mathbf{q}},\hat{\mathbf{q}}_{\mathbf{1}},\hat{\mathbf{q}}_{\mathbf{2}},\omega)=\frac{-2}{V}\sum_{n\neq n'}\sum_{\mathbf{k}}^{BZ}(f_{n\mathbf{k}}-f_{n'\mathbf{k}})\frac{\langle n,\mathbf{k}|\hat{\mathbf{q}}\boldsymbol{\mathcal{R}}|n',\mathbf{k}\rangle\langle n',\mathbf{k}|\hat{\mathbf{q}}_{\mathbf{1}}\hat{\mathbf{r}}|n,\mathbf{k}\rangle\hat{\mathbf{q}}_{\mathbf{2}}\boldsymbol{\Delta}_{n'n}}{(E^{\Sigma}_{n\mathbf{k}}-E^{\Sigma}_{n'\mathbf{k}})^2}$$
$$\left\{\frac{((E_{n\mathbf{k}}-E_{n'\mathbf{k}})+(E^{\Sigma}_{n\mathbf{k}}-E^{\Sigma}_{n'\mathbf{k}}))}{(E_{n\mathbf{k}}-E_{n'\mathbf{k}})}\frac{8}{(E^{\Sigma}_{n\mathbf{k}}-E^{\Sigma}_{n'\mathbf{k}}+2\omega+2i\eta)}\right.$$
$$\left.+\frac{2(E_{n\mathbf{k}}-E_{n'\mathbf{k}})-(E^{\Sigma}_{n\mathbf{k}}-E^{\Sigma}_{n'\mathbf{k}})}{(E_{n\mathbf{k}}-E_{n'\mathbf{k}})}\frac{1}{(E^{\Sigma}_{n\mathbf{k}}-E^{\Sigma}_{n'\mathbf{k}}+\omega+i\eta)}\right\}+(\hat{\mathbf{q}}_{\mathbf{1}}\leftrightarrow\hat{\mathbf{q}}_{\mathbf{2}}) \tag{E.16a}$$

$$\chi_{nl}^{2bnd}(\hat{\mathbf{q}},\hat{\mathbf{q}}_{\mathbf{1}},\hat{\mathbf{q}}_{\mathbf{2}},\omega)=\frac{-2}{V}\sum_{nn'}\sum_{\mathbf{k}}^{BZ}(f_{n\mathbf{k}}-f_{n'\mathbf{k}})\left\{\frac{\langle n,\mathbf{k}|[\hat{\mathbf{q}}\boldsymbol{\mathcal{R}},\hat{\mathbf{q}}_{\mathbf{1}}\hat{\mathbf{v}}]|n',\mathbf{k}\rangle\langle n',\mathbf{k}|\hat{\mathbf{q}}_{\mathbf{2}}\hat{\mathbf{r}}|n,\mathbf{k}\rangle}{(E_{n\mathbf{k}}-E_{n'\mathbf{k}})(E^{\Sigma}_{n\mathbf{k}}-E^{\Sigma}_{n'\mathbf{k}})(E^{\Sigma}_{n\mathbf{k}}-E^{\Sigma}_{n'\mathbf{k}}+\omega+i\eta)}\right.$$
$$\left.+\frac{4\langle n,\mathbf{k}|\hat{\mathbf{q}}\boldsymbol{\mathcal{R}}|n',\mathbf{k}\rangle\langle n,\mathbf{k}|[\hat{\mathbf{q}}_{\mathbf{1}}\hat{\mathbf{r}},\hat{\mathbf{q}}_{\mathbf{2}}\hat{\mathbf{v}}]|n',\mathbf{k}\rangle}{(E_{n\mathbf{k}}-E_{n'\mathbf{k}})(E^{\Sigma}_{n\mathbf{k}}-E^{\Sigma}_{n'\mathbf{k}})(E^{\Sigma}_{n\mathbf{k}}-E^{\Sigma}_{n'\mathbf{k}}+2\omega+i\eta)}\right\}+(\hat{\mathbf{q}}_{\mathbf{1}}\leftrightarrow\hat{\mathbf{q}}_{\mathbf{2}}) \tag{E.16b}$$

The new three-band contributions are included in the definition of the χ_I^{3bnd}, which now reads as

$$\begin{aligned}\chi_{I}^{3bnd}(\hat{\mathbf{q}},\hat{\mathbf{q}}_{\mathbf{1}},\hat{\mathbf{q}}_{\mathbf{2}},\omega)=\frac{2i}{V}\sum_{n\neq n'\neq n''}\sum_{\mathbf{k}}^{BZ}&\langle n,\mathbf{k}|\hat{\mathbf{q}}\boldsymbol{\mathcal{R}}|n',\mathbf{k}\rangle\langle n',\mathbf{k}|\hat{\mathbf{q}}_{\mathbf{1}}\hat{\mathbf{r}}|n'',\mathbf{k}\rangle\langle n'',\mathbf{k}|\hat{\mathbf{q}}_{\mathbf{2}}\hat{\mathbf{r}}|n,\mathbf{k}\rangle\\
&\left\{\frac{(E_{n\mathbf{k}}+E_{n'\mathbf{k}}-2E_{n''\mathbf{k}})}{(E_{n\mathbf{k}}-E_{n'\mathbf{k}})}\frac{4(f_{n\mathbf{k}}-f_{n'\mathbf{k}})}{(E^{\Sigma}_{n\mathbf{k}}-E^{\Sigma}_{n'\mathbf{k}})(E^{\Sigma}_{n\mathbf{k}}-E^{\Sigma}_{n'\mathbf{k}}+2\omega+i\eta)}\right.\\
&-\frac{(2E_{n\mathbf{k}}-E_{n'\mathbf{k}}-E_{n''\mathbf{k}})}{(E_{n''\mathbf{k}}-E_{n\mathbf{k}})}\frac{(f_{n\mathbf{k}}-f_{n''\mathbf{k}})}{(E^{\Sigma}_{n''\mathbf{k}}-E^{\Sigma}_{n\mathbf{k}})(E^{\Sigma}_{n\mathbf{k}}-E^{\Sigma}_{n''\mathbf{k}}+\omega+i\eta)}\\
&\left.+\frac{(2E_{n'\mathbf{k}}-E_{n\mathbf{k}}-E_{n''\mathbf{k}})}{(E_{n'\mathbf{k}}-E_{n''\mathbf{k}})}\frac{(f_{n'\mathbf{k}}-f_{n''\mathbf{k}})}{(E^{\Sigma}_{n'\mathbf{k}}-E^{\Sigma}_{n''\mathbf{k}})(E^{\Sigma}_{n''\mathbf{k}}-E^{\Sigma}_{n'\mathbf{k}}+\omega+i\eta)}\right\}\\
&+(\hat{\mathbf{q}}_{\mathbf{1}}\leftrightarrow\hat{\mathbf{q}}_{\mathbf{2}})\end{aligned} \tag{E.17}$$

F. Macroscopic surface response functions

F.1 Charge conservation and cut-function

We consider the following replacement for the current and for the density $\rho^{(1)}(\mathbf{r},\omega) \to \rho^{(1)S}(\mathbf{r},\omega) = \mathcal{C}(z)\rho^{(1)}(\mathbf{r},\omega)$ and $\mathbf{j}^{(1)}_{\text{ind}}(\mathbf{r},\omega) \to \mathbf{j}^{(1)S}_{\text{ind}}(\mathbf{r},\omega) = \mathcal{C}(z)\mathbf{j}^{(1)}_{\text{ind}}(\mathbf{r},\omega)$ where $\mathcal{C}(z)$ is a cut function introduced here, in order to select the response from a part of the system.
Using vector calculus relations, one can write that

$$\nabla.\left(\mathbf{j}^{S}_{\text{ind}}(\mathbf{r},\omega)\right) = \mathcal{C}(z)\nabla.\left(\mathbf{j}_{\text{ind}}(\mathbf{r},\omega)\right) + \mathbf{grad}\mathcal{C}(z).\mathbf{j}_{\text{ind}}(\mathbf{r},\omega). \tag{F.1}$$

Inserting the continuity relation yields

$$\nabla.\left(\mathbf{j}^{S}_{\text{ind}}(\mathbf{r},\omega)\right) = \omega\rho^{S}(\mathbf{r},\omega) + \mathbf{grad}\mathcal{C}(z).\mathbf{j}_{\text{ind}}(\mathbf{r},\omega). \tag{F.2}$$

Here we choose to assume two approximations:
Approximation 1: The system is invariant under the permutation $z \leftrightarrow -z$.
Approximation 2: The function $\mathcal{C}(z)$ is a step function.

Using Approximation 2, one finds that

$$\mathbf{grad}\mathcal{C}(z).\mathbf{j}_{\text{ind}}(\mathbf{r},\omega) = \hat{\mathbf{e}}_z.\mathbf{j}_{\text{ind}}(\mathbf{r},\omega)\delta(z) = \hat{\mathbf{e}}_z.\mathbf{j}_{\text{ind}}(x,y,z=0,\omega). \tag{F.3}$$

Due to Approximation 1, the plan $z = 0$ is a mirror plan of the system, imposing that $\mathbf{j}_{\text{ind}}$ is contained in the plan [x,y]. Thereby it results that

$$\mathbf{k}.\mathbf{j}^{S}_{\text{ind}}(\mathbf{k},\omega) = \omega\rho^{S}_{\text{ind}}(\mathbf{k},\omega). \tag{F.4}$$

Physically, this result shows that the charge is conserved in each half of the system separately.
Replacing the current and the density by their expressions in terms of response functions [44], we obtain at first order and second-order

$$\omega^2\chi^{S}_{\rho\rho}(\mathbf{k},\mathbf{k}',\omega) = \mathbf{k}.\,\chi^{S}_{\mathbf{jj}}(\mathbf{k},\mathbf{k}',\omega).\,\mathbf{k}' - \langle\rho^{S}\rangle\delta(\mathbf{k}-\mathbf{k}')k^2, \tag{F.5a}$$

$$\omega^3\chi^{S}_{\rho\rho\rho}(\mathbf{k},\mathbf{k}',\mathbf{k}'',\omega) = \mathbf{k}.\,\chi^{S}_{\mathbf{jjj}}(\mathbf{k},\mathbf{k}',\mathbf{k}'',\omega)\colon\mathbf{k}'.\,\mathbf{k}''. \tag{F.5b}$$

Note that if the slab and the cut-function $\mathcal{C}(z)$ are equally shifted by z_0, the same result is obtained.

F.2 Response function to the total macroscopic classical potential at second-order

Let us define the total macroscopic classical potential, as

$$\hat{V}_{\text{mac}}[\rho(\mathbf{1})](\mathbf{1}) = \hat{V}_{\text{ext}}(\mathbf{1}) + \int d^3\mathbf{2}v_{\mathbf{0}}(\mathbf{1}-\mathbf{2})\rho(\mathbf{2}). \tag{F.6}$$

where $v_{\mathbf{0}}$ is the long-range part of the Coulomb potential.
The density of the system reads as

$$\rho(\mathbf{1}) = \rho^{(0)}(\mathbf{1}) + \rho^{(1)}_{\text{ind}}(\mathbf{1}) + \rho^{(2)}_{\text{ind}}(\mathbf{1}), \tag{F.7}$$

where $\rho^{(0)}(\mathbf{1})$ is the unperturbed density. Inserting this expression in Eq. (F.6), yields

$$\hat{V}_{\text{mac}}[\rho(\mathbf{1})](\mathbf{1}) = \hat{V}^{(0)}_{\text{mac}}(\mathbf{1}) + \hat{V}^{(1)}_{\text{mac}}(\mathbf{1}) + \hat{V}^{(2)}_{\text{mac}}(\mathbf{1}), \tag{F.8}$$

where

$$\hat{V}^{(0)}_{\text{mac}}(\mathbf{1}) = \int d^3\mathbf{2} v_{\mathbf{0}}(\mathbf{1}-\mathbf{2})\rho^{(0)}(\mathbf{2}) \tag{F.9a}$$

$$\hat{V}^{(1)}_{\text{mac}}(\mathbf{1}) = \hat{V}^{(1)}_{\text{ext}}(\mathbf{1}) + \int d^3\mathbf{2} v_{\mathbf{0}}(\mathbf{1}-\mathbf{2})\rho^{(1)}_{\text{ind}}(\mathbf{2}) \tag{F.9b}$$

$$\hat{V}^{(2)}_{\text{mac}}(\mathbf{1}) = \hat{V}^{(2)}_{\text{ext}}(\mathbf{1}) + \int d^3\mathbf{2} v_{\mathbf{0}}(\mathbf{1}-\mathbf{2})\rho^{(2)}_{\text{ind}}(\mathbf{2}) \tag{F.9c}$$

I now define the response function to that total macroscopic classical potential, using the short notation of Chap. 3,

$$\rho^{(2)}_{\text{ind}}(\mathbf{1}) = \int d\mathbf{2} \int d\mathbf{3} \bar{\chi}_{\rho\rho\rho}(\mathbf{1},\mathbf{2},\mathbf{3})\hat{V}^{(1)}_{\text{mac}}(\mathbf{2})\hat{V}^{(1)}_{\text{mac}}(\mathbf{3}) + \int d\mathbf{2} \bar{\chi}_{\rho\rho}(\mathbf{1},\mathbf{2})\hat{V}^{(2)}_{\text{mac}}(\mathbf{2}). \tag{F.10}$$

From this definition and the definition of the independent-particle response function and the fully-interaction response functions Eq. (3.36) (see Chap. 3), we obtain the two equations

$$\begin{aligned}\chi^{(2)}_{\rho\rho\rho}(\mathbf{1},\mathbf{2},\mathbf{3}) = \int d\mathbf{4} d\mathbf{5} \bar{\chi}_{\rho\rho\rho}(\mathbf{1},\mathbf{4},\mathbf{5}) \Big[\delta(\mathbf{4}-\mathbf{2}) + \int d\mathbf{6} v_{\mathbf{0}}(\mathbf{4}-\mathbf{6})\chi^{(1)}_{\rho\rho}(\mathbf{6},\mathbf{2})\Big] \\ \times \Big[\delta(\mathbf{5}-\mathbf{3}) + \int d\mathbf{7} v_{\mathbf{0}}(\mathbf{5}-\mathbf{7})\chi^{(1)}_{\rho\rho}(\mathbf{7},\mathbf{3})\Big] \\ + \int d\mathbf{4} \int d\mathbf{5} \bar{\chi}_{\rho\rho}(\mathbf{1},\mathbf{4}) v_{\mathbf{0}}(\mathbf{4}-\mathbf{5})\chi^{(2)}_{\rho\rho\rho}(\mathbf{5},\mathbf{2},\mathbf{3}) \end{aligned} \tag{F.11a}$$

$$\begin{aligned}\bar{\chi}_{\rho\rho\rho}(\mathbf{1},\mathbf{2},\mathbf{3}) = \int d\mathbf{4} \int d\mathbf{5} \chi^{(0)}_{\rho\rho\rho}(\mathbf{1},\mathbf{4},\mathbf{5}) \Big[\delta(\mathbf{4}-\mathbf{2}) + \int d\mathbf{6} \Big(\bar{v}(\mathbf{4}-\mathbf{6}) + f_{\text{xc}}(\mathbf{4},\mathbf{6})\Big)\bar{\chi}_{\rho\rho}(\mathbf{6},\mathbf{2})\Big] \\ \times \Big[\delta(\mathbf{5}-\mathbf{3}) + \int d\mathbf{7} \Big(\bar{v}(\mathbf{5}-\mathbf{7}) + f_{\text{xc}}(\mathbf{5},\mathbf{7})\Big)\bar{\chi}_{\rho\rho}(\mathbf{7},\mathbf{3})\Big] \\ + \int d\mathbf{4} \int d\mathbf{5} \chi^{(0)}_{\rho\rho}(\mathbf{1},\mathbf{4}) \Big(\bar{v}(\mathbf{4}-\mathbf{5}) + f_{\text{xc}}(\mathbf{4},\mathbf{5})\Big)\bar{\chi}_{\rho\rho\rho}(\mathbf{5},\mathbf{2},\mathbf{3}) \\ + \int d\mathbf{4} \int d\mathbf{5} \int d\mathbf{6} \chi^{(0)}_{\rho\rho}(\mathbf{1},\mathbf{4}) g_{\text{xc}}(\mathbf{4},\mathbf{5},\mathbf{6})\bar{\chi}_{\rho\rho}(\mathbf{5},\mathbf{2})\bar{\chi}_{\rho\rho}(\mathbf{6},\mathbf{3}) \end{aligned} \tag{F.11b}$$

where $\bar{v}$ is the Coulomb potential without its long-range part. For obtaining the second relation, I used that

$$\hat{V}^{(1)}_{\text{eff}}(\mathbf{1}) = \hat{V}^{(1)}_{\text{mac}}(\mathbf{1}) + \hat{V}^{(1)}_{\text{xc}}(\mathbf{1}) + \int d^3\mathbf{2} \bar{v}(\mathbf{1}-\mathbf{2})\rho^{(1)}_{\text{ind}}(\mathbf{2}) \tag{F.12a}$$

$$\hat{V}^{(2)}_{\text{eff}}(\mathbf{1}) = \hat{V}^{(2)}_{\text{mac}}(\mathbf{1}) + \hat{V}^{(2)}_{\text{xc}}(\mathbf{1}) + \int d^3\mathbf{2} \bar{v}(\mathbf{1}-\mathbf{2})\rho^{(2)}_{\text{ind}}(\mathbf{2}) \tag{F.12b}$$

G. Analytical expression of $\tilde{v}_{\mathbf{G_1},\mathbf{G_2}}(\mathbf{q})$

In this appendix, I report the derivation of the analytical expression of the modified Coulomb potential. The modified Coulomb potential is defined by, (see Chap. 8)

$$\tilde{v}_{\tilde{\mathbf{G}}_\mathbf{1},\tilde{\mathbf{G}}_\mathbf{2}}(\mathbf{q}) = \frac{1}{L_z^{\text{mat}}}\int_{-L_z}^{0} dz_1 dz_2 e^{-i(q_z+\tilde{G}_{z1})z_1} 2\pi \frac{e^{-|\mathbf{q}_{||}+\mathbf{G}_{\mathbf{1}||}||z_1-z_2|}}{|\mathbf{q}_{||}+\mathbf{G}_{\mathbf{1}||}|} e^{i(q_z+\tilde{G}_{z2})z_2}\delta_{\mathbf{G}_{\mathbf{1}||},\mathbf{G}_{\mathbf{2}||}}. \tag{G.1a}$$

Let us first define some notations, in order to ease the derivation

$$k_{z1} = q_z + \tilde{G}_{z1}, \quad k_{z2} = q_z + \tilde{G}_{z2}, \quad k_{||} = |\mathbf{q}_{||} + \mathbf{G}_{\mathbf{1}||}|, \quad R = L_z^{\text{mat}}.$$

Using these notations, we obtain that

$$\tilde{v}_{\tilde{\mathbf{G}}_\mathbf{1},\tilde{\mathbf{G}}_\mathbf{2}}(\mathbf{q}) = \frac{2\pi}{Rk_{||}}\int_{-R}^{0} dz_1 e^{-ik_{z1}z_1}\left[e^{-k_{||}z_1}\int_{-R}^{z_1} dz_2 e^{(ik_{z2}+k_{||})z_2} + e^{k_{||}z_1}\int_{z_1}^{0} dz_2 e^{(ik_{z2}-k_{||})z_2}\right]\delta_{\mathbf{G}_{\mathbf{1}||},\mathbf{G}_{\mathbf{2}||}} \tag{G.2a}$$

After some tedious algebra, we obtain the expression of the modified Coulomb potential

$$\begin{aligned}\tilde{v}_{\tilde{\mathbf{G}}_\mathbf{1},\tilde{\mathbf{G}}_\mathbf{2}}(\mathbf{q}) = {} & 2\pi e^{i(k_{z1}-k_{z2})R}\left[\frac{sinc([k_{z1}-k_{z2}]R)}{(k_{z2}^2+k_{||}^2)} + \frac{sinc([k_{z1}-k_{z2}]R)}{(k_{z1}^2+k_{||}^2)}\right]\delta_{\mathbf{G}_{\mathbf{1}||},\mathbf{G}_{\mathbf{2}||}} \\ & + \frac{2\pi e^{i(k_{z1}-k_{z2})R}}{Rk_{||}(k_{z2}^2+k_{||}^2)(k_{z1}^2+k_{||}^2)}\Bigg[-\cos([k_{z1}-k_{z2}]R)(k_{||}^2-k_{z1}k_{z2}) \\ & + e^{-2k_{||}R}\Big((k_{||}^2-k_{z1}k_{z2})\cos([k_{z1}+k_{z2}]R) - k_{||}(k_{z1}+k_{z2})\sin([k_{z1}+k_{z2}]R)\Big)\Bigg]\delta_{\mathbf{G}_{\mathbf{1}||},\mathbf{G}_{\mathbf{2}||}}.\end{aligned} \tag{G.3a}$$

It is possible to simplify further this expression, using that $\tilde{G}_{z1} = n_1\frac{2\pi}{L_z^{\text{mat}}}$ and $\tilde{G}_{z2} = n_2\frac{2\pi}{L_z^{\text{mat}}}$, $n_1, n_2 \in \mathbf{Z}$. We have

$$\text{sinc}([k_{z2}-k_{z1}]\frac{R}{2}) = \text{sinc}([n_2-n_1]\pi) = \delta_{k_{z1},k_{z2}},$$

where sinc is defined as $\text{sinc}(x) = \frac{\sin(x)}{x}$. Similarly, we obtain that

$$\cos([k_{z1}-k_{z2}]\frac{R}{2}) = \cos([G_{z2}-G_{z1}]L_z^{\text{mat}}/2) = (-1)^{n_1-n_2} = (-1)^{\frac{R(k_{z1}-k_{z2})}{\pi}}.$$

Without any approximation, we obtain that

$$\begin{aligned}\cos([k_{z1}+k_{z2}]\frac{R}{2}) &= cos(q_zR)(-1)^{\frac{R(k_{z1}+k_{z2})}{\pi}}, \\ \sin([k_{z2}+k_{z1}]\frac{R}{2}) &= sin(q_zR)(-1)^{\frac{R(k_{z1}+k_{z2})}{\pi}}.\end{aligned}$$

Putting everything together, we obtain that

$$\begin{aligned}\tilde{v}_{\tilde{\mathbf{G}}_1,\tilde{\mathbf{G}}_2}(\mathbf{q}) = &\frac{4\pi}{|\mathbf{q}+\tilde{\mathbf{G}}_1|^2}\delta_{\tilde{\mathbf{G}}_1,\tilde{\mathbf{G}}_2} \\ &+ \frac{4\pi\delta_{\mathbf{G}_{1||},\mathbf{G}_{2||}}}{|\mathbf{q}+\tilde{\mathbf{G}}_1|^2|\mathbf{q}+\tilde{\mathbf{G}}_2|^2}\Bigg[-\frac{e^{-|\mathbf{q}_{||}+\mathbf{G}_{1||}|L_z^{\text{mat}}}\sin(q_zR)}{L_z^{\text{mat}}}(2q_z+\tilde{G}_{z1}+\tilde{G}_{z2})\Big) \\ &+ \frac{e^{-|\mathbf{q}_{||}+\mathbf{G}_{1||}|L_z^{\text{mat}}}\cos(q_zR)-1}{L_z^{\text{mat}}|\mathbf{q}_{||}+\mathbf{G}_{1||}|}\Big(|\mathbf{q}_{||}+\mathbf{G}_{1||}|^2-(q_z+\tilde{G}_{z1})(q_z+\tilde{G}_{z2})\Big)\Bigg].\end{aligned}$$

From that expression, we can easily show that, for $R\to\infty$,

$$\tilde{v}_{\tilde{\mathbf{G}}_1,\tilde{\mathbf{G}}_2}(\mathbf{q}) = \frac{4\pi}{|\mathbf{q}+\tilde{\mathbf{G}}_1|^2}\delta_{\tilde{\mathbf{G}}_1,\tilde{\mathbf{G}}_2} = v_{\tilde{\mathbf{G}}_1}(\mathbf{q})\delta_{\tilde{\mathbf{G}}_1,\tilde{\mathbf{G}}_2}. \tag{G.5}$$

H. Mixed-space equations for SHG

Here I show that the mixed-space analytical results of Chap. 8 are also valid for the nonlinear second-order optical properties.

H.1 Second-order dyson equation in the mixed-space

The second-order Dyson equation in real-space and real-time is given by Eq. (3.37). In frequency space, the second-order Dyson equation is

$$\begin{aligned}
\chi^{(2)}_{\rho\rho\rho}(\mathbf{r},\mathbf{r}',\mathbf{r}'',\omega_1,\omega_2) &= \int d\mathbf{r_4} d\mathbf{r_5} \chi^{(2)}_0(\mathbf{r},\mathbf{r_4},\mathbf{r_5},\omega_1,\omega_2) \\
&\times \Big[\delta(\mathbf{r_4}-\mathbf{r}') + \int d\mathbf{r_6} f_{uxc}(\mathbf{r_4},\mathbf{r_6},\omega_1)\chi^{(1)}_{\rho\rho}(\mathbf{r_6}\mathbf{r}',\omega_1)\Big] \\
&\times \Big[\delta(\mathbf{r_5}-\mathbf{r}'') + \int d\mathbf{r_7} f_{uxc}(\mathbf{r_5},\mathbf{r_7},\omega_2)\chi^{(1)}_{\rho\rho}(\mathbf{r_7},\mathbf{r}'',\omega_2)\Big] \\
+ \int d\mathbf{r_4} d\mathbf{r_5} d\mathbf{r_6} \chi^{(1)}_0(\mathbf{r},\mathbf{r_4},\omega_1+\omega_2) g_{xc}(\mathbf{r_4},\mathbf{r_5},\mathbf{r_6},\omega_1,\omega_2)\chi^{(1)}_{\rho\rho}(\mathbf{r_5},\mathbf{r}',\omega_1)\chi^{(1)}_{\rho\rho}(\mathbf{r_6},\mathbf{r}'',\omega_2) \\
+ \int d\mathbf{r_4} d\mathbf{r_5} \chi^{(1)}_0(\mathbf{r},\mathbf{r_4},\omega_1+\omega_2) f_{uxc}(\mathbf{r_4},\mathbf{r_5},\omega_1+\omega_2)\chi^{(2)}_{\rho\rho\rho}(\mathbf{r_5},\mathbf{r}',\mathbf{r}'',\omega_1,\omega_2).
\end{aligned} \tag{H.1}$$

For conciseness, we omit the frequency dependence. Using the definition of Fourier transform (see App. A),we obtain that

$$\begin{aligned}
\chi^{(2)}_{\mathbf{G}_{||},\mathbf{G}'_{||},\mathbf{G}''_{||}}(\mathbf{q}_{||},z,z',z'') &= \sum_{\mathbf{G_4}_{||}\mathbf{G_5}_{||}} \int dz_4 dz_5 \chi^{(2)}_{0,\mathbf{G}_{||}\mathbf{G_4}_{||}\mathbf{G_5}_{||}}(\mathbf{q}_{||},z,z_4,z_5) \\
&\times \Big[\delta(z_4-z')\delta_{\mathbf{G_4}_{||}\mathbf{G}'_{||}} + \sum_{\mathbf{G_6}_{||}} \int dz_6 f_{uxc,\mathbf{G_4}_{||}\mathbf{G_6}_{||}}(\mathbf{q}_{||},z_4,z_6)\chi^{(1)}_{\mathbf{G_6}_{||}\mathbf{G}'_{||}}(\mathbf{q}_{||},z_6,z')\Big] \\
&\times \Big[\delta(z_5-z'')\delta_{\mathbf{G_5}_{||}\mathbf{G}''_{||}} + \sum_{\mathbf{G_7}_{||}} \int dz_7 f_{uxc,\mathbf{G_5}_{||}\mathbf{G_7}_{||}}(\mathbf{q}_{||},z_5,z_7)\chi^{(1)}_{\mathbf{G_7}_{||}\mathbf{G}''_{||}}(\mathbf{q}_{||},z_7,z'')\Big] \\
&+ \sum_{\mathbf{G_4}_{||}\mathbf{G_5}_{||}\mathbf{G_6}_{||}} \int dz_4 dz_5 dz_6 \chi^{(1)}_{0,\mathbf{G}_{||}\mathbf{G_4}_{||}}(\mathbf{q}_{||},z,z_4) g_{xc,\mathbf{G_4}_{||}\mathbf{G_5}_{||}\mathbf{G_6}_{||}}(\mathbf{r_4},\mathbf{r_5},\mathbf{r_6}) \\
&\times \chi^{(1)}_{\mathbf{G_5}_{||}\mathbf{G}'_{||}}(\mathbf{q}_{||},z_5,z')\chi^{(1)}_{\mathbf{G_6}_{||}\mathbf{G}''_{||}}(\mathbf{q}_{||},z_6,z'') \\
+ \sum_{\mathbf{G_4}_{||}\mathbf{G_5}_{||}} \int dz_4 dz_5 \chi^{(1)}_{0,\mathbf{G}_{||}\mathbf{G_4}_{||}}(\mathbf{q}_{||},z,z_4) f_{uxc,\mathbf{G_4}_{||}\mathbf{G_5}_{||}}(\mathbf{q}_{||},z_4,z_5)\chi^{(2)}_{\mathbf{G_5}_{||},\mathbf{G}'_{||}\mathbf{G}''_{||}}(\mathbf{q}_{||},z_5,z',z'').
\end{aligned} \tag{H.2}$$

Assuming the random-phase approximation, we get

$$\begin{aligned}\chi^{(2)}_{\mathbf{G}_{||},\mathbf{G'}_{||},\mathbf{G''}_{||}}(\mathbf{q}_{||},z,z',z'') = \sum_{\mathbf{G_4}_{||}\mathbf{G_5}_{||}} \int dz_4 dz_5 \chi^{(2)}_{0,\mathbf{G}_{||}\mathbf{G_4}_{||}\mathbf{G_5}_{||}}(\mathbf{q}_{||},z,z_4,z_5) \\ \times\Big[\delta(z_4-z')\delta_{\mathbf{G_4}_{||}\mathbf{G'}_{||}} + \int dz_6 v_{\mathbf{G_4}_{||}}(\mathbf{q}_{||},z_4,z_6)\chi^{(1)}_{\mathbf{G_4}_{||}\mathbf{G'}_{||}}(\mathbf{q}_{||},z_6,z')\Big] \\ \times\Big[\delta(z_5-z'')\delta_{\mathbf{G_5}_{||}\mathbf{G''}_{||}} + \int dz_7 v_{\mathbf{G_5}_{||}}(\mathbf{q}_{||},z_5,z_7)\chi^{(1)}_{\mathbf{G_5}_{||}\mathbf{G''}_{||}}(\mathbf{q}_{||},z_7,z'')\Big] \\ + \sum_{\mathbf{G_4}_{||}} \int dz_4 dz_5 \chi^{(1)}_{0,\mathbf{G}_{||}\mathbf{G_4}_{||}}(\mathbf{q}_{||},z,z_4) v_{\mathbf{G_4}_{||}}(\mathbf{q}_{||},z_4,z_5)\chi^{(2)}_{\mathbf{G_4}_{||},\mathbf{G'}_{||}\mathbf{G''}_{||}}(\mathbf{q}_{||},z_5,z',z'').\end{aligned} \tag{H.3}$$

H.2 Isolated system from periodic super-cell calculations

We now define the auxiliary response functions $\tilde{\chi}^{(1)}$, $\tilde{\chi}^{(1)}_0$, $\tilde{\chi}^{(2)}$, and $\tilde{\chi}^{(2)}_0$, similarly to what is done in Chap. 8. We obtain that

$$\begin{aligned}\tilde{\chi}^{(2)}_{\mathbf{G}_{||},\mathbf{G'}_{||},\mathbf{G''}_{||}}(\mathbf{q}_{||},z,z',z'') = \sum_{\mathbf{G_4}_{||}\mathbf{G_5}_{||}} \int_{-L_z^{\mathrm{mat}}}^{0} dz_4 dz_5 \tilde{\chi}^{(2)}_{0,\mathbf{G}_{||}\mathbf{G_4}_{||}\mathbf{G_5}_{||}}(\mathbf{q}_{||},z,z_4,z_5) \\ \times\Big[\delta(z_4-z')\delta_{\mathbf{G_4}_{||}\mathbf{G'}_{||}} + \int_{-L_z^{\mathrm{mat}}}^{0} dz_6 v_{\mathbf{G_4}_{||}}(\mathbf{q}_{||},z_4,z_6)\tilde{\chi}^{(1)}_{\mathbf{G_4}_{||}\mathbf{G'}_{||}}(\mathbf{q}_{||},z_6,z')\Big] \\ \times\Big[\delta(z_5-z'')\delta_{\mathbf{G_5}_{||}\mathbf{G''}_{||}} + \int_{-L_z^{\mathrm{mat}}}^{0} dz_7 v_{\mathbf{G_5}_{||}}(\mathbf{q}_{||},z_5,z_7)\tilde{\chi}^{(1)}_{\mathbf{G_5}_{||}\mathbf{G''}_{||}}(\mathbf{q}_{||},z_7,z'')\Big] \\ + \sum_{\mathbf{G_4}_{||}} \int_{-L_z^{\mathrm{mat}}}^{0} dz_4 dz_5 \tilde{\chi}^{(1)}_{0,\mathbf{G}_{||}\mathbf{G_4}_{||}}(\mathbf{q}_{||},z,z_4) v_{\mathbf{G_4}_{||}}(\mathbf{q}_{||},z_4,z_5)\tilde{\chi}^{(2)}_{\mathbf{G_4}_{||},\mathbf{G'}_{||}\mathbf{G''}_{||}}(\mathbf{q}_{||},z_5,z',z'').\end{aligned} \tag{H.4}$$

Then, using the Fourier tranform Eqs. (8.12) and the fact that the three variables are equivalent, we get

$$\begin{aligned}\tilde{\chi}^{(2)}_{\mathbf{G},\mathbf{G'},\mathbf{G''}}(\mathbf{q}) = \sum_{\mathbf{G_4}_{||}\mathbf{G_5}} \tilde{\chi}^{(1)}_{0,\mathbf{G}\mathbf{G_4}}(\mathbf{q})\tilde{v}_{\mathbf{G_4}\mathbf{G_5}}(\mathbf{q})\tilde{\chi}^{(2)}_{\mathbf{G_5},\mathbf{G'}\mathbf{G''}}(\mathbf{q}) \\ + \sum_{\mathbf{G_4}\mathbf{G_5}} \tilde{\chi}^{(2)}_{0,\mathbf{G}\mathbf{G_4}\mathbf{G_5}}(\mathbf{q})\Big[\delta_{\mathbf{G_4}\mathbf{G'}} + \sum_{\mathbf{G_6}} \tilde{v}_{\mathbf{G_4}\mathbf{G_6}}(\mathbf{q})\tilde{\chi}^{(1)}_{\mathbf{G_6}_{||}\mathbf{G'}_{||}}(\mathbf{q})\Big]\Big[\delta_{\mathbf{G_5}\mathbf{G''}} + \sum_{\mathbf{G_7}} \tilde{v}_{\mathbf{G_5}\mathbf{G_7}}(\mathbf{q})\tilde{\chi}^{(1)}_{\mathbf{G_7}\mathbf{G''}}(\mathbf{q})\Big],\end{aligned} \tag{H.5}$$

where $\tilde{v}$ is defined by Eq. (8.14).
Therefore, we checked that the Selected-**G** method can also be applied to second-order susceptibilities.

I. Optical properties of single surfaces

I presented, in Chap. 7 and Chap. 8, a theory for calculating the optical properties of a single surface, in reciprocal space and using a super-cell technique, now known as the Selected-$\mathbf{G}$ formalism. In the Random-Phase Approximation (RPA), I have shown that the calculation of linear and second-order optical properties of surfaces are based on the knowledge of two quantities, $\chi^{(0)S}_{\rho\rho}$ and $\chi^{(0)S}_{\rho\rho\rho}$. In this section, I briefly review the macroscopic theory of Chap. 7 and I give the analytical expressions of $\chi^{(0)S}_{\rho\rho}$ and $\chi^{(0)S}_{\rho\rho\rho}$, referred here as the surface-averaged independent-particle response functions.
For conciseness, I consider only the case of the nonlocal part of the pseudo-potential as a nonlocal operator, and I assume no scissors correction. Similar formulae are obtained when including the scissors operator.

I.1 Linear optical properties of crystal surfaces

In Chap. 7, I have presented how to calculate, in the framework of TDDFT, the macroscopic dielectric tensor of a semi-infinite system, *i.e.*, with a single surface; referred here as the surface dielectric tensor. Here we also use the Selected-$\mathbf{G}$ approach, see Chap. 8.
In the RPA, and in the optical limit, the surface macroscopic dielectric tensor is given by (see Sec. 7.3)

$$\epsilon_M^{S,LL}(\hat{\mathbf{q}};\omega) = \lim_{\mathbf{q}\to\mathbf{0}} \frac{1}{\Big(1 - v(\mathbf{q})\chi^{(0)S}_{\rho\rho}(\mathbf{q},\mathbf{q};\omega)\Big)^{-1}_{\mathbf{G}=\mathbf{G}'=\mathbf{0}}}. \tag{I.1}$$

Here $\mathbf{q}$ is a vanishing momentum and $\mathbf{G}$, $\mathbf{G}'$ are reciprocal lattice vectors. The frequency of the impinging light is ω. Also v refers to the Coulomb interaction and the notation $\big[\chi^{(0)S}_{\rho\rho}(\mathbf{q};\omega)\big]_{\mathbf{G}\mathbf{G}'}$ stands for $\chi^{(0)S}_{\rho\rho}(\mathbf{q}+\mathbf{G},\mathbf{q}+\mathbf{G}';\omega)$. In our formalism, the matrix $\big[\chi^{(0)S}_{\rho\rho}(\mathbf{q};\omega)\big]_{\mathbf{G}\mathbf{G}'}$, is defined by the following set of equations

$$\begin{aligned} \big[\chi^{(0)S}_{\rho\rho}(\mathbf{q};\omega)\big]_{\mathbf{0}\mathbf{G}'} &= \chi^{(0)S}_{\rho\rho}(\mathbf{q},\mathbf{q}+\mathbf{G}';\omega), \\ \big[\chi^{(0)S}_{\rho\rho}(\mathbf{q};\omega)\big]_{\mathbf{G}\mathbf{G}'} &= \big[\chi^{(0)}_{\rho\rho}(\mathbf{q};\omega)\big]_{\mathbf{G}\mathbf{G}'}, \quad \mathbf{G}\neq\mathbf{0}, \end{aligned} \tag{I.2}$$

where $\chi^{(0)}_{\rho\rho}$ is the independent-particle or Kohn-Sham response function.
The elements $\chi^{(0)S}_{\rho\rho}(\mathbf{q},\mathbf{q}+\mathbf{G}';\omega)$ are obtained from the independent-particle response function by

$$\chi^{(0)S}_{\rho\rho}(\mathbf{q},\mathbf{q}+\mathbf{G}';\omega) = \frac{1}{L_z}\sum_{G_z}\tilde{\mathcal{C}}(-G_z)\big[\chi^{(0)}_{\rho\rho}(\mathbf{q};\omega)\big]_{\mathbf{G_z}\mathbf{G}'}, \tag{I.3}$$

with L_z, the thickness of half of the cell used to model the surface.
Thereby, the construction of the matrix $\big[\chi^{(0)S}_{\rho\rho}(\mathbf{q};\omega)\big]_{\mathbf{G}\mathbf{G}'}$ requires only the knowledge of the independent-particle or Kohn-Sham response function $\chi^{(0)}_{\rho\rho}$, which is given in reciprocal space by Eq. (8.3). By

inserting Eq. (8.3) into Eq. (I.3), we obtain

$$\chi^{(0)S}_{\rho\rho}(\mathbf{q},\mathbf{q}+\mathbf{G}';\omega)=\frac{2}{N_{\mathbf{k}}V_{\text{cell}}}\sum_{n,n'}\sum_{\mathbf{k}}^{BZ}f_{nn'}\frac{\tilde{\rho}^{S}_{n,n',\mathbf{k}}(\mathbf{q})\langle n',\mathbf{k}+\mathbf{q}|e^{i(\mathbf{q}+\mathbf{G}')\mathbf{r}}|n,\mathbf{k}\rangle}{(E_{n,\mathbf{k}}-E_{n',\mathbf{k}+\mathbf{q}}+\omega+i\eta)}, \tag{I.4}$$

with $f_{nn'}=f_n-f_{n'}$[1] and

$$\tilde{\rho}^{S}_{n,n',\mathbf{k}}(\mathbf{q})=\frac{1}{L_z}\sum_{G_z}\tilde{\mathcal{C}}(-G_z)\langle n,\mathbf{k}|e^{-i(\mathbf{q}+\mathbf{G_z})\mathbf{r}}|n',\mathbf{k}+\mathbf{q}\rangle.$$

This quantity has to be evaluated in the optical limit, meaning for $\mathbf{q}\to\mathbf{0}$.
The expression of $\tilde{\rho}^{S}_{n,n',\mathbf{k}}(\mathbf{q})$ is given by

$$\begin{aligned}\tilde{\rho}^{S}_{n,n',\mathbf{k}}(\mathbf{q}) &= \frac{1}{L_z}\sum_{G_z}\tilde{\mathcal{C}}(-G_z)\langle n,\mathbf{k}|e^{-i(\mathbf{q}+\mathbf{G_z})\mathbf{r}}|m,\mathbf{k}+\mathbf{q}\rangle\\ &= \int d^3\mathbf{r}\phi^{*}_{n,\mathbf{k}}(\mathbf{r})\frac{1}{L_z}\sum_{G_z}\tilde{\mathcal{C}}(-G_z)e^{-iG_zz}e^{-i\mathbf{q}\mathbf{r}}\phi_{n,\mathbf{k}+\mathbf{q}}(\mathbf{r})\\ &= \int d^3\mathbf{r}\phi^{*}_{n,\mathbf{k}}(\mathbf{r})\mathcal{C}(z)e^{-i\mathbf{q}\mathbf{r}}\phi_{n,\mathbf{k}+\mathbf{q}},\end{aligned} \tag{I.5}$$

where we recognized the Fourier transform of the cut-function $\mathcal{C}$ in the last equation.
In the optical limit, $\mathbf{q}\to 0$ and therefore, from $\mathbf{k}.\mathbf{p}$ perturbation theory, we get that

$$\tilde{\rho}^{S}_{n,n',\mathbf{k}}(\mathbf{q}\to 0)=\langle n,\mathbf{k}|\mathcal{C}(z)|n',\mathbf{k}\rangle+\sum_{m\notin D_{n'}}\frac{\langle n,\mathbf{k}|\mathcal{C}(z)|m,\mathbf{k}\rangle\langle m,\mathbf{k}|\mathbf{q}\mathbf{v}|n',\mathbf{k}\rangle}{E_{m,\mathbf{k}}-E_{n',\mathbf{k}}}. \tag{I.6}$$

The position operator $\mathbf{r}$ can be expressed into interband $\mathbf{r_i}$ and interband $\mathbf{r_e}$ part defined by [272]

$$\begin{aligned}\langle n,\mathbf{k}|\mathbf{r_i}|m,\mathbf{k}'\rangle &= \delta_{nm}\delta(\mathbf{k}-\mathbf{k}')\left[\xi nn+i\nabla_{\mathbf{k}}\right]\\ \langle n,\mathbf{k}|\mathbf{r_e}|m,\mathbf{k}'\rangle &= (1-\delta_{nm})\delta(\mathbf{k}-\mathbf{k}')\xi nm\end{aligned}$$

where $\mathbf{r}=\mathbf{r_i}+\mathbf{r_e}$.
Using this definition, allows us to remove the restriction of the sum, and we get

$$\tilde{\rho}^{S}_{n,n',\mathbf{k}}(\mathbf{q}\to 0)=\langle n,\mathbf{k}|\mathcal{C}(z)-i\mathbf{q}\mathbf{r_e}\mathcal{C}(z)|n',\mathbf{k}\rangle. \tag{I.7}$$

The generalized derivative of any operator O is given by [272]

$$(O_{nm})_{;\mathbf{k}}=\frac{\partial O_{nm}}{\partial\mathbf{k}}-iO_{nm}(\xi_{nn}-\xi_{mm})$$

In the paper, authors give the following relation [272]

$$\langle n,\mathbf{k}|[\mathbf{r_i},O]|n',\mathbf{k}'\rangle=i\delta(\mathbf{k}-\mathbf{k}')\,(O_{nm})_{;\mathbf{k}}$$

[1] Occupation numbers are independent of the momentum, as we consider a cold semiconductor with filled bands.

From these relations, we obtain that for $n' \notin \mathcal{D}_n$, we have

$$i\langle n,\mathbf{k}|[\mathbf{r_e},H]|n',\mathbf{k}'\rangle = \langle n,\mathbf{k}|\mathbf{v}|n',\mathbf{k}'\rangle, \tag{I.8}$$

because $(H_{nm})_{;\mathbf{k}} = 0$ for $n' \notin \mathcal{D}_n$. From this result, we can compute the last term of Eq. I.7 for $n' \notin \mathcal{D}_n$

$$\begin{aligned} i(E_{n,\mathbf{k}} - E_{n',\mathbf{k}})\langle n,\mathbf{k}|\hat{\mathbf{r}}\mathcal{C}(z)|n',\mathbf{k}\rangle &= i\int d^3\mathbf{r}\mathcal{C}(z)\phi^*_{n,\mathbf{k}}(\mathbf{r})(E_{n,\mathbf{k}}\mathbf{r_e} - \mathbf{r_e}E_{n',\mathbf{k}})\phi_{n',\mathbf{k}}(\mathbf{r}) \\ &= i\int d^3\mathbf{r}\phi^*_{n,\mathbf{k}}(\mathbf{r})\frac{\mathcal{C}(z)(\hat{H}\mathbf{r_e} - \mathbf{r_e}\hat{H}) + (\hat{H}\mathbf{r_e} - \mathbf{r_e}\hat{H})\mathcal{C}(z)}{2}\phi_{n',\mathbf{k}}(\mathbf{r}) \\ &= \langle n,\mathbf{k}|\frac{\mathcal{C}(z)\hat{\mathbf{v}} + \hat{\mathbf{v}}\mathcal{C}(z)}{2}|n',\mathbf{k}\rangle. \end{aligned} \tag{I.9}$$

Here we recognize the expression of the modified velocity (see Eq. (6.11)).
The final expression of $\tilde{\rho}^S_{n,n',\mathbf{k}}(\mathbf{q}\to 0)$ is

$$\tilde{\rho}^S_{n,n',\mathbf{k}}(\mathbf{q}\to\mathbf{0}) = \langle n,\mathbf{k}|\mathcal{C}(z)|n',\mathbf{k}\rangle + \frac{\langle n,\mathbf{k}|\mathbf{q}.\boldsymbol{\mathcal{V}}|n',\mathbf{k}\rangle}{E_{n,\mathbf{k}} - E_{n',\mathbf{k}}}. \tag{I.10}$$

For $\mathbf{G}' = \mathbf{0}$, and in the limit $\mathbf{q}\to\mathbf{0}$, $\chi^{(0)S}_{\rho\rho}$ reads as

$$\begin{aligned} \chi^{(0)S}_{\rho\rho}(\mathbf{q},\mathbf{q};\omega) = \frac{2}{N_{\mathbf{k}}V_{\text{cell}}}\sum_{n,n'}\sum_{\mathbf{k}}^{BZ} f_{nn'}\Bigg[&\frac{\langle n,\mathbf{k}|\mathcal{C}(z)|n',\mathbf{k}\rangle\langle n',\mathbf{k}|i\mathbf{q}.\mathbf{r}|n,\mathbf{k}\rangle\langle n',\mathbf{k}|\mathbf{q}.\mathbf{v}|n',\mathbf{k}\rangle}{(E_{n,\mathbf{k}} - E_{n',\mathbf{k}} + \omega + i\eta)^2} \\ &+\frac{\langle n,\mathbf{k}|\mathcal{C}(z)|n',\mathbf{k}\rangle\langle n',\mathbf{k}|i\mathbf{q}.\mathbf{r}|n,\mathbf{k}\rangle}{(E_{n,\mathbf{k}} - E_{n',\mathbf{k}} + \omega + i\eta)} + \frac{\langle n,\mathbf{k}|\mathbf{q}.\boldsymbol{\mathcal{V}}|n',\mathbf{k}\rangle\langle n',\mathbf{k}|i\mathbf{q}.\mathbf{r}|n,\mathbf{k}\rangle}{(E_{n,\mathbf{k}} - E_{n',\mathbf{k}})(E_{n,\mathbf{k}} - E_{n',\mathbf{k}} + \omega + i\eta)}\Bigg] + \mathcal{O}(q^3), \end{aligned} \tag{I.11}$$

whereas for $\mathbf{G}' \neq \mathbf{0}$, we obtain

$$\begin{aligned} \chi^{(0)S}_{\rho\rho}(\mathbf{q},\mathbf{q}+\mathbf{G}';\omega) = \frac{2}{N_{\mathbf{k}}V_{\text{cell}}}\sum_{n,n'}\sum_{\mathbf{k}}^{BZ} f_{nn'}\Bigg[&\frac{\langle n,\mathbf{k}|\mathcal{C}(z)|n',\mathbf{k}\rangle\langle n',\mathbf{k}|e^{i\mathbf{G}'\mathbf{r}'}|n,\mathbf{k}\rangle\langle n,\mathbf{k}|\mathbf{q}.\mathbf{v}|n,\mathbf{k}\rangle}{(E_{n,\mathbf{k}} - E_{n',\mathbf{k}} + \omega + i\eta)^2} \\ &+\frac{\langle n,\mathbf{k}|\mathbf{q}.\boldsymbol{\mathcal{V}}|n',\mathbf{k}\rangle\langle n',\mathbf{k}|e^{i\mathbf{G}'\mathbf{r}'}|n,\mathbf{k}\rangle}{(E_{n,\mathbf{k}} - E_{n',\mathbf{k}})(E_{n,\mathbf{k}} - E_{n',\mathbf{k}} + \omega + i\eta)} + \frac{\langle n,\mathbf{k}|\mathcal{C}(z)|n',\mathbf{k}\rangle\langle n',\mathbf{k}|e^{i\mathbf{G}'\mathbf{r}'}|n,\mathbf{k}\rangle}{(E_{n,\mathbf{k}} - E_{n',\mathbf{k}} + \omega + i\eta)}\Bigg] + \mathcal{O}(q^2). \end{aligned} \tag{I.12}$$

The first term in Eq. (I.12) and in Eq. (I.11) vanishes, using $\mathbf{k}\to-\mathbf{k}$ and $n\leftrightarrow n'$ two times. The other terms associated with $\mathcal{C}(z)$ do not vanish using the time-reversal symmetry. In order to prove that these terms are zero, we introduce the surface-averaged current-current response function,

$$\begin{aligned} \overleftrightarrow{\chi}^{(0)S}_{\mathbf{jj}}(\mathbf{q}+\mathbf{G},\mathbf{q}+\mathbf{G}';\omega) = \langle\rho^S\rangle\delta_{\mathbf{G}\mathbf{G}'}\overleftrightarrow{\mathbb{1}} + \frac{1}{4N_{\mathbf{k}}V_{\text{cell}}}\sum_{n,n'}\sum_{\mathbf{k}}^{BZ} f_{nn'} \\ \times\frac{\langle n,\mathbf{k}|\left[e^{-i(\mathbf{q}+\mathbf{G})\mathbf{r}}\mathcal{C}(z)\mathbf{v} + \mathbf{v}\mathcal{C}(z)e^{-i(\mathbf{q}+\mathbf{G})\mathbf{r}}\right]|n',\mathbf{k}+\mathbf{q}\rangle\langle n',\mathbf{k}+\mathbf{q}|\left[e^{i(\mathbf{q}+\mathbf{G}')\mathbf{r}}\mathbf{v} + \mathbf{v}e^{i(\mathbf{q}+\mathbf{G}')\mathbf{r}}\right]|n,\mathbf{k}\rangle}{(E_{n,\mathbf{k}} - E_{n',\mathbf{k}+\mathbf{q}} + \omega + i\eta)} \\ -\frac{1}{N_{\mathbf{k}}V_{\text{cell}}}\sum_{n}\sum_{\mathbf{k}}^{BZ} f_n\langle n,\mathbf{k}|e^{-i(\mathbf{q}+\mathbf{G})\mathbf{r}}[\mathbf{r},[\mathbf{r},\tilde{V}_{\text{nl}}]]|n,\mathbf{k}\rangle\delta_{\mathbf{G}\mathbf{G}'}, \end{aligned} \tag{I.13}$$

where $\tilde{V}_{\rm nl}$ stands for $\frac{\mathcal{C}(z)\hat{V}_{\rm nl}+\hat{V}_{\rm nl}\mathcal{C}(z)}{2}$, $\hat{V}_{\rm nl}$ being the nonlocal part of the pseudo-potential (see Chap. 6). In the limit $\mathbf{q}\to 0$, we obtain at the 0-th order in q, after some algebra, that

$$\overset{\leftrightarrow}{\chi}{}^{(0)S}_{\mathbf{jj}}(\mathbf{q},\mathbf{q};\omega) = \langle\rho^S\rangle \overset{\leftrightarrow}{\mathbb{1}} + \frac{1}{N_{\mathbf{k}}V_{\rm cell}}\sum_{\mathbf{k}}^{BZ}\sum_{n,n'} f_{nn'}\frac{\langle n,\mathbf{k}|\boldsymbol{\mathcal{V}}|n',\mathbf{k}\rangle\langle n',\mathbf{k}|\mathbf{v}|n,\mathbf{k}\rangle}{(E_{n,\mathbf{k}}-E_{n',\mathbf{k}}+\omega+i\eta)} - \frac{1}{N_{\mathbf{k}}V_{\rm cell}}\sum_{\mathbf{k}}^{BZ}\sum_{n} f_n\langle n,\mathbf{k}|[\mathbf{r},[\mathbf{r},\tilde{V}_{\rm nl}]]|n,\mathbf{k}\rangle, \tag{I.14a}$$

$$\overset{\leftrightarrow}{\chi}{}^{(0)S}_{\mathbf{jj}}(\mathbf{q},\mathbf{q}+\mathbf{G}';\omega) = \frac{1}{2N_{\mathbf{k}}V_{\rm cell}}\sum_{n,n'}\sum_{\mathbf{k}}^{BZ} f_{nn'}\frac{\langle n,\mathbf{k}|\boldsymbol{\mathcal{V}}|n',\mathbf{k}\rangle\langle n',\mathbf{k}|\left[e^{i\mathbf{G}'\mathbf{r}}\mathbf{v}+\mathbf{v}e^{i\mathbf{G}'\mathbf{r}}\right]|n,\mathbf{k}\rangle}{(E_{n,\mathbf{k}}-E_{n',\mathbf{k}}+\omega+i\eta)}. \tag{I.14b}$$

Using the conservation of charges (see App. F.1), we obtain the two equalities

$$\omega^2\chi^{(0)S}_{\rho\rho}(\mathbf{q},\mathbf{q};\omega) = \mathbf{q}.\overset{\leftrightarrow}{\chi}{}^{(0)S}_{\mathbf{jj}}(\mathbf{q},\mathbf{q};\omega).\mathbf{q} - \langle\rho^S\rangle q^2, \tag{I.15a}$$

$$\omega^2\chi^{(0)S}_{\rho\rho}(\mathbf{q},\mathbf{q}+\mathbf{G}';\omega) = \mathbf{q}.\overset{\leftrightarrow}{\chi}{}^{(0)S}_{\mathbf{jj}}(\mathbf{q},\mathbf{q}+\mathbf{G}';\omega).(\mathbf{q}+\mathbf{G}'). \tag{I.15b}$$

From the comparison between the left-hand side and the right-hand side of Eqs. (I.15), we conclude that, at lowest order in q, $\chi^{(0)S}_{\rho\rho}(\mathbf{q},\mathbf{q};\omega)$ is proportional to q^2, and $\chi^{(0)S}_{\rho\rho}(\mathbf{q},\mathbf{q}+\mathbf{G};\omega)$ is proportional to q.

This proves that the terms associated with $\langle n,\mathbf{k}|\mathcal{C}(z)|n',\mathbf{k}\rangle$ in Eq. I.11 and Eq. I.12 vanish. Finally, we obtain, at the lowest order in q, that

$$\chi^{(0)S}_{\rho\rho}(\mathbf{q},\mathbf{q};\omega) = \frac{2}{N_{\mathbf{k}}V_{\rm cell}}\sum_{n,n'}\sum_{\mathbf{k}}^{BZ} f_{nn'}\frac{\langle n,\mathbf{k}|\mathbf{q}.\boldsymbol{\mathcal{V}}|n',\mathbf{k}\rangle\langle n',\mathbf{k}|i\mathbf{q}.\mathbf{r}|n,\mathbf{k}\rangle}{(E_{n,\mathbf{k}}-E_{n',\mathbf{k}})(E_{n,\mathbf{k}}-E_{n',\mathbf{k}+\mathbf{q}}+\omega+i\eta)}, \tag{I.16a}$$

$$\chi^{(0)S}_{\rho\rho}(\mathbf{q},\mathbf{q}+\mathbf{G}';\omega) = \frac{2}{N_{\mathbf{k}}V_{\rm cell}}\sum_{n,n'}\sum_{\mathbf{k}}^{BZ} f_{nn'}\frac{\langle n,\mathbf{k}|\mathbf{q}.\boldsymbol{\mathcal{V}}|n',\mathbf{k}\rangle\langle n',\mathbf{k}|e^{i\mathbf{G}'\mathbf{r}'}|n,\mathbf{k}\rangle}{(E_{n,\mathbf{k}}-E_{m,\mathbf{k}})(E_{n,\mathbf{k}}-E_{n',\mathbf{k}}+\omega+i\eta)}. \tag{I.16b}$$

These expressions are similar to the usual expressions for matrix elements of $\chi^{(0)}_{\rho\rho}$; except the replacement $\langle n,\mathbf{k}|\mathbf{q}.\mathbf{v}|n',\mathbf{k}\rangle \to \langle n,\mathbf{k}|\mathbf{q}.\boldsymbol{\mathcal{V}}|n',\mathbf{k}\rangle$, which allows us to calculate the optical properties of a single surface. Note that the expression for $\chi^{(0)S}_{\rho\rho}(\mathbf{q},\mathbf{q};\omega)$ was already presented in Chap. 5 for a local-potential. It is worthwhile to note that the quantity $\chi^{(0)S}_{\rho\rho}$ has been found to describe the surface optical response, starting from a macroscopic description of the optical response; but also from a microscopic description, see Chap. 5.

I.1.1 Second-order optical properties of crystal surfaces

In Chap. 7, I have proved that the nonlinear optical properties of surfaces are given, for the case of second-harmonic generation, by

$$\chi^{(2)S,LLL}_{M}(\mathbf{q},\mathbf{q_1},\mathbf{q_2};\omega,\omega) = \frac{-i}{2|\mathbf{q}||\mathbf{q_1}||\mathbf{q_2}|}\epsilon^{S,LL}_{M}(\mathbf{q};2\omega)\hat{\chi}^{S}_{\rho\rho\rho}(\mathbf{q},\mathbf{q_1},\mathbf{q_2};\omega,\omega)\epsilon^{LL}_{M}(\mathbf{q_1};\omega)\epsilon^{LL}_{M}(\mathbf{q_2};\omega), \tag{I.17}$$

where $\hat{\chi}^S_{\rho\rho\rho}$ is obtained by solving Eq. (7.47), whose solution is

$$\begin{aligned}\hat{\chi}^S_{\rho\rho\rho}(\mathbf{q},\mathbf{q_1},\mathbf{q_2};\omega,\omega) = \sum_{\mathbf{G_1G_2G_3}} &\Big[Id - \chi^{(0)S}_{\rho\rho}(\mathbf{q};2\omega)v(\mathbf{q})\Big]^{-1}_{\mathbf{0G_1}} \big[\chi^{(0)S}_{\rho\rho\rho}(\mathbf{q},\mathbf{q_1},\mathbf{q_2};\omega,\omega)\big]_{\mathbf{G_1G_2G_3}} \\ &\times\Big[Id + v(\mathbf{q_1})\chi_{\rho\rho}(\mathbf{q_1};\omega)\Big]_{\mathbf{G_20}}\Big[Id + v(\mathbf{q_2})\chi_{\rho\rho}(\mathbf{q_2};\omega)\Big]_{\mathbf{G_30}}.\end{aligned} \tag{I.18}$$

In the formalism developed in Chap. 7, the matrix $\big[\chi^{(0)S}_{\rho\rho\rho}(\mathbf{q},\mathbf{q_1},\mathbf{q_2};\omega,\omega)\big]_{\mathbf{GG_1G_2}}$ is defined by the following set of equations

$$\begin{aligned}\big[\chi^{(0)S}_{\rho\rho\rho}(\mathbf{q},\mathbf{q_1},\mathbf{q_2};\omega,\omega)\big]_{\mathbf{0G_1G_2}} &= \chi^{(0)S}_{\rho\rho\rho}(\mathbf{q},\mathbf{q_1}+\mathbf{G_1},\mathbf{q_2}+\mathbf{G_2};\omega,\omega), \\ \big[\chi^{(0)S}_{\rho\rho\rho}(\mathbf{q},\mathbf{q_1},\mathbf{q_2};\omega,\omega)\big]_{\mathbf{GG_1G_2}} &= \big[\chi^{(0)}_{\rho\rho\rho}(\mathbf{q},\mathbf{q_1},\mathbf{q_2};\omega,\omega)\big]_{\mathbf{GG_1G_2}}, \quad \mathbf{G}\neq 0.\end{aligned} \tag{I.19}$$

Here $\chi^{(0)S}_{\rho\rho\rho}(\mathbf{q},\mathbf{q_1}+\mathbf{G_1},\mathbf{q_2}+\mathbf{G_2};\omega,\omega)$ is defined by matrix elements of the independent-particle response function, thanks to

$$\chi^{(0)S}_{\rho\rho\rho}(\mathbf{q},\mathbf{q_1}+\mathbf{G_1},\mathbf{q_2}+\mathbf{G_2};\omega,\omega) = \frac{1}{L_z}\sum_{G_z}\tilde{\mathcal{C}}(-G_z)\big[\chi^{(0)}_{\rho\rho\rho}(\mathbf{q},\mathbf{q_1},\mathbf{q_2};\omega,\omega)\big]_{\mathbf{G_zG_1G_2}}, \tag{I.20}$$

where the Kohn-Sham density-density-density response function $\chi^{(0)}_{\rho\rho\rho}$ is given by [41]

$$\begin{aligned}\big[\chi^{(0)}_{\rho\rho\rho}(\mathbf{q},\mathbf{q_1},\mathbf{q_2};\omega,\omega)\big]_{\mathbf{GG_1G_2}} = \frac{2}{N_{\mathbf{k}}V_{\text{cell}}}\sum_{n,n',n''}\sum_{\mathbf{k}}^{BZ}&\frac{\langle n,\mathbf{k}|e^{-i(\mathbf{q}+\mathbf{G})\mathbf{r}}|n',\mathbf{k}+\mathbf{q}\rangle}{(E_{n\mathbf{k}}-E_{n',\mathbf{k}+\mathbf{q}}+2\omega+2i\eta)} \\ \Bigg[(f_{n,\mathbf{k}}-f_{n'',\mathbf{k}+\mathbf{q_2}})&\frac{\langle n',\mathbf{k}+\mathbf{q}|e^{i(\mathbf{q_1}+\mathbf{G_1})\mathbf{r}'}|n'',\mathbf{k}+\mathbf{q_2}\rangle\langle n'',\mathbf{k}+\mathbf{q_2}|e^{i(\mathbf{q_2}+\mathbf{G_2})\mathbf{r}''}|n,\mathbf{k}\rangle}{(E_{n,\mathbf{k}}-E_{n'',\mathbf{k}+\mathbf{q_2}}+\omega+i\eta)} \\ +(f_{n,\mathbf{k}}-f_{n'',\mathbf{k}+\mathbf{q_1}})&\frac{\langle n',\mathbf{k}+\mathbf{q}|e^{i(\mathbf{q_2}+\mathbf{G_2})\mathbf{r}'}|n'',\mathbf{k}+\mathbf{q_1}\rangle\langle n'',\mathbf{k}+\mathbf{q_1}|e^{i(\mathbf{q_1}+\mathbf{G_1})\mathbf{r}''}|n,\mathbf{k}\rangle}{(E_{n,\mathbf{k}}-E_{n'',\mathbf{k}+\mathbf{q_1}}+\omega+i\eta)} \\ +(f_{n',\mathbf{k}+\mathbf{q}}-f_{n'',\mathbf{k}+\mathbf{q_1}})&\frac{\langle n',\mathbf{k}+\mathbf{q}|e^{i(\mathbf{q_2}+\mathbf{G_2})\mathbf{r}'}|n'',\mathbf{k}+\mathbf{q_1}\rangle\langle n'',\mathbf{k}+\mathbf{q_1}|e^{i(\mathbf{q_1}+\mathbf{G_1})\mathbf{r}''}|n,\mathbf{k}\rangle}{(E_{n'',\mathbf{k}+\mathbf{q_1}}-E_{n',\mathbf{k}+\mathbf{q}}+\omega+i\eta)} \\ +(f_{n',\mathbf{k}+\mathbf{q}}-f_{n'',\mathbf{k}+\mathbf{q_2}})&\frac{\langle n',\mathbf{k}+\mathbf{q}|e^{i(\mathbf{q_1}+\mathbf{G_1})\mathbf{r}'}|n'',\mathbf{k}+\mathbf{q_2}\rangle\langle n'',\mathbf{k}+\mathbf{q_2}|e^{i(\mathbf{q_2}+\mathbf{G_2})\mathbf{r}''}|n,\mathbf{k}\rangle}{(E_{n'',\mathbf{k}+\mathbf{q_2}}-E_{n',\mathbf{k}+\mathbf{q}}+\omega+i\eta)}\Bigg].\end{aligned} \tag{I.21}$$

The derivation of the matrix elements of $\chi^{(0)S}_{\rho\rho\rho}$ is similar to the derivation at matrix elements of $\chi^{(0)S}_{\rho\rho}$. Note that the head of the matrix, $\big[\chi^{(0)S}_{\rho\rho\rho}\big]_{\mathbf{000}}$, has already been given in Chap. 6, see Eq. (6.13) and Eqs. (6.14). Therefore, only the expressions for $\big[\chi^{(0)S}_{\rho\rho\rho}\big]_{\mathbf{0G'0'}}$, $\big[\chi^{(0)S}_{\rho\rho\rho}\big]_{\mathbf{00G''}}$ and $\big[\chi^{(0)S}_{\rho\rho\rho}\big]_{\mathbf{0G'G''}}$ remains to be derived.

As their derivations follow exactly the same idea, I do not report the corresponding derivations here. The resulting expressions are found to be similar to the expressions for bulk materials, with only the replacement $\langle n,\mathbf{k}|\mathbf{q}.\,\mathbf{v}|n',\mathbf{k}\rangle \to \langle n,\mathbf{k}|\mathbf{q}.\,\boldsymbol{\mathcal{V}}|n',\mathbf{k}\rangle$ for the matrix elements associated with $\mathbf{q}$.

Matrix elements associated with $\mathbf{q_1}$ and $\mathbf{q_2}$ are identical to those of the "usual" bulk formula.

List of publications related to this work

- Tancogne-Dejean, Nicolas and Mendoza, Bernardo S. and Véniard, Valérie.
  Effect of material properties on the accuracy of antiresonant approximation: Linear and second-order optical responses.
  Phys. Rev. B. 90, 035212 (2014).

- Anderson, Sean M. and Tancogne-Dejean, Nicolas and Mendoza, Bernardo S. and Véniard, Valérie.
  Theory of surface second-harmonic generation for semiconductors including effects of nonlocal operators.
  Phys. Rev. B. 91, 075302 (2015).

- Tancogne-Dejean, Nicolas, Giorgetti Christine and Véniard, Valérie.
  Optical properties of surfaces with supercell calculations: local-field effects.
  Submitted.

- Tancogne-Dejean, Nicolas and Véniard, Valérie.
  Ab initio macroscopic linear and second-order optical properties of crystal surfaces: From the slab to the single surface.
  In preparation.

- Tancogne-Dejean, Nicolas and Véniard, Valérie.
  Local-field effects on second-harmonic generation from surfaces.
  In preparation.

- Tancogne-Dejean, Nicolas and Véniard, Valérie.
  Excitonic effects on second-harmonic generation from silicon surfaces.
  In preparation.

List of the different codes used during this work

- **Abinit** [115].
  Ground state calculation.
  Reciprocal-space and plane-wave basis-set.

- **DP** [116].
  TDDFT in linear response at first order.
  Reciprocal-space and plane-wave basis-set.

- **2light** [117].
  TDDFT in linear response at second-order.
  Reciprocal-space and plane-wave basis-set.

- **TB_Si**.
  Ground-state and linear response at first and second-order, within the IPA.
  Reciprocal-space and tight-binding orbital basis (sp^3, sp^3s^*, and $sp^3d^5s^*$).

Bibliography

[1] Weinberger, P. *Philosophical Magazine Letters*, **88**, 897–907 (2008) .

[2] Franken, P. A., Hill, A. E., Peters, C. W., and Weinreich, G. *Phys. Rev. Lett.*, **7**, 118–119 (1961) .

[3] Bass, M., Franken, P. A., Ward, J. F., and Weinreich, G. *Phys. Rev. Lett.*, **9**, 446–448 (1962) .

[4] New, G. H. C. and Ward, J. F. *Phys. Rev. Lett.*, **19**, 556–559 (1967) .

[5] Lee, C. H., Chang, R. K., and Bloembergen, N. *Phys. Rev. Lett.*, **18**, 167–170 (1967) .

[6] Brabec, T. and Krausz, F. *Rev. Mod. Phys.*, **72**, 545–591 (2000) .

[7] Wu, H., Yu, H., Yang, Z., Hou, X., Su, X., Pan, S., Poeppelmeier, K. R., and Rondinelli, J. M. *Journal of the American Chemical Society*, **135**, 4215–4218 (2013) .

[8] Yu, H., Wu, H., Pan, S., Yang, Z., Hou, X., Su, X., Jing, Q., Poeppelmeier, K. R., and Rondinelli, J. M. *Journal of the American Chemical Society*, **136**, 1264–1267 (2014) .

[9] Li, H., Wu, H., Su, X., Yu, H., Pan, S., Yang, Z., Lu, Y., Han, J., and Poeppelmeier, K. R. *J. Mater. Chem. C*, **2**, 1704–1710 (2014) .

[10] Abudoureheman, M., Wang, L., Zhang, X., Yu, H., Yang, Z., Lei, C., Han, J., and Pan, S. *Inorganic Chemistry*, **54**, 4138–4142 (2015) PMID: 25825990.

[11] Chang, L., Wang, L., Su, X., Pan, S., Hailili, R., Yu, H., and Yang, Z. *Inorganic Chemistry*, **53**, 3320–3325 (2014) PMID: 24617308.

[12] Ren, M.-L., Liu, W., Aspetti, C. O., Sun, L., and Agarwal, R. *Nature communications*, **5** (2014) .

[13] Cazzanelli, M., et al. *Nature materials*, **11**, 148–154 (2012) .

[14] Hsu, W.-T., Zhao, Z.-A., Li, L.-J., Chen, C.-H., Chiu, M.-H., Chang, P.-S., Chou, Y.-C., and Chang, W.-H. *ACS Nano*, **8**, 2951–2958 (2014) PMID: 24568359.

[15] Janisch, C., Wang, Y., Ma, D., Mehta, N., Elías, A. L., Perea-López, N., Terrones, M., Crespi, V., and Liu, Z. *Scientific reports*, **4** (2014) .

[16] Wang, G., Marie, X., Gerber, I., Amand, T., Lagarde, D., Bouet, L., Vidal, M., Balocchi, A., and Urbaszek, B. *Phys. Rev. Lett.*, **114**, 097403 (2015) .

[17] Theodossiou, T. A., Thrasivoulou, C., Ekwobi, C., and Becker, D. L. *Biophysical Journal*, **91**, 4665 – 4677 (2006) .

[18] Nuriya, M., Jiang, J., Nemet, B., Eisenthal, K. B., and Yuste, R. *Proceedings of the National Academy of Sciences of the United States of America*, **103**, 786–790 (2006) .

[19] Yin, X. *science*, **1250564**, 344 (2014) .

[20] Butet, J., Duboisset, J., Bachelier, G., Russier-Antoine, I., Benichou, E., Jonin, C., and Brevet, P.-F. *Nano Letters*, **10**, 1717–1721 (2010) .

[21] Zielinski, M., Oron, D., Chauvat, D., and Zyss, J. *Small*, **5**, 2835–2840 (2009) .

[22] Campagnola, P. J., Millard, A. C., Terasaki, M., Hoppe, P. E., Malone, C. J., and Mohler, W. A. *Biophysical journal*, **82**, 493–508 (2002) .

[23] Cao, H., Wu, J. Y., Ong, H. C., Dai, J. Y., and Chang, R. P. H. *Applied Physics Letters*, **73**, 572–574 (1998) .

[24] Wang, X. K., Zhang, T. G., Lin, W. P., Liu, S. Z., Wong, G. K., Kappes, M. M., Chang, R. P. H., and Ketterson, J. B. *Applied Physics Letters*, **60**, 810–812 (1992) .

[25] Lu, H. A., Wills, L. A., Wessels, B. W., Lin, W. P., Zhang, T. G., Wong, G. K., Neumayer, D. A., and Marks, T. J. *Applied Physics Letters*, **62**, 1314–1316 (1993) .

[26] Ghahramani, E., Moss, D. J., and Sipe, J. E. *Phys. Rev. Lett.*, **64**, 2815–2818 (1990) .

[27] Zhang, C., Xiao, X., Wang, N., Fung, K. K., Loy, M. M. T., Chen, Z., and Zhou, J. *Applied Physics Letters*, **72**, 2072–2074 (1998) .

[28] Daum, W., Krause, H.-J., Reichel, U., and Ibach, H. *Phys. Rev. Lett.*, **71**, 1234–1237 (1993) .

[29] Bertocchi, M., Luppi, E., Degoli, E., Véniard, V., and Ossicini, S. *Phys. Rev. B*, **86**, 035309 (2012) .

[30] Heinz, T. F., Loy, M. M. T., and Thompson, W. A. *Phys. Rev. Lett.*, **54**, 63–66 (1985) .

[31] Shen, Y. *Nature*, **337**, 519–525 (1989) .

[32] Höfer, U. *Applied Physics A*, **63**, 533 (1996) .

[33] Dadap, J. I., Xu, Z., Hu, X. F., Downer, M. C., Russell, N. M., Ekerdt, J. G., and Aktsipetrov, O. A. *Phys. Rev. B*, **56**, 13367–13379 (1997) .

[34] Borensztein, Y., Pluchery, O., and Witkowski, N. *Phys. Rev. Lett.*, **95**, 117402 (2005) .

[35] Ehlert, R., Prem, A., Loumakos, L., and Downer, M. C. (2011) Fingerprinting of si surface bonds using nonresonant optical second-harmonic generation. *Nonlinear Optics*, p. NTuB5, Optical Society of America.

[36] Savoia, A., et al. *Phys. Rev. B*, **80**, 075110 (2009) .

[37] Jackson, J. D., *Classical electrodynamics* (1999) Wiley, 3rd ed. edn.

[38] Del Sole, R. and Fiorino, E. *Phys. Rev. B*, **29**, 4631–4645 (1984) .

[39] Mochán, W. L. and Barrera, R. G. *Phys. Rev. B*, **32**, 4984–4988 (1985) .

[40] Mochán, W. L. and Barrera, R. G. *Phys. Rev. B*, **32**, 4989–5001 (1985) .

[41] Luppi, E., Hübener, H., and Véniard, V. *Phys. Rev. B*, **82**, 235201 (2010) .

[42] Huebener, H., Luppi, E., and Veniard, V. *physica status solidi (b)*, **247**, 1984–1991 (2010) .

[43] Huebener, H. (2010) *Second Harmonic Generation in Solids: Theory and Simulation*. Theses, Ecole Polytechnique X.

[44] Ehrenreich, H. (1966) Electromagnetic transport in solids: optical properties and plasma effects. Tauc, J. (ed.), *The Optical Properties of Solids*, New York, p. 106, Proceedings of the International School of Physics "Enrico Fermi", Academic Press.

[45] Bertocchi, M. (2013) *First principles Second-Harmonic Generation in quantum confined silicon-based systems*. Theses, Ecole Polytechnique X.

[46] Kittel, C., McEuen, P., and McEuen, P., *Introduction to solid state physics* (1976) vol. 8. Wiley New York.

[47] Nozières, P. and Pines, D. *Phys. Rev.*, **109**, 762–777 (1958) .

[48] Strinati, G. *La Rivista del Nuovo Cimento*, **11**, 1–86 (1988) .

[49] Shen, Y.-R., *Principles of nonlinear optics* (1984) Wiley-Interscience, New York, NY, USA.

[50] Bedeaux, D. and Bloembergen, N. *Physica*, **69**, 57 – 66 (1973) .

[51] Armstrong, J. A., Bloembergen, N., Ducuing, J., and Pershan, P. S. *Phys. Rev.*, **127**, 1918–1939 (1962) .

[52] Flytzanis, C. and Ducuing, J. *Phys. Rev.*, **178**, 1218–1228 (1969) .

[53] Maki, J. J., Malcuit, M. S., Sipe, J. E., and Boyd, R. W. *Phys. Rev. Lett.*, **67**, 972–975 (1991) .

[54] Wallis, R. and Balkanski, M., *Many-body Aspects of Solid State Spectroscopy* (1986) North-Holland Physics.

[55] Born, M. and Wolf, E., *Principles of optics: electromagnetic theory of propagation, interference and diffraction of light* (1999) Cambridge university press.

[56] Nozières, P. and Pines, D. *Phys. Rev.*, **113**, 1254–1267 (1959) .

[57] Ambegaokar, V. and Kohn, W. *Phys. Rev.*, **117**, 423–431 (1960) .

[58] Gielis, J. J. H., van den Oever, P. J., Hoex, B., van de Sanden, M. C. M., and Kessels, W. M. M. *Phys. Rev. B*, **77**, 205329 (2008) .

[59] Prokes, S. M. *Journal of Materials Research*, **11**, 305–320 (1996) .

[60] Palummo, M., Pulci, O., Del Sole, R., Marini, A., Schwitters, M., Haines, S. R., Williams, K. H., Martin, D. S., Weightman, P., and Butler, J. E. *Phys. Rev. Lett.*, **94**, 087404 (2005) .

[61] Hahn, P. H., Schmidt, W. G., and Bechstedt, F. *Phys. Rev. Lett.*, **88**, 016402 (2001) .

[62] Bloembergen, N., Chang, R. K., Jha, S. S., and Lee, C. H. *Phys. Rev.*, **174**, 813–822 (1968) .

[63] Bergfeld, S. and Daum, W. *Phys. Rev. Lett.*, **90**, 036801 (2003) .

[64] Tom, H. W. K., Heinz, T. F., and Shen, Y. R. *Phys. Rev. Lett.*, **51**, 1983–1986 (1983) .

[65] Downer, M. C., Mendoza, B. S., and Gavrilenko, V. I. *Surface and Interface Analysis*, **31**, 966–986 (2001) .

[66] Wang, F. X., Rodriguez, F. J., Albers, W. M., Ahorinta, R., Sipe, J. E., and Kauranen, M. *Phys. Rev. B*, **80**, 233402 (2009) .

[67] Yang, S. A., Li, X., Bristow, A. D., and Sipe, J. E. *Phys. Rev. B*, **80**, 165306 (2009) .

[68] Gavrilenko, V. I. *Phys. Rev. B*, **77**, 155311 (2008) .

[69] Savoia, A., et al. *Phys. Rev. B*, **80**, 075110 (2009) .

[70] Kumar, N., Najmaei, S., Cui, Q., Ceballos, F., Ajayan, P., Lou, J., and Zhao, H. *Phys. Rev. B*, **87**, 161403 (2013) .

[71] Li, Y., Rao, Y., Mak, K. F., You, Y., Wang, S., Dean, C. R., and Heinz, T. F. *Nano Letters*, **13**, 3329–3333 (2013) PMID: 23718906.

[72] Bloembergen, N. and Pershan, P. *Phys. Rev.*, **128**, 606–622 (1962) .

[73] Mizrahi, V. and Sipe, J. E. *J. Opt. Soc. Am. B*, **5**, 660–667 (1988) .

[74] McGilp, J. F. *physica status solidi (a)*, **175**, 153–167 (1999) .

[75] Sipe, J. E., Moss, D. J., and van Driel, H. M. *Phys. Rev. B*, **35**, 1129–1141 (1987) .

[76] Qiang An, Y. and Cundiff, S. T. *Applied Physics Letters*, **81**, 5174–5176 (2002) .

[77] Kelly, P., Tang, Z.-R., Woolf, D., Williams, R., and McGilp, J. *Surface Science*, **251–252**, 87 – 91 (1991) .

[78] Falasconi, M., Andreani, L., Malvezzi, A., Patrini, M., Mulloni, V., and Pavesi, L. *Surface Science*, **481**, 105 – 112 (2001) .

[79] An, Y. Q. and Cundiff, S. T. *Phys. Rev. B*, **67**, 193302 (2003) .

[80] Qiang An, Y. and Cundiff, S. T. *Applied Physics Letters*, **81**, 5174–5176 (2002) .

[81] Aktsipetrov, O. A., et al. *Phys. Rev. B*, **60**, 8924–8938 (1999) .

[82] van Hasselt, C. W., Devillers, M. A. C., Rasing, T., and Aktsipetrov, O. A. *J. Opt. Soc. Am. B*, **12**, 33–36 (1995) .

[83] Bagchi, A., Barrera, R. G., and Rajagopal, A. K. *Phys. Rev. B*, **20**, 4824–4838 (1979) .

[84] Botti, S., Schindlmayr, A., Del Sole, R., and Reining, L. *Reports on Progress in Physics*, **70**, 357 (2007) .

[85] Franson, J. D. and Donegan, M. M. *Phys. Rev. A*, **65**, 052107 (2002) .

[86] Born, M. and Oppenheimer, R. *Annalen der Physik*, **389**, 457–484 (1927) .

[87] Hohenberg, P. and Kohn, W. *Phys. Rev.*, **136**, B864–B871 (1964) .

[88] Martin, R. M., *Electronic structure: basic theory and practical methods* (2004) Cambridge university press.

[89] Kohn, W. *Rev. Mod. Phys.*, **71**, 1253–1266 (1999) .

[90] Levy, M. *Phys. Rev. A*, **26**, 1200–1208 (1982) .

[91] Lieb, E. H. (1982) Density functionals for coulomb systems. *Physics as Natural Philosophy: Essays in Honor of Laszlo Tisza on His 75th Birthday*, p. 111, A. Shimony and H. Feshbach (MIT, Cambridge, MA).

[92] Vignale, G. and Rasolt, M. *Phys. Rev. Lett.*, **59**, 2360–2363 (1987) .

[93] Vignale, G. and Rasolt, M. *Phys. Rev. B*, **37**, 10685–10696 (1988) .

[94] Mermin, N. D. *Phys. Rev.*, **137**, A1441–A1443 (1965) .

[95] Thomas, L. H. (1927) The calculation of atomic fields. *Mathematical Proceedings of the Cambridge Philosophical Society*, vol. 23, pp. 542–548, Cambridge Univ Press.

[96] Fermi, E. (1927) Un metodo statistico per la determinazione di alcune priorieta dell'atome. *Rend. Accad. Naz. Lincei*, vol. 6, pp. 602–607.

[97] Kohn, W. and Sham, L. J. *Phys. Rev.*, **140**, A1133–A1138 (1965) .

[98] Ceperley, D. M. and Alder, B. J. *Phys. Rev. Lett.*, **45**, 566–569 (1980) .

[99] Moroni, S., Ceperley, D. M., and Senatore, G. *Phys. Rev. Lett.*, **75**, 689–692 (1995) .

[100] Ortiz, G., Harris, M., and Ballone, P. *Phys. Rev. Lett.*, **82**, 5317–5320 (1999) .

[101] Becke, A. D. *Phys. Rev. A*, **38**, 3098–3100 (1988) .

[102] Perdew, J. P. and Wang, Y. *Phys. Rev. B*, **45**, 13244–13249 (1992) .

[103] Perdew, J. P., Burke, K., and Ernzerhof, M. *Phys. Rev. Lett.*, **77**, 3865–3868 (1996) .

[104] Ullrich, C. A., Gossmann, U. J., and Gross, E. K. U. *Phys. Rev. Lett.*, **74**, 872–875 (1995) .

[105] Kümmel, S. and Perdew, J. P. *Phys. Rev. Lett.*, **90**, 043004 (2003) .

[106] Perdew, J. P., Ernzerhof, M., and Burke, K. *The Journal of Chemical Physics*, **105**, 9982–9985 (1996) .

[107] Goedecker, S., Teter, M., and Hutter, J. *Phys. Rev. B*, **54**, 1703–1710 (1996) .

[108] Runge, E. and Gross, E. K. U. *Phys. Rev. Lett.*, **52**, 997–1000 (1984) .

[109] Marques, M., *Time-Dependent Density Functional Theory* (2006) Lecture Notes in Physics, Springer.

[110] Vignale, G. and Kohn, W. *Phys. Rev. Lett.*, **77**, 2037–2040 (1996) .

[111] Gross, E., Dobson, J., and Petersilka, M. (1996) Density functional theory of time-dependent phenomena. *Density Functional Theory II*, pp. 81–172, Springer.

[112] Onida, G., Reining, L., and Rubio, A. *Rev. Mod. Phys.*, **74**, 601–659 (2002) .

[113] van Leeuwen, R. *Phys. Rev. Lett.*, **80**, 1280–1283 (1998) .

[114] Botti, S., Sottile, F., Vast, N., Olevano, V., Reining, L., Weissker, H.-C., Rubio, A., Onida, G., Del Sole, R., and Godby, R. W. *Phys. Rev. B*, **69**, 155112 (2004) .

[115] Gonze, X., et al. *Computational Materials Science*, **25**, 478–492 (2002) .

[116] http://www.dp-code.org/.

[117] Huebener, H., Luppi, E., and Veniard, V., (unpublished).

[118] Bloch, F. *Zeitschrift für Physik*, **52**, 555–600 (1929) .

[119] Payne, M. C., Teter, M. P., Allan, D. C., Arias, T. A., and Joannopoulos, J. D. *Rev. Mod. Phys.*, **64**, 1045–1097 (1992) .

[120] Kleinman, L. and Bylander, D. M. *Phys. Rev. Lett.*, **48**, 1425–1428 (1982) .

[121] Motta, C., Giantomassi, M., Cazzaniga, M., Gaál-Nagy, K., and Gonze, X. *Computational Materials Science*, **50**, 698 – 703 (2010) .

[122] Choudhury, B. D., Sahoo, P. K., Sanatinia, R., Andler, G., Anand, S., and Swillo, M. *Opt. Lett.*, **40**, 2072–2075 (2015) .

[123] http://en.wikipedia.org/wiki/silicon.

[124] Becker, P., Scyfried, P., and Siegert, H. *Zeitschrift für Physik B Condensed Matter*, **48**, 17–21 (1982) .

[125] Okada, Y. and Tokumaru, Y. *Journal of Applied Physics*, **56**, 314–320 (1984) .

[126] Bludau, W., Onton, A., and Heinke, W. *Journal of Applied Physics*, **45**, 1846–1848 (1974) .

[127] Lautenschlager, P., Garriga, M., Vina, L., and Cardona, M. *Phys. Rev. B*, **36**, 4821–4830 (1987) .

[128] Li, H. *Journal of Physical and Chemical Reference Data*, **9**, 561–658 (1980) .

[129] Cardona, M., Shaklee, K., and Pollak, F. *Phys. Rev.*, **154**, 696–720 (1967) .

[130] Li, H. *Journal of Physical and Chemical Reference Data*, **5**, 329–528 (1976) .

[131] Lyon, K., Salinger, G., Swenson, C., and White, G. *Journal of Applied Physics*, **48**, 865–868 (1977) .

[132] Yim, W. M. and Paff, R. J. *Journal of Applied Physics*, **45**, 1456–1457 (1974) .

[133] Daum, W., Krause, H.-J., Reichel, U., and Ibach, H. *Phys. Rev. Lett.*, **71**, 1234–1237 (1993) .

[134] Qiang An, Y. and Cundiff, S. T. *Applied Physics Letters*, **81**, 5174–5176 (2002) .

[135] Mendoza, B. S., Gaggiotti, A., and Del Sole, R. *Phys. Rev. Lett.*, **81**, 3781–3784 (1998) .

[136] Lim, D., Downer, M. C., Ekerdt, J. G., Arzate, N., Mendoza, B. S., Gavrilenko, V. I., and Wu, R. Q. *Phys. Rev. Lett.*, **84**, 3406–3409 (2000) .

[137] J. E. Mejia, C. S. and Mendoza, B. S. *Revista mexicana de fisica*, **50**, 134 (2004) .

[138] Sano, H., Mizutani, G., Wolf, W., and Podloucky, R. *Phys. Rev. B*, **66**, 195338 (2002) .

[139] Mendoza, B. S., Palummo, M., Onida, G., and Del Sole, R. *Phys. Rev. B*, **63**, 205406 (2001) .

[140] Mejia, J. E. and Mendoza, B. S. *Surface Science*, **487**, 180 (2001) .

[141] N. Arzate, e. a. *Applied Physics B*, **68**, 629–632 (1999) .

[142] Nayfeh, M. H., Akcakir, O., Belomoin, G., Barry, N., Therrien, J., and Gratton, E. *Applied Physics Letters*, **77**, 4086–4088 (2000) .

[143] Dolgova, T. V., Maidykovski, A. I., Martemyanov, M. G., Fedyanin, A. A., Aktsipetrov, O. A., Marowsky, G., Yakovlev, V. A., and Mattei, G. *Applied Physics Letters*, **81**, 2725–2727 (2002) .

[144] Tiwari, S., Rana, F., Hanafi, H., Hartstein, A., Crabbé, E. F., and Chan, K. *Applied Physics Letters*, **68**, 1377–1379 (1996) .

[145] Walters, R. J., Kik, P. G., Casperson, J. D., Atwater, H. A., Lindstedt, R., Giorgi, M., and Bourianoff, G. *Applied Physics Letters*, **85**, 2622–2624 (2004) .

[146] Rao, R., et al. *Solid-State Electronics*, **48**, 1463–1473 (2004) .

[147] Conibeer, G., et al. *Thin Solid Films*, **511**, 654–662 (2006) .

[148] Conibeer, G., et al. *Thin Solid Films*, **516**, 6748–6756 (2008) .

[149] Timmerman, D., Izeddin, I., Stallinga, P., Yassievich, I., and Gregorkiewicz, T. *Nature Photonics*, **2**, 105–109 (2008) .

[150] Liu, C.-Y., Holman, Z. C., and Kortshagen, U. R. *Nano letters*, **9**, 449–452 (2008) .

[151] Figliozzi, P., Sun, L., Jiang, Y., Matlis, N., Mattern, B., Downer, M., Withrow, S., White, C., Mochán, W., and Mendoza, B. *Phys. Rev. Lett.*, **94**, 047401 (2005) .

[152] Jiang, Y., Wilson, P., Downer, M., White, C., and Withrow, S. (2001) Second-harmonic generation from silicon nanocrystals embedded in sio/sub 2/. *Lasers and Electro-Optics, 2001. CLEO '01. Technical Digest. Summaries of papers presented at the Conference on*, May, pp. 552–553.

[153] Bechstedt, F., *Principles of surface physics* (2003) Springer Berlin.

[154] Ramstad, A., Brocks, G., and Kelly, P. *Phys. Rev. B*, **51**, 14504–14523 (1995) .

[155] Badt, D., Wengelnik, H., and Neddermeyer, H. *Journal of Vacuum Science & Technology B*, **12**, 2015–2017 (1994) .

[156] Power, J., O'Mahony, J., Chandola, S., and McGilp, J. *Phys. Rev. Lett.*, **75**, 1138–1141 (1995) .

[157] Lüpke, G., Bottomley, D. J., and van Driel, H. M. *J. Opt. Soc. Am. B*, **11**, 33–44 (1994) .

[158] Ehlert, R., Kwon, J., Loumakos, L., Sharia, O., Demkov, A. A., and Downer, M. C. *J. Opt. Soc. Am. B*, **27**, 981–989 (2010) .

[159] Chadi, D. *Phys. Rev. Lett.*, **43**, 43–47 (1979) .

[160] Himpsel, F. J. and Eastman, D. E. *Journal of Vacuum Science & Technology*, **16**, 1297–1299 (1979) .

[161] Rohlfing, M., Krüger, P., and Pollmann, J. *Phys. Rev. B*, **52**, 13753–13756 (1995) .

[162] Http://www.afm.eei.eng.osaka-u.ac.jp/gallery.html.

[163] Dabrowski, J. and Müssig, H., *Silicon Surfaces and Formation of Interfaces: Basic Science in the Industrial World* (2000) World Scientific.

[164] Over, H., Wasserfall, J., Ranke, W., Ambiatello, C., Sawitzki, R., Wolf, D., and Moritz, W. *Phys. Rev. B*, **55**, 4731–4736 (1997) .

[165] Takahasi, M., Nakatani, S., Ito, Y., Takahashi, T., Zhang, X., and Ando, M. *Surface Science*, **338**, L846 – L850 (1995) .

[166] Felici, R., Robinson, I., Ottaviani, C., Imperatori, P., Eng, P., and Perfetti, P. *Surface Science*, **375**, 55 – 62 (1997) .

[167] Jasinski, J. M., Meyerson, B. S., and Scott, B. A. *Annual Review of Physical Chemistry*, **38**, 109–140 (1987) .

[168] Yablonovitch, E., Allara, D. L., Chang, C. C., Gmitter, T., and Bright, T. B. *Phys. Rev. Lett.*, **57**, 249–252 (1986) .

[169] Oura, K., Lifshits, V., Saranin, A., Zotov, A., and Katayama, M. *Surface Science Reports*, **35**, 1 – 69 (1999) .

[170] Chabal, Y. and Raghavachari, K. *Phys. Rev. Lett.*, **54**, 1055–1058 (1985) .

[171] Boland, J. J. *Phys. Rev. Lett.*, **65**, 3325–3328 (1990) .

[172] Lauridsen, E., Baker, J., Nielsen, M., Feidenhans'l, R., Falkenberg, G., Bunk, O., Zeysing, J., and Johnson, R. *Surface Science*, **453**, 18 – 24 (2000) .

[173] Weast, R. C., Astle, M. J., and Beyer, W. H., *CRC handbook of chemistry and physics* (1988) vol. 69. CRC press Boca Raton, FL.

[174] Fluegel, B., Mascarenhas, A., Geisz, J. F., and Olson, J. M. *Phys. Rev. B*, **57**, R6787–R6790 (1998) .

[175] Sharma, S., Dewhurst, J. K., and Ambrosch-Draxl, C. *Phys. Rev. B*, **67**, 165332 (2003) .

[176] Grüning, M. and Attaccalite, C. *Phys. Rev. B*, **89**, 081102 (2014) .

[177] Bertocchi, M., Luppi, E., Degoli, E., Véniard, V., and Ossicini, S. *The Journal of chemical physics*, **140**, 214705 (2014) .

[178] Attaccalite, C. and Grüning, M. *Phys. Rev. B*, **88**, 235113 (2013) .

[179] Denk, R., et al. *Nature communications*, **5** (2014) .

[180] Hogan, C., Ferraro, E., McAlinden, N., and McGilp, J. F. *Phys. Rev. Lett.*, **111**, 087401 (2013) .

[181] Palummo, M., Witkowski, N., Pluchery, O., Del Sole, R., and Borensztein, Y. *Phys. Rev. B*, **79**, 035327 (2009) .

[182] Hogan, C., Del Sole, R., and Onida, G. *Phys. Rev. B*, **68**, 035405 (2003) .

[183] Reining, L., Del Sole, R., Cini, M., and Ping, J. G. *Phys. Rev. B*, **50**, 8411–8422 (1994) .

[184] Moss, D. J., Ghahramani, E., Sipe, J. E., and van Driel, H. M. *Phys. Rev. B*, **41**, 1542–1560 (1990) .

[185] Ghahramani, E., Moss, D. J., and Sipe, J. E. *Phys. Rev. B*, **43**, 8990–9002 (1991) .

[186] Sipe, J. E. and Shkrebtii, A. I. *Phys. Rev. B*, **61**, 5337–5352 (2000) .

[187] C. Cohen-Tannoudji, B. D. and Laloë, F., *Mecanique quantique I* (1980) Hermann, 293 rue Lecourbe, 75015 Paris.

[188] Sipe, J. E. and Ghahramani, E. *Phys. Rev. B*, **48**, 11705–11722 (1993) .

[189] Leitsmann, R., Schmidt, W. G., Hahn, P. H., and Bechstedt, F. *Phys. Rev. B*, **71**, 195209 (2005) .

[190] Allan, G. and Delerue, C. *Phys. Rev. B*, **86**, 165437 (2012) .

[191] Pi, X. and Delerue, C. *Phys. Rev. Lett.*, **111**, 177402 (2013) .

[192] Mendoza, B. S., Nastos, F., Arzate, N., and Sipe, J. E. *Phys. Rev. B*, **74**, 075318 (2006) .

[193] Caramella, L., Hogan, C., Onida, G., and Del Sole, R. *Phys. Rev. B*, **79**, 155447 (2009) .

[194] Niquet, Y. M., Rideau, D., Tavernier, C., Jaouen, H., and Blase, X. *Phys. Rev. B*, **79**, 245201 (2009) .

[195] Zheng, Y., Rivas, C., Lake, R., Alam, K., Boykin, T., and Klimeck, G. *Electron Devices, IEEE Transactions on*, **52**, 1097–1103 (2005) .

[196] Miranda, A., Vazquez, R., Diaz-Mendez, A., and Cruz-Irisson, M. *Microelectronics Journal*, **40**, 456 – 458 (2009) Workshop of Recent Advances on Low Dimensional Structures and Devices (WRA-LDSD).

[197] Kuhn, W. *Zeitschrift für Physik*, **33**, 408–412 (1925) .

[198] Reiche, F. and Thomas, W. *Zeitschrift für Physik*, **34**, 510–525 (1925) .

[199] Harrison, W. A. and Ciraci, S. *Phys. Rev. B*, **10**, 1516–1527 (1974) .

[200] Anderson, S. M., Tancogne-Dejean, N., Mendoza, B. S., and Véniard, V. *Phys. Rev. B*, **91**, 075302 (2015) .

[201] Graf, M. and Vogl, P. *Phys. Rev. B*, **51**, 4940–4949 (1995) .

[202] Castillo, C., Mendoza, B. S., Schmidt, W. G., Hahn, P. H., and Bechstedt, F. *Phys. Rev. B*, **68**, 041310 (2003) .

[203] Arzate, N. and Mendoza, B. S. *Phys. Rev. B*, **63**, 125303 (2001) .

[204] Barrera, R. G. and Bagchi, A. *Phys. Rev. B*, **20**, 3186–3196 (1979) .

[205] Apell, P. *Physica Scripta*, **17**, 535 (1978) .

[206] van Schilfgaarde, M., Kotani, T., and Faleev, S. *Phys. Rev. Lett.*, **96**, 226402 (2006) .

[207] Levine, Z. H. and Allan, D. C. *Phys. Rev. Lett.*, **63**, 1719–1722 (1989) .

[208] Levine, Z. H. and Allan, D. C. *Phys. Rev. B*, **43**, 4187–4207 (1991) .

[209] Del Sole, R. and Girlanda, R. *Phys. Rev. B*, **48**, 11789–11795 (1993) .

[210] Kipp, L., Biegelsen, D. K., Northrup, J. E., Swartz, L.-E., and Bringans, R. D. *Phys. Rev. Lett.*, **76**, 2810–2813 (1996) .

[211] Gaál-Nagy, K., Incze, A., Onida, G., Borensztein, Y., Witkowski, N., Pluchery, O., Fuchs, F., Bechstedt, F., and Del Sole, R. *Phys. Rev. B*, **79**, 045312 (2009) .

[212] Ismail-Beigi, S., Chang, E. K., and Louie, S. G. *Phys. Rev. Lett.*, **87**, 087402 (2001) .

[213] Luppi, E., Weissker, H.-C., Bottaro, S., Sottile, F., Veniard, V., Reining, L., and Onida, G. *Phys. Rev. B*, **78**, 245124 (2008) .

[214] Hybertsen, M. S. and Louie, S. G. *Phys. Rev. B*, **34**, 5390–5413 (1986) .

[215] Garcıa-González, P. and Godby, R. *Computer physics communications*, **137**, 108–122 (2001) .

[216] Troullier, N. and Martins, J. L. *Phys. Rev. B*, **43**, 1993–2006 (1991) .

[217] Mendoza, B. S., Nastos, F., Arzate, N., and Sipe, J. E. *Phys. Rev. B*, **74**, 075318 (2006) .

[218] V. Véniard, private communication.

[219] Nastos, F., Olejnik, B., Schwarz, K., and Sipe, J. E. *Phys. Rev. B*, **72**, 045223 (2005) .

[220] Rohlfing, M., Krüger, P., and Pollmann, J. *Phys. Rev. B*, **52**, 1905–1917 (1995) .

[221] Asahi, R., Mannstadt, W., and Freeman, A. J. *Phys. Rev. B*, **62**, 2552–2561 (2000) .

[222] Cabellos, J. L., Mendoza, B. S., Escobar, M. A., Nastos, F., and Sipe, J. E. *Phys. Rev. B*, **80**, 155205 (2009) .

[223] Leitsmann, R., Schmidt, W. G., Hahn, P. H., and Bechstedt, F. *Phys. Rev. B*, **71**, 195209 (2005) .

[224] Adolph, B. and Bechstedt, F. *Phys. Rev. B*, **62**, 1706–1712 (2000) .

[225] Incze, A., Del Sole, R., and Onida, G. *Phys. Rev. B*, **71**, 035350 (2005) .

[226] Mendoza, B. S., Gaggiotti, A., and Del Sole, R. *Phys. Rev. Lett.*, **81**, 3781–3784 (1998) .

[227] Gavrilenko, V. I., Wu, R. Q., Downer, M. C., Ekerdt, J. G., Lim, D., and Parkinson, P. *Phys. Rev. B*, **63**, 165325 (2001) .

[228] Mejía, J. E., Mendoza, B. S., Palummo, M., Onida, G., Del Sole, R., Bergfeld, S., and Daum, W. *Phys. Rev. B*, **66**, 195329 (2002) .

[229] Rigamonti, S., Botti, S., Veniard, V., Draxl, C., Reining, L., and Sottile, F. *Phys. Rev. Lett.*, **114**, 146402 (2015) .

[230] The x-axis is defined as the crystallographic direction [011] and the z-axis correspond to the direction [001].

[231] Aspnes, D. E. and Studna, A. A. *Phys. Rev. Lett.*, **54**, 1956–1959 (1985) .

[232] Mantese, L., Bell, K., Aspnes, D., and Rossow, U. *Physics Letters A*, **253**, 93 – 97 (1999) .

[233] Del Sole, R. and Fiorino, E. *Phys. Rev. B*, **29**, 4631–4645 (1984) .

[234] Del Sole, R. and Selloni, A. *Phys. Rev. B*, **30**, 883–893 (1984) .

[235] Hahn, P. H., Schmidt, W. G., Bechstedt, F., Pulci, O., and Del Sole, R. *Phys. Rev. B*, **68**, 033311 (2003) .

[236] Hermann, A., Schmidt, W. G., and Bechstedt, F. *Phys. Rev. B*, **71**, 153311 (2005) .

[237] Fuchs, F., Schmidt, W. G., and Bechstedt, F. *Phys. Rev. B*, **72**, 075353 (2005) .

[238] Nguyen, H. V., Lu, Y., Kim, S., Wakagi, M., and Collins, R. W. *Phys. Rev. Lett.*, **74**, 3880–3883 (1995) .

[239] Yoo, H. G. and Fauchet, P. M. *Phys. Rev. B*, **77**, 115355 (2008) .

[240] Aspnes, D. *Thin Solid Films*, **89**, 249 – 262 (1982) .

[241] Freysoldt, C., Eggert, P., Rinke, P., Schindlmayr, A., and Scheffler, M. *Phys. Rev. B*, **77**, 235428 (2008) .

[242] Silkin, V. M., Chulkov, E. V., and Echenique, P. M. *Phys. Rev. Lett.*, **93**, 176801 (2004) .

[243] Ehlers, D. H. and Mills, D. L. *Phys. Rev. B*, **36**, 1051–1067 (1987) .

[244] Öğüt, S., Burdick, R., Saad, Y., and Chelikowsky, J. R. *Phys. Rev. Lett.*, **90**, 127401 (2003) .

[245] Tiago, M. L. and Chelikowsky, J. R. *Phys. Rev. B*, **73**, 205334 (2006) .

[246] MATLAB, *version 7.14.0 (R2012a)* (2012) The MathWorks Inc.

[247] Del Sole, R., Mochan, W. L., and Barrera, R. G. *Phys. Rev. B*, **43**, 2136–2140 (1991) .

[248] Wijers, C. M. J., Del Sole, R., and Manghi, F. *Phys. Rev. B*, **44**, 1825–1831 (1991) .

[249] Mendoza, B. S. and Mochán, W. L. *Phys. Rev. B*, **53**, R10473–R10476 (1996) .

[250] Mejía, J. and Mendoza, B. *physica status solidi (a)*, **188**, 1393–1400 (2001) .

[251] An, Y. Q., Carriles, R., and Downer, M. C. *Phys. Rev. B*, **75**, 241307 (2007) .

[252] Yilmaz, M. B., Rajagopal, A., and Zimmermann, F. M. *Phys. Rev. B*, **69**, 125413 (2004) .

[253] Gielis, J. J. H., van den Oever, P. J., Hoex, B., van de Sanden, M. C. M., and Kessels, W. M. M. *Phys. Rev. B*, **77**, 205329 (2008) .

[254] Parkinson, P., Lim, D., Büngener, R., Ekerdt, J., and Downer, M. *Applied Physics B*, **68**, 641–648 (1999) .

[255] Scandolo, S. and Bassani, F. *Phys. Rev. B*, **51**, 6925–6927 (1995) .

[256] Schmidt, W. G., Bechstedt, F., and Bernholc, J. *Phys. Rev. B*, **63**, 045322 (2001) .

[257] Palummo, M., Onida, G., Del Sole, R., and Mendoza, B. S. *Phys. Rev. B*, **60**, 2522–2527 (1999) .

[258] Bechstedt, F., Pulci, O., and Schmidt, W. G. *physica status solidi (a)*, **175**, 5–16 (1999) .

[259] Höfer, U. *Applied Physics A*, **63**, 533–547 (1996) .

[260] Power, J. R., O'Mahony, J. D., Chandola, S., and McGilp, J. F. *Phys. Rev. Lett.*, **75**, 1138–1141 (1995) .

[261] Albrecht, S., Reining, L., Del Sole, R., and Onida, G. *Phys. Rev. Lett.*, **80**, 4510–4513 (1998) .

[262] Pulci, O., Marini, A., Palummo, M., and Del Sole, R. *Phys. Rev. B*, **82**, 205319 (2010) .

[263] Onida, G., Reining, L., Godby, R. W., Del Sole, R., and Andreoni, W. *Phys. Rev. Lett.*, **75**, 818–821 (1995) .

[264] Hübener, H., Luppi, E., and Véniard, V. *Phys. Rev. B*, **83**, 115205 (2011) .

[265] Lautenschlager, P., Garriga, M., Vina, L., and Cardona, M. *Phys. Rev. B*, **36**, 4821–4830 (1987) .

[266] Botti, S., Fourreau, A., Nguyen, F. m. c., Renault, Y.-O., Sottile, F., and Reining, L. *Phys. Rev. B*, **72**, 125203 (2005) .

[267] Botti, S., Castro, A., Andrade, X., Rubio, A., and Marques, M. A. L. *Phys. Rev. B*, **78**, 035333 (2008) .

[268] Varsano, D., Marini, A., and Rubio, A. *Phys. Rev. Lett.*, **101**, 133002 (2008) .

[269] Weissker, H.-C., Serrano, J., Huotari, S., Luppi, E., Cazzaniga, M., Bruneval, F., Sottile, F., Monaco, G., Olevano, V., and Reining, L. *Phys. Rev. B*, **81**, 085104 (2010) .

[270] Sagmeister, S. and Ambrosch-Draxl, C. *Phys. Chem. Chem. Phys.*, **11**, 4451–4457 (2009) .

[271] von Helmholtz, H., *Über Integrale der hydrodynamischen Gleichungen, welche den Wirbelbewegungen entsprechen* (1858) Reimer.

[272] Aversa, C. and Sipe, J. E. *Phys. Rev. B*, **52**, 14636–14645 (1995) .

Acknowledgements

I would like to thank all these wonderful people I owe a deep sense of gratitude for support during this thesis. Here I could not thank all these people and I probably forget many names.
First of all, I would like to thank my supervisor Valérie Véniard for her availability and guidance whenever it was necessary, and also for creating a very stimulating working atmosphere suitable for developing my ideas. Her top-level expertise, her rigour and her constant availability in case of doubt or questions have make this thesis feasible.
I also thank the whole group of the Theoretical spectroscopy of the LSI for a very enjoyable, and collaborative and friendly environment. They all have been always available for scientific or informal discussions, in particular Claudia Rödl. Also I am thankful to Andrea Cucca, Francesco Sottile and Valérie Véniard for spending time organizing this greet event which is the Oinos.
Further, I would like to thank all the Italian people who helped me learning Italian during my thesis, and in particular Lorenzo Sponza, Matteo Guzzo and Andrea Cucca. They were always present for pointing me my mistakes and helping me improving my Italian. I also would like to thank Matteo Gatti for all the scientific or informal discussions but more importantly for bringing me this citation of Wolfgang Pauli "God made the bulk. Surfaces were invented by the devil.", which stayed on the door of my office during almost all my PhD.
Finally, I would like to thank all the other organizers of the 12th ETSF Young Researchers' Meeting their very good work during the organisation of this meeting.

Abstract

More than 50 years after the first experimental observation of second-harmonic generation, the theoretical description of second-harmonic generation is still under debate, whereas it is well understood from an experimental point of view. This is the gap that this thesis aims to fill.
This work aims to improve the theoretical description and understanding of the generation of second-harmonic from the surfaces of crystalline semiconductors.
When applying an external electric field to a dielectric material, electric dipoles are created at a microscopic level. These dipoles are responsible for the apparition, inside the material, of an induced field. The fluctuations of the electric field at a microscopic level, the density fluctuations or any kind of microscopic inhomogeneities must be taken into account when describing the optical properties of a system. These effects are often referred as "local-field effects".
These local-field effects have been widely studied in the past and in particular their effects on the optical properties of bulk materials are now well established. In the case of surfaces, the theoretical description and the numerical simulations are more intricate than for bulk materials. The abrupt change in the electronic density leads to a huge variation of the electric field at the interface with vacuum. As a result, strong effects of the local-field are expected, in particular in the direction perpendicular to the plane of the surface.
The goal of this thesis is to quantify how important these effects are for the linear and second-order optical properties of surfaces.
A macroscopic theory of second-harmonic generation from crystal surfaces has been developed in order to account for local-field effects. The latter are calculated from first-principles, in the framework of the Time-Dependent Density-Functional Theory (TDDFT). The primary interest is the description of non-linear optical responses of surfaces, but new theoretical tools for improving the description of local-field effects in the case of linear optics have also been developed.
The numerical simulations have been focused on the Si(001) surface, and the macroscopic formalism developed during this thesis has been applied to three surface reconstructions, namely the clean Si(001)2×1, the monohydride Si(001)2×1:H and the dihydride Si(001)1×1:2H surfaces.
Comparison with available experimental results is also reported.

Résumé

Plus de 50 ans après la première observation expérimentale de la génération de deuxième harmonique, la description théorique de la génération de deuxième harmonique est toujours sujette à débat, alors qu'elle est bien comprise d'un point de vue expérimental. Cette thèse vise à combler ce fossé.
Ce travail a pour but d'améliorer la description théorique ainsi que la compréhension de la génération de deuxième harmonique à la surface des cristaux semi-conducteurs. Lorsque l'on applique un champ électrique extérieur à un matériau diélectrique, des dipôles électriques se créent au niveau microscopique.
Ces dipôles sont responsables de l'apparition, à l'intérieur du matériau, d'un champ induit.
Les fluctuations du champ électrique à l'échelle microscopique, les fluctuations de la densité ou tout type d'inhomogénéités microscopiques doivent être prises en compte lorsque l'on décrit les propriétés optiques d'un système. Ces effets sont souvent appelés "effets des champs locaux".
Les champs locaux ont été largement étudiés par le passé et leurs effets sur les propriétés optiques des matériaux massifs sont maintenant bien établis.
Dans le cas des surfaces, la description théorique et les simulations numériques sont plus compliquées que pour les matériaux massifs. Le changement abrupt de la densité électronique conduit à une variation importante du champ électrique à l'interface avec le vide. Par conséquent, de forts effets dus au champ local sont attendus, en particulier dans la direction perpendiculaire au plan de la surface.
Le but de cette thèse est de quantifier à quel point ces effets affectent les propriétés optiques linéaires et non-linéaires des surfaces.
Une théorie macroscopique de la génération de deuxième harmonique à la surface des cristaux a été développée afin de tenir compte des effets dus aux champs locaux. Ces derniers sont calculés *ab initio*, dans le cadre de la théorie de la fonctionnelle de la densité dépendante du temps (TDDFT). L'intérêt principal de cette thèse est la description de la réponse non-linéaire des surfaces. Néanmoins, de nouveaux outils théoriques permettant une meilleure description des champs locaux et de leurs effets sur les propriétés optiques linéaires ont aussi été développés.
Les simulations numériques se sont focalisées sur la surface Si(001), et le formalisme macroscopique développé durant cette thèse a été appliqué à trois reconstructions de surface, ici la surface propre Si(001)2×1, la surface monohydrique Si(001)2×1:H et la surface dihydrique Si(001)1×1:2H.
Des comparaisons avec les résultats expérimentaux disponibles sont aussi présentées.